

GAS ADSORPTION, DIFFUSION, AND EXCHANGE IN ONE-DIMENSIONAL  
NANOTUBE SYSTEMS BY HYPERPOLARIZED XE-129 NMR

By

CHI-YUAN CHENG

A DISSERTATION PRESENTED TO THE GRADUATE SCHOOL  
OF THE UNIVERSITY OF FLORIDA IN PARTIAL FULFILLMENT  
OF THE REQUIREMENTS FOR THE DEGREE OF  
DOCTOR OF PHILOSOPHY

UNIVERSITY OF FLORIDA

2008

© 2008 Chi-Yuan Cheng

To my family

## ACKNOWLEDGMENTS

Throughout the five years of my graduate career at the University of Florida, there have been many people who helped me. First of all, I would like to appreciate my research advisor: Prof. Russ Bowers. It is a great privilege for me to study physical chemistry and NMR with him. Russ not only gives me the opportunities to share the fun of science, but also reminds me the enjoyable parts of research whenever I encounter the frustrations. His knowledge, hard working and creativity in new ideas will always be an inspiration to me. I would also like to appreciate my supervisory committee, Prof. Angerhofer, Prof. Brucat, Prof. Mareci, and Prof. Omenetto for their advice and the inspiration which I drew from their knowledge and experience.

There are numerous people who contributed to the success of this dissertation. In particular, I would like to express my sincere gratitude to Prof. Cynthia Jameson at the University of Illinois at Chicago who first suggested us to try the hyperpolarized  $^{129}\text{Xe}$  NMR experiments on AV dipeptide nanotubes. She gave us valuable suggestions on our preliminary results during her visit to our lab in 2005. She also encouraged me to participate in the conferences and to discuss the results with people. I benefit a lot in learning from her. I am grateful to Prof. Sergey Vasenkov for his insightful consults on the single-file diffusion. I gratefully acknowledge Prof. George Christou and Dr. Theocharis Stamatatos for their kindly providing the molecular wheel samples. In addition, I appreciate Steve Miles in chemistry electronic shop for his huge assistance on the temperature controller and TTL device. Steve always does perfect works on the troubleshooting of our spectrometer. I thank Joe Shalosky and Todd Prox in chemistry machine shop for teaching me the basic skills of the machining. I also appreciate Marc Link in physics machine shop for generously repairing the broken sample holders as my requests. I am grateful to Joe Caruso in chemistry glass shop who constructed the optical pumping cell and numerous elegant glass components for our experiments. I am indebted

to Greg Labbe and John Graham in physics cryogenic service for supplying us liquid nitrogen and helium, and always give me a hand promptly when I need help in the lab. I would also like to thank Yuying and her husband Liwen for their assistance in collecting the SEM images on the molecular wheels. I am grateful for collaborations, suggestions, discussions, and contributions from the previous and current group members in the Bowers' group: Bhavin Adhyaru, Joshua Caldwell, Jessica Pfeilsticker; Caroline Pointer-Keenan, Yuying Wei and Shea McKeon.

Finally, I would like to appreciate my grandparents, my parents and my wife for their understanding, support, and encouragement in my choosing the career of physical chemistry and NMR.

## TABLE OF CONTENTS

	<u>page</u>
ACKNOWLEDGMENTS .....	4
LIST OF TABLES .....	9
LIST OF FIGURES .....	10
LIST OF ABBREVIATIONS.....	14
ABSTRACT.....	16
1. INTRODUCTION.....	18
2. BACKGROUND.....	21
2.1 Introduction.....	21
2.2 Introduction to NMR .....	21
2.2.1 Spin Polarization .....	22
2.2.2 Chemical Shift Anisotropy .....	25
2.2.3 Exchange NMR .....	30
2.2.4 2D Exchange NMR Spectroscopy.....	33
2.3 Introduction to $^{129}\text{Xe}$ NMR.....	36
2.3.1 Physical Properties of Xe .....	36
2.3.2 One-dimensional van der Waals Guest/Host Systems in Xe NMR .....	38
2.3.3 Xe Chemical Shift .....	39
2.4 Introduction to Hyperpolarized $^{129}\text{Xe}$ NMR.....	40
2.4.1 Improvement of NMR Sensitivity.....	41
2.4.2 Optical Pumping and Spin Exchange.....	43
2.4.3 Continuous-flow Hyperpolarized $^{129}\text{Xe}$ NMR .....	48
2.4.4 Development of Continuous-flow Hyperpolarized Xe Polarizer .....	49
3. INVESTIGATIONS OF THERMODYNAMIC PROPERTIES IN DIPEPTIDE NANOTUBES BY HYPERPOLARIZED XE-129 NMR .....	55
3.1 Introduction.....	55
3.1.1 Determination of Adsorption Enthalpy from Xe Chemical Shift.....	56
3.1.2 Xe Anisotropic NMR Line-shapes in 1D Nanotube Systems .....	58
3.1.3 Dipeptide Nanotubes .....	60
3.2 Experimental.....	62
3.2.1 $^{13}\text{C}$ $T_1$ Relaxation Experiment.....	62
3.2.2 Hyperpolarized $^{129}\text{Xe}$ NMR Experiments .....	63
3.2.3 Scanning Electron Microscopy.....	64
3.3 Results and Discussions.....	65
3.3.1 $^{13}\text{C}$ $T_1$ Relaxation Measurements in AV .....	65
3.3.2 Hyperpolarized $^{129}\text{Xe}$ NMR Spectra in AV.....	67
3.3.3 $^{129}\text{Xe}$ $T_2$ Relaxation Measurements in AV .....	68

3.3.4	Determination of Xe Occupancy in AV .....	70
3.3.5	Isosteric Adsorption Enthalpy of Xe in AV .....	71
3.4	Conclusions.....	74
4.	OBSERVATION OF SINGLE-FILE DIFFUSION IN DIPEPTIDE NANOTUBES BY HYPERPOLARIZED TRACER EXCHANGE XE-129 NMR .....	76
4.1	Introduction.....	76
4.1.1	One-Dimensional Diffusion: Fickian Diffusion and Single-file Diffusion.....	77
4.1.2	Tracer Exchange.....	80
4.2	Experimental.....	83
4.3	Magnetization Exchange Model for Saturation-recovery in 1D Channel .....	86
4.4	Results and Discussions.....	90
4.5	Conclusions.....	94
5.	INVESTIGATIONS OF CHANNEL DIAMETER EFFECT ON GAS DIFFUSION IN GA WHEEL NANOTUBES BY HYPERPOLARIZED XE-129 NMR.....	96
5.1	Introduction.....	96
5.2	Experimental.....	98
5.2.1	Hyperpolarized $^{129}\text{Xe}$ NMR Experiment.....	99
5.2.2	Scanning Electron Microscopy.....	100
5.3	Results and Discussions.....	101
5.3.1	Temperature Dependent Study in $\text{Ga}_{10}$ and $\text{Ga}_{18}$ Nanotubes .....	101
5.3.2	Temperature Dependent Study in $\text{Mn}_{84}$ Nanotubes.....	104
5.3.3	Pressure Dependent Study in $\text{Ga}_{10}$ and $\text{Ga}_{18}$ Nanotubes .....	105
5.3.4	Saturation-recovery Hyperpolarized $^{129}\text{Xe}$ NMR in $\text{Ga}_{10}$ and $\text{Ga}_{18}$ Nanotubes .....	107
5.4	Conclusions.....	112
6.	DIRECT OBSERVATION OF ATOMS ENTERING AND EXITING SINGLE-FILE NANOTUBES BY A TWO-DIMENSIONAL HYPERPOLARIZED XE-129 NMR .....	114
6.1	Introduction.....	114
6.1.1	Thermally-polarized Xe 2D Exchange NMR.....	115
6.1.2	Hyperpolarized Xe 2D Exchange NMR.....	117
6.2	Experimental.....	118
6.3	Magnetization Exchange Model for Continuous-flow Hyperpolarized Xe 2D- EXSY NMR .....	120
6.4	Results and Discussions.....	123
6.5	Conclusions.....	130
7.	SIGNAL ENHANCEMENT OF HYPERPOLARIZED XE-129 2D-NMR EXCHANGE CROSS PEAKs IN NANOTUBES BY INTERRUPTION OF THE GAS FLOW .....	132
7.1	Introduction.....	132
7.2	Experimental.....	135
7.3	Results and Discussions.....	137
7.4	Conclusions.....	141

8.	INVESTIGATIONS OF GAS EXCHANGE IN GA10 WHEEL NANOTUBES BY 2D EXCHANGE HYPERPOLARIZED XE-129 NMR .....	143
8.1	Introduction.....	143
8.2	Experimental.....	145
8.3	Magnetization Exchange Model for 2D-EXSY under Flow Interruption .....	146
8.4	Results and Discussions.....	150
8.5	Conclusions.....	158
9.	CONCLUSIONS AND OUTLOOK .....	161
	APPENDIX .....	166
A.	DERIVATION OF AVERAGE ZEEMAN ORDER IN NANOTUBE PHASE BY GAMMA FUNCTION IDENTITIES.....	166
B.	MATRIX FORMULATION FOR TWO-SITE EXCHANGE SYSTEM.....	169
	LIST OF REFERENCES.....	171
	BIOGRAPHICAL SKETCH .....	185

## LIST OF TABLES

<u>Table</u>		<u>page</u>
2-1	Comparison of NMR properties of $^1\text{H}$ , $^{129}\text{Xe}$ and $^{131}\text{Xe}$ .....	37
3-1	Summary of axial symmetric CSA tensors ( $\eta=0$ ) in 1D single-file channel.....	59
3-2	Summary of $^{13}\text{C}$ $T_1$ relaxation times in AV at 9.4 T and 25 °C .....	67
4-1	Nonlinear regression analysis of saturation-recovery hyperpolarized $^{129}\text{Xe}$ NMR of Xe in AV nanotubes at -10 °C.....	92
5-1	Summary of Xe NMR acquisition parameters of the molecular wheels .....	100
6-1	Best-fit kinetic parameters for CFHP Xe 2D-EXSY spectra in AV at -10 °C.....	126
8-1	Kinetic parameters of Ga <sub>10</sub> nanotubes in CFHP and IFHP 2D-EXSY at 25 °C. ....	158

## LIST OF FIGURES

<u>Figure</u>	<u>page</u>
2-1	Temperature dependence of $^{129}\text{Xe}$ spin polarization at variable magnetic fields.. .....24
2-2	The energy levels of (a) thermal polarization (“hot-spin” system) and (b) hyperpolarization (“cold-spin” system) for spin-1/2 system. ....25
2-3	Chemical shift tensor in different coordinate systems.....27
2-4	Simulated CSA powered spectra of (a) lower symmetry, (b) axial symmetry, (c) cubic symmetry.....29
2-5	Simulated NMR spectra for two-site exchange. (a)(b) fast exchange; (c)(d) intermediate exchange; (e)(f) slow exchange regime. ....32
2-6	NMR pulse sequence of 2D exchange NMR.....33
2-7	Simulated 2D-EXSY spectra with (a) chemical exchange, and (b) no exchange.....36
2-8	Chemical shift range of $^{129}\text{Xe}$ NMR with examples of specified materials. ....40
2-9	The $^{87}\text{Rb}$ energy levels with spin orbital interaction, hyperfine interaction, and Zeeman splitting in the presence of a weak external magnetic field. ....45
2-10	The $^{87}\text{Rb}$ ( $I=3/2$ ) optical pumping for negative circularly polarized light $\sigma^-$ in a weak external magnetic field.. .....46
2-11	Spin-exchange between Rb and Xe.....47
2-12	Continuous-flow hyperpolarized $^{129}\text{Xe}$ apparatus. ....51
2-13	(a) Optical transmission spectra of Rb vapor in the pumping cell at four different cell temperatures (100, 125, 145, 165 °C) at a total gas pressure of 3000 torr (2 % Xe mixture) at 100 W laser power. (b) Flow-rate dependence of Xe spin polarization at different pumping cell temperatures. ....53
2-14	(a) Hyperpolarized $^{129}\text{Xe}$ NMR spectrum. (b) Thermally-polarized $^{129}\text{Xe}$ NMR spectrum.....54
3-1	(a) Molecular structure of L-alanyl- L-valine. (b) Space-filling model of AV nanotube viewed along the channel axis. (c) Stick packing arrangement of AV.. .....61
3-2	Carbon-13 inversion-recovery NMR pulse sequence with proton decoupling during signal acquisition. ....63
3-3	(a) SEM Image of AV polycrystalline nanotubes. (b) Distribution of channel lengths in AV nanotube samples. ....65

3-4	Inversion-recovery $^{13}\text{C}$ NMR spectra recorded as a function of recovery time $\tau$ in AV nanotubes at room temperature.....	66
3-5	Continuous-flow hyperpolarized $^{129}\text{Xe}$ NMR spectra in AV at variable temperatures and 3300 mbar Xe partial pressure at a total gas pressure of 4600 mbar. ....	68
3-6	Hahn spin-echo Xe NMR spectra as a function of interpulse delay at Xe partial pressure of (a) 92 mbar and (b) 3300 mbar at $-10\text{ }^{\circ}\text{C}$ . ....	69
3-7	(a) Experimental thermally-polarized $^{129}\text{Xe}$ spectra at $20\text{ }^{\circ}\text{C}$ at various Xe molar occupancies. <sup>21</sup> (b) The corresponding CSA spectra were simulated to obtain the shielding components.....	70
3-8	Correlation between Xe molar occupancy $\theta_m$ and $\sigma_{\perp}$ component in AV nanotubes. ....	71
3-9	Variation of Xe fractional occupancy $\theta$ with temperature in AV at variable Xe density.....	72
3-10	(a) Variation of the Xe isosteric adsorption enthalpy with the Xe occupancy in AV.(b) Temperature dependence of the Xe equilibrium constant in AV nanotubes.....	74
4-1	The model of asymmetric simple exclusion process (ASEP) with symmetric open boundaries.....	77
4-2	The waveforms of probability density function of (a) normal 1D Fickian diffusion and (b) single-file diffusion corresponding to successively increasing observation time ( $t_1 < t_2 < t_3$ ). ....	79
4-3	Molecular tracer exchange.....	81
4-4	Hyperpolarized NMR tracer exchange.....	82
4-5	NMR pulse sequence of selective continuous-flow saturation-recovery (CFSR) hyperpolarized $^{129}\text{Xe}$ NMR experiment.....	84
4-6	Selective continuous-flow saturation-recovery (CFSR) hyperpolarized $^{129}\text{Xe}$ NMR experiment in AV nanotubes. ....	85
4-7	Least-squares fits to the selective saturation-recovery NMR signal of $^{129}\text{Xe}$ in AV at $T = -10\text{ }^{\circ}\text{C}$ , to the expressions for single-file diffusion (SFD, Eq. (4-20)) and normal diffusion (ND, Eq. (4-22)). (a) Low occupancy: 56 Torr Xe, $\theta = 0.16$ . (c) High occupancy: 2650 Torr Xe, $\theta = 0.66$ . Time-base expansions of (a) and (c) are presented in (b) and (d), respectively.....	91
4-8	(a) Fractional occupancy dependence of the $T_{1c}$ of $^{129}\text{Xe}$ in the adsorbed Xe phase at $T = -10, 10, 25,$ and $40\text{ }^{\circ}\text{C}$ . (b) Fractional occupancy dependence of $C_F(\theta)$ ranged from $\theta = 0.14$ to $0.70$ at $-10\text{ }^{\circ}\text{C}$ .....	93

5-1	Structures of molecular wheels, (a)(d) Ga <sub>10</sub> , (b)(e) Ga <sub>18</sub> , and (c)(f) Mn <sub>84</sub> , with internal diameter of 8.1 Å, 10.4 Å, and 1.9 nm, respectively. (a)(b)(c) are the top view of molecular structures of Ga <sub>10</sub> , Ga <sub>18</sub> , and Mn <sub>84</sub> wheels, respectively. (d)(e)(f) are the corresponding space filling representations of Ga <sub>10</sub> , Ga <sub>18</sub> , and Mn <sub>84</sub> wheel compounds, respectively.....	97
5-2	SEM images of Ga <sub>10</sub> nanotubes shown at length scales of (a) 10µm, (b) 100µm, and (c) 1mm. (d) Length distribution of the Ga <sub>10</sub> crystals.....	101
5-3	Temperature dependence of hyperpolarized <sup>129</sup> Xe NMR Spectra of Xe adsorbed in (a) Ga <sub>10</sub> and (b) Ga <sub>18</sub> molecular wheels.....	102
5-4	Temperature dependence of chemical shift of adsorbed Xe peaks in Ga <sub>10</sub> and Ga <sub>18</sub> nanotubes. ....	104
5-5	Temperature dependence of hyperpolarized Xe NMR spectra of Mn <sub>84</sub> nanotubes.....	105
5-6	Pressure dependence of hyperpolarized Xe NMR Spectra in (a) Ga <sub>10</sub> and (b) Ga <sub>18</sub> nanotubes at 25 °C. ....	106
5-7	Hyperpolarized CFSR <sup>129</sup> Xe NMR experiments in Ga <sub>10</sub> nanotubes with variable Xe partial pressures at room temperature.....	108
5-8	Hyperpolarized CFSR <sup>129</sup> Xe NMR experiments in Ga <sub>18</sub> nanotubes in (a)16.7% and (b)100% Xe with total gas pressure of 4000 mbar. The corresponding time-axis expansions of (a) and (c) are presented in (b) and (d), respectively.....	109
5-9	Xe pressure dependence of (a) $T_{Ic}$ and (b) $C_F$ determined by least-squares fit of Eq. (4-20) in Ga <sub>10</sub> nanotubes. Xe pressure dependence of (c) $T_{Ic}$ and (d) $C_D$ determined by least-squares fit of Eq. (4-22) in Ga <sub>18</sub> nanotubes.....	111
6-1	Simulated mixing-time dependence of (a) diagonal-peak and (b) cross-peak intensities in 2D-EXSY based on two-site exchange model. ....	116
6-2	NMR pulse sequence of CFHP 2D-EXSY. ....	119
6-3	Steady-state continuous-flow hyperpolarized <sup>129</sup> Xe NMR spectra in AV nanotubes, acquired at -10 °C, at the following Xe partial pressures: (a) 92 mbar (b) 1320 mbar (c) 3300 mbar.....	123
6-4	Continuous-flow hyperpolarized <sup>129</sup> Xe 2D-EXSY spectra in AV nanotubes at -10 °C acquired at the mixing times yielding maximum cross-peak intensities: (a) 92 mbar, $\tau_m=35$ ms (b) 1320 mbar, $\tau_m=100$ ms (c) 3300 mbar, $\tau_m=100$ ms.....	125
6-5	Mixing-time dependence of cross- and diagonal-peak signal integrals in the CFHP <sup>129</sup> Xe 2D-EXSY spectra in AV nanotubes at -10 °C. (a) Channel-to-gas, (b) Gas-to-channel cross-peak integrals. (c) Gas-to-gas, (d) channel-to-channel diagonal peak mixing time dependences at 92, 1320 and 3300 mbar.....	127

7-1	Simulated mixing-time dependence of cross-peak signals at variable gas residence time $\tau_R$ and constant desorption rate constant ( $k_d = 3 \text{ s}^{-1}$ ).....	134
7-2	Pulse sequence for (a) continuous-flow (CF) and (b) interrupted-flow (IF) hyperpolarized 2D-EXSY.....	136
7-3	HP $^{129}\text{Xe}$ 2D-EXSY spectra of Xe in AV at $-10^\circ\text{C}$ with mixing times of (a,b) 300 ms and (c,d) 1s. Spectra in (b) and (d) were acquired in continuous-flow (CF) mode. Spectra in (a) and (c) were acquired in interrupted-flow (IF) mode .....	139
7-4	3D representation of HP $^{129}\text{Xe}$ 2D-EXSY spectra of Xe in AV at $-10^\circ\text{C}$ , acquired in (a) IF mode and (b) CF mode, each with a mixing time of $\tau_m=1\text{s}$ .....	140
8-1	Simulated mixing-time dependences of normalized cross-peak signals at (a) variable $T_{lc}$ ( $k_d = 2.5 \text{ s}^{-1}$ ) and (b) variable $k_d$ ( $T_{lc} = 5 \text{ s}$ ). Y-axis expansions of (a) and (b) are presented in (c) and (d), respectively.....	149
8-2	Hyperpolarized $^{129}\text{Xe}$ 2D-EXSY spectra in (a)(b) continuous-flow and (c)(d) interrupted-flow modes in $\text{Ga}_{10}$ nanotubes at $25^\circ\text{C}$ at variable mixing times.....	151
8-3	3D representations of HP 2D-EXSY spectra of Xe in $\text{Ga}_{10}$ nanotubes at $25^\circ\text{C}$ , acquired in (a) IF mode and (b) CF mode.....	152
8-4	Mixing-time dependences of (a) gas-to-gas, (b) channel-to-channel diagonal-peak integrals; (c) gas-to-channel and (d) channel-to-gas cross-peak integrals in CFHP Xe 2D-EXSY spectra of $\text{Ga}_{10}$ nanotubes at $25^\circ\text{C}$ .....	154
8-5	Mixing-time dependences of (a) gas-to-gas, (b) channel-to-channel diagonal-peak integral; (c) gas-to-channel, and (d) channel-to-gas cross-peak integrals in IFHP Xe 2D-EXSY spectra of $\text{Ga}_{10}$ nanotube at $25^\circ\text{C}$ . .....	155

## LIST OF ABBREVIATIONS

1D	one dimensional
2D	two dimensional
3D	three dimensional
ASEP	asymmetric simple exclusion process
AV	L-alanyl-L-valine
CF	continuous flow
CSA	chemical shift anisotropy
DNP	dynamic nuclear polarization
EXSY	exchange spectroscopy
FT	Fourier transformation
FWHM	full width at half maximum
HP	hyperpolarized
IF	interrupted flow
LAB	laboratory axis system
ND	normal diffusion
NOESY	nuclear Overhauser enhancement spectroscopy
OD	outside diameter
OP	optical pumping
PAS	principal axis system
PDF	probability density function
PEEK	polyetheretherketone
PFA	perfluoroalkoxy
PFG	pulsed-field gradient
PHIP	para-hydrogen induced polarization

QENS	quasi-elastic neutron scattering
RF	radio frequency
SAT	saturation pulse train
SE	spin exchange
SEM	scanning electron microscope
SEOP	spin-exchange optical-pumping
SFD	single-file diffusion
SMM	single molecular magnet
SN	solenoid valve
SPINOE	spin polarization induced nuclear Overhauser effect
TMS	tetramethylsilane
TPP	tris( <i>o</i> -phenylenedioxy) cyclotriphosphazene
TTL	transistor-to-transistor logic gate

Abstract of Dissertation Presented to the Graduate School  
of the University of Florida in Partial Fulfillment of the  
Requirements for the Degree of Doctor of Philosophy

GAS ADSORPTION, DIFFUSION, AND EXCHANGE IN ONE-DIMENSIONAL  
NANOTUBE SYSTEMS BY HYPERPOLARIZED XE-129 NMR

By

Chi-Yuan Cheng

August 2008

Chair: Clifford R. Bowers

Major: Chemistry

One-dimensional (1D) nanotube materials hold great promise for a vast range of practical applications. Understanding the fundamental adsorption and transport properties of guest molecules in 1D nanotubes is essential to optimize their performance in such applications. At thermal equilibrium, the symmetric simple exclusion model for 1D channels too narrow for particles to pass one-another predicts the emergence of anomalous diffusion properties. Depending on the density and time-scale, single-file diffusion (SFD) may be observed, where the mean-squared displacement increases as  $t^{1/2}$  rather than  $t$ , as in normal Fickian diffusion (ND). While there are numerous theoretical works on SFD, it is noted that SFD has not been investigated experimentally in detailed.

We have employed continuous-flow hyperpolarized  $^{129}\text{Xe}$  NMR to systematically investigate molecular adsorption, diffusion and exchange of Xe in two types of 1D nanotube systems: the self-assembled L-alanyl-L-valine (AV) dipeptide nanotubes and gallium based wheel-shaped nanotubes ( $\text{Ga}_{10}$  and  $\text{Ga}_{18}$ ), which have the internal channel diameter of 5.13 Å, 8.1 Å and 10.4 Å, respectively. The Xe spectral line-shape in AV exhibits an axially symmetric chemical shielding anisotropy, whereas Xe adsorbed peaks in  $\text{Ga}_{10}$  and  $\text{Ga}_{18}$  nanotubes demonstrate the isotropic NMR line-shapes, implying that Xe in the gallic-wheel nanotubes is

less restricted than Xe in AV nanotubes. Xe occupancy at variable temperature and pressure can be determined from Xe chemical shift. The isosteric enthalpy of Xe adsorption in AV becomes increasing exothermic with increasing Xe occupancy. Moreover, Xe chemical shifts in Ga<sub>10</sub> and Ga<sub>18</sub> nanotubes are almost independent of Xe occupancy over a wide range of Xe pressures at room temperature, indicating Xe-wall interaction is dominated in gallic-wheel nanotube system.

The selective saturation-recovery pulse sequence has been utilized to explore the Xe diffusion in AV and gallic channels. The kinetic model assuming diffusion-limited Langmuir adsorption and the distribution of desorption rate has been proposed. The data clearly showed that the mean-squared displacements of Xe in AV and Ga<sub>10</sub> nanotubes are proportional to the square root of time,  $\langle z^2 \rangle(t) \propto t^{1/2}$ , as in SFD. However, the mean-squared displacement of Xe in Ga<sub>18</sub> nanotubes was observed to be proportional to the diffusion time,  $\langle z^2 \rangle(t) \propto t$ , revealing that the SFD and ND time-scaling of Xe in 1D nanotube systems with different internal diameters can be evidently distinguished by the saturation-recovery hyperpolarized <sup>129</sup>Xe NMR.

Xe exchange in the vicinity of the nanotube openings has been investigated by hyperpolarized <sup>129</sup>Xe 2D exchange NMR (2D-EXSY) in AV and Ga<sub>10</sub> nanotubes. Kinetic analysis of cross and diagonal-peak signals as a function of exchange time yielded the mean desorption rate, which was observed to decrease with increased Xe occupancy in AV channels. Furthermore, our kinetic model indicates that cross-peak amplitudes in the 2D spectrum are strongly attenuated under flow conditions. By incorporating a brief interrupting of the gas flow during the exchange period, we demonstrated that the cross-peak signals can be dramatically enhanced, thereby providing a way to probe slow exchange and diffusion processes in 1D nanotube systems. The results are relevant to potential applications of nanotubes, including gas storage, gas separations, catalysis, drug-delivery and nanofluidics.

## CHAPTER 1 INTRODUCTION

Recently, the physical and chemical properties of materials with one-dimensional (1D) atomic or molecular arrangements have become the subject of intense studies for the developments and applications of future molecular-sized devices, such as gas storage, gas separation, nanofluidics, and catalysts.<sup>1</sup> The adsorption and kinetic processes play a key role in the functions and performances of nanoporous solids. In channels with inner diameters too narrow for the confined particles to mutual passage, normal 1D Fickian diffusion,  $\langle z^2 \rangle(t) = 2D_0t$ , no longer be valid. Instead, the mean-squared displacement of a particle at sufficiently long diffusion time follows  $\langle z^2 \rangle(t) = 2Ft^{1/2}$ , where  $F$  is the single file mobility. The single-file mobility can be affected by several factors, including channel internal structure, adsorbate occupancies, presence of other adsorbates, and guest-guest/guest-host interactions.

<sup>129</sup>Xe NMR spectroscopy has evolved into a unique technique in nanoporous materials over the past three decades.<sup>2</sup> Its large chemical shift range allows the physisorbed phase to be distinguished from the free gas, revealing the interactions with the surface and Xe atoms. For these reasons, <sup>129</sup>Xe NMR has become one of the most powerful techniques available to investigate the local structure in nanoporous materials, such as zeolite<sup>3-12</sup>, polymer<sup>13-18</sup>, nanotube<sup>19-24</sup>, as well as protein<sup>25-31</sup> and liquid crystal.<sup>32-34</sup> Over the past few decades, hyperpolarized <sup>129</sup>Xe has been extensively developed to improve the sensitivity of <sup>129</sup>Xe NMR.<sup>16</sup> Hyperpolarized <sup>129</sup>Xe NMR signals can be enhanced up to four orders of magnitude or more compared to thermally-polarized Xe NMR.<sup>35</sup> Therefore, hyperpolarized <sup>129</sup>Xe NMR can provide exceptionally high sensitivity in the applications of materials characterization, thereby requiring relatively small sample quantities and short instrumentation time for the experiments. It should

be noted that most of the previous works on the nanoporous materials, particularly nanotubes, have focused on the guest-guest/guest-host interactions, pore-space connectivity and structure architectures.<sup>13-23</sup> However, many significant aspects, such as gas adsorption/desorption, exchange, and transport behaviors in nanotubes, are still unclear and need to be investigated further. In this dissertation, the feasibility of applying continuous-flow hyperpolarized  $^{129}\text{Xe}$  NMR to explore Xe gas adsorption/desorption, diffusion, and exchange in single-file nanotubes and other types of 1D nanotube systems will be demonstrated.

This dissertation is organized as follows: In Chapter 2, the relevant portions of theoretical and experimental NMR, particularly hyperpolarized NMR, and the physical properties of Xe gas are briefly reviewed. The development of continuous-flow hyperpolarized Xe polarizer will be presented. Chapter 3 concerns the use of hyperpolarized  $^{129}\text{Xe}$  NMR to explore the adsorption properties of Xe in 1D self-assembled L-alanyl L-valine (AV) dipeptide nanotubes. Chemical shift anisotropy (CSA) powder patterns of Xe in AV nanotubes were recorded as a function of temperature and pressure. The sign inversion of the anisotropy was achieved over the experimental temperature and pressure ranges. The Xe  $\sigma_{\perp}$  shielding component can be utilized to quantitatively determine Xe occupancy in 1D channels. The determinations of isosteric Xe adsorption enthalpy and equilibrium constant in the AV nanotubes according to the Clausius-Clapeyron equation and Langmuir equation will be demonstrated. Chapter 4 describes how selective saturation-recovery hyperpolarized Xe NMR can be used to study the gas diffusion inside the AV channels. A theoretical formalism for the quantitative analysis of saturation-recovery experiments in single-file diffusion and normal 1D Fickian diffusion will be presented. The data in AV nanotubes exhibits the clear signature of single-file diffusion over time scales ranging from 0.5-150 sec. It will be shown that it is feasible to measure  $F$  by saturation-recovery

hyperpolarized  $^{129}\text{Xe}$  NMR. Chapter 5 presents the saturation-recovery hyperpolarized  $^{129}\text{Xe}$  NMR experiments on the molecular wheels nanotubes,  $\text{Ga}_{10}$  and  $\text{Ga}_{18}$ . The internal diameters of gallic-wheel nanotubes are relatively larger than that of AV nanotubes.<sup>36</sup> (*i.e.* 8.1 Å for  $\text{Ga}_{10}$ ; 10.4 Å for  $\text{Ga}_{18}$ ; 5.13 Å for AV) It will be shown that the cross-over of time-scaling of single-file diffusion and normal 1D Fickian diffusion in gallic-wheel nanotubes can be distinguished by saturation-recovery hyperpolarized  $^{129}\text{Xe}$  experiments. In Chapter 6, it will be demonstrated that it is possible to directly observe Xe atoms entering and exiting the single-file nanotube, AV, by continuous-flow hyperpolarized  $^{129}\text{Xe}$  2D exchange NMR (CFHP 2D-EXSY). The theoretical expressions will be presented to quantitatively extract the average desorption rates of Xe in AV nanotube systems. From the expressions, it becomes evident that the cross-peak intensities of 2D-EXSY are strongly attenuated by the finite residence time of hyperpolarized gas in the sample space. By briefly interrupting the gas flow during the exchange periods, the cross-peak intensities are dramatically enhanced. The significant cross-peak signal enhancements of 2D-EXSY in AV nanotubes will be demonstrated in Chapter 7. The mixing-time dependences of 2D-EXSY in  $\text{Ga}_{10}$  nanotubes under continuous-flow and interrupted-flow conditions associated with the corresponding theoretical analysis will be presented in Chapter 8. Chapter 9 summarizes the dissertation and provides some promising future directions of this exciting area.

## CHAPTER 2 BACKGROUND

### 2.1 Introduction

A brief review of the essential aspects of NMR and hyperpolarized NMR that will be used in the following chapters is presented. Section 2.2 presents the basics of NMR, including spin polarization, chemical shift anisotropy, and exchange NMR, following the classic NMR texts of Spiess<sup>37</sup>, Ernst<sup>38</sup>, and Levitt<sup>39</sup>. The physical properties of <sup>129</sup>Xe, Xe chemical shifts and potential applications will be discussed in Section 2.3. In NMR, the signal is typically weak under the ambient conditions. The technique of spin-exchange optical-pumping is a way to overcome this limitation. This aspect will be discussed in Section 2.4.

### 2.2 Introduction to NMR

Magnetic resonance spectroscopy is one of the most powerful tools for studies of molecular structures and dynamics in both liquid and solid systems. It has been extensively used in numerous applications in physics, chemistry and biology since its first discovery by Bloch<sup>40</sup> and Purcell<sup>41</sup> in 1946. The NMR experiment involves a study of interactions of nuclear spins. The bulk NMR sample consists of an ensemble spin systems, which can be described by the total Hamiltonian composed of several spin interaction terms. In principle, the total Hamiltonian in the nuclear spin system is the summation of individual Hamiltonians that describes particular spin interactions:

$$\hat{H} = \sum_{\lambda}^{\text{inter-}} \hat{H}_{\lambda} = \hat{H}_z + \hat{H}_J + \hat{H}_D + \hat{H}_{CS} + \hat{H}_Q + \hat{H}_1 \quad (2-1)$$

where  $\hat{H}_z$  is the Zeeman interaction, which is much greater than any of the other interactions in a strong external magnetic field.  $\hat{H}_J$  is the scalar coupling, which is the interaction of two nuclear-spins through bonding electrons. It is also called the “indirect dipolar” or “ $J$  coupling”.

$\hat{H}_D$  is the dipolar coupling, which is the magnetic interaction of two nuclear-spins through space.  $\hat{H}_{CS}$  corresponds to the chemical shift interaction, which results from the shielding of the magnetic field due to the electron cloud surrounding the nuclear spin.  $\hat{H}_Q$  represents the quadrupole interaction for  $I > 1/2$  nuclei, which is due to the coupling of the electric field gradient and nuclear quadrupole moment.  $\hat{H}_1$  is the time-dependent, applied radiofrequency (RF) field. It can be applied to manipulate the nuclear spins into unique quantum mechanical spin states in such a way that the measured spin dynamics reports selective information about the chemical structures, molecular motions, spin interactions, and the distribution of spin densities.

### 2.2.1 Spin Polarization

When a static external magnetic field  $B_0$  is applied, it breaks the degeneracy and causes each  $(2I + 1)$  sublevel to have a slightly different energy. The interaction between the magnetic dipole moment ( $\mu$ ) and the external magnetic field is known as the Zeeman interaction. The Hamiltonian for the Zeeman interaction is

$$\hat{H}_z = -\gamma\hbar B_0 \hat{I}_z \quad (2-2)$$

where  $\gamma$  is gyromagnetic ratio, and  $\hat{I}_z$  is angular momentum operator along  $B_0$  field (z-axis) with the eigenstate of  $m$ , following  $\hat{I}_z |m\rangle = m|m\rangle$ . According to Boltzmann distribution, the nuclear spin polarization is determined by the population difference between  $m$ -states. For instance, the polarization of  $I = 1/2$  nuclei is

$$P_0 \equiv 2\langle I_z \rangle = \frac{N_\uparrow - N_\downarrow}{N_\uparrow + N_\downarrow} = \frac{1 - \exp\left(\frac{-\gamma\hbar B_0}{k_B T}\right)}{1 + \exp\left(\frac{-\gamma\hbar B_0}{k_B T}\right)} \quad (2-3)$$

where  $N_{\uparrow}$  and  $N_{\downarrow}$  are the populations of spin in  $\alpha$  (spin-up,  $m = +1/2$ ) and  $\beta$  (spin-down,  $m = -1/2$ ) states, respectively,  $k_B$  is the Boltzmann constant, and  $T$  is temperature. The observed NMR signal is proportional to the z-magnetization<sup>42</sup>, which is the product of the nuclei spin polarization  $P_0$ , the fractional isotopic abundance  $f$ , and the total number of detected nuclei in the RF coil region  $n_{NMR}$ .

$$NMR\ signal \propto M_z = P_0 \cdot f \cdot n_{NMR} \quad (2-4)$$

Hence, NMR signal is proportional to the nuclear spin polarization. If  $\alpha$  and  $\beta$  state are equally populated,  $P_0 \rightarrow 0$ , leading to no NMR signal. This situation occurs at thermal equilibrium at sufficiently high temperature or can be reached by “saturating” the spin system by irradiation in a continuous-wave RF field or by application of a single  $\pi/2$  RF pulse followed by a delay longer than the  $T_2$  relaxation time but shorter than the  $T_1$  relaxation time.

At thermal equilibrium, the population difference between the  $\alpha$  and  $\beta$  states is very small, thereby yielding an extremely weak NMR signal. For  $^{129}\text{Xe}$  in the field of 9.4 T (400 MHz NMR) at 300 K, the polarization is only  $P_0 \approx 9 \times 10^{-6}$ . In Eq. (2-3), it is obvious that lower  $T$  and higher  $B_0$  can achieve higher  $P_0$ . For example, at a magnetic field strength of 4.7 T (200 MHz NMR,  $P_0 \rightarrow 1$  can be achieved at  $\sim 10^{-3}$  K (*see* Figure 2-1). The sensitivity improvement obtained using a cryogenic NMR probe<sup>43</sup> has been demonstrated in a variety of applications in solid<sup>44-46</sup> and liquid<sup>47-49</sup> systems. While it is feasible to enhance the NMR signal by cooling the sample to cryogenic temperatures, this approach is usually limited by the increasingly long  $T_1$  relaxation times which result from quenching of molecular motions and/or phonon modes upon lowering the temperature which prevents the nuclear spin system from reaching thermal equilibrium. On

the other hand, the polarization can also be increased by increasing the magnetic field. In the high temperature regime, where  $|\gamma\hbar B_0| \ll k_B T$ , the polarization increases in proportion to the magnetic field. Thus, for  $^{129}\text{Xe}$  spin at 298 K and 21 T (900 MHz NMR), which is the highest magnetic field of the commercial NMR spectrometer to date, the thermal equilibrium polarization is  $P_0 \approx 2 \times 10^{-5}$ . Therefore, the sensitivity increase that can be achieved by simply increasing the magnetic field is relatively modest.

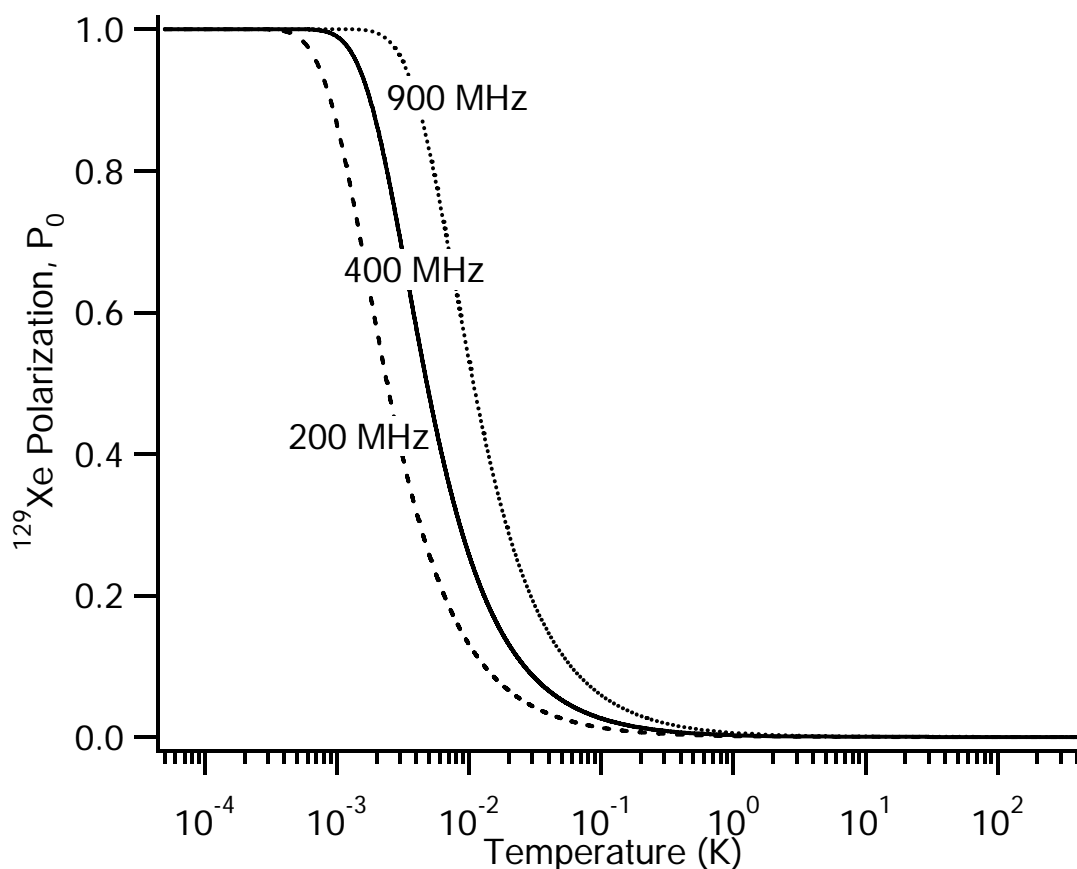


Figure 2-1. Temperature dependence of  $^{129}\text{Xe}$  spin polarization at variable magnetic fields, based on Eq. (2-3).

In hyperpolarized NMR, the nuclear spin polarization is not limited by  $T$  and  $B_0$ . In Eq. (2-3), the spin polarization can be alternatively expressed in terms of a “spin temperature”  $T_s$ . At thermal equilibrium, the ensemble of spin systems has relatively low spin polarization, or

equivalently, high spin temperature. High nuclear spin polarization corresponds to low spin temperature. The schematic diagram for the population distribution among the energy levels for thermal polarization and hyperpolarization is illustrated in Figure 2-2. The aim of hyperpolarized NMR is to increase the population difference between the spin states, *i.e.* to “cool down” the spins, leading to NMR signal enhancement. The details of hyperpolarized NMR will be discussed in Section 2.4.

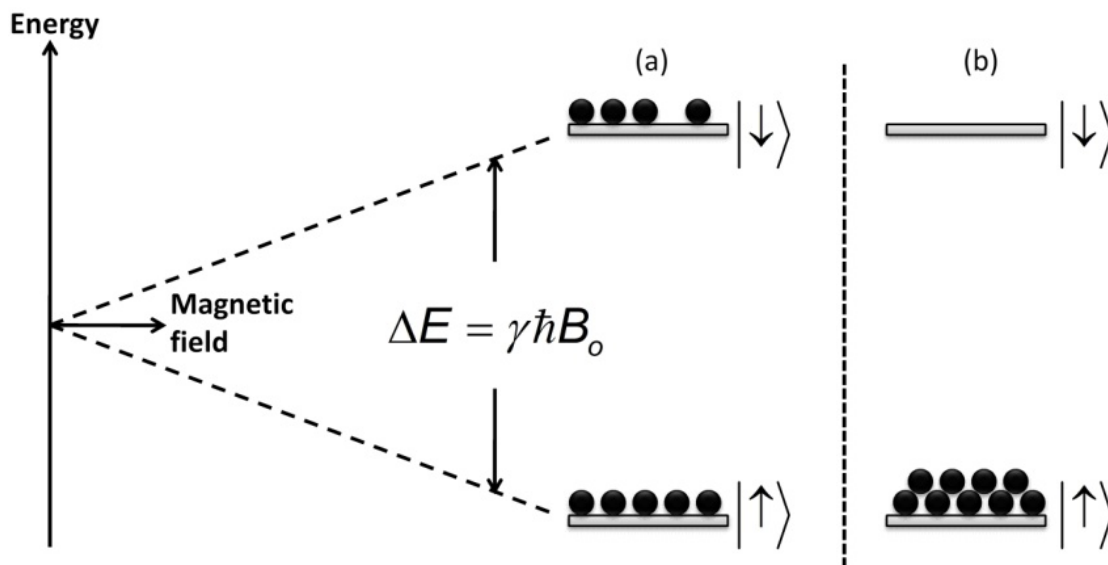


Figure 2-2. The energy levels of (a) thermal polarization (“hot-spin” system) and (b) hyperpolarization (“cold-spin” system) for spin-1/2 system.

### 2.2.2 Chemical Shift Anisotropy

In the presence of a static external magnetic field  $B_0$ , the motion of electron cloud around a nuclear spin can generate a localized anisotropic magnetic field that interacts with the nuclear spin. This induced magnetic field is proportional to  $B_0$ , but opposite in direction. At the  $i$ -th nucleus, a local magnetic field is induced by the surrounding electrons

$$\vec{B}_{induced}(i) = -\hat{\sigma}(i) \cdot \vec{B}_0 \quad (2-5)$$

where  $\hat{\sigma}(i)$  is the chemical shift tensor (or shielding tensor). The chemical shielding tensor can be expressed as a  $3 \times 3$  matrix. The energy of chemical shift resulting from the induced field of each nucleus is

$$E_{CS}(i) = -\bar{\mu}_i \cdot \bar{B}_{induced}(i) = \bar{\mu}_i \cdot \hat{\sigma}(i) \cdot \bar{B}_0 \quad (2-6)$$

Since the local environments of each nucleus are different, the shielding tensors of nuclei in a spin system are generally different. Replacing the magnetic moment  $\bar{\mu}$  with its quantum equivalent  $\gamma \hbar \bar{I}$  and summing over all the spins in the systems, the Hamiltonian of chemical shift in a spin system yields

$$\hat{H}_{CS} = \sum_i^{spins} \hat{H}_{CS}(i) = \hbar \sum_i^{spins} \gamma_i \bar{I}(i) \cdot \hat{\sigma}(i) \cdot \bar{B}_0 \quad (2-7)$$

The Hamiltonian of individual spin can be described by the tensor in the laboratory frame (LAB)

$$\hat{H}_{CS}^{LAB}(i) = \hbar \gamma_i \bar{I}(i) \cdot \hat{\sigma}^{LAB}(i) \cdot \bar{B}_0 \quad (2-8)$$

Because the chemical shift interaction has a specifically spatial orientation with respect to  $B_0$ , any molecular motions in space must include the rotation of its three components in the chemical shift tensor. To simplify the problem, the chemical shielding tensor can be treated on its own principal axis system (PAS), yielding a diagonal tensor. The axes of PAS point in the same directions as the eigenvectors of the shielding tensor,  $\hat{\sigma}$ . By convention, the z-axis of the PAS points along the largest eigenvector of the chemical shielding tensor and x-axis points along the smallest eigenvector.<sup>50,51</sup> The eigenvalues,  $\sigma_{11}$ ,  $\sigma_{22}$ , and  $\sigma_{33}$ , are the principal components of the tensor ( $\sigma_{33} \geq \sigma_{22} \geq \sigma_{11}$ ). The shielding tensor in PAS is

$$\hat{\sigma}^{PAS} = \begin{bmatrix} \sigma_{11} & 0 & 0 \\ 0 & \sigma_{22} & 0 \\ 0 & 0 & \sigma_{33} \end{bmatrix} \quad (2-9)$$

Here the numerical subscripts are used in PAS, while the elements are denoted by  $x$ ,  $y$ , and  $z$  in LAB. The chemical shielding tensor can be transformed from PAS to LAB coordination system by operating with rotation matrices in terms of Euler angle transformation<sup>37,52</sup>

$$\hat{\sigma}^{LAB} = R^{-1}(\alpha, \beta, \gamma) \cdot \hat{\sigma}^{PAS} \cdot R(\alpha, \beta, \gamma) \quad (2-10)$$

where  $\alpha$ ,  $\beta$ , and  $\gamma$  are the Euler angles.<sup>52</sup> In Figure 2-3, the shape of three-dimensional ellipsoid is defined by the principal tensor components ( $\sigma_{11}, \sigma_{22}, \sigma_{33}$ ).

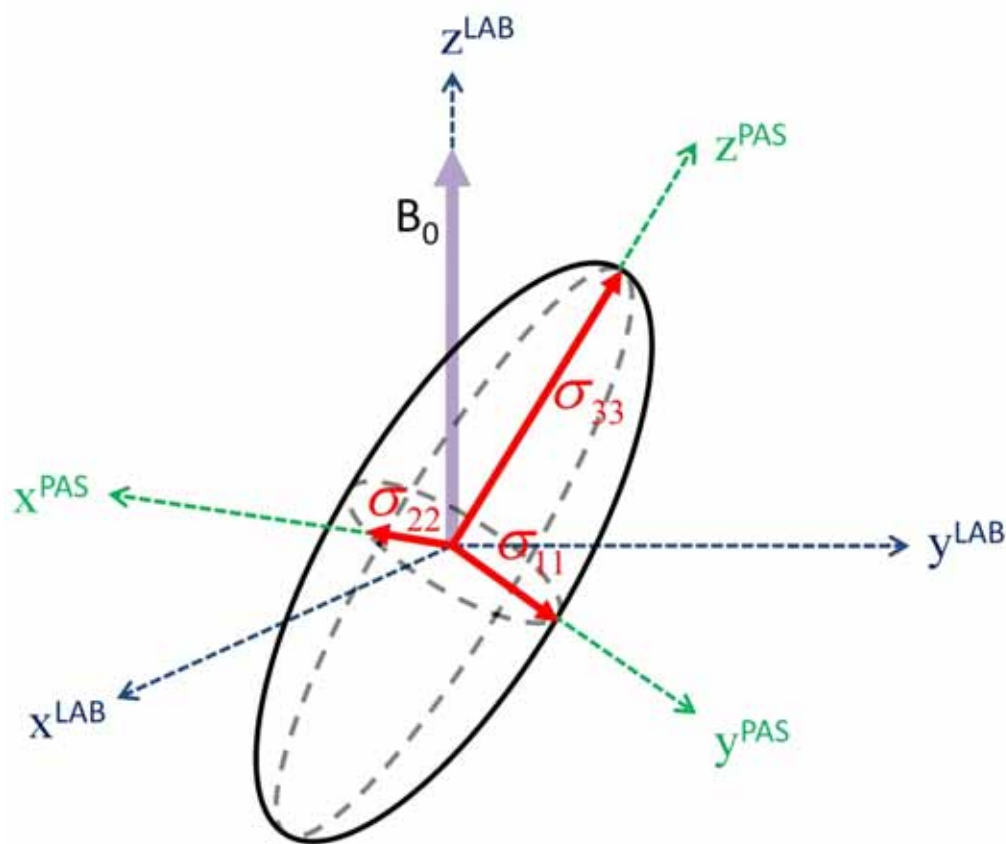


Figure 2-3. Chemical shift tensor in different coordinate systems. In CSA tensor, the  $\sigma_{33}$  points along the value of the largest shielding.  $\sigma_{22}$  and  $\sigma_{11}$  are orthogonal to  $\sigma_{33}$ .

Since the Hamiltonian of chemical shift is a small perturbation of Zeeman Hamiltonian, the terms in Eq. (2-8) which do not commute with  $I_z$  can be neglected. Therefore, in a high external magnetic field, only  $\sigma_{zz}$  in the LAB is of interest and Eq. (2-8) can be rewritten as

$$\hat{H}_{CS}(i) \cong \hbar \gamma_i I_z \sigma_{zz} B_0 \quad (2-11)$$

An expression of the experimental measurable quantity of shielding tensor,  $\sigma_{zz}$ , in terms of the principal values of shielding tensor and the Euler angles of PAS to LAB can be obtained by applying the rotation operators to  $\hat{\sigma}^{PAS}$ .<sup>37</sup>

$$\begin{aligned} \sigma \cong \sigma_{zz} &= \left[ R^{-1}(\alpha, \beta, \gamma) \cdot \hat{\sigma}^{PAS} \cdot R(\alpha, \beta, \gamma) \right]_{zz} \\ &= \sin^2 \beta \cdot \cos^2 \alpha \cdot \sigma_{11} + \sin^2 \beta \cdot \sin^2 \alpha \cdot \sigma_{22} + \cos^2 \beta \cdot \sigma_{33} \\ &= \sigma_{iso} + \frac{1}{2} \Delta \sigma \cdot (3 \cos^2 \beta - 1 + \eta \cdot \sin^2 \beta \cdot \sin^2 2\alpha) \end{aligned} \quad (2-12)$$

where  $\sigma_{iso}$  is isotropic chemical shift,  $\Delta \sigma \equiv \sigma_{33} - \sigma_{iso}$  is shielding anisotropy,  $\eta \equiv (\sigma_{22} - \sigma_{11}) / (\sigma_{33} - \sigma_{iso})$  is asymmetric parameter. The powder sample with randomly orientated crystallites has the characteristic spectral line-shape. It is typically called “powder pattern”, in which  $\sigma$  is weighted according to the isotropic probability distribution.<sup>42</sup> The CSA line-shapes are shown in Figure 2-4. Three typical CSA powder patterns are summarized as follows:

- (1) If three shielding components are not equal,  $\sigma_{33} \neq \sigma_{22} \neq \sigma_{11}$ , it yields the asymmetric spectra ( $\eta \neq 0$ ), as shown in Figure 2-4a.
- (2) For a tensor with an axially symmetry, where the asymmetric parameter is  $\eta = 0$ , the line-shape can be simplified to Figure 2-4b.  $\sigma_{\parallel}$  and  $\sigma_{\perp}$  can be referred to the shielding along and perpendicular to the principle z-axis, where  $\sigma_{\parallel} \equiv \sigma_{33}$  and  $\sigma_{\perp} \equiv \sigma_{22} = \sigma_{11}$ . The anisotropy of axially symmetry tensor is  $\xi = \sigma_{\parallel} - \sigma_{\perp}$ . As shown in Figure 2-4b, the spectra line-shapes with opposite anisotropy signs are the mirror images with respect to  $\sigma_{iso}$ .

(3) If three tensor components are equal,  $\sigma_{33} = \sigma_{22} = \sigma_{11}$ , the spectrum collapses to an isotropic peak at  $\sigma_{iso}$  frequency (Figure 2-4c).

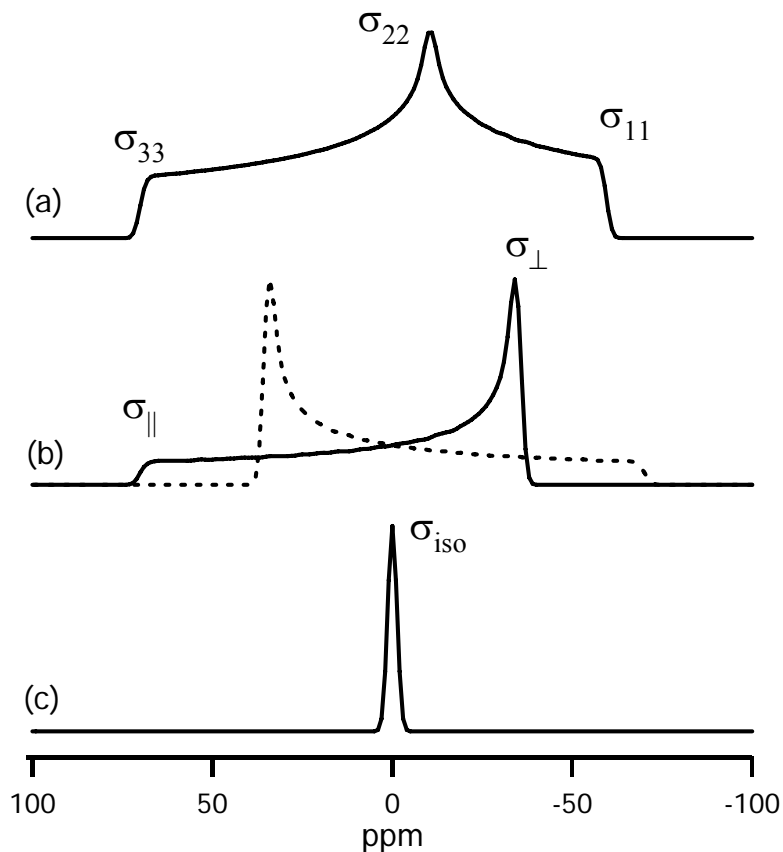


Figure 2-4. Simulated CSA powered spectra of (a) lower symmetry ( $\sigma_{33} \neq \sigma_{22} \neq \sigma_{11}$ ),  $\eta=0.7$ ,  $\Delta\sigma=70$  ppm, (b) axial symmetry ( $\sigma_{33} \neq \sigma_{22} = \sigma_{11}$ ),  $\eta=0.7$ ,  $\xi=70$  ppm. (dash line,  $\xi=-70$  ppm), (c) cubic symmetry ( $\sigma_{33} = \sigma_{22} = \sigma_{11}$ ),  $\eta=0$ ,  $\Delta\sigma=0$  ppm. The spectral width =200 ppm, Gaussian broadening =0.3 kHz. Larmor frequency=100 MHz,  $\sigma_{iso} = 0$ . ( $\eta$  is asymmetric parameter.  $\Delta\sigma$  is shielding anisotropy.  $\xi$  is shielding anisotropy for axially symmetry tensor)

If the molecules are randomly tumbling, the chemical shift interaction is average to zero, allowing the observation of an isotropic peak. The isotropic chemical shift value can be taken as average of the trace:

$$\bar{\sigma} \equiv \sigma_{iso} = \frac{1}{3}(\sigma_{11} + \sigma_{22} + \sigma_{33}) = \frac{1}{3}Tr\{\hat{\sigma}\} \quad (2-13)$$

For a single crystal sample, where discrete molecular orientations are present, the NMR spectrum consists of a sharp isotropic peak, if the chemical shift interaction is dominated. The frequencies of these peaks depend on the orientations of the crystal *c*-axis with respect to the external magnetic field. By measuring these frequencies as a function of crystal orientation, the shielding tensor can be determined. However, for some materials, it is infeasible to grow a crystal to an appropriate size for NMR measurements. In addition, some solid samples, such as amorphous polymers, do not have regular crystalline structures. Instead, they contain a distribution of orientations of the CSA tensor with respect to the external magnetic field. Therefore, the spectral line-shape from such substances is broadened by the distribution of resonance frequencies. For solid samples, the magic-angle spinning (MAS) can be utilized to produce high resolution NMR spectrum by averaging the chemical shift anisotropy to its isotropic value.<sup>42</sup>

### **2.2.3 Exchange NMR**

Another important feature of NMR is its sensitivity to molecular dynamics in the presence of exchange processes. In the exchange system, the species (*e.g.* nuclei, molecules, or particles) can generally exchange among one-another in two or multiple states. In most cases, the exchange rate of such process is within the range of NMR time-scale, which refers to the lifetimes of the order of 1 second to  $10^{-6}$  second for each state.<sup>39</sup> It allows NMR to be a unique tool to extract the dynamic information in the exchange systems, the result which is not usually achievable by other spectroscopic techniques.

Several NMR techniques have been developed for the studies of exchange processes, including line-shape analysis<sup>53,54</sup>, selective inversion<sup>55,56</sup>, and two-dimensional exchange NMR spectroscopy (2D-EXSY).<sup>57,58</sup> For simplicity, considering exchange between two magnetically

inequivalent sites A and B with frequency  $\omega_A$  and  $\omega_B$ , the two-site exchange processes can be easily analyzed by the NMR line-shapes, since the exchange processes can be evidently observed from the characteristic changes in the NMR spectral line-shapes.

The details of NMR line-shapes in different exchange regimes are described as follows:

### Fast exchange

In fast exchange regime, the exchange rate constant  $k_{ex}$  (assuming equally forward and reverse exchange rates,  $k_{ex} = k_{A \rightarrow B} = k_{B \rightarrow A}$ ) is greater than the chemical shift offset between two sites:  $\Delta\Omega^0 = |\omega_A - \omega_B|$ , leading to the two signals completely collapse to a single sharp peak (Figure 2-5a and b). The resonance frequency  $\omega_0^{fast}$  can be expressed by the weighing average of two sites ( $p_A + p_B = 1$ ),

$$\omega_0^{fast} = p_A \omega_A + p_B \omega_B \quad (2-14)$$

The peak can be characterized by an averaged transverse relaxation rate

$$\frac{1}{T_2^{fast}} = \frac{p_A}{T_{2A}} + \frac{p_B}{T_{2B}} \quad (2-15)$$

where  $T_2^{fast}$  is the observed  $T_2$  relaxation time in the fast exchange limit (*i.e.*  $k_{ex} \gg \Delta\Omega^0$ ). The full width at half maximum (FWHM) of Lorentzian peak is given by  $\Delta\omega_{1/2} = 1/\pi T_2^{fast}$ .

### Slow exchange

If the exchange of observed nucleus between site A and B is in slow exchange regime, the individual frequencies for each site can be resolved with offset of  $\Delta\Omega^0 = |\omega_A - \omega_B|$ , and the exchange rate constant must be less than  $\Delta\Omega^0$  (*i.e.*  $k_{ex} \ll \Delta\Omega^0$ ), as seen in Figure 2-5e and f. In this case, the adsorption Lorentzian peaks of both sites can be obtained by solving the Bloch equation on two exchange sites<sup>59</sup>, and the FWHM of A site is

$$\Delta\omega_{1/2} = \frac{1}{\pi} \left( \frac{1}{T_{2A}} + k_{ex} \right) \quad (2-16)$$

Similar expression can be obtained for site B. On the contrary to the fast exchange, slow exchange results in two separated peaks with an excess line broadening factor,  $k_{ex} / \pi$  (in Hz), of the signal at each site.

### Intermediate exchange

As the exchange time-scale between the above two regimes, a broader line-width is observed in an intermediate exchange spectrum. A decrease in sensitivity in the intermediate exchange regime is apparent in Figure 2-5c and d due to broader line-width and lower amplitude.

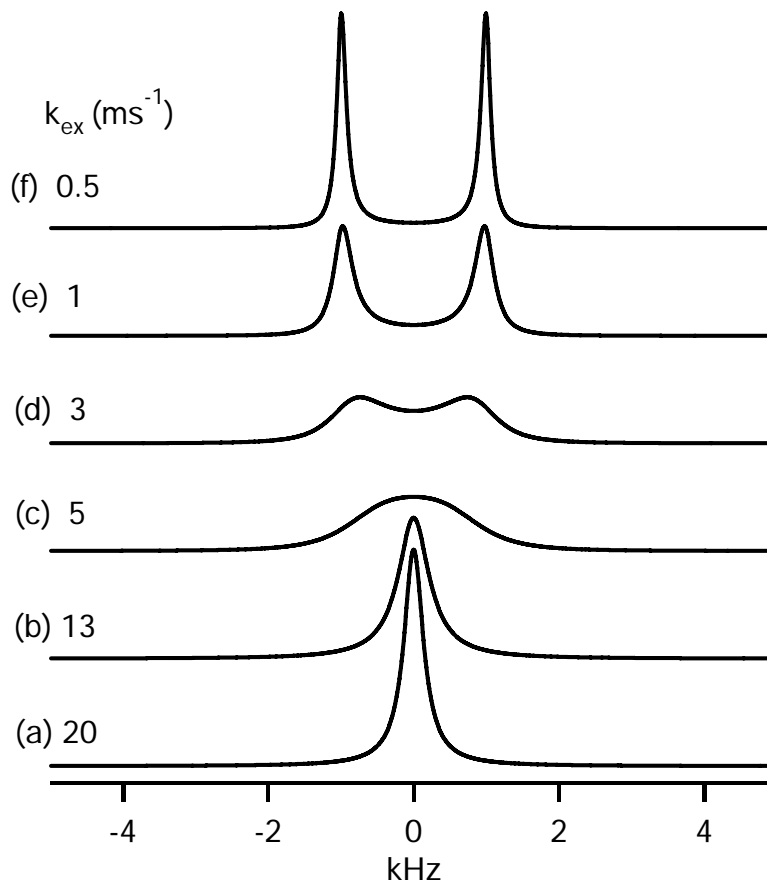


Figure 2-5. Simulated NMR spectra for two-site exchange. (a)(b) fast exchange; (c)(d) intermediate exchange; (e)(f) slow exchange regime. Chemical shift offset between two sites:  $\Delta\Omega^0 = 1.3 \times 10^4 \text{ rad / sec}$ , populations:  $p_A = p_B = 0.5$ .  $T_{1A} = T_{1B} = 1 \text{ s}$ .

## 2.2.4 2D Exchange NMR Spectroscopy

2D-EXSY experiment is a technique to explore the frequency exchange in slow exchange limit ( $1/T_1 < k_{ex} \ll \Delta\Omega^0$ ). 2D-EXSY is in principle identical to the Nuclear Overhauser Enhancement Spectroscopy (NOESY). However, the mixing time of 2D-EXSY is usually shorter than that of NOESY, because the exchange rate is generally much faster than the cross-relaxation rate.<sup>39</sup>

The use of 2D-EXSY NMR for the study of molecular exchange was first proposed by Jeener and co-workers.<sup>57</sup> The pulse sequence of EXSY is shown in Figure 2-6.

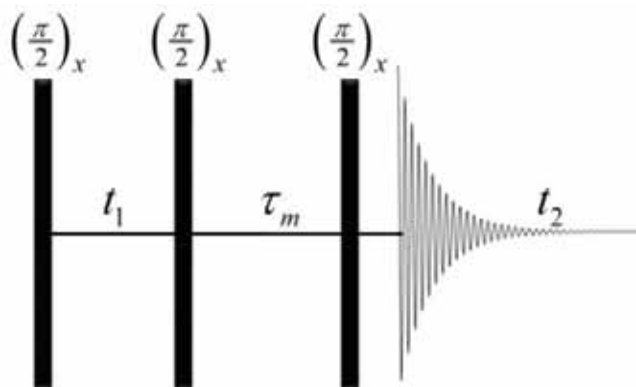


Figure 2-6. NMR pulse sequence of 2D exchange NMR.  $\tau_m$  is mixing time.

The NMR signal of 2D-EXSY experiment can be calculated in terms of product operators.<sup>38,39,60</sup> In the case of two-spin system (spin-A and spin-B) without J-coupling and spin relaxations, the equilibrium magnetization prior to the first  $\pi/2$  pulse is  $M_z(t=0) \propto I_z^A + I_z^B$ . For simplicity, the magnetization from spin-A is first considered. The first  $(\pi/2)_x$  pulse rotates the magnetization onto  $-y$

$$I_z^A \xrightarrow{(\pi/2)I_x^A} \xrightarrow{(\pi/2)I_x^B} -I_y^A \quad (2-17)$$

Following the evolution during  $t_1$

$$-I_y^A \xrightarrow{(\Omega^A t_1) I_z^A} \xrightarrow{(\Omega^B t_1) I_z^B} -\cos(\Omega^A t_1) I_y^A + \sin(\Omega^A t_1) I_x^A \quad (2-18)$$

The second arrows in Eq. (2-17) and Eq. (2-18) have no effect, since  $I^A$  and  $I^B$  are commute. The second  $(\pi/2)_x$  pulse rotates first term of Eq. (2-18) onto z-axis and leaves the second term unaffected.

$$\begin{aligned} -\cos(\Omega^A t_1) I_y^A &\xrightarrow{(\pi/2) I_x^A} \xrightarrow{(\pi/2) I_x^B} -\cos(\Omega^A t_1) I_z^A \\ \sin(\Omega^A t_1) I_x^A &\xrightarrow{(\pi/2) I_x^A} \xrightarrow{(\pi/2) I_x^B} \sin(\Omega^A t_1) I_x^A \end{aligned} \quad (2-19)$$

During the mixing time  $\tau_m$ , only longitudinal magnetizations lead to cross-peaks by exchange; therefore, the  $I_x^A$  term in Eq. (2-19) can be ignored. In the EXSY experiment, it can be achieved by selecting an appropriate coherence transfer pathway by the phase cycling.<sup>39</sup> In the beginning of mixing time  $\tau_m$ , the magnitude of z-magnetization of spin-A depends on  $t_1$  and processing frequency  $\Omega^A$  (*i.e.*  $-\cos(\Omega^A t_1) I_z^A$ ). This z-magnetization is called “frequency labeled” during 2D preparation time  $t_1$ . During  $\tau_m$ , spin-A may undergo site exchange with spin-B. If so, for the spin-B after  $\tau_m$ , it carries the information with the frequency labeled of spin-A recorded during  $t_1$ . If a fraction  $f_{ex}$  of spin-A is lost due to exchange with spin-B, the effect of mixing process can be written

$$-\cos(\Omega^A t_1) I_z^A \xrightarrow{\tau_{mix}} -(1-f_{ex}) \cos(\Omega^A t_1) I_z^A - f_{ex} \cos(\Omega^A t_1) I_z^B \quad (2-20)$$

The final  $(\pi/2)_x$  rotates the z-magnetization back onto y-axis for signal detection

$$\begin{aligned} -(1-f_{ex}) \cos(\Omega^A t_1) I_z^A &\xrightarrow{(\pi/2) I_x^A} \xrightarrow{(\pi/2) I_x^B} (1-f_{ex}) \cos(\Omega^A t_1) I_y^A \\ -f_{ex} \cos(\Omega^A t_1) I_z^B &\xrightarrow{(\pi/2) I_x^A} \xrightarrow{(\pi/2) I_x^B} f_{ex} \cos(\Omega^A t_1) I_y^A \end{aligned} \quad (2-21)$$

Although the magnetization started on spin-A, there is a magnetization presented on spin-B at the end of EXSY sequence. This process is also called “longitudinal magnetization transfer”.

Finally,  $I_y^A$  and  $I_y^B$  evolve during detection period  $t_2$

$$\begin{aligned}
 (1-f_{ex}) \cos(\Omega^A t_1) I_y^A &\xrightarrow{(\Omega^A t_2) I_z^A} \xrightarrow{(\Omega^B t_2) I_z^B} \\
 &\quad (1-f_{ex}) \cos(\Omega^A t_1) \cos(\Omega^A t_2) I_y^A - (1-f_{ex}) \cos(\Omega^A t_1) \sin(\Omega^A t_2) I_x^A \\
 f \cos(\Omega^A t_1) I_y^B &\xrightarrow{(\Omega^A t_2) I_z^A} \xrightarrow{(\Omega^B t_2) I_z^B} \\
 &\quad f_{ex} \cos(\Omega^A t_1) \cos(\Omega^B t_2) I_y^B - f_{ex} \cos(\Omega^A t_1) \sin(\Omega^B t_2) I_x^B
 \end{aligned} \tag{2-22}$$

If assuming y-magnetization is detected during  $t_2$ , the NMR signal on time domain yields

$$(1-f_{ex}) \cos(\Omega^A t_1) \cos(\Omega^A t_2) I_y^A + f_{ex} \cos(\Omega^A t_1) \cos(\Omega^B t_2) I_y^B \tag{2-23}$$

Similarly, repeat the same procedure on spin-B from the initial condition, time-domain signals is

$$(1-f_{ex}) \cos(\Omega^B t_1) \cos(\Omega^B t_2) I_y^B + f_{ex} \cos(\Omega^B t_1) \cos(\Omega^A t_2) I_y^A \tag{2-24}$$

By taking the Fourier transformation along  $t_2$  and  $t_1$  on Eq. (2-23) and Eq. (2-24), it results in four absorption line-shapes in 2D spectrum. The first terms of Eq. (2-23) and Eq. (2-24) form diagonal peaks, which are located at  $(f_1, f_2) = (\Omega^A, \Omega^A)$  and  $(f_1, f_2) = (\Omega^B, \Omega^B)$  with amplitudes  $(1-f_{ex})$ . The second terms of Eq. (2-23) and Eq. (2-24) form cross peaks which are located at  $(f_1, f_2) = (\Omega^A, \Omega^B)$  and  $(f_1, f_2) = (\Omega^B, \Omega^A)$  with amplitudes  $f_{ex}$  (Figure 2-7a). Obviously, as shown in Figure 2-7b, if no exchange takes place between two sites ( $f_{ex} = 0$ ), cross peaks are absent in 2D-EXSY spectrum.

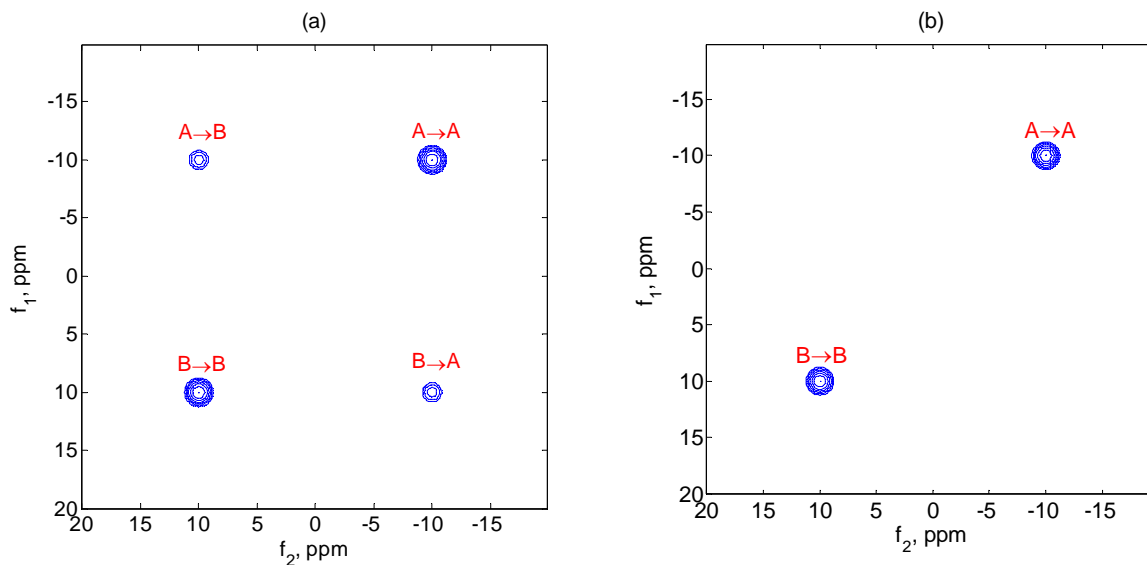


Figure 2-7. Simulated 2D-EXSY spectra with (a) chemical exchange ( $k_{AB} = k_{BA} = 50\text{ms}^{-1}$ ,  $T_{1A} = T_{1B} = 1\text{s}$ ), and (b) no exchange ( $k_{AB} = k_{BA} = 0$ ). Larmor frequency=100MHz.

In principle, the exchange rate constant can be determined by fit the cross and diagonal-peak signals of 2D EXSY spectra as a function of mixing time with the appropriate kinetic model. The thermodynamic parameters, such as activation energy and enthalpy, in the exchange process can be calculated by measuring exchange rates from a serial of  $\tau_m$ -dependence 2D-EXSY experiments at variable temperatures.<sup>39</sup>

### 2.3 Introduction to $^{129}\text{Xe}$ NMR

Xenon was first experimentally brought into NMR spotlight by Ito and Fraissard<sup>12</sup>, the pioneers of  $^{129}\text{Xe}$  NMR, for the study of porous solids. Their motivation was to utilize the sensitivity of  $^{129}\text{Xe}$  to (1) its local environment, (2) physical interactions with other chemical species, such as other nuclei, and (3) the nature of adsorption sites in the materials.

#### 2.3.1 Physical Properties of Xe

The Xe atom has an atomic weight of 131.29 u. It possesses the electron configuration  $[\text{Kr}]4\text{d}^{10}5\text{s}^25\text{d}^6$  and has 54 electrons. Due to its small size and chemical inertness, Xe atom can serve

as an ideal atomic probe for characterizations of materials on the nanometer length scales. From 13 known isotopes of Xenon (9 stable ones and 4 radioactive ones)<sup>61</sup>, only two of them are NMR observable:  $^{129}\text{Xe}$  with  $I = 1/2$  and  $^{131}\text{Xe}$  with  $I = 3/2$ .

Because of its fully occupied external electronic orbital, Xe is chemically inert. However, this highly polarizable electron cloud makes Xe strongly hydrophobic, thereby leading to significant interactions between Xe and other hydrophobic molecules in solution or on solid surface. In ambient condition, gaseous Xe exists in nature, but liquid and solid phases can be easily obtained within an experimental accessible range of temperatures and pressures. The boiling and melting points of Xe at 1 bar are 165.02 K and 161.38 K, respectively.<sup>2</sup> It makes the separation of hyperpolarized Xe from gas mixture at temperature of liquid nitrogen (77 K) practical. The extremely lengthy  $T_1$  relaxation time of  $^{129}\text{Xe}$  is the key characteristic that makes Xe feasible to be optically polarized prior to NMR experiments.

The NMR properties of Xe isotopes and proton are listed in Table 2-1.

Table 2-1. Comparison of NMR properties of  $^1\text{H}$ ,  $^{129}\text{Xe}$  and  $^{131}\text{Xe}$

	$^1\text{H}$	$^{129}\text{Xe}$	$^{131}\text{Xe}$
Spin $I$	1/2	1/2	3/2
$\gamma$ ( $10^8 \text{ s}^{-1} \text{ Tesla}^{-1}$ )	2.675	-0.74	0.22
Natural abundance (%)	99.99	26.44	21.18

$\gamma$  : gyromagnetic ratio

For  $^{129}\text{Xe}$ , the low gyromagnetic ratio combined with the low natural isotopic abundance yields much lower NMR sensitivities in comparison to the  $^1\text{H}$  nuclei. Thus, for the thermally-polarized  $^{129}\text{Xe}$ , it is necessary to significantly increase the number of scans and acquisition time to achieve acceptable signal-to-noise ratios in NMR measurements. This problem can be overcome by hyperpolarized NMR which makes the “single shot” of  $^{129}\text{Xe}$  NMR measurement feasible. It will be discussed in Section 2.4.

In addition to  $^{129}\text{Xe}$ , the quadrupole nuclei in the noble gases, such as  $^{131}\text{Xe}$  and  $^{83}\text{Kr}$ , have been optically polarized, and the surface studies by hyperpolarized  $^{83}\text{Kr}$  NMR have been reported.<sup>62-65</sup> These nuclei possess electric quadrupole moments which lead to quadrupole relaxation and short  $T_1$  relaxation time, making the storage of hyperpolarization infeasible. However, the quadrupole moments of  $^{131}\text{Xe}$  and  $^{83}\text{Kr}$  can provide a wealth of information in the local structures directly through the observed quadrupolar splitting in the NMR spectrum.

### 2.3.2 One-dimensional van der Waals Guest/Host systems in Xe NMR

The sizes of Xe atom and pore-spaces of materials strongly affect the  $^{129}\text{Xe}$  NMR spectral line-shape. Here the definitions of the Xe diameter and the pore sizes of the host materials, 1D channel diameter in the present case, are discussed. The van der Waals diameter of Xe atom is 4.4 Å, which can be estimated from the b coefficient of the van der Waals equation by assuming Xe is a hard-sphere atom. While the Xe diameter can be measured from other methods, such as Stokes-Einstein equation<sup>66</sup>, the van der Waals diameter is mostly used to describe the size of Xe atom in  $^{129}\text{Xe}$  NMR studies in the literature.<sup>20-22,24,67-72</sup>

For 1D nanotubes, the channel diameter can be measured from the space group of the nanotubular structure assuming the channel is the van der Waals surface, where each atom on the cross section of channel is considered as the van der Waals atom.<sup>73</sup> For example, the L-alanyl-L-valine (AV) dipeptide nanotubes are the polycrystalline materials in which the AV molecules can form a self-assembled host channel structure. The crystal of AV is hexagonal with a  $P6_1$  space group. Since the channel pore of AV is not a round shape and the atoms forming the channel interior are not uniformly distributed, the average value of diameter is used to express the van der Waals internal diameter of AV channel, which is 5.13 Å.<sup>74</sup>

### 2.3.3 Xe Chemical Shift

The  $^{129}\text{Xe}$  chemical shift is well-known as its extremely high sensitivity to the interactions with the local environments. It is a mono-atomic gas with a very large and spherically symmetrical electron cloud. Any distortion of the electron cloud can be reflected directly at the level of the nucleus and is consequently expressed as a variation of  $^{129}\text{Xe}$  NMR chemical shifts. An overview over the accessible chemical shift range of  $^{129}\text{Xe}$  NMR is given in Figure 2-8. It shows that the range of Xe chemical shift is up to 7500 ppm, extremely large compared with most other NMR sensitive nuclei. In Xe gas phase, interatomic collisions can distort the Xe electron clouds so that the nucleus becomes deshielded and  $^{129}\text{Xe}$  resonance frequency increases (or shifts to down-field) with increasing Xe gas density. The natural reference of Xe chemical shift in the gas phase is typically extrapolated the chemical shift to zero pressure. Jameson and co-workers<sup>75,76</sup> described the chemical shift of dilute Xe gas in terms of virial expansion

$$\sigma_{Xe,gas}(T, \rho_{Xe}) = \sigma_0 + \sigma_1(T)\rho_{Xe} + \sigma_2(T)\rho_{Xe}^2 + \dots \quad (2-25)$$

where  $\sigma_0$  is reference chemical shift,  $\rho_{Xe}$  is Xe density,  $T$  is temperature, and  $\sigma_i$  are the virial coefficients of the shielding. Likewise, the observed Xe chemical shift can be expressed by the weighted average of several interactions on the NMR time scale.<sup>77</sup>

$$\sigma_{Xe,s} = \sigma_0 + \sigma_s + \sigma_{Xe-Xe} + \sigma_E + \sigma_M \quad (2-26)$$

where  $\sigma_0$  is Xe reference shift,  $\sigma_s$  reflects the interactions between Xe and solid surface, which does not contain any electrical charges. In such a case,  $\sigma_s$  depends only on the dimensions and shapes of pores in solids, and does not depend on Xe density.  $\sigma_{Xe-Xe}$  arises from Xe-Xe interactions. It is expected to vary linearly with Xe density at low Xe pressure and to become predominant at high Xe density.<sup>78</sup>  $\sigma_E$  and  $\sigma_M$  are due to the electrical and magnetic field caused

by cations in the porous materials, respectively. In general, the smaller pore dimensions and/or slower Xe diffusivity inside the pores, the larger the  $\sigma_s$  chemical shift value.<sup>78</sup>

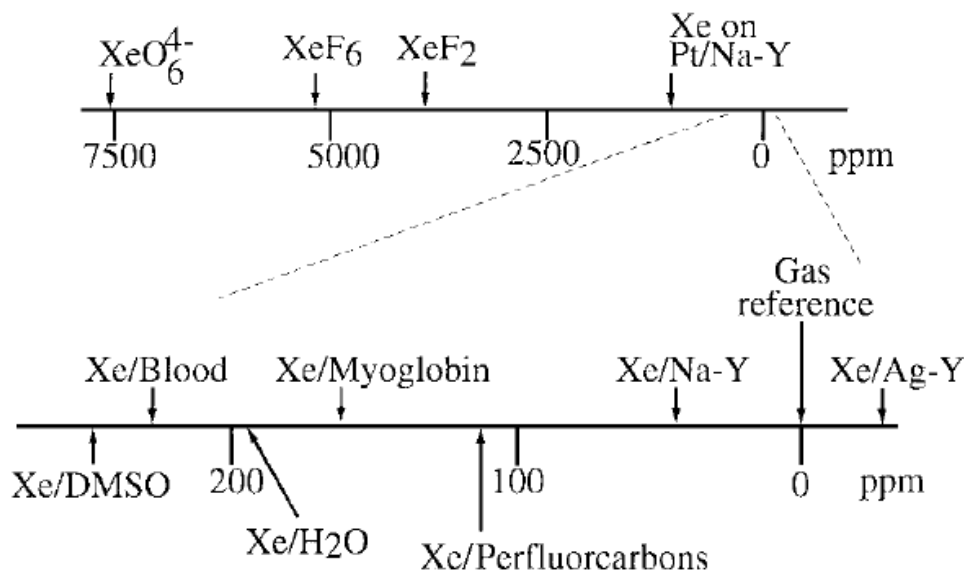


Figure 2-8. Chemical shift range of  $^{129}\text{Xe}$  NMR with examples of specified materials. The chemical shift is referenced to Xe gas extrapolated to zero Xe density. (Adapt from Ref<sup>79</sup>)

Currently, the studies of zeolites by thermally-polarized  $^{129}\text{Xe}$  NMR have already been highly successful.<sup>5,6,12,80-84</sup> Several models have been proposed to quantify the relations of  $\sigma_s$  chemical shift and porous geometry in nanoporous systems, especially in zeolites, under various experimental conditions.<sup>19,83,85-88</sup> It has formed a standard technique for the characterizations of nanoporous materials.<sup>78</sup>

## 2.4 Introduction to Hyperpolarized $^{129}\text{Xe}$ NMR

In light of quantum physics picture, the nuclear spin polarization can be artificially aligned along the quantization axis defined by a uniform magnetic field, yielding “hyperpolarization”, which is far beyond the polarization in Boltzmann equilibrium. There are various techniques which can achieve the “hyperpolarization”. In this dissertation, the hyperpolarized  $^{129}\text{Xe}$  gas was generated from spin-exchange optical-pumping (SEOP), which will be discussed in Section

2.4.2. With four to five orders of magnitude of the signal enhancement over Boltzmann polarization, hyperpolarized  $^{129}\text{Xe}$  NMR can greatly facilitate the studies of surfaces, nanotubes, and biological applications.

### 2.4.1 Improvement of NMR Sensitivity

In addition to achieve high  $B_0$  and low  $T$ , there are a variety of techniques developed to improve NMR sensitivities. For example, transferring polarization from high- $\gamma$  nucleus to low- $\gamma$  nucleus in solid is used routinely and is well-known as “cross-polarization” (CP).<sup>89,90</sup> More recently, NMR remote detection technique has been successfully developed, and allowed to separately optimizing the encoding and detection for NMR and imaging experiments.<sup>91-98</sup> It has demonstrated a significant amplification of signals on NMR and MRI.

Besides NMR sensitivity enhanced techniques mentioned above, in the past two decades, it has witnessed the developments of several methods to enhance polarization of nuclear spins, including dynamic nuclear polarization (DNP), *para*-hydrogen induced polarization (PHIP), and optical-pumping NMR.

#### Dynamic Nuclear Polarization (DNP)

In DNP, the large spin polarization of electrons can be transferred to nuclei, leading to an enhancement of nuclear spin polarization, which is maximally  $\gamma_e / \gamma_n$  (e.g.,  $\sim 600$  for  $^1\text{H}$ ). The polarization transfer relies on the electron-nuclear mutual spin-flip which was first predicted by Overhauser<sup>99</sup> and was demonstrated experimentally by Slichter *et al.*<sup>100</sup> DNP has been integrated with high resolution solid-state NMR experiments in polymers<sup>101,102</sup> and biological solids.<sup>103-105</sup> More recently, with the developments of soluble polarized agents, DNP has been employed in the aqueous systems to investigate metabolism<sup>106</sup>, proteins dynamics,<sup>107</sup> and paramagnetic ligand

systems.<sup>108</sup> Additionally, DNP has been used to enhance the contrast of NMR imaging by polarizing the protons in water molecules.<sup>109-111</sup>

### **Para-Hydrogen Induced Polarization (PHIP)**

Twenty years ago, Bowers and Weitekamp<sup>112,113</sup> discovered that the catalyzed hydrogenation of small organic molecules with *para*-hydrogen (*p*-H<sub>2</sub>) can produce a highly ordered spin state, leading to intense and antiphase NMR signals for the corresponding protons. This phenomenon arises from the quantum statistical mechanical properties of dihydrogen. The equilibrium ortho/para ratio is about 3:1 at room temperature, whereas at liquid nitrogen temperature (~77 K) the ratio shifts toward almost pure *p*-H<sub>2</sub>. However, to detect the enhanced NMR signal, the equivalence of two hydrogen atoms has to be broken. The symmetry of *p*-H<sub>2</sub> can be eventually broken by appropriate hydrogenation reactions, where two protons of *p*-H<sub>2</sub> attach at the magnetically inequivalent sites on the substrate molecules. The *p*-H<sub>2</sub> has a long lifetime at room temperature, and transfer of the polarization from *p*-H<sub>2</sub> to interesting nuclei has been demonstrated.<sup>114-116</sup> The induced polarization of *p*-H<sub>2</sub> in the heterogeneous hydrogenation reaction has recently been reported.<sup>117</sup> This technique allows a direct visualization of mechanism of heterogeneous hydrogenation reactions<sup>118</sup>, and has been used to study the micro-fluidic device.<sup>119</sup>

### **Optical Pumping NMR**

Optical pumping NMR (OPNMR) experiments transfer polarization from photons of circularly polarized light to electron spins and/or nuclear spins. Applications of OPNMR have been involved in the studies of semiconductors<sup>120-123</sup> (*e.g.* GaAs quantum wells, and InP semiconductors) and in the productions of hyperpolarized noble gases through optically pumped rubidium vapors.<sup>2</sup> Four to five order of magnitude of sensitivity enhancement has been achieved

by OPNMR. Moreover, hyperpolarized  $^{129}\text{Xe}$  can further transfer the polarization to neighboring nuclei, especially to the surface nuclei, through SPINOE (Spin Polarization Induced nuclear Overhauser Effect) <sup>124-126</sup>, Cross-Polarization<sup>127-129</sup>, and thermal mixing<sup>130,131</sup> mechanism. Recently, a biosensor containing hyperpolarized  $^{129}\text{Xe}$  has been developed and several applications in aqueous systems have been reported.<sup>26,132-135</sup>

## 2.4.2 Optical Pumping and Spin Exchange

Spin-exchange optical-pumping (SEOP) is the technique commonly applied for producing hyperpolarized noble gases. The utilization of SEOP for the polarization of noble gases was first demonstrated by Happer and co-workers.<sup>136,137</sup> SEOP involves two processes: Firstly, in optical pumping, angular momentum is transferred from photons of a circularly polarized laser beam to alkali metal electrons. Secondly, the angular momentum is transferred from polarized electron spins of alkali metal to unpolarized nuclear spins of noble gas through spin-exchange collisions.

### Optical Pumping

The large population difference between sublevels of ground state in an atom can be obtained by polarized light, which was first discovered by A. Kastler.<sup>138</sup> This idea was named “optical pumping”. Rubidium metal is the most common alkali metal in optical pumping experiments because it has an appropriate vapor density (*i.e.*  $6 \times 10^{12} \sim 10^{15} \text{ cm}^{-3}$ ) at moderate temperatures (100-200 °C).<sup>139</sup> Another advantage is the D1 transition line (794.7 nm) for Rb is available for high power tunable commercial diode lasers.

Rubidium has two stable isotopes:  $^{85}\text{Rb}$  ( $I = 5/2$ ) with 72.2% and  $^{87}\text{Rb}$  ( $I = 3/2$ ) with 27.2% natural abundance. The electron total angular momentum is  $\vec{J} = \vec{S} + \vec{L}$ , where electron spin is  $S = 1/2$ ,  $\vec{L}$  is the orbital angular momentum, with  $L = 0$  for  $s$  state and  $L = 1$  for  $p$

states. The atomic total angular momentum is defined as  $\vec{F} = \vec{J} + \vec{I}$ . When an external magnetic field  $B_0$  is applied, the Hamiltonian of Rb is<sup>137,140</sup>

$$\hat{H}_{Rb} = A \mathbf{I} \cdot \mathbf{S} + \left( g_s \mu_B S_z - \frac{\mu_I}{I} I_z \right) B_0 \quad (2-27)$$

where the first term is hyperfine interaction between nuclear spin  $I$  and electron spin  $S$  of Rb, and  $A$  is the hyperfine coupling constant. The last two terms represent the magnetic-dipole couplings of electron and nuclear spins to the magnetic field, in which  $g_s = 2.00232$  is  $g$  value of electron,  $I$  is nuclear spin quantum number;  $\mu_B$  and  $\mu_I$  are Bohr magneton and nuclear magnetic moment, respectively. A weak magnetic field, such as 10-20 gauss, is typically used in the optical-pumping experiment, such that the hyperfine interaction is dominant and the eigenstates of the Hamiltonian in Eq. (2-27) are also eigenstates of total angular momentum  $F$  and its projection along magnetic field  $F_z$ .

Figure 2-9 is displayed the schematic diagram of  $^{87}\text{Rb}$  energy levels as various interactions applied to the Bohr model. A similar diagram can be obtained for  $^{85}\text{Rb}$  isotope with additional total angular momentum values of  $F=2$  and  $3$  for  $5S_{1/2}$  and  $5P_{1/2}$ . In the presence of a weak external magnetic field, the Zeeman splitting of atomic energy levels can be neglected. The electron in the ground state can transit to higher energy states by the absorption of photons with matching D1 transition wavelengths.

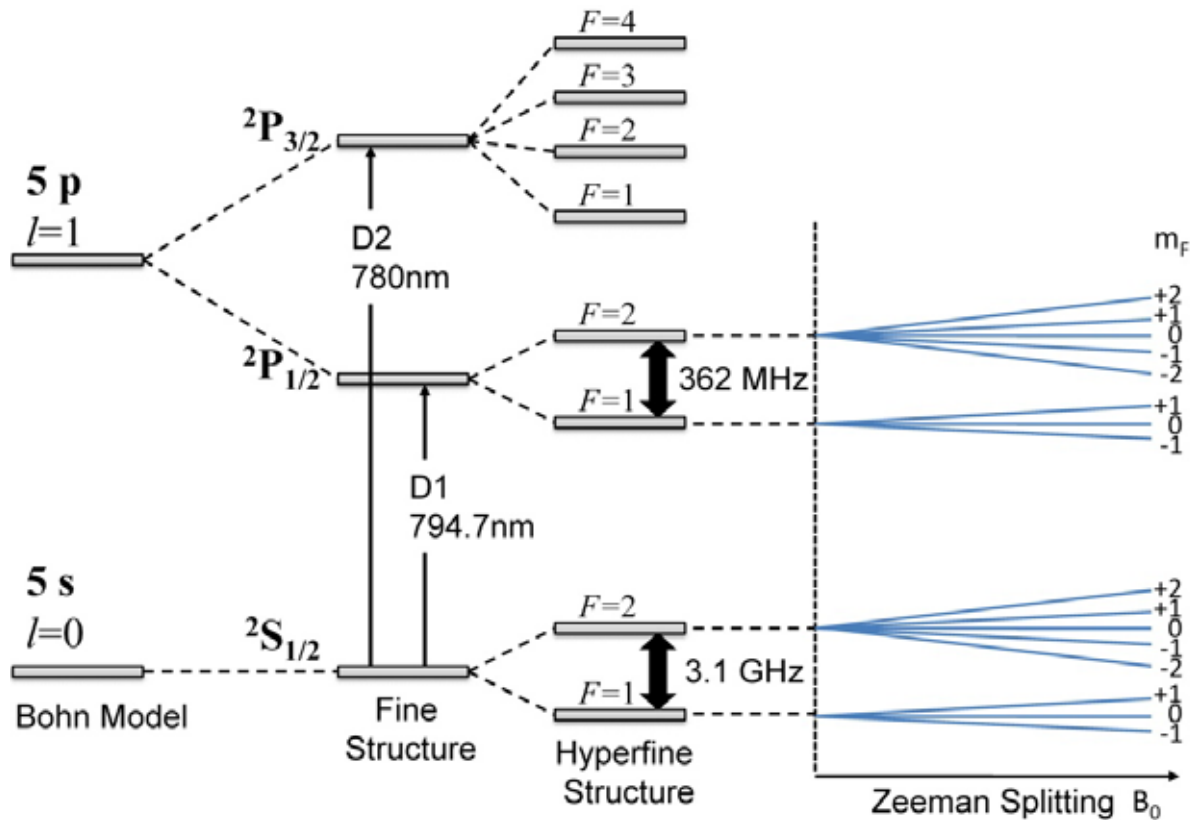


Figure 2-9. The  $^{87}\text{Rb}$  energy levels with spin orbital interaction, hyperfine interaction, and Zeeman splitting in the presence of a weak external magnetic field. (The splitting of energy levels is not shown on the same scale)

The selection rules for the allowed transition correspond to the incident photon polarization with respect to the magnetic field. By irradiating with a  $\sigma_{\pm}$  circularly polarized light to Rb atoms, the allowed transition of electric dipole radiation is  $\Delta m_F = \pm 1$ . If negative helicity of light ( $\sigma_{-}$ ) with respect to the magnetic field direction is applied, the transition of electron is restricted to  $\Delta m_F = -1$ . The lifetime of excited state is about  $10^{-8}$ - $10^{-9}$  sec. and electrons relax back into ground states following the selection rule of  $\Delta m_F = 0, \pm 1$ .<sup>137</sup> If the  $\sigma_{-}$  pumping light is continuously irradiated, it causes strong depopulation of high  $m_F$  ground state towards lower  $m_F$  ground state. The net result is that the population will be eventually accumulated on the lowest  $m_F$  ground state. For example, for  $\sigma_{-}$  pumping light, the electrons will be ultimately

populated onto  $m_F = -2$  state for  $^{87}\text{Rb}$ , as shown in Figure 2-10. It results in the highly polarized electron spins of  $^{87}\text{Rb}$ . If the positive helicity of polarized light ( $\sigma_+$ ) is applied with respect to the magnetic field direction, transition process is reversed, yielding the highest  $m_F$  ground state being polarized.

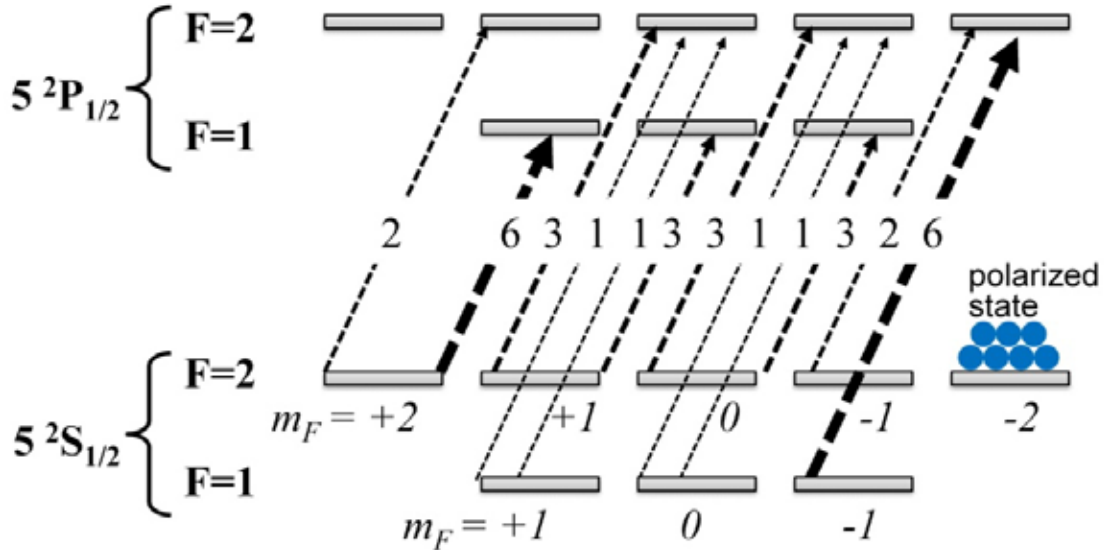


Figure 2-10. The  $^{87}\text{Rb}$  ( $I=3/2$ ) optical pumping for negative circularly polarized light  $\sigma^-$  in a weak external magnetic field. According to selection rule, allowed transition is  $\Delta m_F = -1$  for  $\sigma^-$  light. The values on each transition lines are represented the relative transition intensity  $I_t \propto |\vec{\mu}_E \cdot \vec{E}|^2$ . The emissive transitions from the excited states, which follow the  $\Delta m_F = \pm 1, 0$ , and non-radiative decay processes, which lead to the accumulation of atoms in the polarized state are not shown.

### Spin Exchange

In the spin-exchange collision, the Rb electron is flipped by coupling with the nuclear spin of colliding Xe atom. A spin exchange can be described schematically in Figure 2-11. The Fermi-contact hyperfine interaction between electron spins ( $S$ ) and nuclear spins of noble gas ( $I$ ) is given by

$$\alpha \mathbf{S} \cdot \mathbf{I} = \frac{\alpha}{2} (S^+ I^- + S^- I^+) + \alpha S_z I_z \quad (2-28)$$

where  $\alpha$  is the coupling constant, which is depended upon the relative distance between electron and nucleus. The flip-flop term in the bracket of Eq. (2-28) is responsible to the spin exchange. This process is critical because the spin temperature of Xe nuclear spin is reduced through the collisions with Rb spin by forming van der Waals complexes.<sup>137</sup>

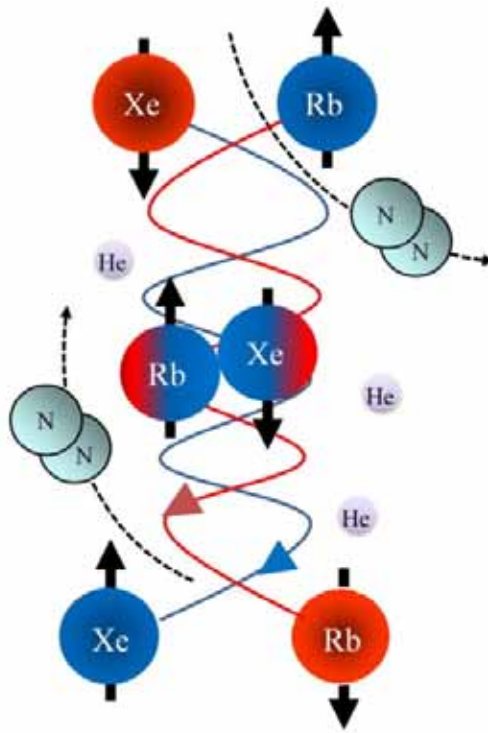


Figure 2-11. Spin-exchange between Rb and Xe. Blue color represents “cold spin” with higher polarization, and red color represents “hot spin” with lower polarization. The polarization is transferred from highly polarized electron spin of Rb to unpolarized nuclear spin of Xe through collisions.

Buffer gases, usually nitrogen and helium gases, are mixed with Rb vapor in order to increase the optical-pumping efficiency. There are several reasons for the presence of buffer gases in the optical-pumping gas mixtures: (1) quenching the fluorescence of the excited state, (2) collision mixing of excited state, and (3) pressure broadening of D1 adsorption line. Nitrogen gas is commonly used in the gas mixture to quench the Rb excited state energy into its vibrational level.<sup>136</sup> Collisions of Rb atoms with buffer gases, especially helium, result in a mixing of atomic sublevels. It has been reported the optical-pumping efficiency can be increased

1/3 to 1/2 by the collision mixing of Rb excited states.<sup>137</sup> Another advantage of using large quantities of buffer gases in optical pumping is the pressure broadening of Rb spectral lines, which is a consequence of interactions between Rb electronic cloud and buffer gases through collisions. The Rb adsorption profile is characterized by the Doppler broadening with the value  $\approx 1\text{GHz}$ .<sup>35</sup> The spectral width of commercially available high-power laser diode array (LDA) is typically 760-1500 GHz, which is much greater than Rb adsorption line.<sup>35</sup> The pressure broadening by buffer gases can increase the Rb D1 absorption line-width up to  $\sim 20\text{ GHz/bar}$  in order to improve the adsorption efficiency of LDA.<sup>141</sup>

### 2.4.3 Continuous-flow Hyperpolarized $^{129}\text{Xe}$ NMR

In the case of thermally-polarized  $^{129}\text{Xe}$  NMR, numerous studies have demonstrated that it is an extremely sensitive probe for chemical and physical environments. However, due to the typically long  $^{129}\text{Xe}$   $T_1$  relaxation time and low spin polarization, thermally-polarized  $^{129}\text{Xe}$  NMR usually requires long recycle delay and numerous signal averaging, resulting in lengthy acquisition time. As mentioned previously, the development of SEOP has led to the use of hyperpolarized (HP)  $^{129}\text{Xe}$  for NMR sensitivity enhancement. The “batch” method of hyperpolarized  $^{129}\text{Xe}$  NMR was first developed by Alex Pines’ group at Berkeley.<sup>16</sup> An isolated pumping cell with valves is regularly filled with Rb metal and fresh Xe gas mixtures. After Xe is optically polarized, the gas mixture is transferred to NMR probe by gas expansion. Several surface studies have been successfully investigated by hyperpolarized  $^{129}\text{Xe}$  NMR batch method.

<sup>16,142,143</sup>

The continuous-flow hyperpolarized (CFHP)  $^{129}\text{Xe}$  NMR method was developed in Happer’s group at Princeton.<sup>144</sup> The gas flow rate, typically 2 to 20 sccm<sup>a</sup> for  $^{129}\text{Xe}$ , allowed for

---

<sup>a</sup> sccm: standard cubic centimeters per minute

$^{129}\text{Xe}$  gas to be polarized to hyperpolarization steady state during few minutes and to pass through the pumping cell.<sup>35</sup> After leaving the pumping cell, the gas mixture containing polarized Xe flowed through NMR sample and  $^{129}\text{Xe}$  NMR signal was acquired. It takes advantage of retaining high Xe spin polarization during the entire course of NMR experiments. For CFHP  $^{129}\text{Xe}$  NMR, Xe spin polarization can be replenished on a time-scale determined by the gas flow rate, not by the  $^{129}\text{Xe}$  longitudinal relaxation time. As a consequence, the NMR recycle delay is not limited by the long  $^{129}\text{Xe}$   $T_1$  relaxation time, permitting phase cycling, signal averaging, and a variety of multi-dimensional NMR experiments. In particular, the sensitivity of hyperpolarized  $^{129}\text{Xe}$  NMR is 4 to 5 orders of magnitude greater than thermally-polarized  $^{129}\text{Xe}$  NMR, thereby making the applications of  $^{129}\text{Xe}$  NMR or MRI more practical.

In addition, a variety of systems that deliver polarized  $^{129}\text{Xe}$  gas to NMR sample have been designed.<sup>35,145-148</sup> All of these developments aim to achieve maximum  $^{129}\text{Xe}$  polarization that can be delivered to NMR samples. Moreover, a number of experimental variables, including gas pressure, flow rate, laser power, and gas composition, have been carefully examined in an attempt to optimize the  $^{129}\text{Xe}$  polarization.<sup>35,145</sup> A polarization of 2-20 % is currently a standard degree for  $^{129}\text{Xe}$  continuously-flow optical polarizer with an output to 1 L/hour of hyperpolarized Xe.<sup>2</sup> For large quantities, a much higher degree of polarization of approximately 70% has been reported.<sup>145</sup> To extend the application of  $^{129}\text{Xe}$  NMR to a wide range of systems, it would be significant to develop an apparatus which can efficiently perform hyperpolarized  $^{129}\text{Xe}$  NMR experiments, especially in the continuous-flow operation mode.

#### **2.4.4 Development of Continuous-flow Hyperpolarized Xe Polarizer**

The NHMFL-UF  $^{129}\text{Xe}$  polarizer was designed by Anthony Zook, a former Ph.D. student in our group.<sup>35</sup> By using a 150 Watt fiber-optic coupled laser diode array (LDA) and after

systematic optimization of the pumping gas composition and operating conditions, the UF polarizer achieved a record of 68 % Xe spin polarization.<sup>35</sup> When our lab moved from Leigh Hall to the New Physics Building in November 2005, we took the opportunity to redesign and reassemble the gas handling system to improve the efficiency and flexibility for various types of experiments. The schematic design is presented in Figure 2-12. The optical pumping systems, including optical polarizer, pumping cell, and Helmholtz pairs, were installed on the laser table. The gas handling system was mounted on a home-built aluminum table which was built on the top of optical pumping system. The entire gas handling system was located in the fringe field of 20 gauss Helmholtz pairs to retain the Xe polarization during gas recirculation. In addition, the gas handling system is about 2 ft. closed to 9.4 T NMR magnet to prevent the depolarization of hyperpolarized <sup>129</sup>Xe gas during the transportation to NMR samples.

Approximately 0.2 g of Rubidium metal<sup>b</sup> was filled into the optical pumping cell. The procedure of filling the Ru metal was performed in a dry N<sub>2</sub> glove box to prevent Rb from oxidation and contaminations. The oxygen trap<sup>c</sup> was installed outside the gas re-circulating loop in order to remove the oxygen in gas cylinders before entering the gas handling system. To extend the lifetime of pumping cell, the gas purification device, such as a rubidium reservoir or titanium getter, can be installed in the inlet of the pumping cell.<sup>147</sup> Such device can help pick up the impurities before entering the pumping cell and reacting with rubidium. For experiments which required the accumulation of hyperpolarized Xe gas, 1 Liter of ballast tank can be used to increase the volume of Xe gas. Two 3-way valves<sup>d</sup> were installed in the inlet and outlet of NMR sample holder. It allows the gas handling system to be isolated while changing the NMR samples. The total volume of the gas re-circulating system (without 1L ballast tank) is approximately

---

<sup>b</sup> part no.: 44214; Alfa-Aesar, *Ward Hill, WA*.

<sup>c</sup> part no.: Model-4002; Alltech Associates Inc., *Deerfield, IL*.

<sup>d</sup> part no.: B-42XS4; Swagelok, *Solon, OH*.

350 mL. The details of spin-exchange optical-pumping apparatus were described in our previous work.<sup>35</sup>

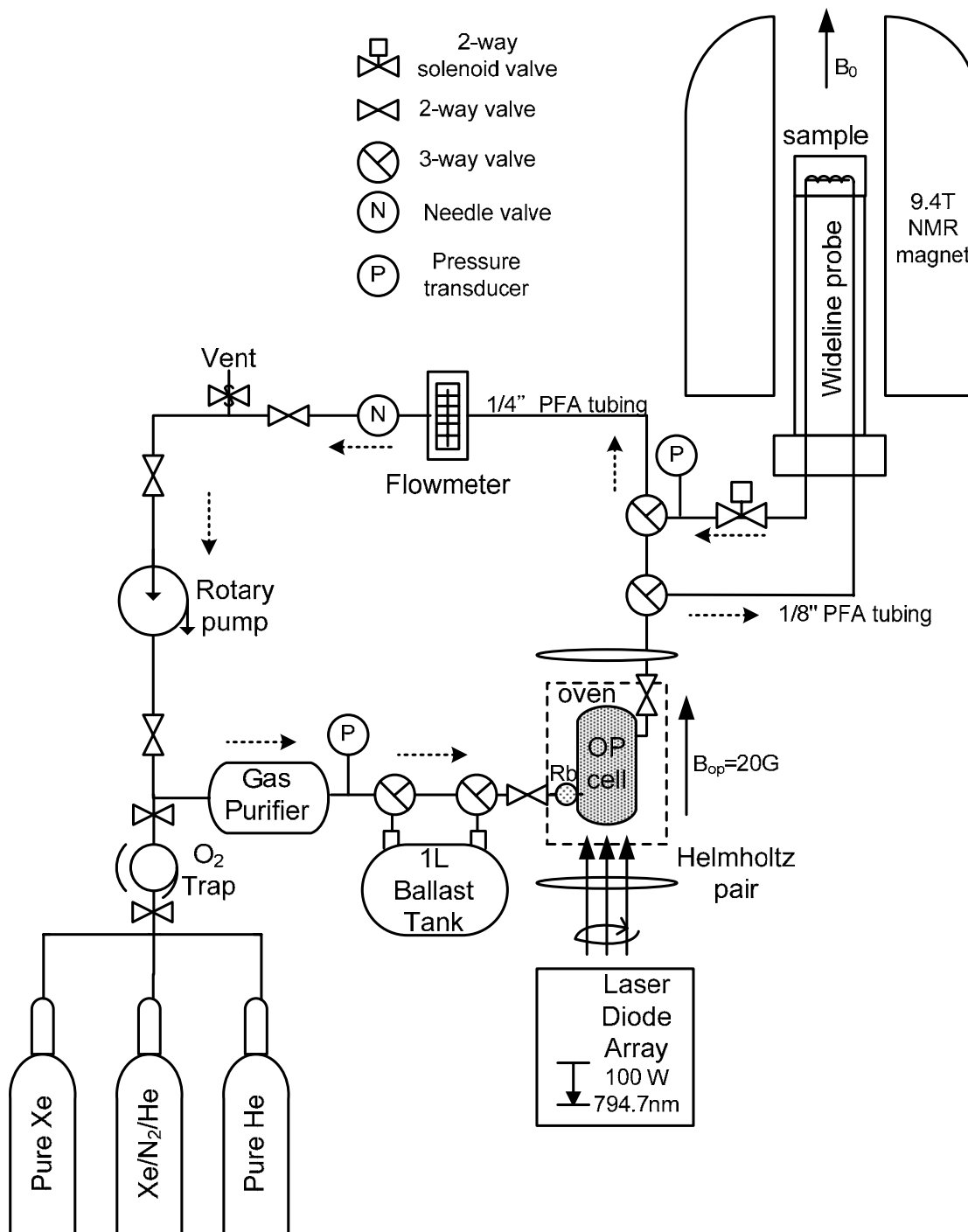


Figure 2-12. Continuous-flow hyperpolarized  $^{129}\text{Xe}$  apparatus.

We have completed the modification of the Bruker wideline probe for continuous-flow hyperpolarized  $^{129}\text{Xe}$  NMR experiments on solid samples. The NMR sample holder was constructed using 1/4" O.D. (outside diameter) PEEK (polyetheretherketone) tube with two vacuum-tight fittings<sup>c</sup> on both ends. The inside diameter of sample holder is 1/16" and the length of sample holder in the detection coil region is 0.3". The volume of sample holder within RF coil region is only 15  $\mu\text{L}$ , and it is particularly well adapted to the experiments with relatively small amounts of sample (*i.e.* 10-20 mg). The 1/8" PFA (perfluoroalkoxy) tubings were connected to the inlet and outlet of the sample holder (*see* Figure 2-12). This assembly allows polarized Xe gas flow through the entire sample in order to retain the maximum Xe polarization during experiments. A 9-turn detection coil for  $^{129}\text{Xe}$  resonance frequency (=110.7 MHz at 9.4 Tesla magnet) was wound directly around the sample holder. The  $\pi/2$  pulse width is typically 4  $\mu\text{s}$ .

The Rb absorption has been optimized as a function of the optical pumping cell temperature, as shown in Figure 2-13a. Figure 2-13b presents the flow-rate dependence of  $^{129}\text{Xe}$  spin polarization at four different pumping cell temperatures. The temperatures of optical pumping cell were read directly from the thermal couple located outside the inlet of the pumping cell. The measured temperature in Figure 2-13 may not reflect the actual temperature of Rb in the pumping cell, since it was found the temperature in the pumping cell was not uniformly distributed during the optical pumping process in the current setup.<sup>35</sup> The maximum  $^{129}\text{Xe}$  polarization obtained by the current polarizer is about 20 % at a flow rate of 150  $\text{mL}/\text{min}$  and at pumping cell temperature of 125  $^{\circ}\text{C}$  with 100 W LDA laser power. The Xe polarization measurements were conducted by using 2% Xe /2%  $\text{N}_2$  /96% He gas mixture.<sup>f</sup> The typical hyperpolarized and thermally-polarized  $^{129}\text{Xe}$  NMR spectra in the gas phase were shown in

---

<sup>c</sup> Nuts, part no.: AT37075; Ferrules, part no.: AT201271; Alltech Associates Inc., *Deerfield, IL.*

<sup>f</sup> part no.: ISO-XHN-C; Spectra Gases Inc., *West Branchburg, NJ.*

Figure 2-13. The application of CFHP  $^{129}\text{Xe}$  apparatus affords enormous NMR sensitivity, allowing numerous experiments to be rapidly and systematically performed under varying conditions (*i.e.* variable temperatures and Xe partial pressures).

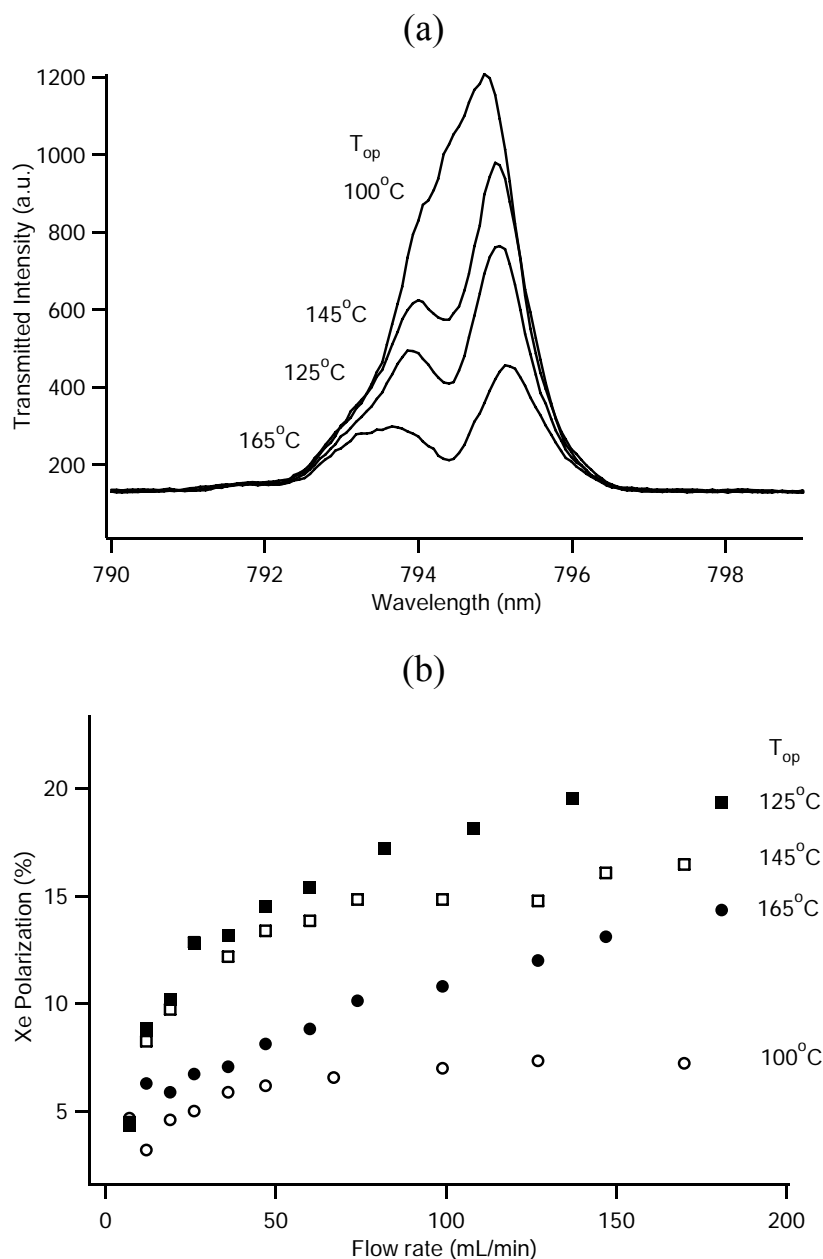


Figure 2-13. (a) Optical transmission spectra of Rb vapor in the pumping cell at four different cell temperatures (100, 125, 145, 165 °C) at a total gas pressure of 3000 torr (2 % Xe mixture) at 100 W laser power. (b) Flow-rate dependence of Xe spin polarization at different pumping cell temperatures.

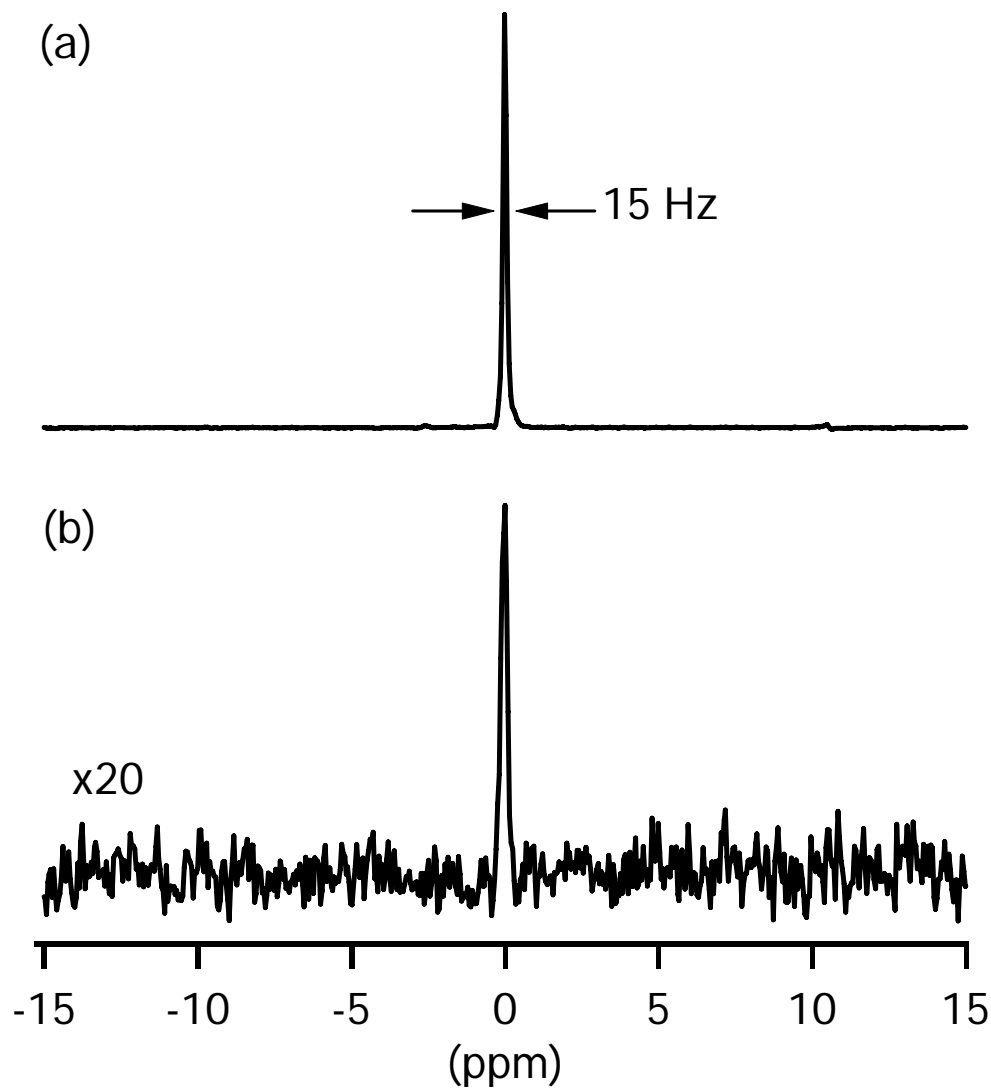


Figure 2-14. (a) Hyperpolarized  $^{129}\text{Xe}$  NMR spectrum (single scan). 2% Xe mixture with total gas pressure of 2327 torr under flow rate of 100 mL/min. Pumping cell temperature is 145 °C with 100 W laser power. The Xe polarization is about 27 %. (b) Thermally-polarized  $^{129}\text{Xe}$  NMR spectrum (16 scans). Xe pressure is 1557 torr in the presence of 635 torr  $\text{O}_2$  to reduce the Xe  $T_1$ . Both spectra were acquired by the modified Bruker wideline probe with empty sample holder at room temperature.

CHAPTER 3  
INVESTIGATIONS OF THERMODYNAMIC PROPERTIES IN DIPEPTIDE NANOTUBES  
BY HYPERPOLARIZED XE-129 NMR

**3.1 Introduction**

Xenon-129 NMR has been extensively used in the structural characterizations of porous materials. As mentioned previously, the major advantage of  $^{129}\text{Xe}$  NMR is the extremely high sensitivity of the Xe chemical shift to the local environment of Xe atoms. Although in many cases the  $^{129}\text{Xe}$  chemical shifts of the adsorbed sites and free Xe gases can be clearly distinguished, the main obstacle to using  $^{129}\text{Xe}$  NMR for structural characterizations is that as the Xe atoms are in fast exchange among the multiple-adsorbed sites, an observed chemical shift represents a dynamical average of Xe on each adsorbed site; therefore, it cannot be attributed to a specific location. Analysis of all the contributions of Xe to the observed chemical shift is usually very complicated. In recent decades, numerous empirical relations between the Xe chemical shift and pore geometry have been successfully developed to solve this problem.<sup>3,9,149-151</sup> However, the extraction of the structural information, such as porosity and pore dimensions, still requires the combination of  $^{129}\text{Xe}$  NMR and other methods, such as adsorption isotherm.

The adsorption property of porous materials has been emerging as an attractive issue of recent researches boosted by promising industrial and environmental applications, such as gas storage.<sup>69,72,152,153</sup> The key issues of the development of novel porous materials for the gas storage are to understand (1) how the adsorbates interact with the frameworks, (2) which specific regions adsorbates are located, and (3) how long adsorbates reside in the specific regions. Hyperpolarized  $^{129}\text{Xe}$  NMR is particularly suitable to answer these questions.

More recently, the organic-based frameworks, such as self-assembled dipeptide nanochannels, have attracted considerable attention in the basis of gas storage. Unlike artificially

created nanotubular materials, dipeptide nanotubes can be constructed naturally by self-assembly of dipeptide molecules. Recent adsorption studies of dipeptide nanotubes have revealed that the peptide-based adsorbents have large gas storage capacities to particular guest molecules (He and Xe).<sup>68,74</sup> In addition, the adsorption behaviors of dipeptide nanotubes with small sizes of cavities match the zeolite-mimics, and have been recognized as “biozeolite”.<sup>68</sup> Therefore, it is of great interest to use the dipeptide nanotubes as simple models to investigate the molecular architectures and adsorption properties by hyperpolarized  $^{129}\text{Xe}$  NMR.

In this chapter, the continuous-flow hyperpolarized  $^{129}\text{Xe}$  NMR has been utilized to explore the adsorption properties of Xe in the 1D self-assembled AV dipeptide nanotubes. The anisotropic Xe line-shapes arising from confinement of Xe atoms in the AV channels were observed. Additionally, the Xe adsorption properties in AV and the quantitative measurements of thermodynamic parameters will be described.

### 3.1.1 Determination of Adsorption Enthalpy from Xe Chemical Shift

Xenon has a van der Waals diameter of 4.4 Å, comparable in the size to that of methane (4.3 Å). The small atomic diameter of Xe enables it to penetrate almost any sizes of porous materials through exchange and diffusion, consequently adsorbing onto the specific locations. The observed chemical shift of the adsorbed Xe varies by over 300 ppm for most materials, and it is extremely sensitive to the local environment of Xe.<sup>2</sup> In most of the continuous-flow hyperpolarized  $^{129}\text{Xe}$  NMR studies, a gas mixture containing a low density (*c.a.* 20-200 mbar) of  $^{129}\text{Xe}$  is optically polarized and transported to the NMR sample space<sup>35</sup>, and thus the dilute adsorption regime (Henry’s law) can be applicable. The isotropic spectral line-shape in the adsorbed Xe phase, which is typically observed in the hyperpolarized  $^{129}\text{Xe}$  NMR spectrum, can be interpreted as a result of a fast exchange between adsorbed Xe and free Xe atoms located in

the interporous spaces of the materials. In such a case, the temperature dependence of observed Xe chemical shift can be expressed by the equation based on the fast-exchange model<sup>154</sup>

$$\sigma_{obs} = \sigma_s \left( 1 + \frac{V}{SK_0 R \sqrt{T} \cdot \exp(\Delta H_a / RT)} \right)^{-1} \quad (3-1)$$

where  $\sigma_s$  is the characteristic chemical shift, representing the chemical shift arising from Xe-surface interactions,  $V$  and  $S$  is the free volume inside the adsorbent and specific surface area of the materials, respectively.  $K_0$  is Henry's law constant,  $\Delta H_a$  is the adsorption enthalpy,  $R$  is the gas constant, and  $T$  is the temperature. This equation exhibits that the observed chemical shift must be Xe pressure independent, since Xe-Xe interactions in the dilute Xe system can be neglected. The values of  $V$  and  $S$  can be obtained from a volumetric N<sub>2</sub> adsorption isotherm, and other parameters,  $\sigma_s$ ,  $K_0$ , and  $\Delta H_a$ , can be determined by the non-linear least-squares fits of the observed Xe chemical shifts ( $\sigma_{obs}$ ) as a function of temperature according to Eq. (3-1).

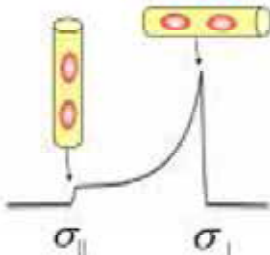
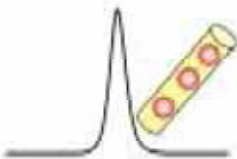
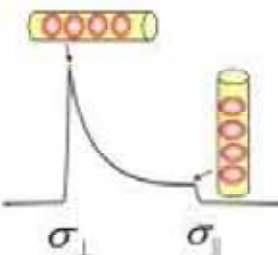
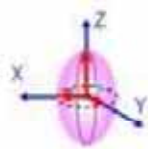
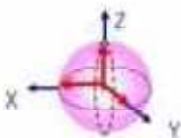
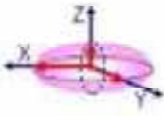
Since hyperpolarized <sup>129</sup>Xe NMR only requires a low Xe density to achieve high NMR sensitivity and gas mixtures of low Xe compositions are commercially available, the Xe adsorption enthalpy in porous materials determined by Eq. (3-1) has recently become a standard technique for hyperpolarized <sup>129</sup>Xe NMR. The adsorption enthalpies of several materials, such as silica<sup>155-157</sup>, Vycor Glass<sup>158</sup>, and zeolite<sup>159,160</sup>, have been measured according to this technique. However, for some unique systems, such as 1D nanotubes with narrow pores, much higher Xe pressures are required to force Xe atoms adsorb into the pores.<sup>161-165</sup> In this case, the chemical shift arising from Xe-Xe interactions becomes more pronounced, and Henry's law is no longer valid. Therefore, in such systems, alternative approaches to measure the Xe adsorption enthalpy are needed.

### 3.1.2 Xe Anisotropic NMR Line-shapes in 1D Nanotube Systems

In most cases, Xe exhibits a symmetric NMR line-shape; however, when Xe is confined in a small void space where the size is on the same order as the Xe atom, the chemical shift depends on the geometry of the pore space and its orientation with respect to the external magnetic field, resulting in an anisotropic chemical shift powder pattern in polycrystalline samples. The information on the symmetry of the pore spaces can be extracted by the chemical shift tensor, thereby providing a useful tool for the characterizations of the porous structure.<sup>19</sup> The Xe anisotropic NMR line-shape has been discovered previously in various materials, including clathrates<sup>166</sup>, aluminophosphate (AlPO<sub>4</sub>)<sup>167</sup>, tris(ethylenediamine) cobalt (III) chloride ((±)-[Co(en)<sub>3</sub>]Cl<sub>3</sub>)<sup>165</sup>, tris(*o*-phenylenedioxy) cyclotriphosphazene (TPP)<sup>20,24</sup>, and dipeptide nanotubes.<sup>21,68,74</sup> Although the components of the chemical shift tensor can be characterized by the orientations of the tensor with respect to the external magnetic field, in a 1D cylindrical channel its orientation is identical to the orientation with respect to the principle channel frame system. In the axially symmetric chemical shift tensor,  $\sigma_{\parallel}$  and  $\sigma_{\perp}$  are assigned to be parallel and perpendicular to the channel axis, respectively. The anisotropy of the axially symmetric shielding tensor is given by  $\xi \equiv \sigma_{\parallel} - \sigma_{\perp}$ .

An inversion in the sign of the CSA has been discovered previously by increasing the Xe density at constant temperature in several materials with 1D pore structure, such as TPP<sup>20</sup> and dipeptide nanotubes.<sup>21</sup> This CSA sign inversion is the result of a competition between the Xe-Xe and Xe-wall interactions which have different contributions to the shielding tensor.<sup>19,20</sup> The Xe occupancy dependence of the axially symmetric CSA line-shape, and the corresponding tensors and interactions are summarized in Table 3-1.

Table 3-1. Summary of axial symmetric CSA tensors ( $\eta=0$ ) in 1D single-file channel

Xe occupancy	low	moderate	high
Xe Spectral Line-shape			
Anisotropy $\xi \equiv \sigma_{\parallel} - \sigma_{\perp}$	$\xi > 0$	$\xi = 0$	$\xi < 0$
Tensor	prolate 	sphere 	oblate 
Interactions	Xe-wall > Xe-Xe	Xe-wall $\approx$ Xe-Xe	Xe-Xe > Xe-wall

The intermolecular Xe shielding of Xe confined in 1D nanochannels has been studied theoretically by Jameson.<sup>19</sup> In 1D channel, two types of interactions need to be considered: Xe-wall and Xe-Xe interactions. In the case where the confined Xe cannot transversely pass one-another inside the channel,  $\sigma_{\parallel}$  is mainly attributed to the Xe-wall interaction, while  $\sigma_{\perp}$  is mainly influenced by the Xe-Xe interaction. The shielding tensor in 1D channels can be described by an ellipsoidal, as shown in Table 3-1. At low Xe density, the Xe becomes prolate where  $\sigma_{\parallel}$  includes the interaction with the atoms forming the interiors of channel wall. On the basis of this fact,  $\sigma_{\parallel}$  must be the smaller shielded component,  $\sigma_{\parallel} < \sigma_{\perp} < \sigma_{free}$ , where  $\sigma_{free}$  represents the chemical shift of free Xe. Such order is valid when Xe-Xe interaction is relatively small in the channel. When a sufficient amount of Xe atoms are adsorbed into the channel such that Xe-Xe interactions become significant, a change in the  $\sigma_{\perp}$  component can result. The Xe-Xe interactions will give rise to an observable contribution to  $\sigma_{\perp}$ , leading to less shielded

component,  $\sigma_{\perp} < \sigma_{\parallel} < \sigma_{free}$ . This effect will be more pronounced as the Xe occupancy progressively increases. A much larger deshielding on  $\sigma_{\perp}$  than  $\sigma_{\parallel}$  is expected by increasing the number of adsorbed Xe atoms in the channels. Therefore, the Xe occupancy of the 1D channel can be inferred from the  $\sigma_{\perp}$  component.

### 3.1.3 Dipeptide Nanotubes

Recently, various inorganic and carbon-based nano-materials, such as nanocavities and nanotubes, have been used as building blocks to assemble the nanometer-scale supramolecular structures. In particular, the class of self-assembled dipeptide nanotubes has been proven to be practical in the design of solid-state porous materials<sup>168-170</sup>, soluble cylindrical supramolecular structures<sup>171</sup>, and biologically relevant ion channels and transmembrane pore assemblies.<sup>172,173</sup> While the concept of applying biological nano-materials, such as dipeptide nanotubes, as building blocks is relatively new, the self-assembly of peptides has been investigated extensively for decades.<sup>174-177</sup> Since the dipeptide molecules can efficiently form into exact 1D crystal structures with certain hydrophobicities by the self-assembly, they can serve as an ideal model system for the advanced studies.<sup>178</sup>

L-alanyl-L-valine (AV) is one of the dipeptide compounds which can form essentially defect-free 1D cylindrical structure through self-assembly. Confinement of Xe atoms into such structures results in an effectively 1D Xe nanotube phase. The chemical structure of AV and its self-assembled 1D channel are illustrated in Figure 3-1a and b, respectively. The inner diameter of the AV nanotube is 5.13 Å, which is slightly larger than the 4.4 Å van der Waals diameter of Xe atom.<sup>74</sup> Furthermore, AV is thermally stable and does not decompose or have any phase transitions up to the melting point of 238 °C.<sup>74</sup> As shown in Figure 3-1c, the hydrophobic channels of AV are lined with -CH<sub>3</sub> groups,<sup>74,179</sup> providing a favorable Xe adsorption

environment with extremely high Xe storage capacity ( $\approx 60$  mL/g).<sup>74</sup> In addition, the polycrystalline sample of AV is commercially available and inexpensive ( $\sim$ \\$35 USD for 250 mg of AV samples). Hence, AV represents an ideal single-file model system in the present study.

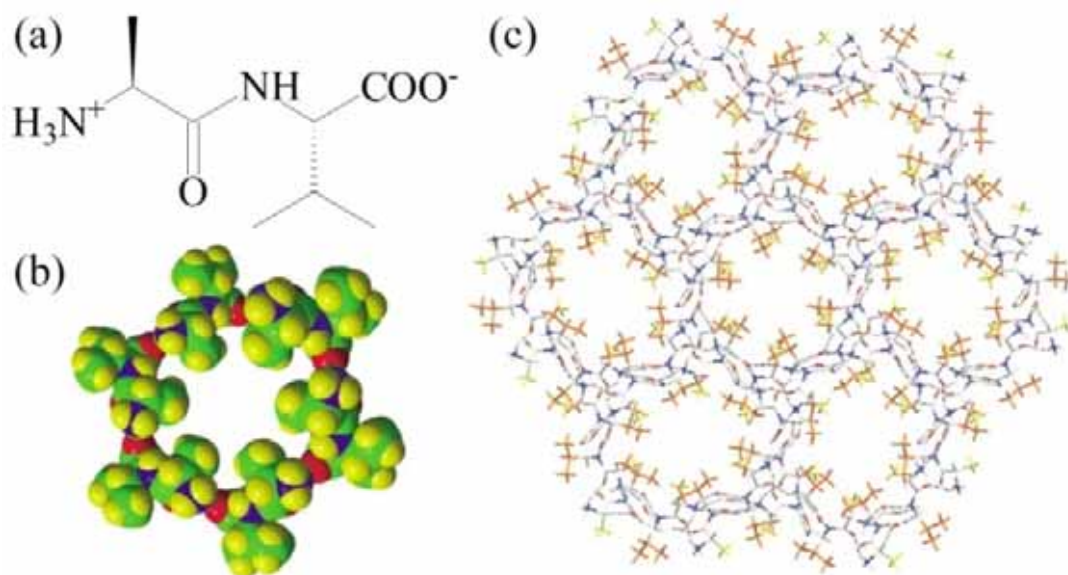


Figure 3-1. (a) molecular structure of L-alanyl-L-valine. (b) Space-filling model of AV nanotube viewed along the channel axis.<sup>74</sup> (H: yellow, C:green, O:red, N:blue) (c) Stick packing arrangement of AV.<sup>178</sup> The channel walls are lined with  $-\text{CH}_3$  groups, providing the hydrophobic interior of AV nanotubes.

It has been reported recently that the  $^{129}\text{Xe}$  NMR line-shapes in AV nanotubes strongly depend on Xe-Xe and Xe-wall interactions. Ripmeester *et al.* studied the Xe occupancy dependence of  $^{129}\text{Xe}$  NMR chemical shifts in AV nanotubes and found that the adsorption properties of AV are very similar to TPP.<sup>21,68,74</sup> A sign inversion of the Xe shielding anisotropy in AV as varying the Xe density has been observed by the thermally-polarized  $^{129}\text{Xe}$  NMR at room temperature.<sup>21</sup> Moreover, as Xe atoms adsorbed into the AV nanotubes, they come into close proximity to the protons and carbons of the methyl groups on the interior channel walls, and the  $^{129}\text{Xe}-^1\text{H}$  and  $^{129}\text{Xe}-^{13}\text{C}$  dipolar interactions can become significant. In principle, such dipolar couplings and the associated dipole-dipole induced nuclear spin cross-relaxation could facilitate polarization transfer from hyperpolarized  $^{129}\text{Xe}$  to the nuclei of AV, such as in the

SPINOE. However, the efficiency of polarization transfer depends strongly on the  $T_1$  relaxation time of the contacted nuclei. While the  $^{129}\text{Xe}$   $T_1$  relaxation time in AV nanotube is on the order of 50-150 sec in 9.4 T, depending on the Xe density<sup>180</sup>, the  $^{13}\text{C}$   $T_1$  relaxation times on the various carbon atoms of AV can be expected to vary with the local environment. For example, the methyl group  $^{13}\text{C}$   $T_1$  can be expected to be very short (*c.a.* several 100 ms, *see* Table 3-2) due to the methyl rotation which provides an efficient leakage mechanism for any non-equilibrium nuclear spin polarization that might be built-up by the SPINOE. Thus, it is essential to understand the  $T_1$  relaxation times of  $^{13}\text{C}$  in AV nanotubes when contemplating spin polarization transfer experiments.

## 3.2 Experimental

### 3.2.1 $^{13}\text{C}$ $T_1$ Relaxation Experiment

All  $^{13}\text{C}$  magic-angle spinning NMR spectra were acquired on a Bruker Avance 400 MHz spectrometer operating at a  $^{13}\text{C}$  frequency of 100.62 MHz and at room temperature using a triple resonance probe with a 4.0 mm rotor. Approximate 100 mg of AV<sup>a</sup> sample was packed into a 4 mm Zirconia rotor with a Kel-F cap. For this amount of material, 32 transients were required to obtain  $^{13}\text{C}$  spectra with an acceptable signal-to-noise ratio.  $^{13}\text{C}$  chemical shifts were referenced to tetramethylsilane (TMS), and NMR parameters were optimized on a sample of adamantane. Typical experimental parameters were as follows:  $^{13}\text{C}$   $\pi/2$  pulse width, 2  $\mu\text{s}$ ; recycle delay, 100 s; spectral width, 40 kHz; sample spinning rate, 6 kHz. The time-domain signals were apodized using a line broadening of 50 Hz prior to the Fourier transformation. High-power proton decoupling (*see* Figure 3-2) was utilized in the  $^{13}\text{C}$   $T_1$  inversion-recovery measurements.

---

<sup>a</sup> part no.: 0210032883; MP Biochemicals, Santa Ana, CA

The  $T_1$  values were obtained by the least-squares fits of a mono-exponential function to the  $\tau$ -dependent inversion-recovery signals of the  $^{13}\text{C}$  nuclei in AV.

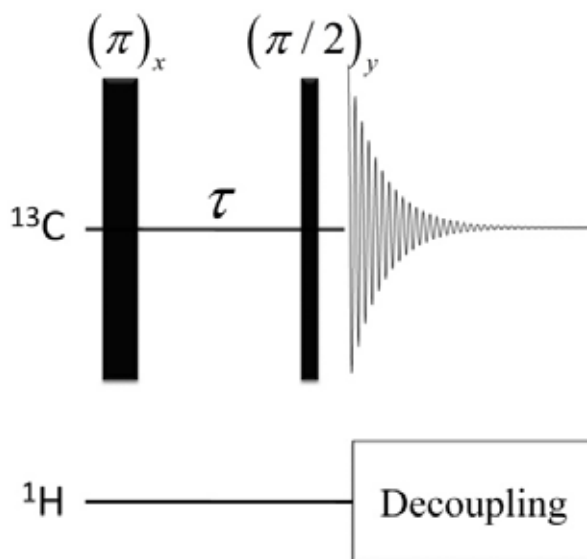


Figure 3-2. Carbon-13 inversion-recovery NMR pulse sequence with proton decoupling during signal acquisition.

### 3.2.2 Hyperpolarized $^{129}\text{Xe}$ NMR Experiments

Continuous-flow hyperpolarized  $^{129}\text{Xe}$  NMR experiments were performed on a 15 mg sample of AV in a magnetic field of 9.4 T field using a modified variable temperature wideline probe. The polycrystalline AV sample was loosely packed into the sample holder and evacuated at  $100\text{ }^\circ\text{C}$  for 2-3 hours prior to NMR measurements. Details of the Rb-Xe spin-exchange optical-pumping system were described in Section 2.4.4. The ultra-pure (99.999%)  $^4\text{He}$  gas<sup>b</sup> was used as a buffer gas to adjust the concentration of nature abundance  $^{129}\text{Xe}$ <sup>c</sup> at a total pressure of 4600 mbar Xe/He gas mixture. The gas was continuously re-circulated between the optical pumping cell and the NMR sample space at a flow rate of  $100\text{ mL}/\text{min}$ .

Hyperpolarized  $^{129}\text{Xe}$  NMR spectra were acquired on the Bruker Avance 400 NMR spectrometer using a one-pulse sequence with a  $\pi/2$  pulse width of  $4\text{ }\mu\text{s}$  and a recycle delay of

<sup>b</sup> part no.: UN1046; Praxair, Danbury, CT

<sup>c</sup> part no.: XE5.0RS-D8; Praxair, Danbury, CT

200 s. With the hyperpolarization signal enhancement, only a single scan was necessary to obtain the sufficient signal-to-noise ratio. Variable temperature experiments were carried out over a temperature range of 100 to -70 °C. The  $^{129}\text{Xe}$  chemical shift was referenced to dilute Xe gas as 0 ppm. The CSA spectral line-shapes were fit by a Matlab program<sup>d</sup> to obtain the components of chemical shift tensor,  $\sigma_{\perp}$  and  $\sigma_{\parallel}$ . Hyperpolarized Xe  $T_2$  measurements were performed at two Xe partial pressures (92 mbar and 3300 mbar) at -10 °C using the Hahn spin-echo pulse sequence,  $(\pi/2)_x - \tau_{echo} - (\pi)_x - \tau_{echo} - (Acq.)_x$ .

### 3.2.3 Scanning Electron Microscopy

The scanning electron microscopes (SEM) image of the polycrystalline AV sample is shown in Figure 3-3a. It was recorded using a JEOL 6400 at the UF Major Analytical Instrumentation Center. The nanotube lengths of AV were measured in the SEM images taken from four different areas of the polycrystalline AV sample. The length distribution of the AV crystallites is presented in Figure 3-3b. The average crystallite length in the AV sample was found to be  $29.4 \pm 2.1 \mu\text{m}$ . Assuming no internal defects that might block the channels, the distribution of crystallite lengths should be equivalent to the distribution of channel lengths.

---

<sup>d</sup> The Mathworks Inc., Natick, MA.

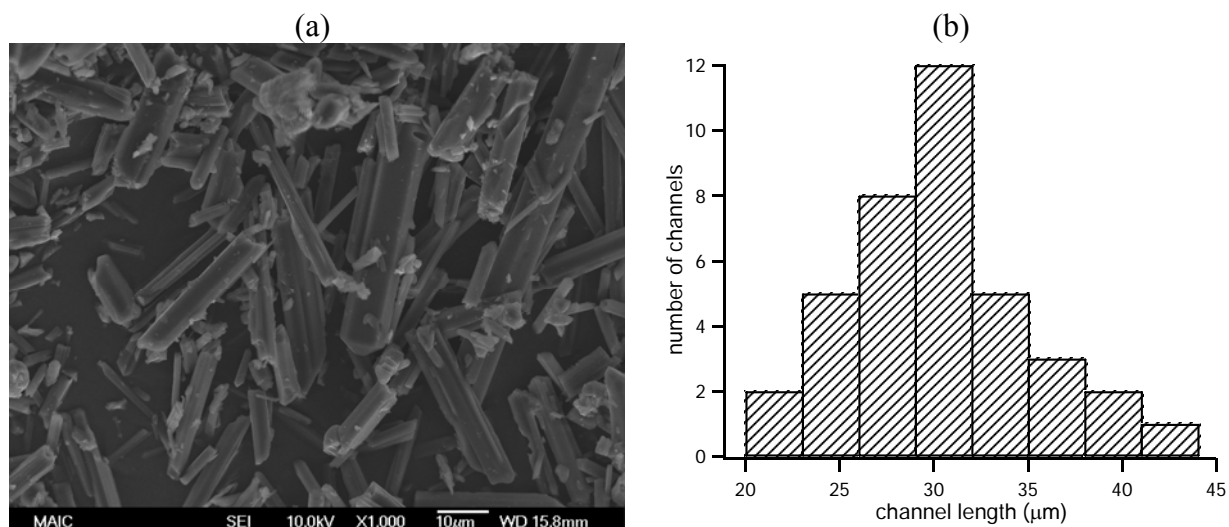


Figure 3-3. (a) SEM Image of AV polycrystalline nanotubes. (b) Distribution of channel lengths in AV nanotube samples. The average channel length is  $29.4 \pm 2.1 \mu\text{m}$  ( $n=38$ ).

### 3.3 Results and Discussions

#### 3.3.1 $^{13}\text{C}$ $T_1$ Relaxation Measurements in AV

Inversion-recovery  $^{13}\text{C}$  NMR spectra acquired as a function of recovery time  $\tau$  in AV nanotubes at  $25^\circ\text{C}$  are shown in Figure 3-4, and the assignment of the  $^{13}\text{C}$  NMR peaks is listed in Table 3-2. In most solid samples, molecular motions are generally in the slow motion regime, where the correlation time of the motion is greater than the inverse Larmor frequency ( $\tau_c > \omega_o^{-1}$ ), leading to an increase in  $T_1$  as molecular motions are reduced (corresponding to an increase in the correlation time of the motion). Therefore, in the solid state of AV nanotubes, the rigid carbonyl groups (carbon f and g) have longer  $^{13}\text{C}$   $T_1$  relaxation times, while the mobile  $-\text{CH}_3$  side chain (carbon a) on the interior wall of AV nanotube has shorter  $T_1$ .

Because the  $^{13}\text{C}$   $T_1$  of the methyl group (carbon a), which is anticipated to be in direct dipolar contact with Xe in AV nanotubes, is extremely short ( $366 \pm 76$  ms), it is likely infeasible to perform the  $^{129}\text{Xe} \rightarrow ^{13}\text{C}$  polarization transfer experiments. However, as the Xe atoms accumulate into the AV channels, the motion of methyl groups may be sterically hindered by the

confined Xe, leading to an increase in  $^{13}\text{C}$   $T_1$  of the methyl group. In addition, the cross polarization transfer efficiency may be increased at low temperatures via the anticipated reduction in the correlation time for the  $^{13}\text{C}$ - $^{129}\text{Xe}$  dipolar coupling. Therefore, it may still be practical to transfer the polarization of hyperpolarized  $^{129}\text{Xe}$  to  $^{13}\text{C}$  nuclei on methyl groups in AV. Furthermore, it was found that  $^{13}\text{C}$  spectra in AV powder samples were not resolved under the static condition (non-spinning) due to strong  $^{13}\text{C}$  dipolar interactions. For the  $^{129}\text{Xe} \rightarrow ^{13}\text{C}$  polarization transfer experiments, the combination of continuous-flow hyperpolarize  $^{129}\text{Xe}$  NMR and magic-angle spinning may be required.<sup>126</sup>

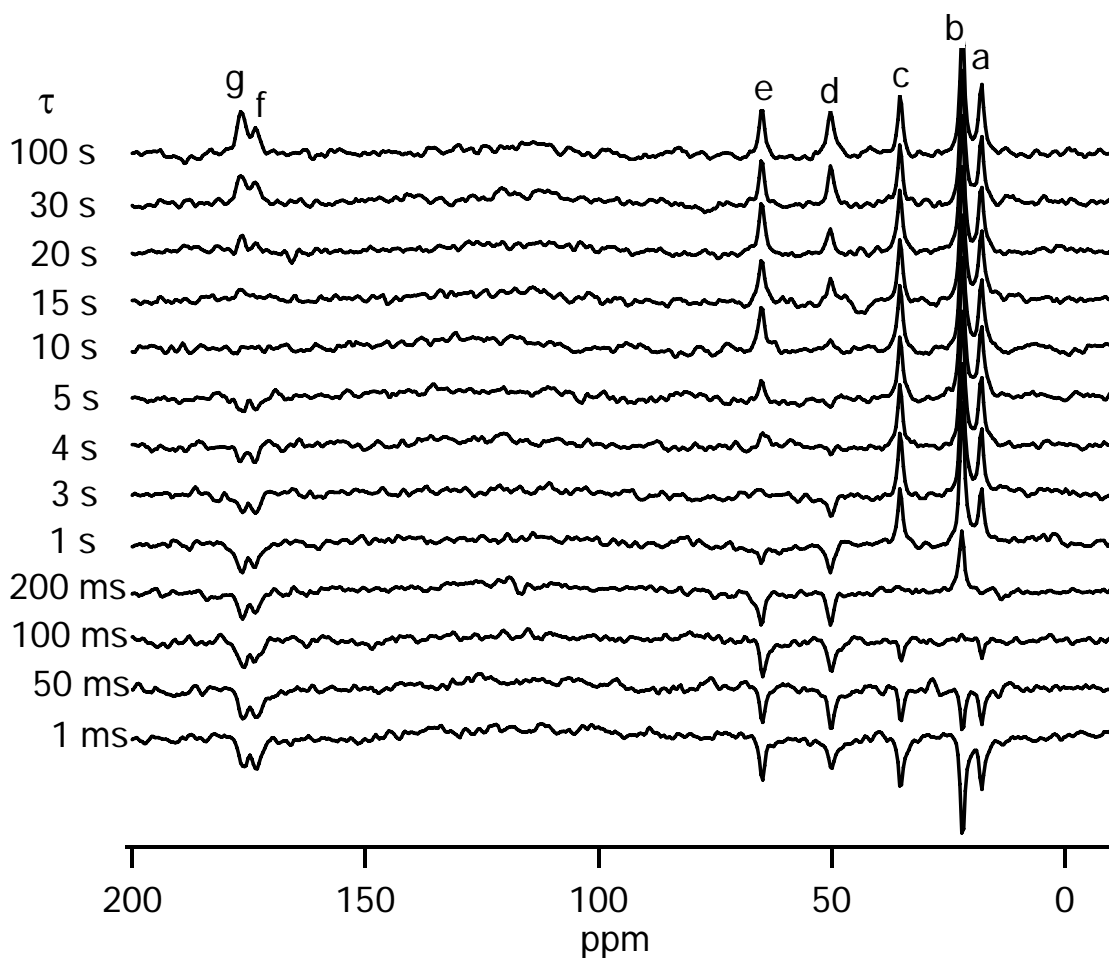
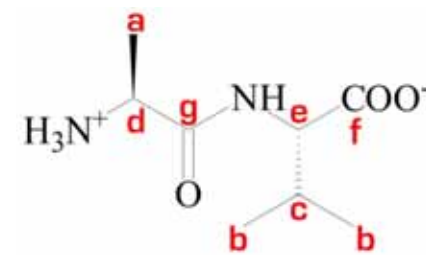


Figure 3-4. Inversion-recovery  $^{13}\text{C}$  NMR spectra recorded as a function of recovery time  $\tau$  in AV nanotubes at room temperature. The labels above the spectra correspond to the carbon atoms in AV shown in Table 3-2. Chemical shifts were referenced to TMS.

Table 3-2. Summary of  $^{13}\text{C}$   $T_1$  relaxation times in AV at 9.4 T and 25 °C

Structure of AV	carbon	$T_1$
	a	$366 \pm 76\text{ms}$
	b	$173 \pm 29\text{ms}$
	c	$342 \pm 50\text{ms}$
	d	$14 \pm 1.8\text{s}$
	e	$5 \pm 0.3\text{s}$
	f	$18 \pm 2.5\text{s}$
	g	$18 \pm 1.8\text{s}$

### 3.3.2 Hyperpolarized $^{129}\text{Xe}$ NMR Spectra in AV

In the sample space of the CFHP  $^{129}\text{Xe}$  NMR probe, the Xe density is increased as the temperature is reduced. Therefore, two factors will be changed simultaneously in the sample space in variable-temperature CFHP  $^{129}\text{Xe}$  NMR experiments: Xe density and temperature. Hyperpolarized  $^{129}\text{Xe}$  NMR spectra in AV nanotube phase at variable temperatures are presented in Figure 3-5. When  $^{129}\text{Xe}$  atoms adsorb into AV, the  $^{129}\text{Xe}$  NMR line-shape exhibits an axially symmetric CSA powder pattern, as in TPP nanotubes.<sup>20</sup> The isotropic chemical shielding value ( $\sigma_{iso}$ ) of Xe in AV increases as the temperature is lowered or as the Xe density is increased. The chemical shift anisotropy is strongly depended on the Xe density and temperature. As illustrated in Figure 3-5, the sign of the anisotropy of the shielding tensor changes from positive ( $\xi = \sigma_{\parallel} - \sigma_{\perp} > 0$ ), at high temperature (or low Xe density), to negative ( $\xi = \sigma_{\parallel} - \sigma_{\perp} < 0$ ), at low temperature (or high Xe density).

Since the Xe spectral line-shape arises from an axially symmetric shielding tensor, two unique principle tensor components,  $\sigma_{\parallel}$  and  $\sigma_{\perp}$ , can be measured, as described previously. The former is collinear with the channel axis, while the latter points towards the channel walls. The chemical shielding of  $\sigma_{\perp}$  is absent in the limit of infinitely dilute Xe, and increases with increasing Xe density inside the channels, whereas  $\sigma_{\parallel}$  is almost independent of Xe density.<sup>19</sup>

Therefore, the  $\sigma_{\perp}$  component can be used to quantitatively determine the Xe density inside the channels.

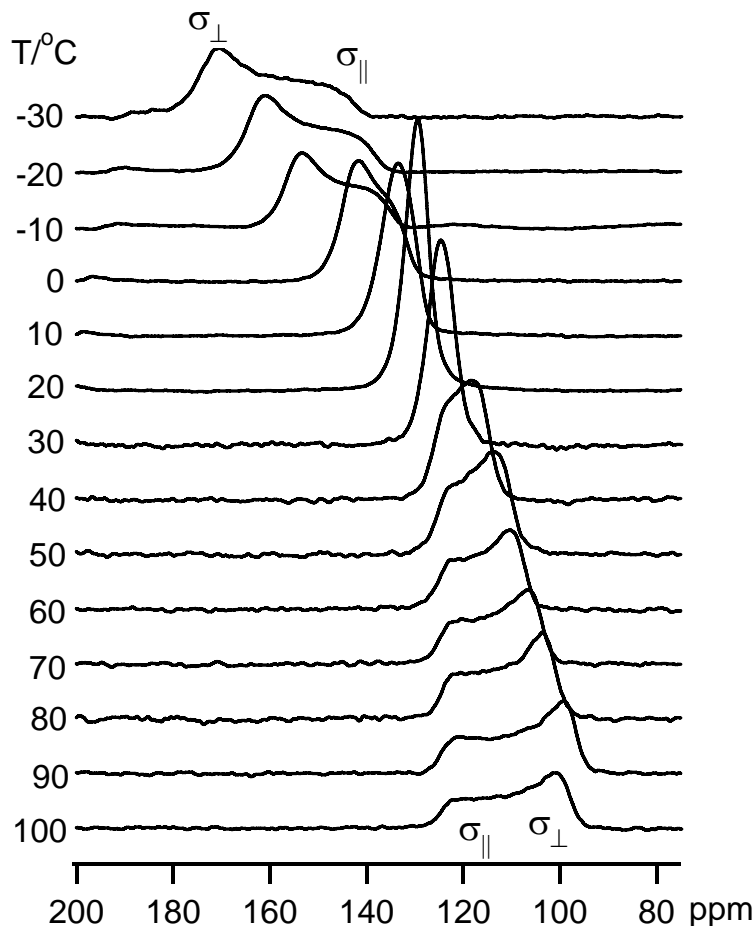


Figure 3-5. Continuous-flow hyperpolarized  $^{129}\text{Xe}$  NMR spectra in AV at variable temperatures and 3300 mbar Xe partial pressure at a total gas pressure of 4600 mbar.

### 3.3.3 $^{129}\text{Xe}$ $T_2$ Relaxation Measurements in AV

In addition to the orientation dependence of the chemical shielding of Xe in AV nanotubes, it was found that the transverse  $T_2$  relaxation of Xe in AV is also orientation dependent. The transverse relaxation times at two Xe gas pressures (92 mbar and 3300 mbar) with different signs of the anisotropy in AV were studied at  $-10^\circ\text{C}$  by typical Hahn spin-echo experiments, and the hyperpolarized  $^{129}\text{Xe}$  NMR spectra are presented in Figure 3-6. The  $T_2$  values were determined

by the least-squares fits to the mono-exponential decay of the signal integrations over the powder peaks as a function of inter-pulse delay,  $\tau_{echo}$ . The Xe  $T_2$  relaxation times at 92 mbar and 3300 mbar Xe pressures in AV at  $-10^\circ\text{C}$  are about  $10.1\text{ ms}$  and  $7.1\text{ ms}$ , respectively. As more Xe atoms adsorbed into the channels, the Xe-Xe interaction dominates over the Xe-wall interaction, which appears to accelerate the  $T_2$  relaxation, leading to shorter  $T_2$  relaxation time at higher Xe density. Moreover, the  $T_2$  relaxations of two shielding components,  $\sigma_{\perp}$  and  $\sigma_{\parallel}$ , are qualitatively compared in Figure 3-6a and b. Interestingly, Xe  $T_2$  relaxation of  $\sigma_{\perp}$  decays more rapidly than that of  $\sigma_{\parallel}$  in both Xe densities. As mentioned previously,  $\sigma_{\perp}$  is mainly attributed to the Xe-Xe interactions. The observed rapid  $T_2$  decay rate in the  $\sigma_{\perp}$  component which results from the pronounced Xe-Xe interaction is in good agreement with the results of shorter  $T_2$  at higher Xe density.

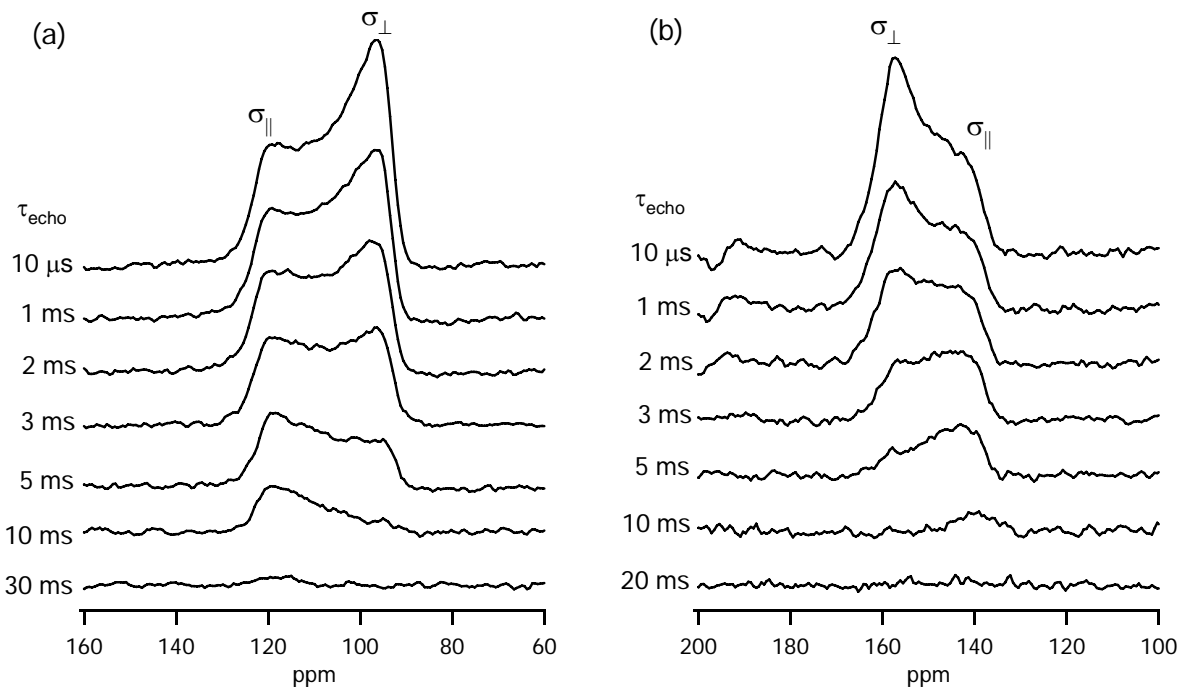


Figure 3-6. Hahn spin-echo Xe NMR spectra as a function of inter-pulse delay at Xe partial pressure of (a) 92 mbar and (b) 3300 mbar at  $-10^\circ\text{C}$ .

### 3.3.4 Determination of Xe Occupancy in AV

Ripmeester and co-worker have acquired thermally-polarized  $^{129}\text{Xe}$  NMR spectra in AV as a function of Xe molar occupancy at  $20^\circ\text{C}$ .<sup>21</sup> The experimental and simulated spectra in AV are presented in Figure 3-7. By performing least-squares fits of the CSA tensor to the  $^{129}\text{Xe}$  spectral line-shapes, the two shielding components,  $\sigma_{\perp}$  and  $\sigma_{\parallel}$ , in the axially symmetric CSA tensor can be determined. Since  $\sigma_{\perp}$  is less sensitive to temperature and most sensitive to Xe density, it can be used to determine the Xe occupancies at variable experimental conditions. Figure 3-8 demonstrates the correlation between  $\sigma_{\perp}$  and Xe molar occupancy,  $\theta_m$ . The empirical relationship between  $\theta_m$  and  $\sigma_{\perp}$  is

$$\theta_m = 0.00536 \cdot \sigma_{\perp} - 0.51964 \quad (3-2)$$

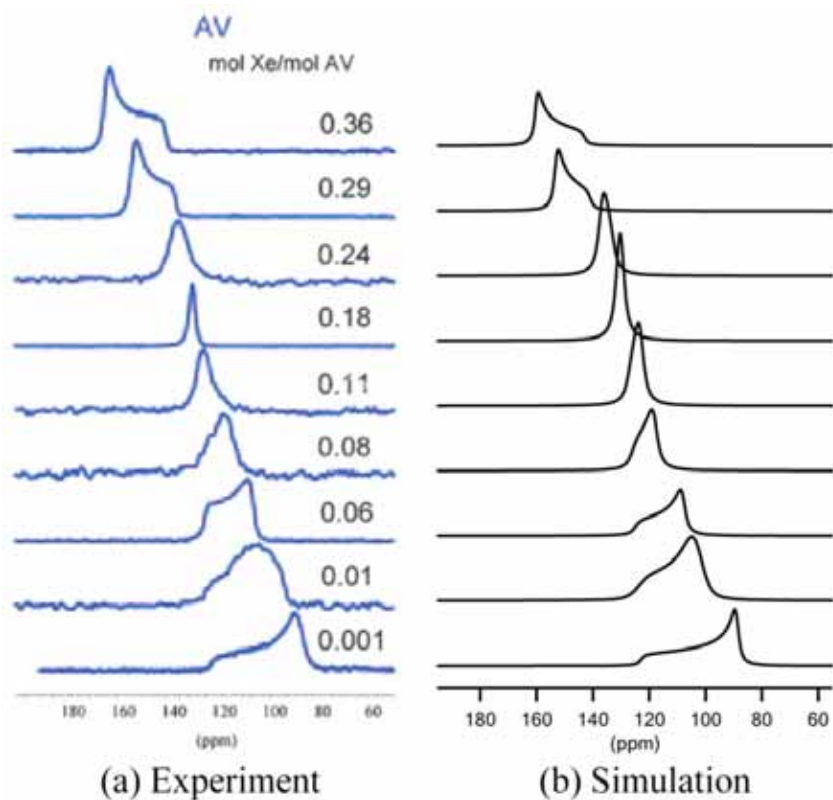


Figure 3-7. (a) Experimental thermally-polarized  $^{129}\text{Xe}$  spectra at  $20^\circ\text{C}$  at various Xe molar occupancies.<sup>21</sup> (b) The corresponding CSA spectra were simulated to obtain the shielding components.

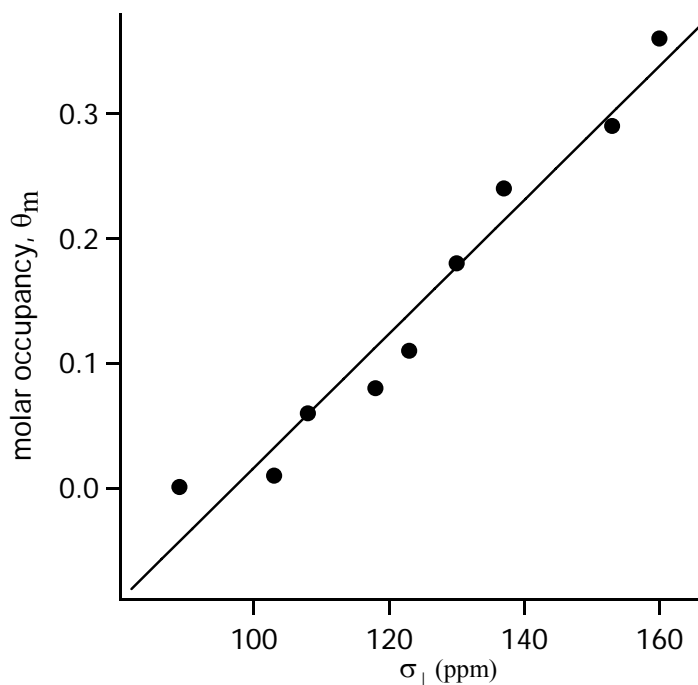


Figure 3-8. Correlation between Xe molar occupancy  $\theta_m$  and  $\sigma_{\perp}$  component in AV nanotubes. The solid line is the linear regression of the data points. The correlation equation is  $\theta_m = 0.00536 \cdot \sigma_{\perp} - 0.51964$  ( $r^2 = 0.9780$ ) at 20 °C.

The maximum Xe molar occupancy in AV nanotubes is about 0.525 mol Xe/mol AV, where the AV nanotube is fully occupied by Xe atoms.<sup>21</sup> In such a case, the Xe fractional occupancy is  $\theta = 1$ . The Xe fractional occupancy can be expressed as  $\theta = \theta_m / 0.525$ . Therefore, the fraction occupancy  $\theta$  at arbitrary Xe pressure and temperature can be determined from the  $\sigma_{\perp}$  shielding component. The determination of  $\theta$  from the Xe chemical shift is extremely convenient and useful for the systematic hyperpolarized  $^{129}\text{Xe}$  kinetic studies in 1D nanotube systems as a function of this key variable.

### 3.3.5 Isothermic Adsorption Enthalpy of Xe in AV

Figure 3-9 demonstrates the temperature dependences of Xe fractional occupancies  $\theta$  at variable Xe densities. The plot is equivalent to a Xe adsorption isobar. Thus, it can be anticipated

that the Xe isobar curves in Figure 3-9 can provide the information of the adsorption thermodynamics of Xe in AV nanotubes.

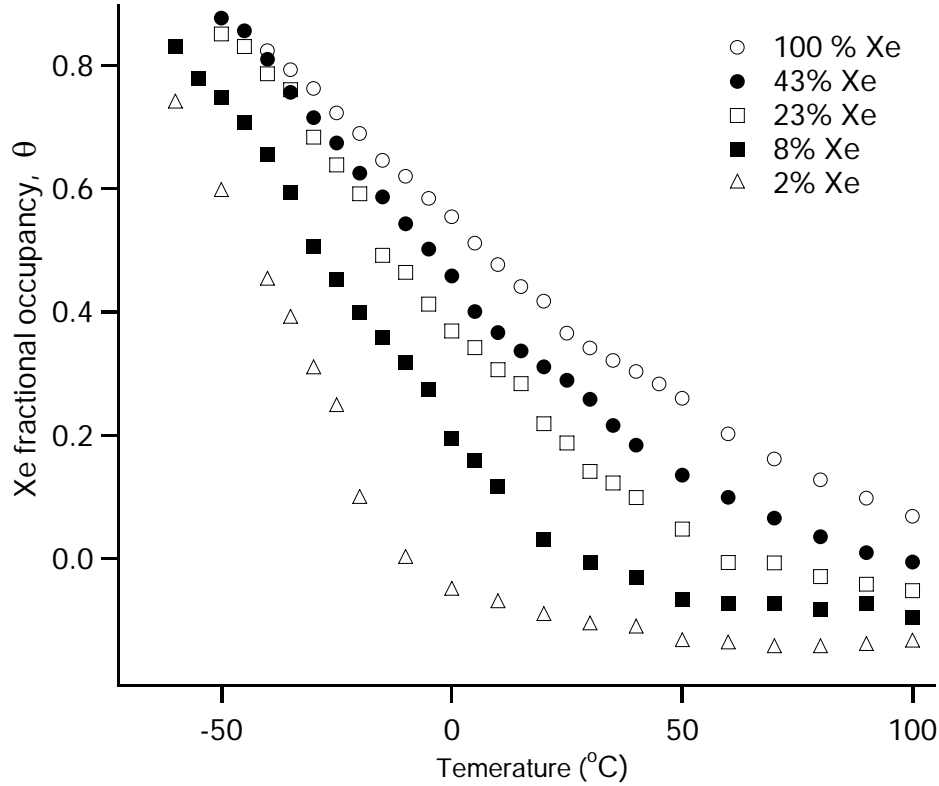


Figure 3-9. Variation of Xe fractional occupancy  $\theta$  with temperature in AV at variable Xe density. (Total gas pressure is 4300 mbar)

To analyze the plot of Xe adsorption isobar in Figure 3-9, the Clausius-Clapeyron equation at a given Xe occupancy was applied

$$\left[ \frac{d \ln p_{Xe}}{d(1/T)} \right]_{\theta} = \frac{\Delta H_{a,\theta}}{R} \quad (3-3)$$

where  $\Delta H_{a,\theta}$  is the isosteric enthalpy of adsorption,  $R$  is the ideal gas constant,  $p_{Xe}$  is the Xe partial pressure, and  $T$  is temperature. A series of hyperpolarized  $^{129}\text{Xe}$  spectra were acquired at variable Xe pressures and temperatures, and the corresponding Xe fractional occupancies were

measured. The slope of each  $\ln p_{Xe}$  vs.  $1/T$  plot gives the isosteric adsorption enthalpy,  $\Delta H_{a,\theta}$ , at a given  $\theta$  based on Eq. (3-3). As seen in Figure 3-10a, it clearly shows that  $\Delta H_{a,\theta}$  increases with increasing  $\theta$ , suggesting the importance of Xe-Xe interactions in the adsorption enthalpy at high Xe density. The negative sign of the adsorption enthalpy indicates Xe adsorption is exothermic. The enthalpy can be further extrapolated to zero Xe occupancy, yielding  $\Delta H_{a,\theta}(\theta \rightarrow 0) \sim -10 \text{ kJ mol}^{-1}$ , which is primarily dependent on the nature of the interior AV channel structure and is typical for a process of physisorption. The enthalpy of vaporization at the boiling point of Xe is  $12.6 \text{ kJ mol}^{-1}$ . Therefore, the estimated value of Xe adsorption enthalpy at zero occupancy implies the stabilization energy due to the Xe-wall interaction in AV is about  $22.6 \text{ kJ mol}^{-1}$ . It can be considered that the Xe-wall interaction results in an effective stabilization of Xe inside the hydrophobic AV channels.

It has been proven by using a standard volumetric Xe adsorption isotherm that Xe adsorption in AV nanotubes follows the Langmuir equation<sup>74</sup>

$$\theta = \frac{Kp_{Xe}}{1 + Kp_{Xe}} \quad (3-4)$$

where  $K \equiv k_a / k_d$  is the equilibrium constant, which is temperature dependent. The equilibrium constant at a given temperature can be consequently determined from Figure 3-9 based on Eq. (3-4). As shown in Figure 3-10b, the thermodynamic equilibrium constant increases as the temperature decreases. Furthermore, the equilibrium constant in AV at  $20^\circ\text{C}$  is about  $0.195 \pm 0.114 \text{ bar}^{-1}$ , which is consistent with the literature value of  $0.12 \text{ bar}^{-1}$ .<sup>74</sup> As the temperature is reduced at  $T < -10^\circ\text{C}$ ,  $k_a$  gradually increases to the values greater than  $k_d$ , implying Xe adsorption in AV is more favorable at reduced temperatures.

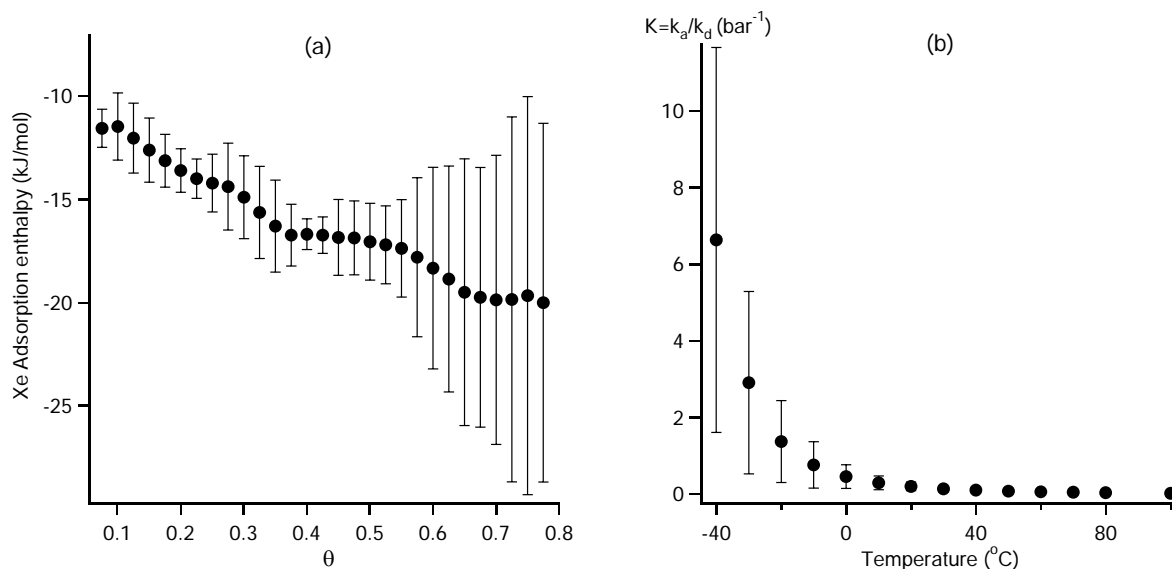


Figure 3-10. (a) Variation of the Xe isosteric adsorption enthalpy with the Xe occupancy in AV. (b) Temperature dependence of the Xe equilibrium constant in AV nanotubes. Error bars indicate 95% confidence intervals.

### 3.4 Conclusions

Continuous-flow hyperpolarized  $^{129}\text{Xe}$  NMR experiments have been carried out to examine the thermodynamic properties of Xe in AV nanotubes. The  $^{129}\text{Xe}$  spectral line-shape exhibited a typical powder pattern broadened by the anisotropy of an axially symmetric chemical shift tensor. The temperature dependence of the CSA in AV showed a sign inversion, which is known as a result of the competition between Xe-wall and Xe-Xe interactions in the nanotubes. The Xe fractional occupancy in AV nanotubes has been quantitatively determined from the  $\sigma_{\perp}$  shielding component. Moreover, the Xe isosteric adsorption enthalpy in AV has been estimated according to the Clausius-Clapeyron equation. The approach is based on the extraction of Xe adsorption isobar under the steady-state condition imposed by continuous-flow hyperpolarized  $^{129}\text{Xe}$  NMR. The Xe adsorption enthalpy extrapolated to zero occupancy is about  $-10 \text{ kJ} \cdot \text{mol}^{-1}$ . The increase of the adsorption enthalpy at high Xe occupancy suggests that Xe-Xe interaction assists the Xe adsorption in AV nanotubes. The equilibrium constant of Xe in AV, estimated

from Langmuir equation, increases at lower temperature, implying Xe is more favorable to enter AV channels at low temperature. The technique demonstrated in the present work may become a useful tool for the evaluation of fundamental thermodynamic properties and quantitative understanding of the adsorption of guest molecules in the 1D host nanotubes in a wide range of nanoporous materials.

It was found that large uncertainties of adsorption enthalpy and equilibrium constant appear at high Xe occupancy and low temperature regions in Figure 3-10. It may be due to the experimental errors of Xe pressures, resulting from the difficulty in accurately measuring the Xe partial pressures under continuous-flow and optical-pumping conditions. As pressurizing the polarizer, Xe/He mixture was mixed manually and gas pressures were directly recorded from the pressure gauge. The recorded values of the Xe pressures may be overestimated due to the heating of the optical pumping cell which causes an expansion of the gas mixture. In addition, the Xe gas may not be distributed uniformly throughout the continuous-flow spin-exchange optical-pumping setup. An easy way to improve the accuracy of the Xe partial pressures would be to use pre-mixed pumping gas mixtures with accurately known gas compositions in continuous-flow hyperpolarized  $^{129}\text{Xe}$  NMR experiments.

CHAPTER 4  
OBSERVATION OF SINGLE-FILE DIFFUSION IN DIPEPTIDE NANOTUBES BY  
HYPERPOLARIZED TRACER EXCHANGE XE-129 NMR

**4.1 Introduction**

Nanotube systems are currently of great interests in a variety of fields, including biosensor, catalysis, molecular confinement, and selective adsorption.<sup>1</sup> Compared to the molecular motions in free-space, dynamic properties of confined particles in the nanotubes are extremely different. The restricted diffusion of guest particles in 1D channels, where the individual pores are too narrow for particles to pass one-another, is known as “single-file diffusion” (SFD).<sup>1,181,182</sup> The concept of SFD was originally introduced in biophysics about 30 years ago to account for the transport of water and ions through channel proteins in the membranes.<sup>183</sup> Since then, in addition to biological systems, SFD has been explored in the context of transport of adsorbates through 1D zeolites<sup>184-186</sup> and diffusion of colloidal particles in narrow tubes.<sup>187-190</sup> SFD has shown particularly interesting characteristics with extreme difference from normal Fickian diffusion. The important distinguishing feature of SFD is that the mean-squared displacement is proportional to the square root of the observation time. This correlation is reflected in the long-time behavior of the mean-squared displacement in a single-file system.<sup>191</sup>

The study of SFD is motivated not only by its ubiquity indicated above, but it has shown that 1D driven diffusion systems with non-equilibrium steady state exhibit a remarkably interesting phenomena. Most of these phenomena have been noticeable in the past decade. Asymmetric simple exclusion process (ASEP), a discrete non-equilibrium model that usually describes the stochastic dynamics of multi-particle transport along 1D lattices<sup>192</sup>, has been successfully modeled the macro/microscopic 1D systems with the *universal* phenomena. The examples of the 1D systems are listed as follows:

- The reptation of entangled polymers where the motions of polymer chains are restricted by the surrounding chains.<sup>193-195</sup>
- The motion of ribosome along m-RNA during protein synthesis.<sup>196-199</sup>
- Molecular motors along microtubuli or actin filaments.<sup>200,201</sup>
- Boundary-induced phase transition.<sup>202-204</sup>
- Vehicular traffic problems on road networks.<sup>205,206</sup>

In principle, ASEP lattice model with symmetric open boundaries illustrated in Figure 4-1 can be used to model the single-file process, and exact analytical solutions have been obtained.<sup>207</sup>

The rules of ASEP with symmetric boundaries are:

- Each site along 1D lattice can be either empty or occupied by a single particle.
- If neighboring site of the particle is empty, the particle can move onto it with a hopping rate of  $1/\tau_a$ .
- Particles interact only through hard-sphere exclusion potential.
- Particles cannot pass one-another in 1D lattice (SFD behavior).

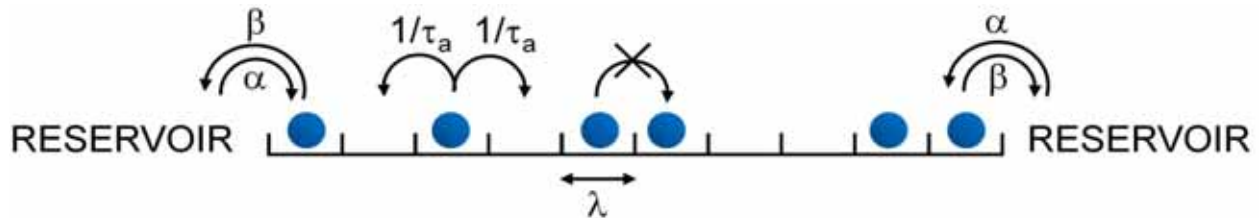


Figure 4-1. The model of asymmetric simple exclusion process (ASEP) with symmetric open boundaries.  $\alpha$  is the probability of moving a particle from the reservoir to the last site of lattice.  $\beta$  is a reverse process of  $\alpha$ . A particle is moved to the next unoccupied site in the lattice with the rate  $1/\tau_a$ .

#### 4.1.1 One-Dimensional Diffusion: Fickian Diffusion and Single-file Diffusion

In a normal 1D system with infinite length, the probability density function (PDF), or commonly named “diffusion propagator”, of tagged particles at position  $z$ , initially starting at

$z_0$ , approaches the Gaussian at long diffusion time, and it can be expressed based on the Fick's law:

$$P_{ND}(z_0|z, t) = \frac{1}{\sqrt{4\pi D_0 t}} \exp\left(-\frac{(z-z_0)^2}{4D_0 t}\right) \quad (4-1)$$

where the mean-squared displacement increasing as diffusion time (*i.e.*  $\langle z^2 \rangle(t) = 2D_0 t$ ), as in normal (random-walk) diffusion, and  $D_0$  is the diffusion coefficient. For a single-file system, where the tagged particles are too large to pass one-another inside the channels, the displacement of particles are upon collisions. The restricted motion of particles in SFD systems makes the diffusion of individual tagged particles anomalously slow. The propagator of SFD particles is also Gaussian, but with mean-squared displacement increasing as square root of time<sup>181,184</sup> (*i.e.*  $\langle z^2 \rangle(t) = 2F\sqrt{t}$ )

$$P_{SFD}(z_0|z, t) = \frac{1}{\sqrt{4\pi F t^{0.5}}} \exp\left(-\frac{(z-z_0)^2}{4F t^{0.5}}\right) \quad (4-2)$$

where  $F$  is single-file mobility.

In SFD system, anomalous diffusion properties may also depend on the density of confined particles  $\rho$  and the observation NMR time-scale  $t_{NMR}$ . At sufficiently low  $\rho$  or short  $t_{NMR}$ , particles in the channels are essentially isolated from one another, leading to normal 1D diffusion (Figure 4-2a). However, at higher  $\rho$  or longer  $t_{NMR}$ , the net displacement over longer length scales requires correlated movement of particles in the channel, leading to single-file diffusion (Figure 4-2b). For an idealized single-file system of hard-sphere particles with density  $\rho$  and diameter  $d$ , single-file mobility is given by<sup>208-210</sup>

$$F = \frac{1-\rho d}{\rho} \sqrt{\frac{D_0}{\pi}} = \frac{1-\theta}{\theta} d \sqrt{\frac{D_0}{\pi}} \quad (4-3)$$

As  $\theta \rightarrow 1$ , the channels become fully occupied and the particles immobilized ( $F \rightarrow 0$ ).

According to the Ansatz of Lin *et al.*<sup>189</sup>

$$\frac{1}{\langle z^2 \rangle(t)} = \frac{1}{2D_0 t} + \frac{1}{2F\sqrt{t}} \quad (4-4)$$

The mean-squared displacement in Eq. (4-4) leads to

$$\langle z^2 \rangle(t) = \frac{2D_0 t}{1+(D_0/F)\sqrt{t}} = \frac{2D_0 t}{1+(t/t_x)^{1/2}} \quad (4-5)$$

It follows that a cross-over between the two diffusion regimes occurs at a characteristic time,  $t_x = (F/D_0)^2$ . A third regime, referred to as “center-of-mass” diffusion, emerges at still longer observations times, where SFD in finite systems with rapid exchange at the channel boundaries involves the correlated motion of all particles in the channel, resulting in normal Fickian diffusion once again (as in the short observation time regime) but with greatly reduced diffusivity.<sup>211</sup>

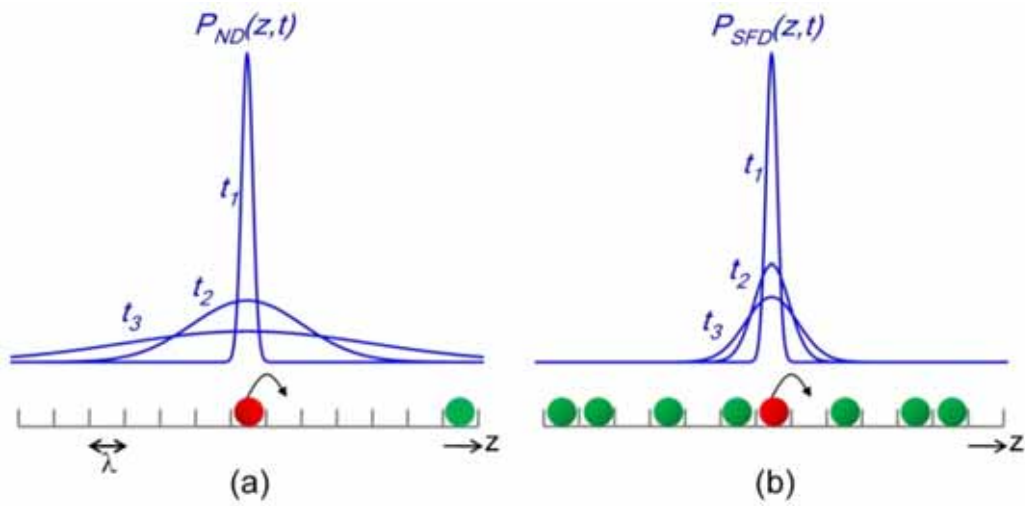


Figure 4-2. The waveforms of probability density function of (a) normal 1D Fickian diffusion (Eq. (4-1)) and (b) single-file diffusion (Eq. (4-2)) corresponding to successively increasing observation time ( $t_1 < t_2 < t_3$ ).  $\lambda$  is the length of each lattice.

While theoretical considerations make definite predictions about the cross-over between the different regimes, validation of theory in nanoporous systems has been severely hampered by the limitations of the available experimental methods and the lack of sufficiently ideal single file host-guest systems. In real nanotube materials,  $F(\theta)$  can be expected to deviate from the simple hard-spheres model due to particle-particle and particle-channel interactions, the presence of an exchange barrier at the single-file boundaries, and non-cylindrical channel topology. Experimental investigations of anomalous diffusion in single-file systems have been limited mostly to macroscopic channels, where it is possible to use direct video analysis of the statistics of the trajectories of micrometer-size colloidal particles in circular channels or channels created by optical tweezers.<sup>187,190</sup> Proton pulsed-field gradient (PFG) NMR, the standard method for measuring the molecular diffusivity in porous solids, is generally restricted to relatively short time scales due to the typically short proton transverse relaxation time in heterogeneous media. For measuring molecular displacement in nanometer length scales, it requires extremely strong pulse-gradient strength for PFG NMR. For example, Kärger *et al.*<sup>212</sup> have measured the single-file mobility of methane in AlPO<sub>4</sub>-5 zeolites by using PFG NMR with maximum gradient strength of 24 T/m.

#### **4.1.2 Tracer Exchange**

Alternatively, the “tracer exchange” method can be experimentally and theoretically employed to study diffusion at arbitrarily long time-scales by observing the time-dependence of the accumulation of labeled molecules, initially located outside the channels, under steady-state adsorption conditions. The schematic diagram of molecular tracer exchange is shown in Figure 4-3. In tracer exchange experiments, the molecular tracer can generally be radioactive or isotopic labeled. The quasi-elastic neutron scattering (QENS) can also be utilized to trace

molecular displacements in nanometer length scales.<sup>213,214</sup> In principle, the tracer exchange curve  $\gamma(t)$  can be defined as

$$\gamma(t) \equiv \frac{\text{number of labeled particle at } t}{\text{number of labeled particle at } t \rightarrow \infty} \quad (4-6)$$

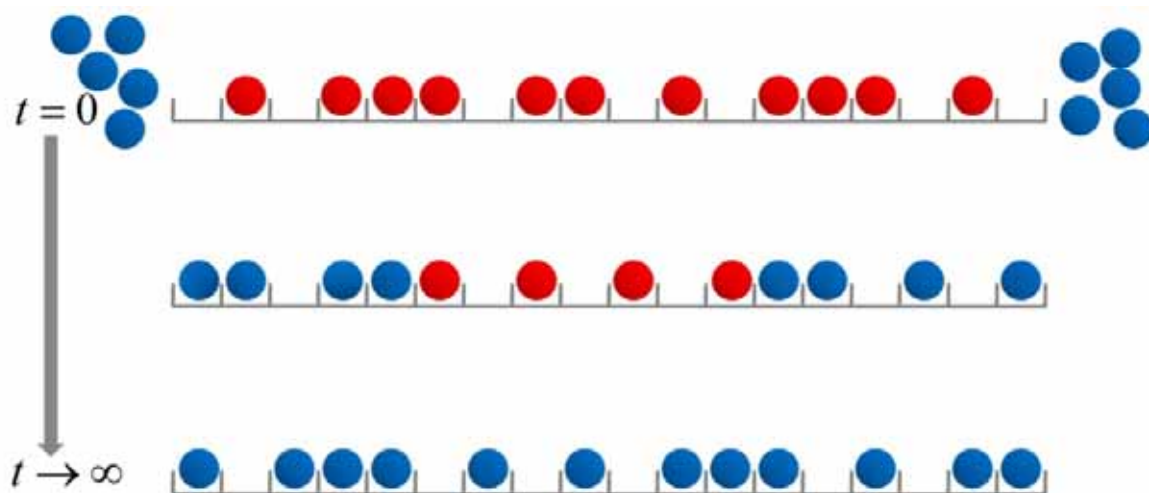


Figure 4-3. Molecular tracer exchange. Red balls represent unlabeled molecules. Blue balls represent labeled molecules. The system reaches to steady-state adsorption at  $t \rightarrow \infty$ .

In the “NMR tracer exchange” method, the nuclear spin serves as the particle label, while spin interactions (*e.g.* chemical shift) report on the particle location. There are several approaches to “label” the spins by NMR. For instance, in nanotube systems, if the spins located inside and outside channels are in the slow exchange regime where the chemical shifts can be distinguished, the frequency selective pulse can be applied to invert the spins outside the channels, and the spins inside the channels remain at thermal equilibrium. By monitoring the decay and growth of NMR signals inside and outside the channels, the information of molecular diffusion in the nanotubes can be obtained. Moreover, hyperpolarized NMR can also be used on the tracer exchange experiments. The schematic diagram of hyperpolarized NMR tracer exchange is illustrated in Figure 4-4. The polarized spins or “cold spins” can be used as the

tracers, since unpolarized spins or “hot spins” are not NMR observable. At sufficient long diffusion time, the signals inside the channel will eventually decay due to the relaxation.

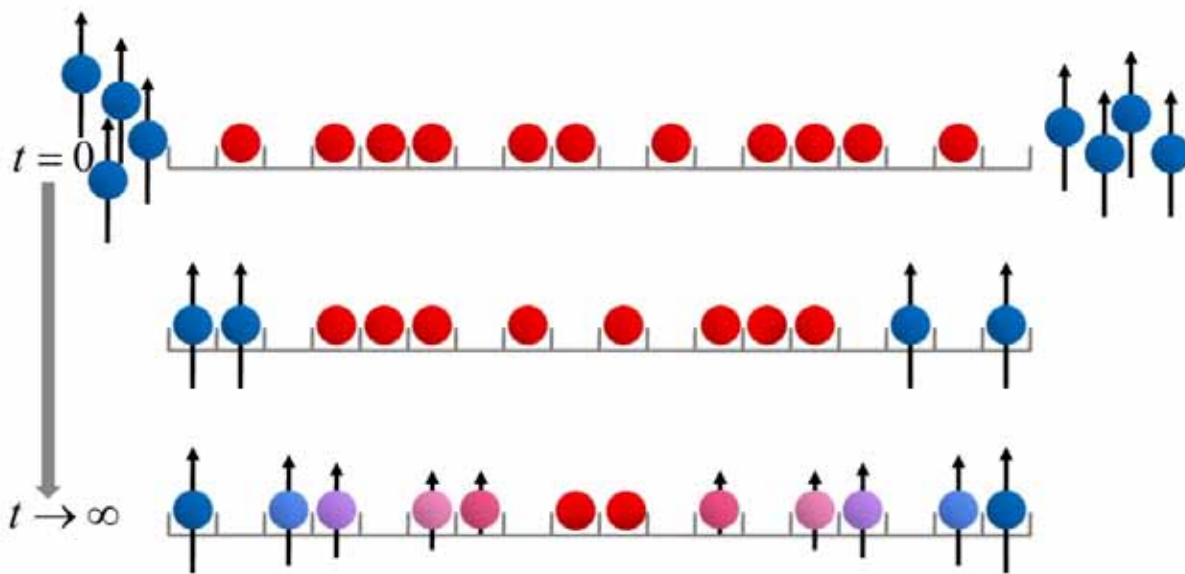


Figure 4-4. Hyperpolarized NMR tracer exchange. Red balls represent “hot” spins (unpolarized). Blue balls represent “cold” spins (polarized). The arrows indicate spin with different polarizations. At  $t \rightarrow \infty$ , the spins are depolarized due to the relaxation. Note that only polarized spins give rise to observable NMR signals.

As first demonstrated by Meersmann *et al.*<sup>215</sup>, Xe diffusion inside the TPP nanochannels has been monitored over a three orders of magnitude range of time-scales due to the long  $T_1$  in this material as a function of temperature and occupancy by continuous-flow hyperpolarized  $^{129}\text{Xe}$  saturation-recovery NMR. In their experiments, the non-selective saturation RF pulse train was first employed to destroy all the Xe magnetizations in the sample space, and the recovery of Xe signals inside the channels was monitored as a function of diffusion time under the continuous-flow condition. Although the SFD behavior of Xe in TPP has been confirmed in their work, the experiments were noted to have a few problems: Firstly, the recovery of Xe adsorbed-phase magnetization can interfere with the recovery of Xe gas magnetization at very short diffusion time, where the exchange occurs near the channel openings. Secondly, when the CFHP  $^{129}\text{Xe}$

saturation-recovery NMR experiments carried out at variable temperatures, the Xe occupancies were also varied with the temperatures. It is not appropriate to discuss the results with two dependent variables in the experiment. Finally, they did not provide the quantitative expression for the single-file mobility.

In this chapter, we report the results of continuous-flow hyperpolarized  $^{129}\text{Xe}$  “selective” saturation-recovery (CFSR) NMR experiments performed over a wide range of Xe occupancies and observation times in the dipeptide nanotubes, AV. It will be shown that the hyperpolarized  $^{129}\text{Xe}$  tracer exchange signals can be analyzed in terms of a magnetization exchange model to obtain the theoretical dependence on the single-file mobility. The derived  $\theta$ -dependence of the nanotube/gas phase signal ratio, assuming the idealized hard-spheres expression for  $F$ , is compared to the experimental data. Finally, the  $\theta$ -dependence of the nuclear longitudinal relaxation time ( $T_{1c}$ ) of  $^{129}\text{Xe}$  inside the channels will be presented.

## 4.2 Experimental

Hyperpolarized  $^{129}\text{Xe}$  NMR experiments were performed on a 15 mg sample of AV<sup>a</sup> at a magnetic field of 9.4 T field (110.7 MHz  $^{129}\text{Xe}$  resonance frequency ) using a modified variable temperature wideline probe. Details of the Rb-Xe spin-exchange optical-pumping system and NMR sample preparations were described in Section 2.4.4. The sample was immersed in a flowing mixture of hyperpolarized  $^{129}\text{Xe}$  in  $^4\text{He}$  carrier gas<sup>b</sup> at a total pressure of 3500 torr. As indicated previously, in the optical-pumping process,  $\text{N}_2$  gas is usually added to the Xe/ $^4\text{He}$  gas mixture to reduce radiation trapping in order to enhance the efficiency of laser polarization. However, it was removed in the experiments to avoid interference with Xe gas diffusion, since  $\text{N}_2$  molecule, with the van der Waals diameter of 3.64 Å, may affect the motion of Xe inside the

---

<sup>a</sup> part no.: 0210032883; MP Biochemicals, Santa Ana, CA

<sup>b</sup> part no.: UN1046; Praxair, Danbury, CT.

channel.  $^4\text{He}$  gas is much smaller compared with  $^{129}\text{Xe}$ , and it is assumed not to alter SFD behavior of Xe. The gas mixture was continuously re-circulated between the optical pumping cell and the sample space at a flow rate of 100 mL/min.

The NMR pulse sequence of selective saturation-recovery experiment is illustrated in Figure 4-5. As shown in Figure 4-6, after reaching a hyperpolarization steady state, the  $^{129}\text{Xe}$  magnetization in the nanotubes was destroyed by a frequency-selective saturation pulse train with Gaussian-shaped pulses, which left the magnetization in the gas phase unaffected. Following a delay  $\tau$  to allow the accumulation of hyperpolarized Xe in the channel, the longitudinal magnetization was converted into an observable NMR signal by a  $4\mu\text{s}$ , non-selective  $\pi/2$  pulse.

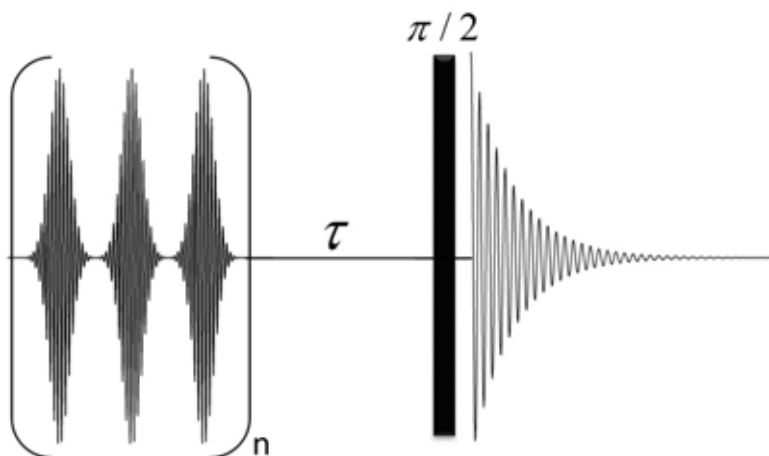


Figure 4-5. NMR pulse sequence of selective continuous-flow saturation-recovery (CFSR) hyperpolarized  $^{129}\text{Xe}$  NMR experiment.

It should be noted that only the hyperpolarized  $^{129}\text{Xe}$  contributes to NMR signal, since the thermally-polarized  $^{129}\text{Xe}$  signal cannot be detected without signal averaging. The molar occupancies  $\theta_m$  were inferred using the correlation between Xe molar occupancy  $\theta_m$  and  $\sigma_{\perp}$ , as determined from Figure 3-8 in Chapter 3:  $\theta_m = 0.00536 \cdot \sigma_{\perp} - 0.51964$  (at  $T = 20^{\circ}\text{C}$ ). The molar

occupancies  $\theta_m$  were converted to volumetric fractional occupancies  $\theta$  using the published value for the Xe gas adsorption capacity of AV.<sup>74</sup>

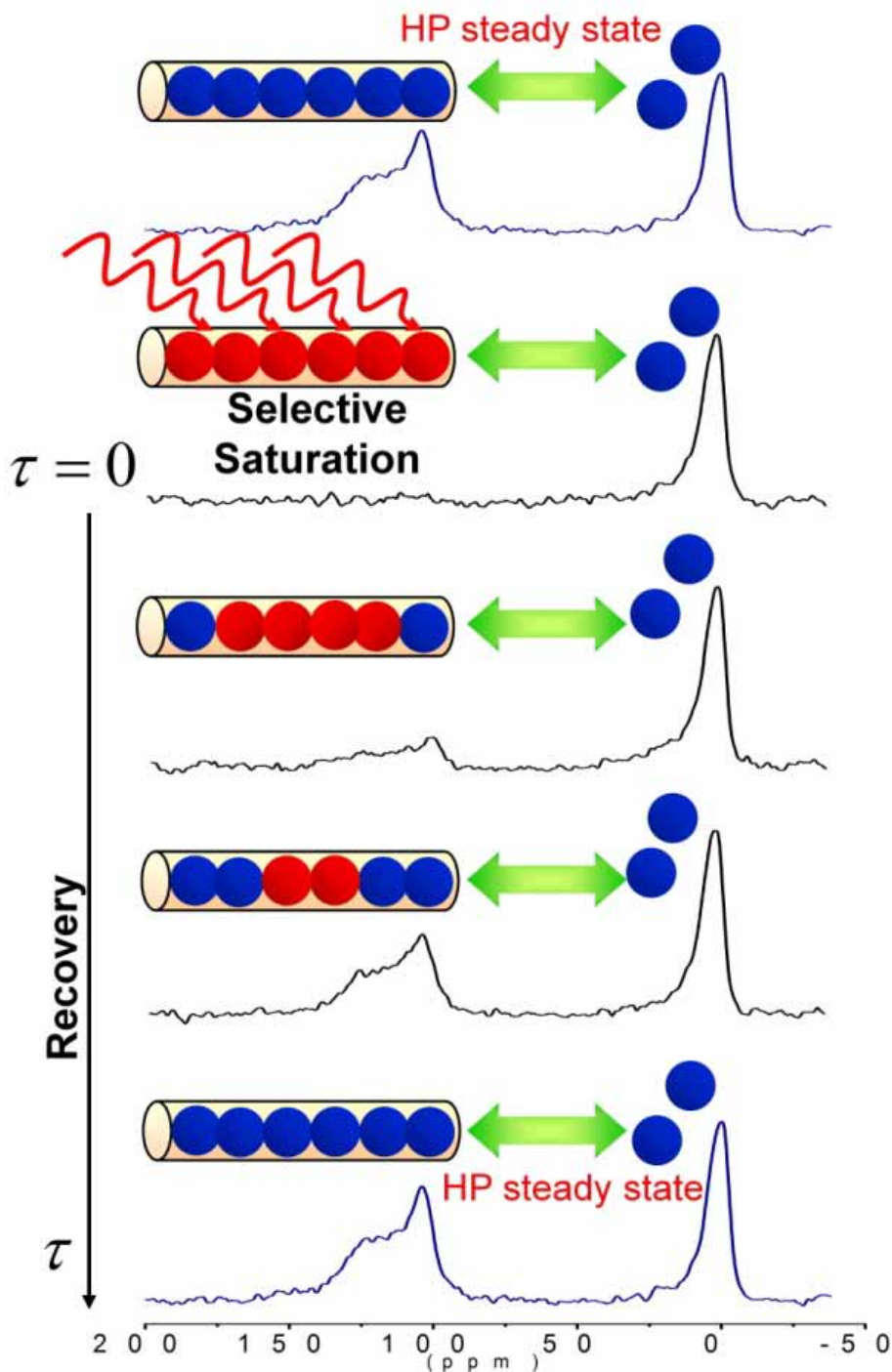


Figure 4-6. Selective continuous-flow saturation-recovery (CFSR) hyperpolarized  $^{129}\text{Xe}$  NMR experiment in AV nanotubes. Blue balls represent “cold” polarized Xe, and red balls represent “hot” unpolarized Xe.

### 4.3 Magnetization Exchange Model for Saturation-recovery in 1D Channel

To extract quantitative information from selective continuous-flow saturation recovery (CFSR) experiments, the derivation of an analytical expression is required. Since the selective CFSR experiment does not affect Xe magnetization in the gas phase, only time-dependence of nanotube phase signal is considered. Base on diffusion-limited Langmuir adsorption, the magnetization in nanotube phase is:

$$M_c = N_a f \theta I_{zc} \quad (4-7)$$

where  $f$  is fractional isotopic abundance of  $^{129}\text{Xe}$ ,  $\theta$  is the monolayer coverage ( $0 < \theta < 1$ ),  $N_a$  is number of adsorbed sites, and  $I_{zc}$  is the average longitudinal nuclear spin angular momenta (*i.e.* Zeeman orders) inside the channels. In the case of nanotubes,  $\theta$  is equivalent to a filling factor. In the CFSR experiment, time-dependence of  $M_c$  was not affected by the gas flow rate. Therefore, the rate of magnetization in nanotube phase is

$$\frac{dM_c}{dt} = k_a p_{Xe} N_a (1 - \theta) f I_z - k_d N_a \theta f I_{zc} - M_c T_{1c}^{-1} \quad (4-8)$$

where  $p_{Xe}$  is the vapor pressure,  $k_a$  and  $k_d$  are the adsorption and desorption rate constants,  $T_{1c}^{-1}$  is the longitudinal relaxation rate of adsorbed phases, and  $I_z$  is the average Zeeman order in the gas phase. In the steady-state condition,  $\theta$  is time-independent; therefore, Eq. (4-7) yields

$$\frac{dM_c}{dt} = N_a f \theta \frac{dI_{zc}}{dt} \quad (4-9)$$

Combined Eq. (4-8) and Eq. (4-9)

$$\frac{dI_{zc}}{dt} = k_a p_{Xe} \frac{1 - \theta}{\theta} I_z - k_d I_{zc} - I_{zc} T_{1c}^{-1} \quad (4-10)$$

Based on the assumption of steady-state Langmuir adsorption, where  $k_d \theta N_a = k_a p_{Xe} (1 - \theta) N_a$ ,

Eq. (4-10) can be rewritten in terms of  $k_d$ :

$$\frac{dI_{zc}}{dt} = k_d I_z - k_d I_{zc} - I_{zc} T_{1c}^{-1} \quad (4-11)$$

Under the conditions where the surface has negligible depolarizing effect on the gas phase,  $dI_z/dt = 0$  and  $I_z \rightarrow I_{zi}$ , where  $I_{zi}$  is the Zeeman order induced by optical-pumping spin-exchange. Thus, for a homogeneous surface comprised of identical adsorption sites, the solution to Eq. (4-11) is

$$I_{zc}(t) = I_{zi} \frac{k_d}{k_d + T_{1c}^{-1}} \left[ 1 - \exp(-k_d + T_{1c}^{-1})t \right] \quad (4-12)$$

Clearly, this expression goes to the appropriate limits as  $k_d \rightarrow 0, \infty$  or  $T_{1c} \rightarrow 0, \infty$ . However, the molecular adsorption “sites” in a nanotube, while exhibiting Langmuir adsorption<sup>74</sup>, are not uniformly accessible to the gas phase. The desorption of a Xe atom with a displacement  $z$  from the channel opening can be considered as a two-step sequential process: the atom must first make its way to the channel opening, and then it must overcome a potential energy barrier to enter the gas phase. The equilibrium is preserved by the reverse process. In the case where the barrier does not affect the overall rate of desorption and desorption is *diffusion-limited*, the nanotube may be modeled as a surface with a distribution of desorption rates  $k_d \approx \tau_d^{-1}$ , where  $\tau_d$  is the diffusion time from a site with a mean displacement

$$\bar{z} = \int_0^{\infty} z P_d(z, \tau_d) dz \quad (4-13)$$

where  $P_d$  is the diffusion propagator. Thus,  $\tau_d^{-1} \approx (D_0/\pi)/\bar{z}^2$  and  $\tau_d^{-1} \approx (F/\pi)^2/\bar{z}^4$  are for normal and single file diffusion, respectively. The average Zeeman order of a nanotube of average length  $L$  is calculated from the distribution of rates, or displacements  $\bar{z}$  :

$$\overline{I_{zc}}(\tau) = \frac{I_{zi}}{L} \int_0^L \frac{k_d}{k_d + T_{1c}^{-1}} \left[ 1 - \exp\left(-\left(k_d + T_{1c}^{-1}\right)\tau\right) \right] d\bar{z} \quad (4-14)$$

It can be shown that in the long channel limit, where  $(F^2 T_{1c} / \pi^2)^{1/4} \ll L$ , Eq. (4-14) can be rewritten using the identities for the incomplete  $\Gamma$  function.

$$\overline{I_{zc}}(\tau) \approx I_{zi} \frac{\sqrt{\pi F}}{2^{3/2} L \Gamma(1/4)} \int_0^\tau t^{-3/4} e^{-t/T_{1c}} dt \quad (4-15)$$

The deviation from Eq. (4-14) to Eq. (4-15) will be demonstrated in Appendix A. The analogous result for normal diffusion is

$$\overline{I_{zc}}(\tau) \approx I_{zi} \frac{\sqrt{\pi D_0}}{4L} \int_0^\tau t^{-1/2} e^{-t/T_{1c}} dt \quad (4-16)$$

The observed NMR signal of the adsorbed phase is proportional to the total longitudinal magnetization of  $^{129}\text{Xe}$  inside the channels,  $M_c$ , which is obtained by multiplying  $\overline{I_{zc}}$  by  $N_c$ , the number of channels in the sample, and  $\theta f(L/d)$ , the number of  $^{129}\text{Xe}$  atoms per channel. Hence, the total NMR signal in the nanotube phase for SFD systems is

$$S_c^{SFD}(\tau) \propto M_c = N_c \theta f I_{zi} \frac{\sqrt{F}}{4d} \int_0^\tau t^{-3/4} e^{-t/T_{1c}} dt \quad (4-17)$$

The corresponding expression for normal diffusion is:

$$S_c^{ND}(\tau) \propto M_c = N_c \theta f I_{zi} \frac{\sqrt{D_0}}{4d} \int_0^\tau t^{-1/2} e^{-t/T_{1c}} dt \quad (4-18)$$

Notably, the  $S_c^{SFD}(\tau) \propto \sqrt{F}$  dependence also emerges in the derivation of  $S_c^{SFD}(\tau)$  from the standard tracer exchange curve<sup>211</sup>

$$\gamma(\tau) = \frac{S_c^{SFD}(\tau)}{S_c^{SFD}(\tau \rightarrow \infty)} = \frac{1}{L} \sqrt{\frac{8 \langle z^2(\tau) \rangle}{\pi}} = \frac{4}{L} \sqrt{\frac{F\sqrt{\tau}}{\pi}} \quad (4-19)$$

which gives the fraction of labelled molecules in the channels at time  $\tau$ .

Eq. (4-17) can also be validated on the basis of simple considerations: the signal contribution due to atoms reaching the channel segment  $z \rightarrow z + dz$  is exponentially damped due to longitudinal relaxation:  $S_c(z) \propto e^{-t/T_c} dz$ , where  $dz = (2F)^{1/2} t^{-3/4} dt$ . Integration up to the observation time yields Eq. (4-17). The analogous expression for normal diffusion (Eq. (4-18)) can be obtained similarly.

In principle, the  $\theta$ -dependence of the steady-state <sup>129</sup>Xe signal expressed in Eq. (4-17) could form the basis for experimental determination of  $F(\theta)$ , except for a technical complication:  $I_{zi}$  varies with the optical pumping gas composition,<sup>35</sup> and even at a fixed composition,  $I_{zi}$  may drift during the course of an experiment due to factors that are hard to control. Therefore, to compare the signal intensities obtained at different Xe pressures, it is necessary to standardize the signals to an intensity reference. As suggested by Meersmann *et al.*<sup>215</sup>, it is convenient to take the ratio of the nanotube and gas phase signals,  $S_c(\tau)/S_{gas}$ , which eliminates the variation of  $I_{zi}$  due to optical pumping with different Xe pressures in the gas mixture. Since magnetization in gas phase is  $M_g \approx n_{gas} f I_{zi}$ ,

$$\frac{S_c^{SFD}(\tau)}{S_{gas}} = C_F(\theta, T) \int_0^\tau t^{-3/4} e^{-t/T_c} dt \quad (4-20)$$

$$\text{where } C_F(\theta, T) = \frac{\pi^{1/2}}{2^{3/2} \Gamma(1/4)} \frac{\theta \sqrt{F}}{d} \frac{N_c}{n_{gas}} \quad (4-21)$$

The corresponding expression for 1D normal diffusion is

$$\frac{S_c^{ND}(\tau)}{S_{gas}} = C_D(\theta, T) \int_0^\tau t^{-1/2} e^{-t/T_{1c}} dt \quad (4-22)$$

$$\text{where } C_D(\theta, T) = \frac{\pi^{1/2}}{4} \frac{\theta \sqrt{D_0}}{d} \frac{N_c}{n_{gas}} \quad (4-23)$$

Eq. (4-20) and Eq. (4-22) have comparable expressions as Eq. (3) and Eq. (4) of Ref. <sup>215</sup>, but advantageously, our derivation yields an explicit expression for the coefficient  $C_F(\theta)$ , revealing its proportionality to (1) ratio of the number of channels ( $N_c$ ) to the number of gas phase atoms ( $n_{gas}$ ) and (2) the square root of the single file mobility. However,  $n_{gas}$  is infeasible to determine from gas peak integral since the peak area in gas phase is relative to hyperpolarized Xe gas in the sample space, not the total number of Xe gas molecules. In principle, if  $N_c/n_{gas}$  is known, a quantitative estimation of  $F$  can be obtained from measurement of  $C_F(\theta)$  and Eq. (4-21).

#### 4.4 Results and Discussions

Representative selective saturation-recovery signals acquired at -10 °C for two Xe partial pressures, 2650 torr and 56 torr, corresponding to occupancies of  $\theta = 0.66$  and 0.16, respectively, are presented in Figure 4-7, along with the non-linear least-squares fits to Eq. (4-20) and (4-22). The NMR signals were integrated over the powder pattern and divided by the integrated gas signals. The two variable parameters in the fits were the longitudinal relaxation time  $T_{1c}$  in nanotube phase and  $C_F$ . Results of the regression analysis are summarized in Table 4-1.

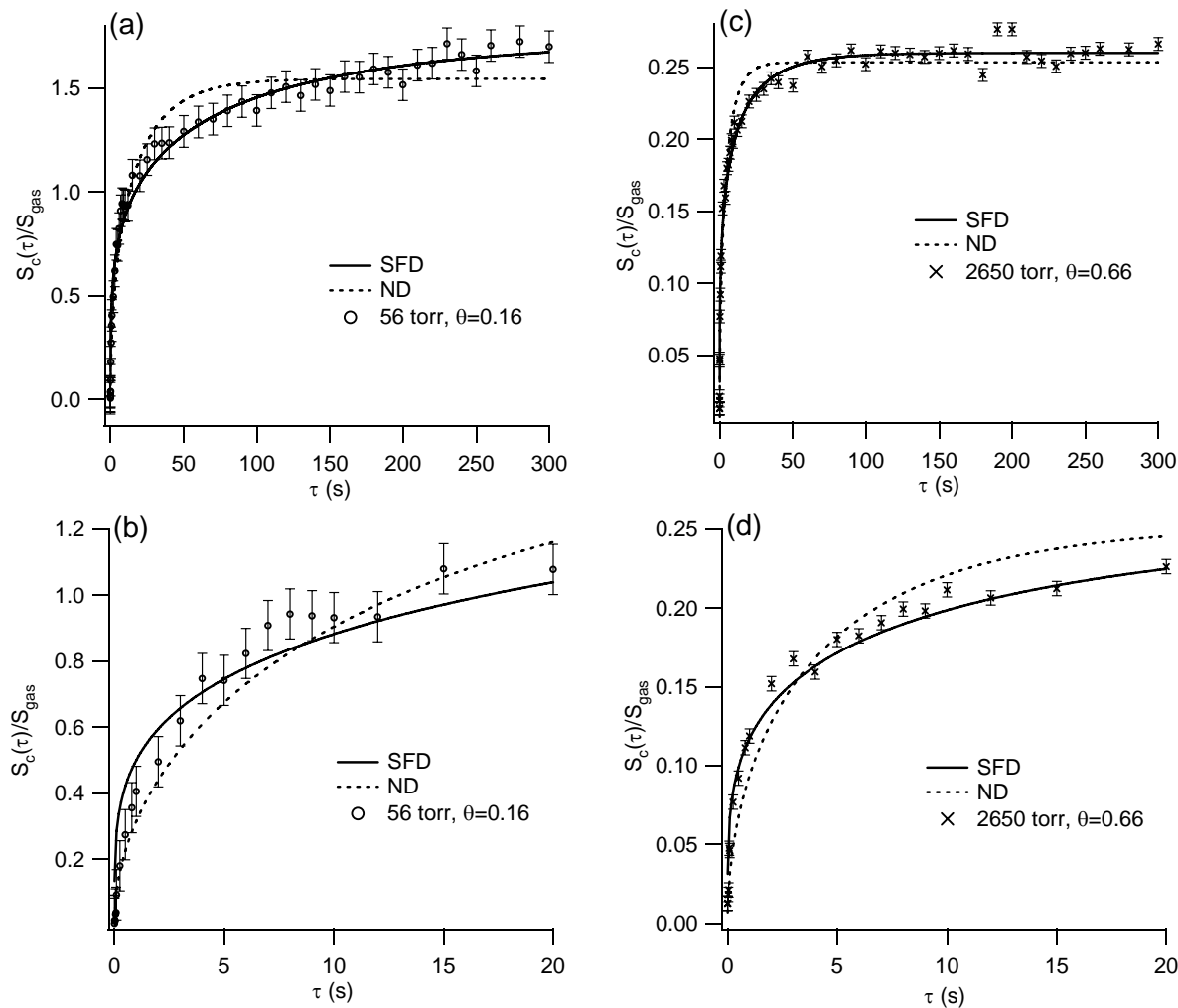


Figure 4-7. Least-squares fits to the selective saturation-recovery NMR signal (normalized to the steady-state gas phase signal) of  $^{129}\text{Xe}$  inside 15mg AV, obtained at  $T = -10^\circ\text{C}$ , to the expressions for single-file diffusion (SFD, Eq. (4-20)) and normal diffusion (ND, Eq. (4-22)). (a) Low occupancy: 56 Torr Xe,  $\theta = 0.16$ . (c) High occupancy: 2650 Torr Xe,  $\theta = 0.66$ . Error bars indicate 90% confidence intervals. Time-base expansions of (a) and (c) are presented in (b) and (d), respectively. Values for fitted parameters are given in Table 4-1.

Table 4-1. Nonlinear regression analysis of saturation-recovery hyperpolarized  $^{129}\text{Xe}$  NMR of Xe in AV nanotubes at  $-10\text{ }^\circ\text{C}$ .

$p_{\text{Xe}}/\text{torr}$	$p_{\text{total}}/\text{torr}$	$\theta$	DIFFUSION MODEL				
			Single-File; Eq.(4-20)			Normal; Eq.(4-22)	
			$T_{1c} \pm \lambda_{95}$ (s)	$C_F \pm \lambda_{95}$	$r^2$	$T_{1c} \pm \lambda_{95}$ (s)	$r^2$
56	3500	0.16	$217 \pm 90$	$0.125 \pm 0.006$	0.974	$30 \pm 5$	0.973
2560	3500	0.66	$35 \pm 6$	$0.029 \pm 0.001$	0.981	$8.5 \pm 1.3$	0.969

Although the SFD model yielded superior agreement to the data at both low and high occupancy for all  $\tau$ , the most decisive comparison was obtained for the  $\theta = 0.66$  run, which unequivocally confirmed single-file diffusion of Xe in AV nanotubes. The tabulated results also reveal a substantial decrease in  $T_{1c}$  with increasing Xe occupancy. Figure 4-8a presents the  $\theta$  - dependence at  $T = -10, +10, +25$  and  $+40\text{ }^\circ\text{C}$ , all of which show a monotonic decrease in  $T_{1c}(\theta)$ . The measured  $T_{1c}$  did not change after re-packing the sample, and was not affected by changing the gas flow rate. Spin relaxation inside the channels of AV can occur via several possible mechanisms, including the dipolar ( $^{129}\text{Xe}$ - $^{129}\text{Xe}$  and  $^{129}\text{Xe}$ - $^1\text{H}$ ) and chemical shift mechanisms, and spin-rotation relaxation in transient Xe-Xe complexes. Rotational modes are expected to be suppressed due to the spatial confinement of the channels. The spectral density due to fluctuations of the  $^{129}\text{Xe}$ - $^1\text{H}$  dipolar interaction with the methyl groups of the channel could vary with  $\theta$ . The chemical shift interaction, which increases in proportion to occupancy, could also account for the spin relaxation inside the channels. Variable magnetic field studies would identify the dominant relaxation mechanism, but are beyond the scope of the present work.

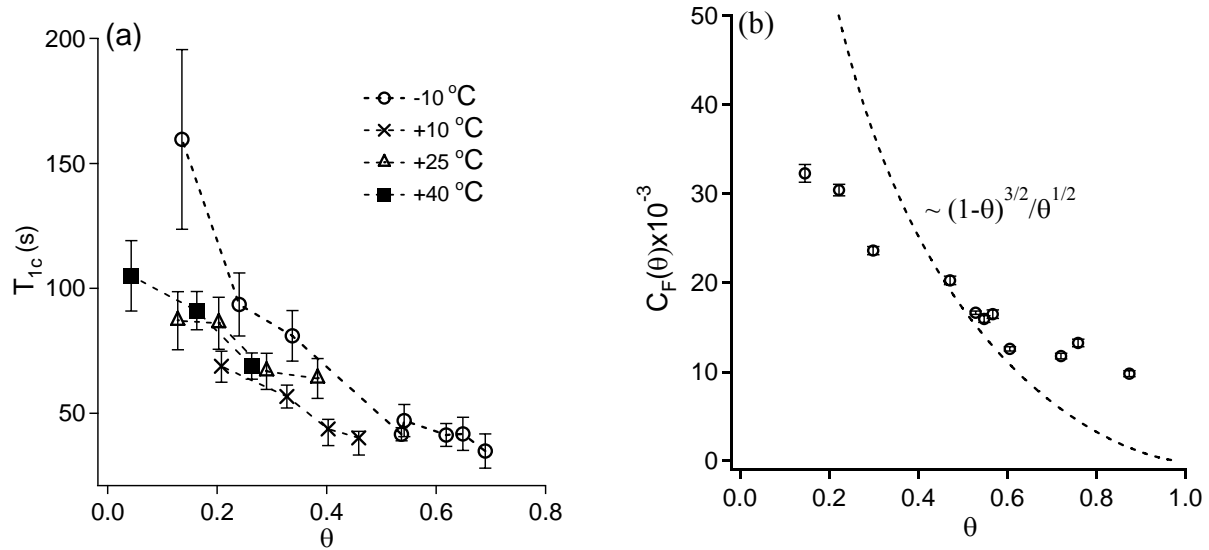


Figure 4-8. (a) Fractional occupancy dependence of the  $T_{1c}$  of  $^{129}\text{Xe}$  in the adsorbed Xe phase. The  $T_{1c}$  values were extracted from non-linear least-squares fitting of Eq. (4-20) to the measured saturation-recovery data at  $T = -10, 10, 25,$  and  $40^\circ\text{C}$ . (b) The experimental values of  $C_F(\theta)$  ranged from  $\theta = 0.14$  to  $0.70$  at  $-10^\circ\text{C}$  were also extracted in the non-linear least squares fitting. The dashed line is the theoretical function  $C_F(\theta) \propto (1-\theta)^{3/2} / \theta^{1/2}$  scaled vertically to overlap with the experimental data points to aid qualitative comparison to the theoretical trend.

Figure 4-8b presents plots of  $C_F(\theta)$  extracted from the non-linear least-squares fits for the data acquired in a second series of experiments, performed after re-packing the sample, at  $T = -10^\circ\text{C}$ , with varying Xe pressure at a fixed total pressure of 3500 torr, spanning a occupancy range of 14-70 %. The theoretical dependence  $C_F(\theta) \propto (1-\theta)^{3/2} / \theta^{1/2}$ , which follows from Eq. (4-3) when Langmuir adsorption and the hard-spheres expression for  $F(\theta)$  are assumed, is consistent with the experimentally observed monotonic decrease in  $C_F(\theta)$  with increasing  $\theta$ . Therefore, we can conclude that the single-file diffusion in AV nanotubes is attenuated as the Xe occupancy increased.

## 4.5 Conclusions

Hyperpolarized (saturation-recovery) NMR tracer exchange method has proven to be an effective method for characterizing diffusion in self-assembled nanotube systems. The NMR signal enhancement afforded by spin-exchange optical-pumping facilitated studies on milligram-scale quantities of material at occupancies down to  $\approx 10\%$ . Expressions for the NMR saturation-recovery signals for normal diffusion and SFD have been derived from the magnetization rate equations, assuming a distribution of desorption rates. The nonlinear regression analysis is clear indicative of SFD for Xe in AV, especially at high occupancy. The theoretical occupancy dependence of the channel-to-gas signal ratio agrees qualitatively with the data, although the deviation between experiment and theory appears to be greater at low occupancy, which suggesting that the mobility of the Xe is probably more restricted at low occupancy than is predicted by the simple hard-spheres mobility in ideal linear channels. The helium gas background, particularly at low Xe partial pressure, will also have an effect on the single-file mobility. In the gas phase, the diffusivity of Xe in He has been found to decrease with increasing Xe/He mole ratio.<sup>216</sup> The helical topology of the channels of AV will reduce the mobility in comparison to that of ideal, cylindrical nanotubes.

The observation of single-file Xe diffusion in AV is consistent with a  $t_x$  that is shorter than the minimum observation time that can be probed under our experimental conditions, which is limited to  $\tau \gg 500\text{ms}$  by the signal-to-noise. Unfortunately, neither  $F$  nor  $D_0$  has been measured in this system, so it is impossible to estimate  $t_x$  with any certainty.

Although the magnetization exchange kinetic analysis might not be realistic in describing the actual physical process of incorporation of the tracer into the single-file channels, it does yield the same analytical form of the saturation-recovery signal (Eq. (4-17)) as is obtained from

the standard diffusion propagator description in the limit of long channels. Both models yield the same  $\sqrt{F}$  dependence on the single-file mobility.<sup>211</sup> This leads us to conclude that the statistic for hyperpolarized atom accumulation in an ensemble of channels is the same in each model. The advantage of our magnetization exchange model is that it is easily adapted to samples with distributions of channel lengths. Moreover, in samples for which the long channel approximation does not apply, or under condition for which the polarization of the gas phase is significantly affected by exchange with unpolarized gas inside the channels, it will still be possible to obtain the theoretical saturation-recovery curve by numerical integration of the rate equations.

CHAPTER 5  
INVESTIGATIONS OF CHANNEL DIAMETER EFFECT ON GAS DIFFUSION IN GA  
WHEEL NANOTUBES BY HYPERPOLARIZED XE-129 NMR

**5.1 Introduction**

In recent years, rapid developments of nanotubular frameworks with their intrinsic beauty and potential applications have been witnessed. In particular, inorganic nanotubes constructed from the molecular wheels have recently been the subject of intense researches because of the fundamental interests in the magnetic properties, such as single molecular magnets (SMM)<sup>217-219</sup> and their quantum phenomena.<sup>220-223</sup> In addition, theoretical works have proposed that the spin states of the transition-metal clusters can be the basis for the quantum computation.<sup>224-226</sup> Following the pioneering works of Dr. George Christou (UF Chemistry) in synthesizing transition-metal molecular clusters, a variety of novel supramolecular channels with highly symmetric building blocks have been constructed. One of the characteristic molecular clusters, the “gallic” wheel, has been successfully synthesized by nontemplate methods.<sup>36</sup> As shown in Figure 5-1a and b, the Ga<sub>10</sub> and Ga<sub>18</sub> wheel structures consist of 10 and 18 Ga(III) atoms bridged by the ligands in nearly octahedral geometry. Moreover, the molecular wheels stack along the crystal *c*-axis to form the elegant nanotubular structures. The crystal structures of the Ga<sub>10</sub> and Ga<sub>18</sub> wheels viewed along their crystal *c*-axis are illustrated in Figure 5-1 d and e, respectively. The inner diameters of the Ga<sub>10</sub> and Ga<sub>18</sub> channels are 8.1 Å and 10.4 Å, respectively.<sup>36</sup> In 2004, Christou *et al.* reported a giant molecular wheel compound composed of 84 manganese atoms (Figure 5-1c). The Mn<sub>84</sub> structure is in a hexagonal symmetry space group.<sup>227</sup> The tubular structure of the Mn<sub>84</sub> wheel has a cylindrical 1D channel with an internal diameter of 1.9 nm (Figure 5-1f).

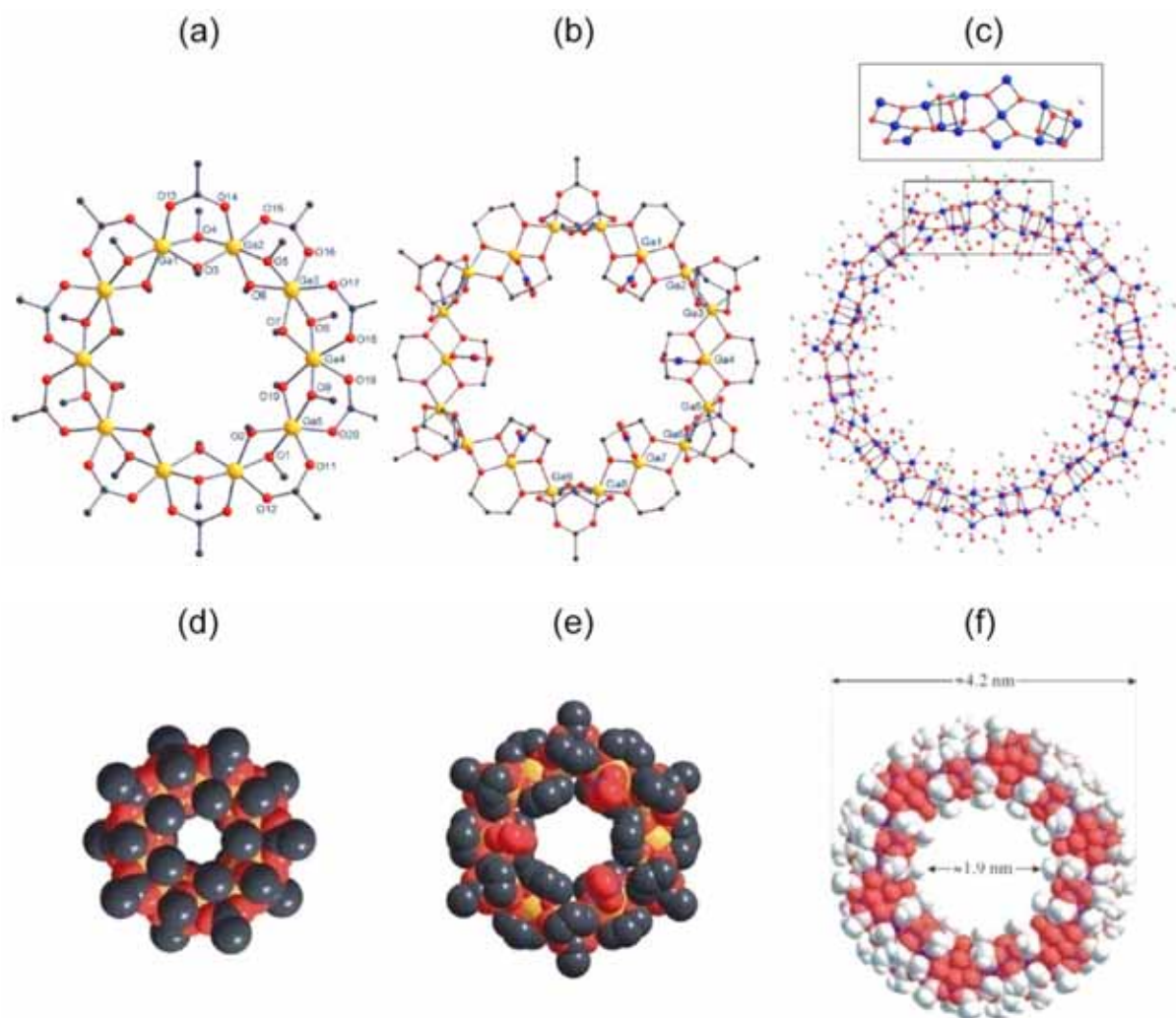


Figure 5-1. Structures of molecular wheels, (a)(d) Ga<sub>10</sub>, (b)(e) Ga<sub>18</sub>, and (c)(f) Mn<sub>84</sub>, with inner diameter of 8.1 Å, 10.4 Å, and 1.9 nm, respectively. (a)(b)(c) are the top view of molecular structures of Ga<sub>10</sub>, Ga<sub>18</sub>, and Mn<sub>84</sub> wheels, respectively. (d)(e)(f) are the corresponding space filling representations of Ga<sub>10</sub>, Ga<sub>18</sub>, and Mn<sub>84</sub> wheel compounds, respectively. The structures are not represented on the same scale. (Ga: yellow; O: red; C: gray; H: white; N: blue in (b); Mn: blue in (c)) (Adapt from Ref 36 and <sup>227</sup>)

The kinetics of gas diffusion in 1D nanotube systems has been investigated by saturation-recovery hyperpolarized  $^{129}\text{Xe}$  NMR, and the results of Xe diffusion in the model single-file system, dipeptide nanotube AV, have been presented in Chapter 4. The diffusion properties of Xe may be expected to drastically depend on the diameter of the channel relative to the size of Xe atom. In our previous studies of Xe diffusion in AV nanotubes, where Xe diameter exceeds the radius of channel but is smaller than channel diameter, compliance with SFD behavior has been observed.<sup>180</sup> The normal 1D diffusion of Xe should emerge in the channel with an inner diameter  $\geq 2$  times the Xe diameter (*i.e.*  $\geq 8.8 \text{ \AA}$ ), because the confined Xe can transversely pass one-another in the channel. Hence, it would be interesting if the CFSR technique developed herein could be applied to nanotubes with larger pores in order to verify this prediction. However, the inside diameters of self-assembled dipeptide nanotubes with hydrophobic interiors are limited to  $\sim 5 \text{ \AA}$ .<sup>178</sup> Thus, the molecular wheel nanochannels with controllable channel sizes are excellent candidates to study the channel-size dependence of molecular diffusion in 1D nanotube systems. Additionally, in the paper of Christou, it has been pointed out that the supramolecular architecture of the molecular wheel nanotubes may be suitable for a variety of applications, such as the insertion of guest molecules.<sup>227</sup> These considerations motivated us to explore the kinetics of gas diffusion in the molecular wheel nanotubes. Here we present the gas diffusion studies of Xe in gallic-wheel nanotubes ( $\text{Ga}_{10}$  and  $\text{Ga}_{18}$ ) using selective continuous-flow saturation-recovery (CFSR) hyperpolarized  $^{129}\text{Xe}$  NMR.

## 5.2 Experimental

The molecular wheels,  $\text{Ga}_{10}$ ,  $\text{Ga}_{18}$ , and  $\text{Mn}_{84}$ , were synthesized by Dr. Theocharis Stamatatos in Prof. George Christou's group. The detailed procedures of the molecular wheels synthesis associated with their crystal structure identifications can be found in the literature.<sup>36 227</sup> It is noted that the samples of molecular wheel nanotubes are not stable in air or elevated

temperatures. Additionally, the samples readily adsorb moisture, which causes the collapse of the nanotubular structures. For example, the nanotubular structures of Ga<sub>18</sub> samples were found to be completely collapsed by SEM after their exposure to air for 1-2 weeks. Therefore, after the molecular wheel samples were synthesized, NMR measurements were performed promptly and completed within 2-3 days to ensure the nanotubular structures were not collapsed in the samples. The stock molecular wheel samples were stored in a dry N<sub>2</sub> glove box for further studies. Approximately 40-50 mg of the polycrystalline samples were loosely packed into the NMR sample holder and evacuated to  $\sim 10^{-5}$  torr at room temperature overnight prior to NMR measurements. It is crucial to remove the solvent in the samples because an additional Xe solvent peak at  $\sim 100$  ppm can be observed in hyperpolarized <sup>129</sup>Xe NMR spectra when the evacuation of solvent was not complete. On the other hand, the extremely high sensitivity of hyperpolarized Xe NMR allows the small amount of solvent in the samples to be detected.

### 5.2.1 Hyperpolarized <sup>129</sup>Xe NMR Experiment

Hyperpolarized Xe gas was generated by continuous-flow Rb-Xe spin-exchange optical-pumping polarizer described in Section 2.4.4. The gas mixture was re-circulated through the sample space during the experiments at a flow rate of 100 mL/min. The total gas pressure was 4000 mbar in all the experiments. The 2%/2%/96% natural isotopic abundance Xe/N<sub>2</sub>/He gas mixture<sup>a</sup> was used for the variable temperature experiments. The natural isotopic abundance <sup>129</sup>Xe gas<sup>b</sup> and <sup>4</sup>He gas<sup>c</sup> were used to adjust the Xe gas composition for the continuous-flow selective saturation-recovery (CFSR) hyperpolarized <sup>129</sup>Xe NMR experiments at room temperature. The pulse sequence of selective CFSR hyperpolarized <sup>129</sup>Xe NMR is shown in Figure 4-5. The principles of CFSR <sup>129</sup>Xe NMR were discussed in Chapter 4.

---

<sup>a</sup> part no.: ISO-XHN-C; Spectra Gases Inc., West Branchburg, NJ.

<sup>b</sup> part no.: XE5.0RS-D8; Praxair, Danbury, CT.

<sup>c</sup> part no.: UN1046; Praxair, Danbury, CT.

All the NMR measurements were carried out on a 9.4 T Bruker Avance NMR spectrometer operating on a  $^{129}\text{Xe}$  Larmor frequency of 110.7 MHz. The  $\pi/2$  pulse width was about 4.5  $\mu\text{s}$ . The single-pulse sequence was applied to acquire variable-temperature  $^{129}\text{Xe}$  NMR spectra in  $\text{Ga}_{10}$  and  $\text{Ga}_{18}$  nanotubes. For  $\text{Mn}_{84}$  nanotubes, the typical Hahn spin-echo pulse sequence was used in order to refocus the signal dephasing due to the field inhomogeneity. The inter-pulse delay of Hahn spin-echo was optimized to 50  $\mu\text{s}$ . The  $^{129}\text{Xe}$  NMR acquisition parameters are listed in Table 5-1. For  $\text{Ga}_{18}$  nanotubes, 128 transients were averaged in CFSR experiments in order to obtain the sufficient signal-to-noise ratio on the adsorbed peaks for the quantitative measurements. A Gaussian line-broadening factor was applied to the free induction decay prior to the Fourier transformation. Since the structures of molecular wheels are not stable at high temperature, all the NMR measurements were conducted at or below room temperature.

Table 5-1. Summary of Xe NMR acquisition parameters of the molecular wheels

polycrystalline samples	recycle delay	transients	spectral width (kHz)	line broadening (Hz)
$\text{Ga}_{10}$	1 sec	16	60	300
$\text{Ga}_{18}$	1 sec	32	55	300
$\text{Mn}_{84}$	1 sec	128	250	500

### 5.2.2 Scanning Electron Microscopy

The scanning electron microscopy (SEM) was performed using JOEL 6400 with acceleration voltage as low as 5 kV in order to get sufficient resolution to study the morphology of nanotubes. The SEM images of  $\text{Ga}_{10}$  nanotubes with variable magnifications are presented in Figure 5-2a-c. The additional substances around the nanotubular structures in Figure 5-2c may be the collapsed nanotubes since  $\text{Ga}_{10}$  nanotubes can be collapsed in the exposure to air or moisture. The channel lengths were measured manually in the SEM images taken from six different areas of polycrystalline sample. The length distribution of  $\text{Ga}_{10}$  channels is presented in Figure 5-2d. The average length of  $\text{Ga}_{10}$  channel is  $606.5 \pm 49.3 \mu\text{m}$ .

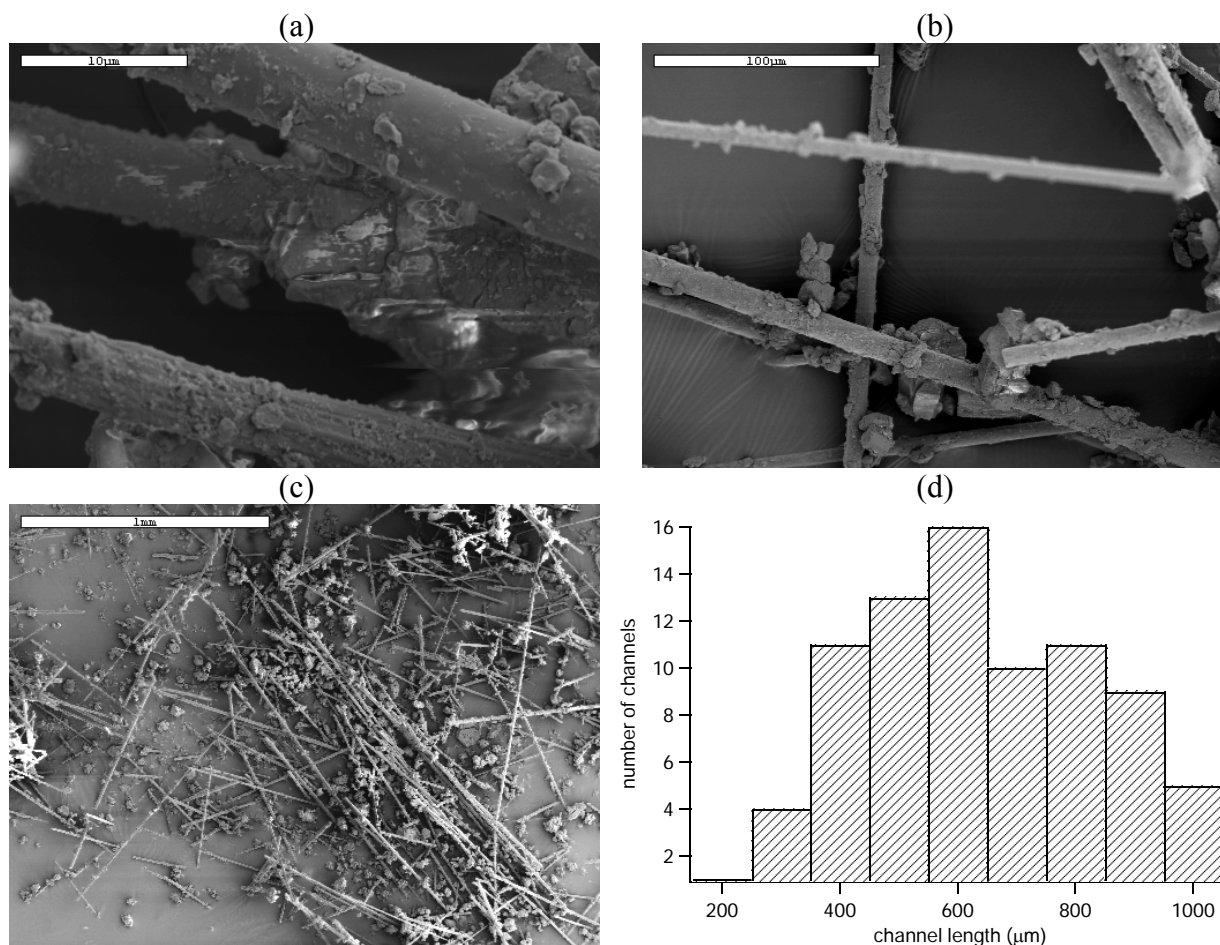


Figure 5-2. SEM images of Ga<sub>10</sub> nanotubes shown at length scales of (a) 10μm, (b) 100μm, and (c) 1mm. (d) Length distribution of the Ga<sub>10</sub> crystals. The average length is 606.5±49.3 μm. (n=83)

### 5.3 Results and Discussions

#### 5.3.1 Temperature Dependent Study in Ga<sub>10</sub> and Ga<sub>18</sub> Nanotubes

The temperature dependences of <sup>129</sup>Xe NMR spectra of Xe adsorbed in the Ga<sub>10</sub> and Ga<sub>18</sub> wheel nanotubes are presented in Figure 5-3. The morphology of the Ga<sub>10</sub> and Ga<sub>18</sub> wheel polycrystalline samples is expected to be very similar. From the X-ray crystal structure analysis<sup>36</sup>, the inner diameters of Ga<sub>10</sub> (8.1 Å) and Ga<sub>18</sub> (10.4 Å) are relatively larger than that of AV or TPP channel (*i.e.* ~5 Å). Therefore, the motions of Xe atoms in Ga<sub>10</sub> and Ga<sub>18</sub> nanotubes are less restricted than in AV or TPP, leading to the isotropic NMR line-shapes of Xe in Ga<sub>10</sub> and Ga<sub>18</sub> nanotube phases over the range of experimental temperatures (Figure 5-3). Such isotropic

$^{129}\text{Xe}$  NMR spectral line-shapes are completely different from the CSA powder pattern of AV or TPP.<sup>20,21,180</sup>

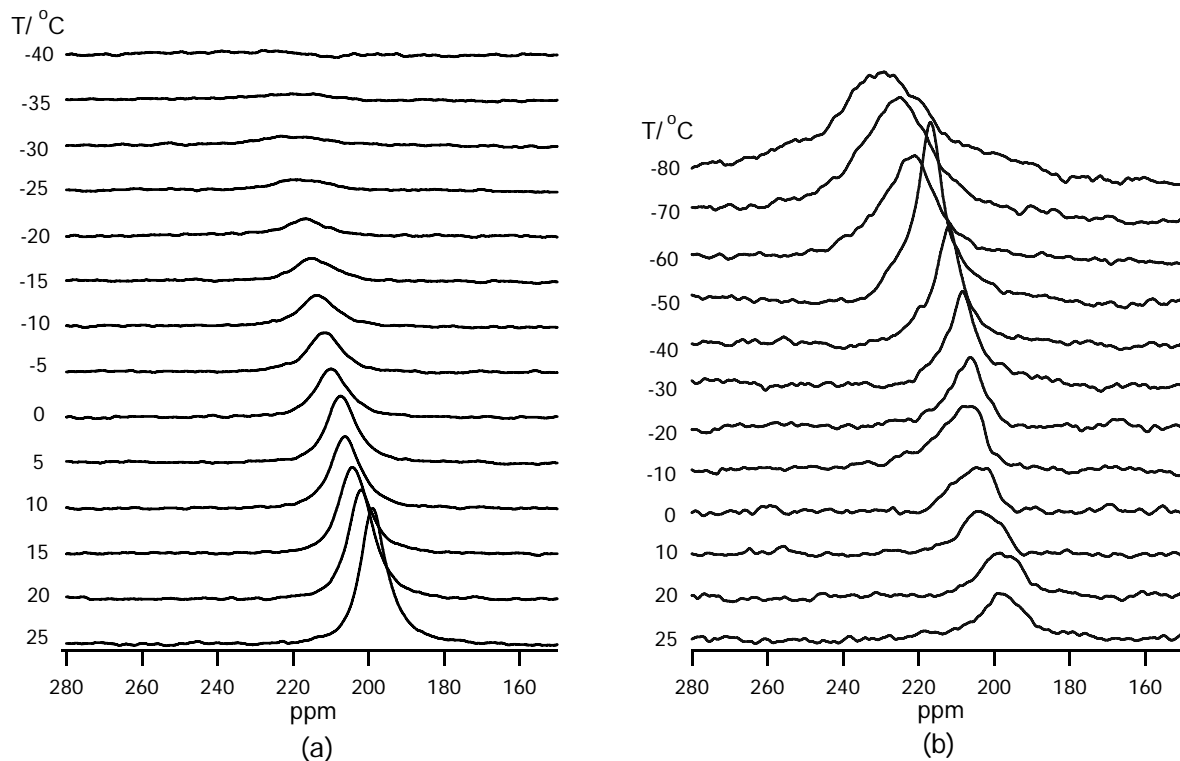


Figure 5-3. Temperature dependence of hyperpolarized  $^{129}\text{Xe}$  NMR Spectra of Xe adsorbed in (a)  $\text{Ga}_{10}$  and (b)  $\text{Ga}_{18}$  molecular wheels.

In Figure 5-3, the adsorbed Xe peaks in both nanotubes become broader as the temperature is reduced. At low temperature, more Xe atoms accumulate into the channels and the Xe-Xe interaction is dominant, resulting in a deshielding of Xe chemical shift in  $\text{Ga}_{10}$  and  $\text{Ga}_{18}$  nanotubes. As more Xe atoms adsorb into the channels at low temperature, the confinement of Xe may break the symmetry of shielding tensor, leading to an observed anisotropic NMR line-shape. However, due to low signal-to-noise ratio of Xe in gallic nanotubes in Figure 5-3, more signal averaging may be required in order to identify the spectral line-shapes at low temperature. Moreover, two distinctions were found in the temperature-dependent  $^{129}\text{Xe}$  NMR spectra of  $\text{Ga}_{10}$  and  $\text{Ga}_{18}$  wheel nanotubes: (1) The intensity of the adsorbed Xe peak in  $\text{Ga}_{18}$  nanotubes is much

weaker than its gas peak intensity, implying Xe  $T_{1c}$  relaxation time in Ga<sub>18</sub> nanotubes may be relatively shorter or the density of unobstructed channels may be lower. (2) The signal intensity of the adsorbed Xe peak in Ga<sub>18</sub> nanotubes increases when the temperature is lowered. Conversely, in Ga<sub>10</sub> nanotubes, the intensity of Xe adsorbed peak decreases and broadens upon lowering the temperature, and eventually disappears at -40 °C. It can be interpreted by a reduction of Xe motion inside the Ga<sub>10</sub> nanotubes upon cooling the system. As the temperature is lowered, more Xe atoms adsorb into the Ga<sub>10</sub> channels and the Xe diffusivity is reduced, consequently reducing the  $T_2$  relaxation time. Therefore, the adsorbed Xe peak in Ga<sub>10</sub> nanotubes becomes broadened and weaker at lower temperature. Since the Ga<sub>18</sub> nanotube has a large inner diameter than Ga<sub>10</sub> nanotube, Xe motion in Ga<sub>18</sub> nanotubes should be more mobile than in Ga<sub>10</sub> nanotubes. Thus, Xe  $T_2$  in Ga<sub>18</sub> nanotubes does not exhibit such a drastic change upon lowering the temperature.

The temperature dependences of the chemical shifts of the adsorbed <sup>129</sup>Xe peaks in Ga<sub>10</sub> and Ga<sub>18</sub> nanotubes are summarized in Figure 5-4. Because Xe is more tightly confined in Ga<sub>10</sub> nanotubes than in Ga<sub>18</sub> nanotubes, the chemical shift of Xe in Ga<sub>10</sub> nanotubes is more deshielded than that in Ga<sub>18</sub> nanotubes over the range of experimental temperatures.

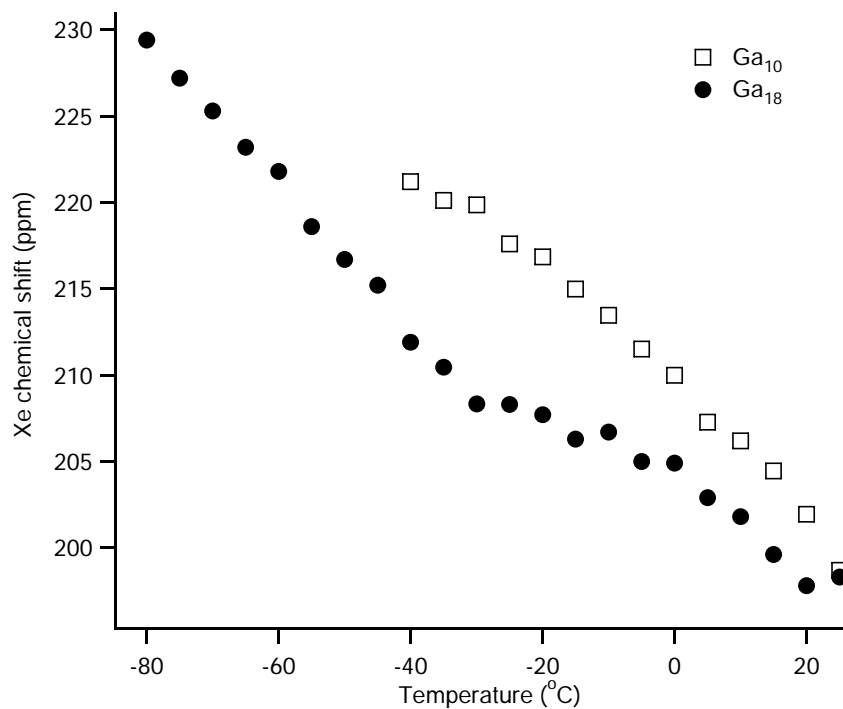


Figure 5-4. Temperature dependence of chemical shift of adsorbed Xe in Ga<sub>10</sub> and Ga<sub>18</sub> nanotubes.

### 5.3.2 Temperature Dependent Study in Mn<sub>84</sub> Nanotubes

The hyperpolarized <sup>129</sup>Xe spin-echo NMR spectra in Mn<sub>84</sub> nanotubes at variable temperatures are presented in Figure 5-5. Extreme broadening of the adsorbed <sup>129</sup>Xe peaks occurs. The chemical shifts of Xe adsorbed peaks up to 400 ppm were observed in the variable-temperature hyperpolarized <sup>129</sup>Xe NMR spectra. The line-shape appears to consist of more than one peak or perhaps even a continuous distribution of adsorbed Xe peaks. As the temperature is reduced, the line-shape of Xe adsorbed into Mn<sub>84</sub> nanotubes becomes increasingly broadened. The Xe *T*<sub>1</sub> relaxation time in the adsorbed phase of Mn<sub>84</sub> nanotubes was approximately 10 ms at room temperature, as measured by the time-dependence of the peak amplitude in the non-selective saturation-recovery hyperpolarized <sup>129</sup>Xe NMR signal. The manganese atom is paramagnetic and can induce fast nuclear spin relaxation on <sup>129</sup>Xe in the Mn<sub>84</sub> channels. It might be the reason for the weak and strongly broadened Xe signals in this nanotube system. This type

of spectral line-broadening is typically seen in the  $^{129}\text{Xe}$  NMR spectra of carbon nanotubes in the presence of metallic particles.<sup>228-230</sup> In addition, since the  $\text{Mn}_{84}$  wheel is known as a single molecular magnet<sup>227</sup>, the difference of magnetic susceptibility distribution in  $\text{Mn}_{84}$  sample may present a spatial dependence of the magnetic environments seen by the  $^{129}\text{Xe}$  nuclear spin, leading to a dispersion of the Xe resonance frequency that consequently yields the drastic line-broadening.

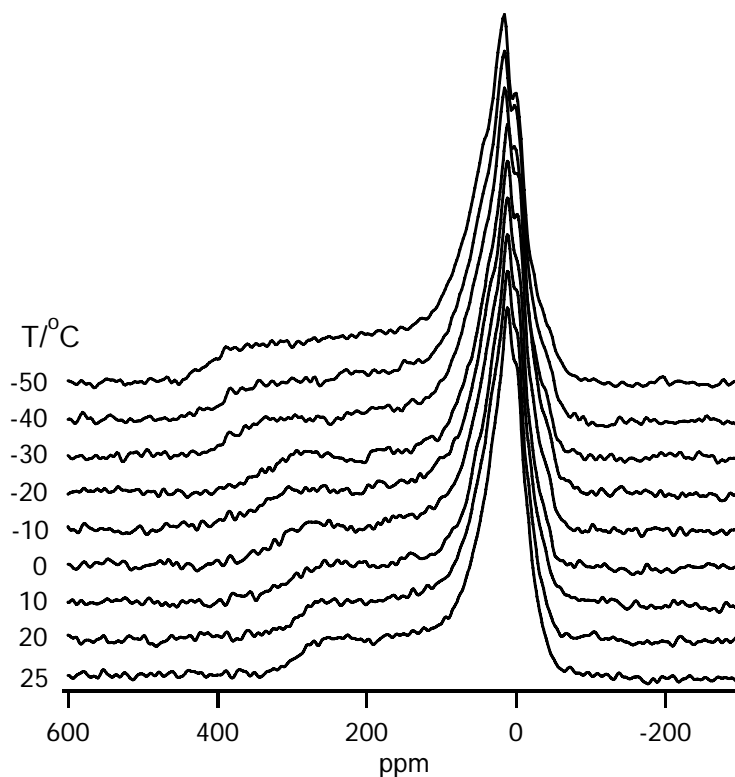


Figure 5-5. Temperature dependence of hyperpolarized Xe NMR spectra of  $\text{Mn}_{84}$  nanotubes.

### 5.3.3 Pressure Dependent Study in $\text{Ga}_{10}$ and $\text{Ga}_{18}$ Nanotubes

The pressure dependences of the hyperpolarized  $^{129}\text{Xe}$  NMR spectra of Xe adsorbed in  $\text{Ga}_{10}$  and  $\text{Ga}_{18}$  nanotubes are presented in Figure 5-6. Interestingly, the Xe chemical shifts in the  $\text{Ga}_{10}$  and  $\text{Ga}_{18}$  nanotubes were almost independent of Xe pressure at 25 °C over a wide range of Xe partial pressures. The chemical shift of adsorbed Xe can be expressed by the contributions of

several interactions, as shown in Eq. (2-26). Among the interactions in Eq. (2-26), only the  $\sigma_s$  term arises from Xe-surface interactions, or in the present case Xe-wall interactions, and this term does not depend on the Xe pressure. Hence, the results indicate that the chemical shift of Xe inside the Ga<sub>10</sub> and Ga<sub>18</sub> nanotube is governed by Xe-wall interactions over a wide range of Xe densities. Such pressure-independent behavior has been observed previously in the system of Xe gas adsorbed in the nanoporous materials.<sup>14,155,231,232</sup> For example, Nagasaka *et al.*<sup>232</sup> have recently reported chemical shifts of adsorbed Xe in two polymer systems, bisphenol-A polycarbonate (PC) and polytetrafluoroethylene (PTFE), with pore size of 4.7 Å and 7.9 Å, respectively, were not affected by a drastic variation of the Xe density, and suggested the Xe chemical shifts in these systems are dominated by the Xe-wall interactions.

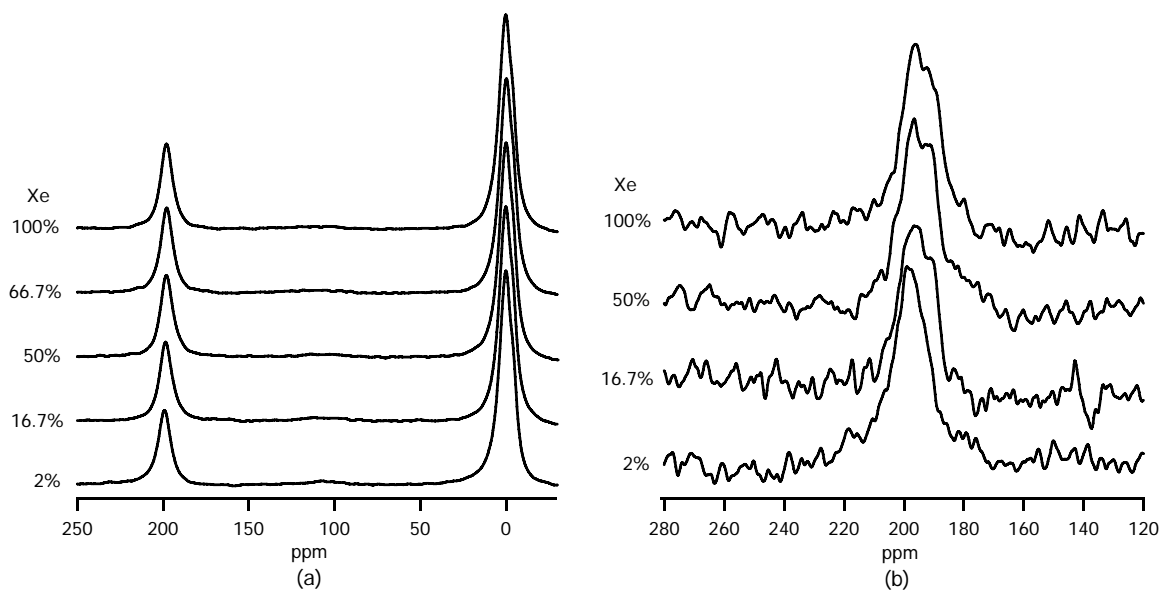


Figure 5-6. Pressure dependence of hyperpolarized Xe NMR Spectra in (a) Ga<sub>10</sub> and (b) Ga<sub>18</sub> nanotubes at 25 °C. The total pressure of Xe/He gas mixture is 4000 mbar. The chemical shifts are reference to the dilute Xe gas (0 ppm). Since Xe gas peak is much larger than Xe adsorbed peak in Ga<sub>18</sub> sample, the gas peaks of Ga<sub>18</sub> nanotubes were neglected for easily visualized the Xe adsorbed peaks in Ga<sub>18</sub> samples.

At 25 °C and 80 mbar of Xe partial pressure, the Xe chemical shifts of Ga<sub>10</sub> and Ga<sub>18</sub> nanotubes are about 198 ppm, which are mainly governed by the Xe-wall interactions. As noted

above, Xe-wall interactions can be reflected in  $\sigma_{\parallel}$  in 1D nanotube systems with an axial symmetry, such as AV or TPP.<sup>19</sup> Under the same experimental condition as present studies,  $\sigma_{\parallel}=121$  ppm was reported in the Xe/AV system, a value which is substantially smaller than that observed in the gallic wheel nanotubes. It appears that Xe-wall interactions in gallic nanotubes are stronger than those in AV nanotubes at 25 °C. However, since the channel walls in both systems are completely different, the Xe-wall interactions may influence the Xe shielding tensor differently in both nanotube systems.

#### 5.3.4 Saturation-recovery Hyperpolarized <sup>129</sup>Xe NMR in Ga<sub>10</sub> and Ga<sub>18</sub> Nanotubes

The continuous-flow selective saturation-recovery (CFSR) hyperpolarized <sup>129</sup>Xe NMR experiments were carried out in Ga<sub>10</sub> and Ga<sub>18</sub> nanotubes in order to compare the effect of channel diameters on the Xe diffusion. The inner diameters of Ga<sub>10</sub> and Ga<sub>18</sub> nanotube are 8.1 Å and 10.4 Å, respectively.<sup>36</sup> Thus, it is possible for two Xe atoms to fit side-by-side in the channels of Ga<sub>18</sub>, but not in Ga<sub>10</sub>. The rigid nanotubular structure formed by stacking of gallic wheels has a uniform internal diameter. As shown in Figure 5-3, the adsorbed peaks of Xe in Ga<sub>10</sub> and Ga<sub>18</sub> nanotubes can be distinguished from the gas peaks. Such features make Ga<sub>10</sub> and Ga<sub>18</sub> wheel compounds unique model systems to probe the different diffusion time-scaling of Xe inside the channels. Since the Xe adsorbed peak cannot be resolved and the Xe  $T_{1c}$  is too short in Mn<sub>84</sub> nanotube, it is infeasible to conduct the Xe CFSR experiments on Mn<sub>84</sub> nanotubes.

The selective saturation-recovery hyperpolarized <sup>129</sup>Xe NMR experiments in Ga<sub>10</sub> nanotubes acquired at four different Xe compositions, 16.7%, 33.3%, 66.7% and 100%, as well as least-squares fits of normal Fickian diffusion (Eq. (4-22)) and single-file diffusion (Eq. (4-20)) are presented in Figure 5-7. In Ga<sub>10</sub> nanotubes at 25 °C, it is apparent that the expression for single-file diffusion has the best fit to the saturation-recovery curves over four different Xe

densities. Therefore, it can be concluded that the diffusion of Xe inside the Ga<sub>10</sub> channels is still single-file over a wide range of Xe pressures at 25 °C. The inner diameter of the Ga<sub>10</sub> nanotubes is slightly smaller than two times the Xe van der Waals diameter, and therefore the mutual passage of confined Xe atoms inside the channel is still forbidden.

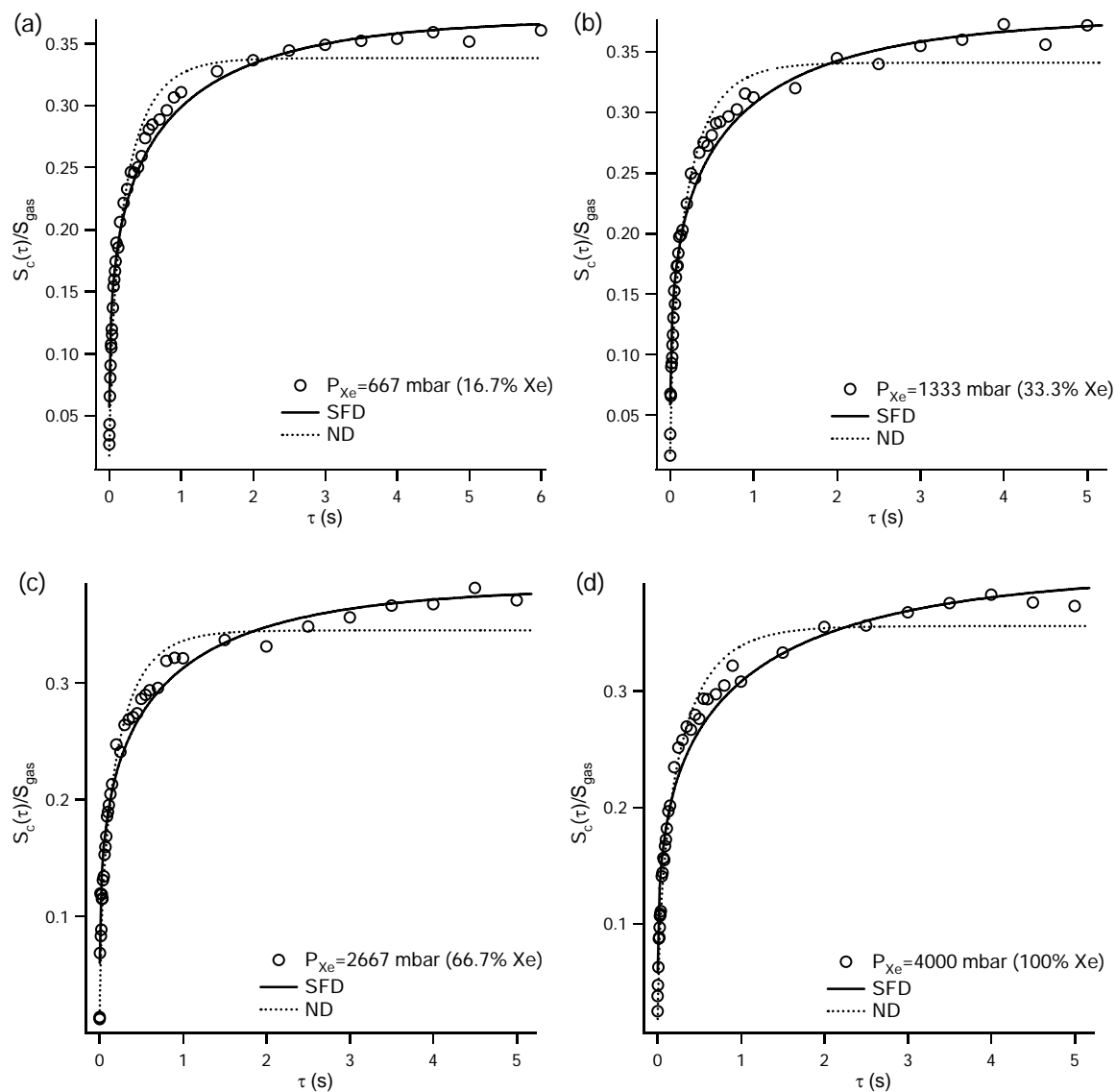


Figure 5-7. Hyperpolarized CFSR <sup>129</sup>Xe NMR experiments in Ga<sub>10</sub> nanotubes with variable Xe partial pressures at room temperature. Least-squares fits of Eq. (4-20) and Eq. (4-22) are represented as solid line and dash line, respectively. Total pressure of Xe/He gas mixture is 4000 mbar.

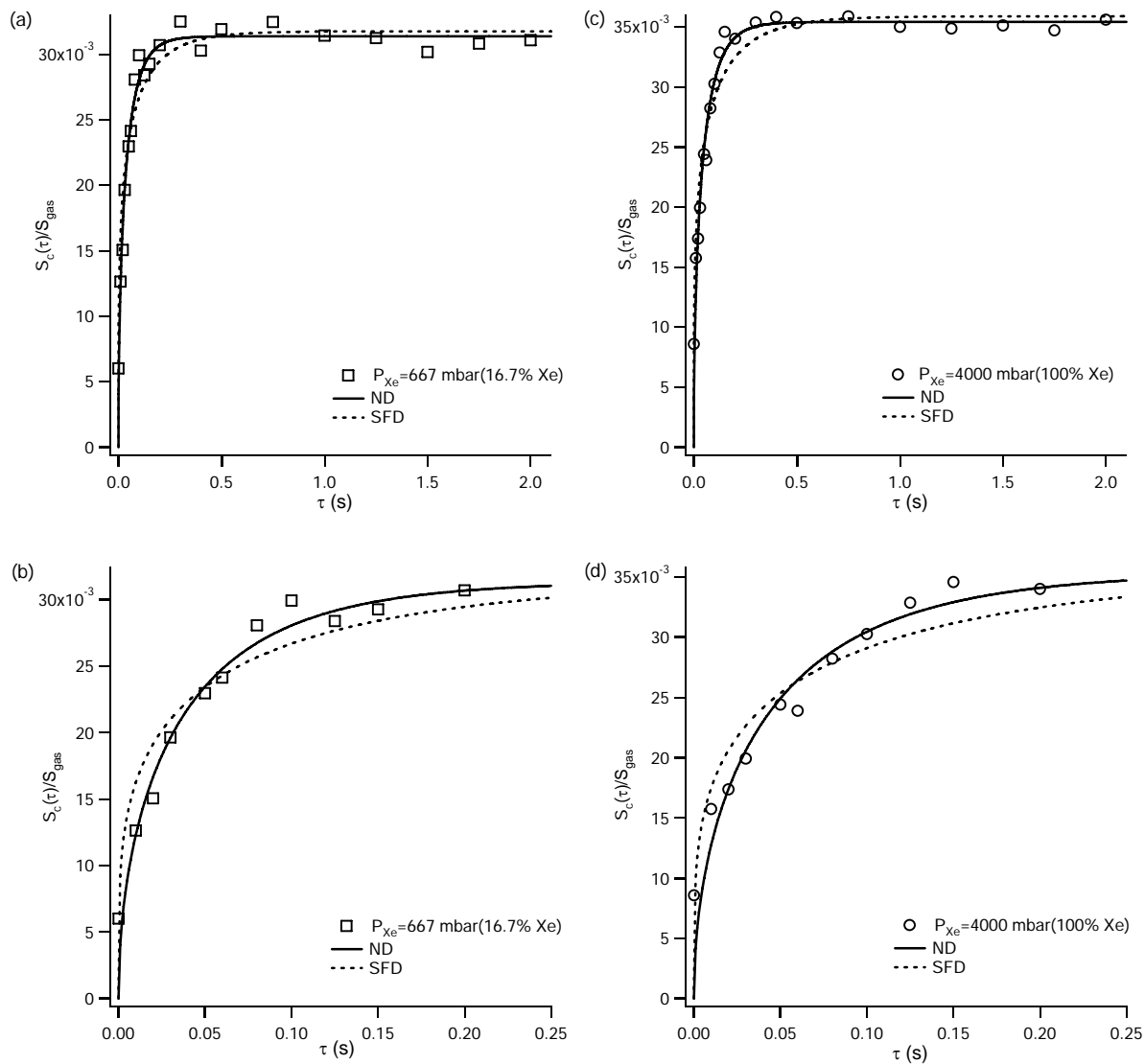


Figure 5-8. Hyperpolarized CFSR  $^{129}\text{Xe}$  NMR experiments in  $\text{Ga}_{18}$  nanotubes in (a) 16.7% and (b) 100% Xe with total gas pressure of 4000 mbar. The corresponding time-axis expansions of (a) and (c) are presented in (b) and (d), respectively. Least-squares fits of Eq. (4-22) and Eq. (4-20) are represented as solid line and dash line, respectively.

Selective CFSR hyperpolarized  $^{129}\text{Xe}$  NMR experiments were also performed in  $\text{Ga}_{18}$  nanotubes at 25 °C, where the inner diameter is about 22% larger than that of  $\text{Ga}_{10}$  nanotubes. The representative selective saturation-recovery curves, along with the least-squares fits to Eq. (4-22) and Eq. (4-20), are shown in Figure 5-8a and c. The fitting curves for SFD and ND in  $\text{Ga}_{18}$  nanotubes are very similar. However, with the expansion of time-axis at short recovery-time in 16.7% and 100% Xe gas mixture (Figure 5-8b and d), the normal 1D diffusion function (Eq. (4-22)) evidently yields the best fit, revealing that Xe in the  $\text{Ga}_{18}$  system obeys normal 1D Fickian diffusion time-scaling. The results suggest that CFSR technique has the capability to distinguish between normal 1D Fickian diffusion and single-file diffusion of the confined atoms inside the nanotube systems with different internal diameters.

The  $T_{1c}$  and pre-factor terms of Eq. (4-20) and Eq. (4-22) (*i.e.*  $C_F$  and  $C_D$ ) in  $\text{Ga}_{10}$  and  $\text{Ga}_{18}$  nanotubes extracted from CFSR hyperpolarized  $^{129}\text{Xe}$  NMR experiments are summarized in Figure 5-9. Both Xe  $T_{1c}$  relaxation times in gallic wheel nanotubes are much shorter than Xe  $T_{1c}$  in AV.<sup>180</sup> From SEM analysis of  $\text{Ga}_{10}$  nanotubes, the average length of the nanotube crystals is longer by a factor of  $\sim 30$  than that of AV nanotube crystals, suggesting that the fast  $^{129}\text{Xe}$  NMR signal recovery observed in the gallic nanotubes is not due to short channel length. While  $T_{1c}$  relaxation time of Xe in  $\text{Ga}_{18}$  was found to be shorter than that in  $\text{Ga}_{10}$  nanotubes, the  $T_{1c}$  values in either gallic nanotube system are roughly the same, within the experimental uncertainties, at variable Xe pressures (Figure 5-9a and c). The rapid  $T_{1c}$  relaxation of Xe in  $\text{Ga}_{18}$  nanotubes may result from the presence of paramagnetic impurities. The relaxation mechanisms in Xe/ $\text{Ga}_{10}$  and Xe/ $\text{Ga}_{18}$  systems appear to be dominated by the Xe-wall interactions, because the spin relaxation time does not depend on the density of Xe atoms inside the channels. This is in good agreement with the pressure independence of the Xe chemical shift of the adsorbed phase in  $\text{Ga}_{10}$  and  $\text{Ga}_{18}$

nanotubes. The pre-factor terms,  $C_F$  and  $C_D$ , of Eq. (4-20) and Eq. (4-22) in  $\text{Ga}_{10}$  and  $\text{Ga}_{18}$  nanotubes are on the same order of magnitude as  $C_F$  in AV nanotubes.<sup>180</sup> As shown in Figure 5-9b and d,  $C_F$  and  $C_D$  in  $\text{Ga}_{10}$  and  $\text{Ga}_{18}$  nanotubes are nearly pressure independent. However, due to lack of the information about the Xe adsorption capacity of  $\text{Ga}_{10}$  and  $\text{Ga}_{18}$  nanotubes, a quantitative interpretation has not been yet possible. If Xe adsorption into the channels is favorable, the channels might be readily saturated ( $\theta=1$ ) at very low Xe density, resulting in a lack of pressure dependence of the  $C_F$  or  $C_D$  over the pressure range studied. To clarify it, the measurements of Xe adsorption isotherm and Xe fractional occupancy in  $\text{Ga}_{10}$  and  $\text{Ga}_{18}$  nanotubes are needed.

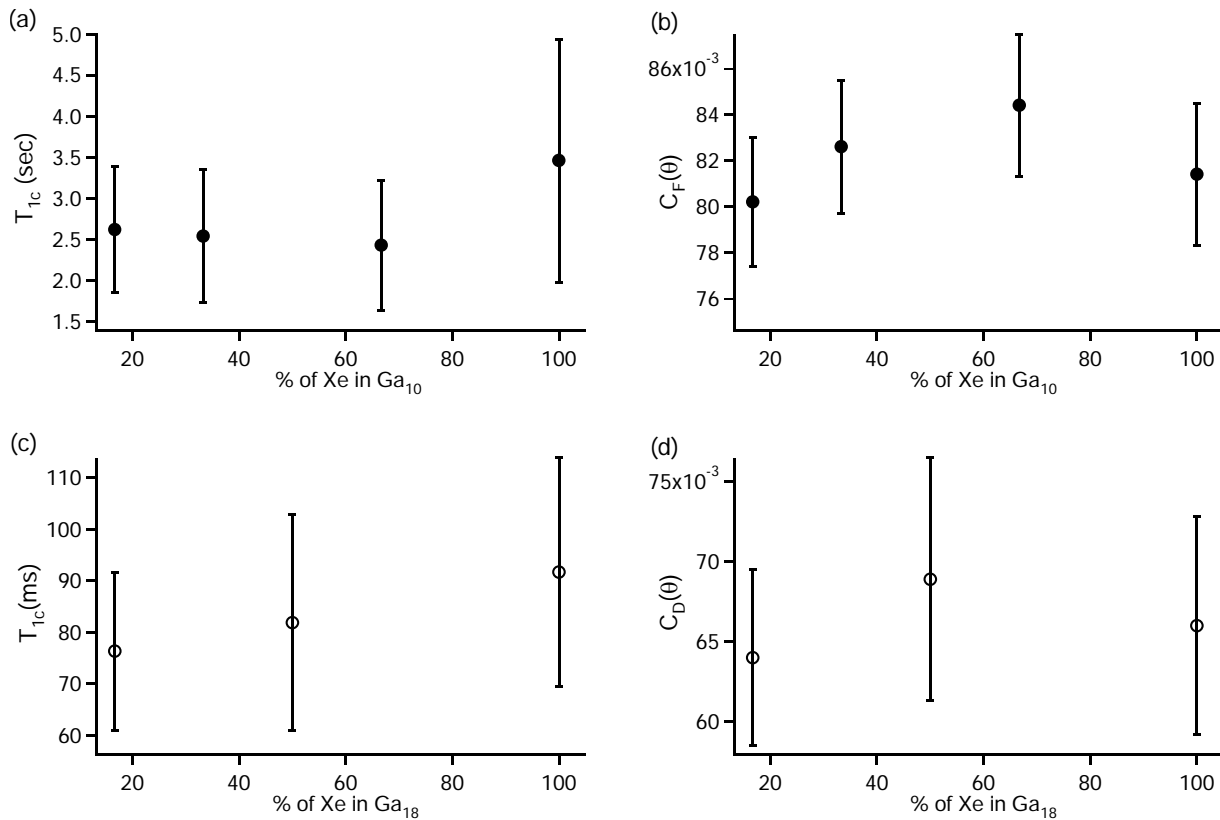


Figure 5-9. Xe pressure dependence of (a)  $T_{1c}$  and (b)  $C_F$  determined by least-squares fit of Eq. (4-20) in  $\text{Ga}_{10}$  nanotubes. Xe pressure dependence of (c)  $T_{1c}$  and (d)  $C_D$  determined by least-squares fit of Eq. (4-22) in  $\text{Ga}_{18}$  nanotubes. Error bars indicate 95% confidence intervals. Total pressure of Xe/He gas mixture is 4000 mbar.

## 5.4 Conclusions

In addition to the dipeptide nanotube system, the diffusion properties of Xe in two gallic molecular wheel nanotube systems with different channel diameters have been investigated. The isotropic spectral line-shapes of Xe inside the Ga<sub>10</sub> and Ga<sub>18</sub> nanotubes were observed, indicating the motion of Xe atoms in Ga<sub>10</sub> and Ga<sub>18</sub> is less restricted than in AV nanotubes. The observed Xe chemical shifts in the nanotube phase of Ga<sub>10</sub> and Ga<sub>18</sub> nanotubes do not depend on Xe pressure at room temperature. The results suggest that the Xe-wall interaction dominates over the Xe-Xe interaction in the gallic-wheel nanotubes at 25 °C. The kinetic analysis of the selective CFSR hyperpolarized <sup>129</sup>Xe NMR based on the magnetization exchange model successfully distinguished between drastically different diffusion time-scaling behaviors in the gallic nanotubes. Single-file diffusion and normal 1D Fickian diffusion have been observed in the Ga<sub>10</sub> and Ga<sub>18</sub> nanotubes, respectively. These results are consistent with expectations in the basis of different inner diameters relative to the size of Xe atom. The  $T_{1c}$  relaxation time of Xe in Ga<sub>18</sub> was found to be shorter than that in Ga<sub>10</sub> nanotubes. The relative short relaxation time is likely due to paramagnetic impurities in the sample. Furthermore, Xe  $T_{1c}$  relaxation times in Ga<sub>10</sub> and Ga<sub>18</sub> nanotubes were found to be almost independent of Xe pressure, a result which is consistent with a spin-lattice relaxation mechanism dominated by Xe-wall interactions in these gallic nanotube systems at 25 °C. Moreover, the observed pressure independence of  $C_D$  and  $C_F$  over the 667 - 4000 mbar pressure range may be attributed to the full occupation of channels at low Xe pressure. While the  $T_{1c}$  relaxation time and  $C_F$  or  $C_D$  value can be quantitatively obtained from CFSR technique, the information of channel lengths and adsorption properties must be determined from other types of characterization techniques, such as SEM and adsorption isotherm studies.

Although the  $T_{1c}$  relaxation time in the gallic nanotubes was observed to be relatively short, the Xe diffusion inside the channels, as investigated by CFSR experiments, was not limited by such short  $T_{1c}$  relaxation time. As noted previously, in the steady-state continuous-flow hyperpolarization condition, fresh hyperpolarized  $^{129}\text{Xe}$  gas in the sample space can be replenished on the time-scale of the gas residence time, not the  $T_1$  relaxation time, as in thermally polarized NMR experiments. Therefore, the complete diffusion route of hyperpolarized gas in the channels can be traced by CFSR even under conditions where  $T_1$  relaxation is rapid. In summary, single-file diffusion and normal-diffusion nanotube systems can be explicitly distinguished by the CFSR technique presented herein, suggesting that this approach can be potentially applicable to diverse 1D nanotube systems with different channel dimensions and chemical compositions.

CHAPTER 6  
DIRECT OBSERVATION OF ATOMS ENTERING AND EXITING SINGLE-FILE  
NANOTUBES BY A TWO-DIMENSIONAL HYPERPOLARIZED XE-129 NMR

**6.1 Introduction**

In single-file systems, the rates of adsorption and desorption are expected to be determined by the rate at which molecules enter or escape at the channel openings, rather than the internal displacement.<sup>1</sup> However, such effects of the molecular exchange and diffusion localized in the vicinity of channel openings have not been investigated experimentally in detail. We have demonstrated the gas adsorption and diffusion in AV and gallic wheel nanotubes by CFHP <sup>129</sup>Xe NMR. The locations of Xe in the channels and gas phases can be explicitly reported by the chemical shifts at variable experimental conditions. It is therefore of great interests to study the microscopic molecular exchange in the single-file nanotubes by <sup>129</sup>Xe NMR.

Two-dimensional exchange <sup>129</sup>Xe NMR spectroscopy (2D-EXSY) has been utilized to investigate the slow exchange processes among the multiple adsorbed sites in diverse systems, including liquid crystals,<sup>33,233</sup> zeolites,<sup>5,234,235</sup> polymers,<sup>13,236,237</sup> aerogels,<sup>238,239</sup> and carbon nanotubes.<sup>229,230</sup> The presence of molecular exchange within a time scale on the order of longitudinal  $T_1$  relaxation time gives rise to cross peaks in the 2D-EXSY spectrum between the frequencies of exchange sites.<sup>38</sup> Numerous thermally-polarized <sup>129</sup>Xe NMR studies in the basis of quantitative kinetic analysis of gas exchange in the nanoporous materials have been reported in few decades. With the advent of continuous-flow hyperpolarized <sup>129</sup>Xe NMR, it is now feasible to overcome conventional sensitivity limitations.<sup>35,144,240</sup> While CFHP <sup>129</sup>Xe 2D-EXSY is well-suited for the kinetic studies of gas exchange in nanoporous materials, the information obtained by most of the previous CFHP <sup>129</sup>Xe 2D-EXSY NMR works has been of a qualitative nature, such as the determination of pore-space interconnectivity<sup>238,239,241</sup>, pore geometry<sup>153</sup>, and

exchange pathways.<sup>147,238,242</sup> It would appear that extraction of quantitative exchange rates has been hampered by the lack of an appropriate kinetic formalism to the analysis of 2D-EXSY spectra acquired under CFHP condition. The quantitative kinetic studies of thermally-polarized and hyperpolarized Xe 2D-EXSY in the literature are briefly summarized as follows.

### 6.1.1 Thermally-polarized Xe 2D Exchange NMR

For quantitative interpretation of the thermally-polarized <sup>129</sup>Xe 2D-EXSY experiments, the time evolution of integrated diagonal and cross-peak signals can be substantially fit to an appropriate kinetic model, which is fundamentally based on Ernst *et al.*<sup>38</sup> In the case of two-site exchange, a simple exchange model with first-order exchange process is



where A and B represent the exchange sites;  $k_{A \rightarrow B}$  and  $k_{B \rightarrow A}$  are the exchange rate constants. The time evolutions of z magnetizations,  $M_z^A(t)$  and  $M_z^B(t)$ , are given by the following master equation:

$$\frac{d}{dt} \begin{pmatrix} M_z^A(t) - M_z^A(0) \\ M_z^B(t) - M_z^B(0) \end{pmatrix} = \mathfrak{R} \begin{pmatrix} M_z^A(t) - M_z^A(0) \\ M_z^B(t) - M_z^B(0) \end{pmatrix} \quad (6-2)$$

where  $\mathfrak{R}$  is the kinetic matrix. If cross relaxation is absent in the system, it is a sum of exchange and relaxation matrices.

$$\mathfrak{R} = \begin{pmatrix} -k_{A \rightarrow B} - T_{1A}^{-1} & k_{B \rightarrow A} \\ k_{A \rightarrow B} & -k_{B \rightarrow A} - T_{1B}^{-1} \end{pmatrix} \quad (6-3)$$

$T_{1A}$  and  $T_{1B}$  are longitudinal relaxation times in the two exchange sites. The analytical solutions of Eq. (6-2) provides time-dependence of diagonal and cross-peak intensities, which can be found in Ref 38. An example of matrix representation for the two-site exchange will be given in Appendix B. The advantage of using matrix representation to deal with the site exchange

problem is the multi-site exchange is non-trivial, and exchange rates corresponding to multi-site exchange can be solved easily. The typical graphs of time-dependent diagonal and cross-peak integrals are shown in Figure 6-1. In the simplest case of the two-site exchange with equal exchange rates ( $k_{A \rightarrow B} = k_{B \rightarrow A}$ ) and relaxation time ( $T_{1A} = T_{1B}$ ), the diagonal-peak intensity monotonically decays as increasing the mixing time (Figure 6-1a), whereas the cross-peak intensity initially raises to its maximum and decays gradually with the mixing time due to the  $T_1$  relaxation (Figure 6-1b).

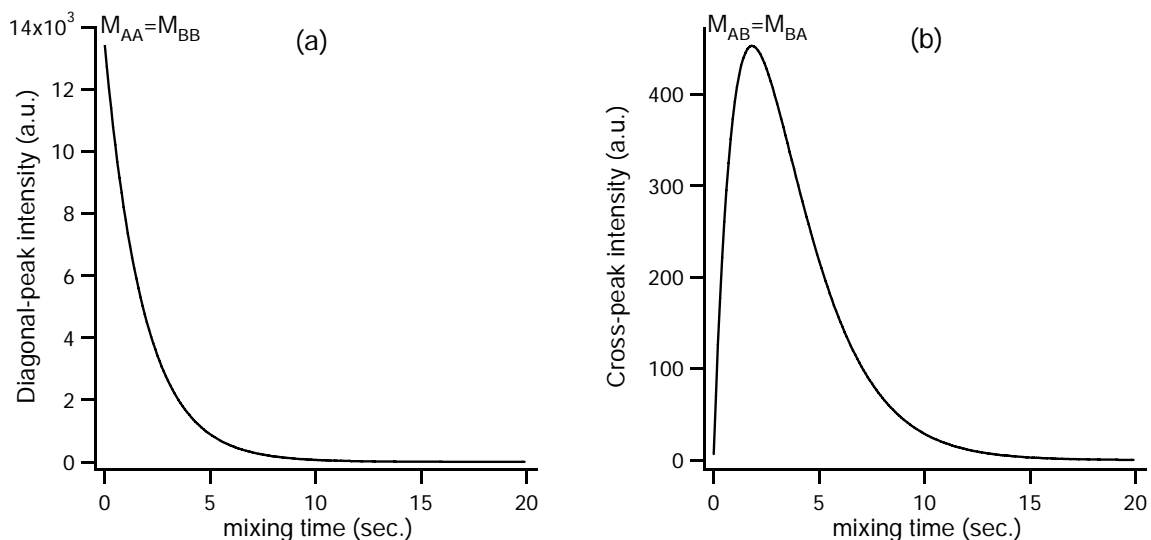


Figure 6-1. Simulated mixing-time dependence of (a) diagonal-peak and (b) cross-peak intensities in 2D-EXSY based on two-site exchange model. ( $k_{A \rightarrow B} = k_{B \rightarrow A} = 50 \text{ ms}^{-1}$ ;  $T_{1A} = T_{1B} = 2 \text{ s}$ )

It was noted that almost all the previous quantitative works of thermally-polarized  $^{129}\text{Xe}$  2D-EXSY NMR were analyzed according to the matrix representation. Ripmeester *et al.*<sup>5</sup> have first investigated the intra- and inter-particle exchanges of Xe in zeolites by thermally-polarized  $^{129}\text{Xe}$  2D-EXSY NMR associated with matrix representation analysis. Since then, several reports were following this approach to determine Xe exchange rates in various porous materials. Jokisaari *et al.*<sup>33,243</sup> performed a series of kinetic studies on liquid-crystalline systems confined in

controlled glass. Brotin *et al.*<sup>244</sup> investigated the gas dynamics in the Xe/cryptophane complex in the aqueous systems. The kinetic parameters, including Xe exchange rate constant,  $T_1$  relaxation time, diffusion coefficient, and activation energy of diffusion, as well as adsorption enthalpy and free energy of Xe on the adsorbed site can be determined accordingly. These parameters significantly depend on the particle size, pore geometry, and Xe  $T_1$  relaxation times on the exchange sites.<sup>5</sup> To quantitatively extract such information, a series of 2D-EXSY spectra must be acquired as a function of mixing time. However, as noted above, total experimental time per 2D-EXSY spectrum may take several hours due to lengthy  $T_1$  relaxation time and inherently low sensitivity of thermally-polarized  $^{129}\text{Xe}$  NMR. Therefore, although the kinetic model is available to apply on thermally-polarized  $^{129}\text{Xe}$  2D-EXSY NMR, mixing-time dependent study is generally impractical.

### 6.1.2 Hyperpolarized Xe 2D Exchange NMR

The analytical expressions for the mixing-time dependences of the cross and diagonal-peak signals found in the literature<sup>5,58</sup> are validated only in the case of (1) thermally-polarized spins in the absence of flow (*e.g.* in a sealed NMR tube) and (2) equal cross-peak signals represent the forward and reverse exchange processes. However, the conventional matrix formalism was applied without modification to estimate exchange rates in recent CFHP  $^{129}\text{Xe}$  2D-EXSY study of gas exchange in porous silicon.<sup>242</sup> The low integrated intensities of the exchange cross-peaks and correspondingly low exchange rates in their studies may not reflect the true intrinsic exchange rates under CFHP condition. As the kinetic model presented below reveals, flow effects must be considered when the gas residence time in the sample space is shorter than exchange time:  $\tau_R < k_d^{-1}$ . In this regime, flow attenuates the exchange cross-peaks involving the gas phase, leading to a possible underestimation of the exchange rates. Moreover, the cross-

peaks representing the forward and reverse exchange processes in CFHP  $^{129}\text{Xe}$  2D-EXSY spectra are generally asymmetric with respect to the spectrum diagonal, as discussed in qualitative terms by Anala *et al.* in a study of the combustion process.<sup>245</sup>

Here we demonstrate how CFHP  $^{129}\text{Xe}$  2D-EXSY can be used to detect Xe atoms entering and exiting the channel openings in AV. The mixing-time dependence of the diagonal and cross-peak signal integrals will be fit to analytical expressions assuming slow exchange between the gas phase and a surface exhibiting Langmuir adsorption. The mean desorption rate was determined at low, moderate and high Xe fractional occupancies in AV, yielding semi-quantitative information about molecular exchange in the vicinity of the channel openings.

## 6.2 Experimental

15 mg sample of polycrystalline AV<sup>a</sup> was packed loosely into NMR sample holder and evacuated to about  $10^{-5}$  mbar at 100 °C for 2-3 hours prior to NMR measurements. Spectra were acquired at a field of 9.4 T (110.7 MHz  $^{129}\text{Xe}$  resonance frequency) with a Bruker Avance spectrometer. The Rapid accumulation of spectra was achieved by pre-pending the standard 2D-EXSY pulse sequence with a saturating RF pulse train (SAT) followed by a fixed re-polarization delay  $\tau_1$ . The modification serves to (1) circumvent the lengthy acquisition recycle delay that would be required using thermally-polarized  $^{129}\text{Xe}$  NMR due to lengthy  $T_1$  relaxation time and (2) produce a reproducible polarization distribution as a function of displacement from the channel openings. Prior to each repetition of the 2D-EXSY pulse program, the  $^{129}\text{Xe}$  magnetization in the sample space is initially destroyed by the application of a non-selective  $\pi/2$  pulse train followed by a re-polarization delay of  $\tau_1=4\text{s}$  to allow the build-up of hyperpolarized Xe inside the channels. The complete CFHP 2D-EXSY pulse sequence is shown

---

<sup>a</sup> part no.: 0210032883; MP Biochemicals, Santa Ana, CA

in Figure 6-2, where  $\tau_m$  is the mixing time. An 8-step phase-cycle was employed for coherence transfer pathway selection.<sup>38</sup> It should be noted that under the present experimental conditions only hyperpolarized  $^{129}\text{Xe}$  gives rise to observable NMR signal, since thermally-polarized  $^{129}\text{Xe}$  signal cannot be detected without signal averaging.

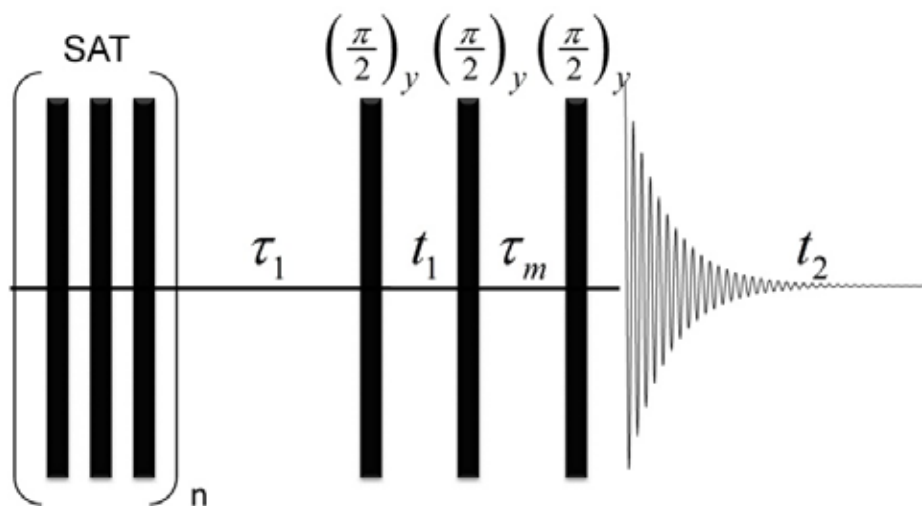


Figure 6-2. NMR pulse sequence of CFHP 2D-EXSY. (SAT is the non-selective saturation RF pulse train.)

A series of ten CFHP 2D-EXSY spectra were acquired with mixing times ranging from  $\tau_m = 10$  to 600 ms at Xe partial pressures of 92, 1320, and 3300 mbar at  $-10\text{ }^\circ\text{C}$ . Typically, 64 and 1024 points were collected in the  $t_1$  and  $t_2$  dimensions. A line-broadening of 300 Hz was applied in both time dimensions prior to Fourier transformation. Chemical shifts were referenced to dilute Xe gas (0 ppm).

Hyperpolarized  $^{129}\text{Xe}$  gas was generated by the home-built continuous-flow Rb-Xe spin-exchange optical-pumping system described in Section 2.4.4. The Xe gas mixture was recirculated through the sample space at a flow rate of 100 *ml/min*, as measured on a calibrated flow meter. The experiments at 92 mbar were carried out using a 2%/2%/96% natural isotopic

abundance  $^{129}\text{Xe}/\text{N}_2/\text{He}$  gas mixture.<sup>b</sup> At this pressure, the  $^{129}\text{Xe}$  spin polarization reached levels as high as about 20 %. The total gas pressure was 4600 mbar in all experiments. A mixture of natural abundance  $^{129}\text{Xe}$  gas<sup>c</sup> and helium<sup>d</sup> was used for the experiments at 1320 mbar and 3300 mbar Xe partial pressure. The fractional occupancies of Xe in AV were estimated from the perpendicular component of the cylindrically symmetric chemical shielding tensor,  $\sigma_{\perp}$ , of NMR spectra, as described in Section 3.3.4. Although the experiments presented herein were performed at  $-10^{\circ}\text{C}$ , the temperature dependence of  $\sigma_{\perp}$  (at constant  $\theta_m$ ) is assumed to be only weak since  $\sigma_{\perp}$  depends primarily on Xe-Xe interactions.<sup>19,22</sup>

### 6.3 Magnetization Exchange Model for Continuous-flow Hyperpolarized Xe 2D-EXSY NMR

A kinetic model is postulated on the basis of the master equations describing the continuous-flow hyperpolarized  $^{129}\text{Xe}$  2D exchange NMR. In the assumption of steady-state adsorption on a Langmuir surface, the rate equations of gaseous and nanotube phase magnetizations,  $M_g$  and  $M_c$ , can be described as

$$\frac{dM_g}{dt} = -k_d \frac{n_c \theta}{n_g} M_g + k_d M_c - \frac{M_g}{T_{1g}} + \frac{M_i - M_g}{\tau_R} \quad (6-4)$$

$$\frac{dM_c}{dt} = k_d \frac{n_c \theta}{n_g} M_g - k_d M_c - \frac{M_c}{T_{1c}} \quad (6-5)$$

where  $n_c / n_g \equiv$  ratio of total adsorption sites to gas atoms,  $k_d \equiv$  desorption rate constant, and  $M_i$  is the magnetization of freshly hyperpolarized gas entering the sample space.  $\tau_R$  is the gas residence time in the sample space, which is inversely proportional to the gas flow rate. The

<sup>b</sup> part no.: ISO-XHN-C; Spectra Gases Inc., West Branchburg, NJ.

<sup>c</sup> part no.: XE5.0RS-D8; Praxair, Danbury, CT

<sup>d</sup> part no.: UN1046; Praxair, Danbury, CT

longitudinal relaxation times of Xe inside the channels and in the gas phase are given by  $T_{1c}$  and  $T_{1g}$ , respectively. For  $^{129}\text{Xe}$  in AV at 9.4 T,  $T_{1c} = 50 \sim 150 \text{ s}$ , depending on  $\theta$ ,<sup>180</sup> and  $T_{1g} > 600 \text{ s}$ . Since the re-polarization delay of  $\tau_1 = 4 \text{ s}$ , during which the hyperpolarized atoms enter and diffuse into the channels, is much shorter than either longitudinal relaxation time, the longitudinal relaxation terms can be neglected in Eq. (6-4) and Eq. (6-5). Assuming an excess of Xe gas (*i.e.*  $n_c\theta/n_g \ll 1$ ), the re-polarization of the gas during  $\tau_1$  will be dominated by the influx of freshly hyperpolarized gas into the sample space. This assumption is validated by the observation that selective saturation of the nanotube phase  $^{129}\text{Xe}$  transition did not significantly affect the gas phase signal.<sup>180</sup>

During pre-polarization delay  $\tau_1$ , Eq. (6-4) and Eq. (6-5) can be solved by the steady-state approximation, where  $dM_g/dt = dM_c/dt \approx 0$ . Hence, the initial magnetizations in the gas and channels at the beginning of the mixing delay ( $\tau_m = 0$ ) are as follows:

$$M_g^o \equiv M_g(\tau_1) \approx M_i(1 - e^{-\tau_1/\tau_R}) \quad (6-6)$$

$$M_c^o \equiv M_c(\tau_1) \approx M_i \left[ \frac{n_c\theta}{n_g} \right] \frac{(1 - e^{-k_d\tau_1})\tau_R^{-1} - (1 - e^{-\tau_1/\tau_R})k_d}{\tau_R^{-1} - k_d} \quad (6-7)$$

Longitudinal magnetizations (stored from transverse magnetization which evolves during  $t_1$ ) that do not exchange during  $\tau_m$  yield the “diagonal” peaks in the 2D-EXSY spectrum. The gas and channel diagonal-peaks are expected to decay mono-exponentially:

$$M_{g \rightarrow g}(\tau_1, \tau_m) = M_g^o \exp \left[ -\tau_m \left( \frac{1}{\tau_R} + k_d \frac{n_c\theta}{n_g} \right) \right] \quad (6-8)$$

$$M_{c \rightarrow c}(\tau_1, \tau_m) = M_c^o e^{-k_d\tau_m} \quad (6-9)$$

The mixing-time dependences of the longitudinal magnetizations representing Xe entering and exiting the channels during the mixing time (assuming excess gas) are

$$M_{g \rightarrow c}(\tau_1, \tau_m) \approx M_g^\circ \frac{k_d}{\tau_R^{-1} - k_d} \frac{n_c \theta}{n_g} \left( e^{-k_d \tau_m} - e^{-\tau_m / \tau_R} \right) \quad (6-10)$$

$$M_{c \rightarrow g}(\tau_1, \tau_m) \approx M_c^\circ \frac{k_d}{\tau_R^{-1} - k_d} \left( e^{-k_d \tau_m} - e^{-\tau_m / \tau_R} \right) \quad (6-11)$$

The expressions reveal that the cross-peaks will generally have unequal amplitudes, vanish in the limit  $\tau_R \rightarrow 0$  or  $k_d \rightarrow 0$ , and are significantly affected by the flow when  $\tau_R^{-1} > k_d$ . However, the time dependence of the two cross-peaks will be approximately the same in this model, and each is predicted to pass through a maximum at  $\tau_m^{\max} = \ln(k_d \tau_R) / (k_d - \tau_R^{-1})$ .

Eq. (6-10) and Eq. (6-11) pertain to a homogeneous surface consisting of  $n_c$  adsorption sites. It is important to note that the average channel length in our AV sample is roughly five orders of magnitude greater than the diameter of Xe atom. For an atom to escape from the channel, it must first diffuse to the opening and sequentially overcome a potential energy barrier. In Chapter 4, we have postulated that the diffusion-limited exchange kinetics in 1D channel can be modeled by taking a distribution of desorption rates:  $k_d \approx \tau_d^{-1} = (F/\pi)^2 / \bar{z}^4$  for single-file diffusion or  $k_d \approx \tau_d^{-1} = (D_0/\pi) / \bar{z}^2$  for normal 1D diffusion. In the present work, the distribution  $k_d(z)$  will be replaced by a single mean value,  $\bar{k}_d$ . This should yield semi-quantitative results at sufficiently short mixing times.

## 6.4 Results and Discussions

Xe adsorption in AV nanotubes is known to obey the Langmuir equation<sup>74</sup> where the steady-state fractional occupancy is given by  $\theta = \text{occupied sites}/\text{total sites} = Kp_{\text{Xe}}/(1 + Kp_{\text{Xe}})$ ,  $K \equiv k_a/k_d$  is the equilibrium constant, and  $p_{\text{Xe}}$  is Xe partial pressure. By varying  $p_{\text{Xe}}$  at constant  $T$ , the effect of occupancy on the exchange rate can be explored under steady-state adsorption condition. Figure 6-3 presents the 1D CFHP  $^{129}\text{Xe}$  spectra in AV acquired at Xe partial pressures of 92, 1320 and 3300 mbar at  $-10^\circ\text{C}$ . The contribution of Xe-Xe interactions to the isotropic chemical shift becomes significant as the Xe occupancy increases. The chemical shielding anisotropy exhibits a sign inversion at  $\theta \approx 0.4$  due to the relative contributions of Xe-Xe and Xe-wall interactions to the perpendicular and parallel components of the shielding tensor.<sup>19,179</sup> At 92 mbar, the anisotropy is dominated by the Xe-wall interactions (Figure 6-3a), while at 3300 mbar (Figure 6-3c), Xe-Xe interactions dominate. Validating the assumption of steady-state Langmuir adsorption, the estimated equilibrium constants reported in Table 6-1 are within experimental error the same at all three pressures.

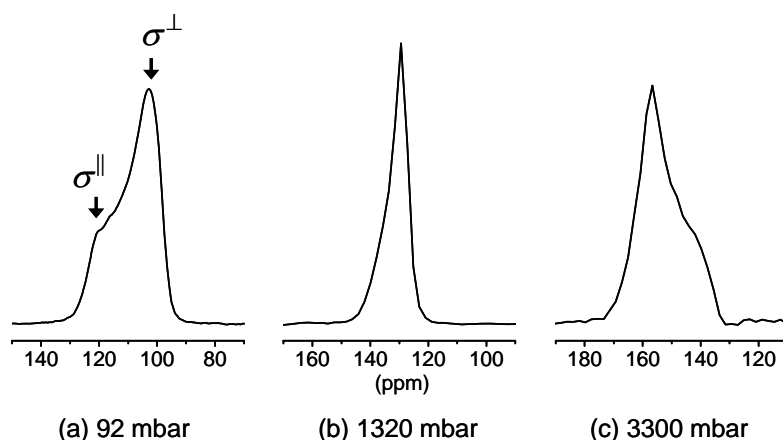


Figure 6-3. Steady-state continuous-flow hyperpolarized  $^{129}\text{Xe}$  NMR spectra in AV nanotubes, acquired at  $-10^\circ\text{C}$ , at the following Xe partial pressures: (a) 92 mbar (b) 1320 mbar (c) 3300 mbar. The chemical shift scale is referenced to dilute Xe gas (0 ppm).

The  $^{129}\text{Xe}$  2D-EXSY spectra at 92, 1320 and 3300 mbar are presented in Figure 6-4. The gas→channel and channel→gas cross-peaks are strongly attenuated by the gas flow rate which limits the residence time  $\tau_R$  of gas atoms in the sample space. The observation of gas atoms entering (upper left cross-peak) and exiting (lower right cross-peak) the single-file nanotubes is evidenced by the appearance of cross-peaks. Elongated diagonal-peaks due to Xe which did not exchange during  $\tau_m$  are observed at 92 mbar (Figure 6-4a) and 3300 mbar (Figure 6-4c), while the contours of the diagonal peak at 1320 mbar exhibit a roughly circular shape (Figure 6-4b). As in the 1D spectra presented in Figure 6-3, the shape of the adsorbed-phase diagonal peaks in the 2D-EXSY spectrum reflects the orientation of AV crystallites with different orientations with respect to the magnetic field. Cross-peaks corresponding to exchange between different individual channel orientations are not observed, indicating that multiple Xe exchange events between different channels cannot be detected under the present experimental conditions.

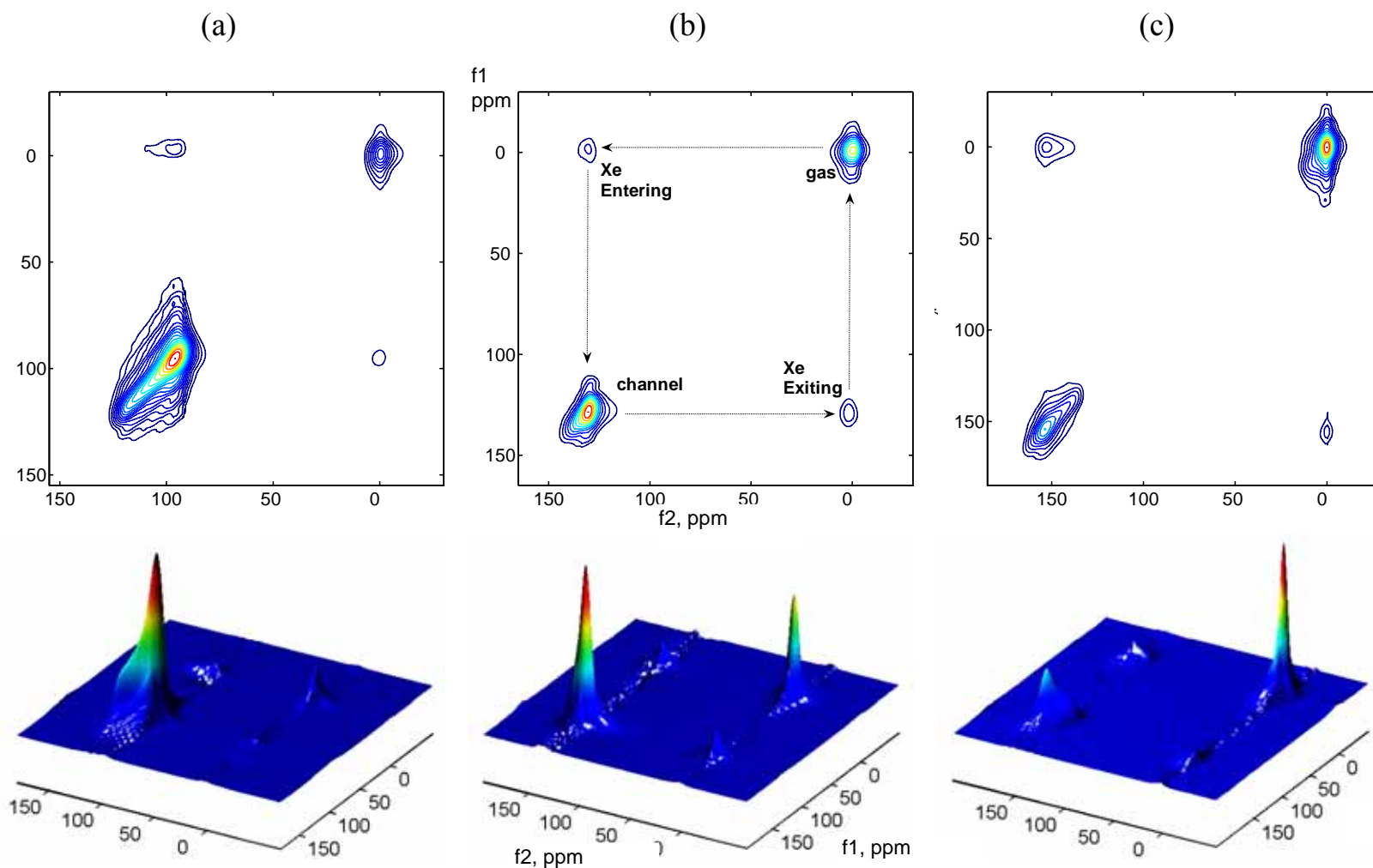


Figure 6-4. Continuous-flow hyperpolarized  $^{129}\text{Xe}$  2D-EXSY spectra in AV nanotubes at  $-10^\circ\text{C}$  acquired at the mixing times yielding maximum cross-peak intensities: (a) 92 mbar,  $\tau_m = 35$  ms (b) 1320 mbar,  $\tau_m = 100$  ms (c) 3300 mbar,  $\tau_m = 100$  ms. The spectra were recorded with  $64 \times 1024$  data points with 8 scans per spectrum. A Gaussian line-broadening of 300 Hz was applied in both time dimensions. The total experiment time per 2D spectrum with  $\tau_1 = 4$  s was about 30 min.

Figure 6-5 presents the  $\tau_m$ -dependence of the cross- and diagonal-peak integrals along with the non-linear least squares fits to Eq. (6-8) - (6-11). Note that each data point in Figure 6-5 represents a full 2D spectrum, but due to hyperpolarized Xe signal enhancement, the acquisition time of each point requires only 30 minutes. The fitted values for  $\bar{k}_d$  and  $\tau_R$  at each pressure are reported in Table 6-1. Although a mono-exponential decay of gas-phase diagonal peak is expected in Eq. (6-8), a bi-exponential function yielded better fits. However, the pre-exponential factors obtained from least-squares fits show that the more rapidly decaying exponential term of the two accounts for about 90% of the initial gas signal at 92 and 3300 mbar. Although the 2D-EXSY spectra were acquired at a nominal flow rate of 100 mL/min at all three pressures (as indicated by the gas flow meter), no correction was made for gas composition. The actual residence times at 1320 and 3300 mbar appear to have been substantially longer than in the experiments at 92 mbar. The gas phase diagonal-peak at 1320 mbar yielded  $\tau_R = 68$  ms.

Table 6-1. Best-fit kinetic parameters for CFHP Xe 2D-EXSY spectra in AV at -10 °C. (Uncertainties represent 95% confidence intervals.)

			tube-tube	gas → gas	gas → channel Eq.(6-10)		channel → gas Eq.(6-11)	
$P_{Xe}$ /mbar	$\theta$	$K / bar^{-1}$	$\bar{k}_d / s^{-1}$	$\tau_R / ms$	$\bar{k}_d / s^{-1}$	$\tau_R / ms$	$\bar{k}_d / s^{-1}$	$\tau_R / ms$
92	0.047	$0.52 \pm 0.03$	$2.5 \pm 1$	$19 \pm 3$	$6.1 \pm 2$	19(fixed)	$3.2 \pm 1$	19 (fixed)
					$4.2 \pm 2$	$11 \pm 5$	$2.2 \pm 1.4$	$13.4 \pm 5$
1320	0.39	$0.48 \pm 0.15$	$1.5 \pm 0.6$	$68 \pm 35$	-	68(fixed)	-	68(fixed)
					$2.3 \pm 0.5$	$35 \pm 3$	$2.7 \pm 0.5$	$43 \pm 3$
3300	0.64	$0.54 \pm 0.08$	n/a	$28 \pm 5$	$1.9 \pm 0.8$	28(fixed)	< 2.2	28 (fixed)
					-	-	-	-

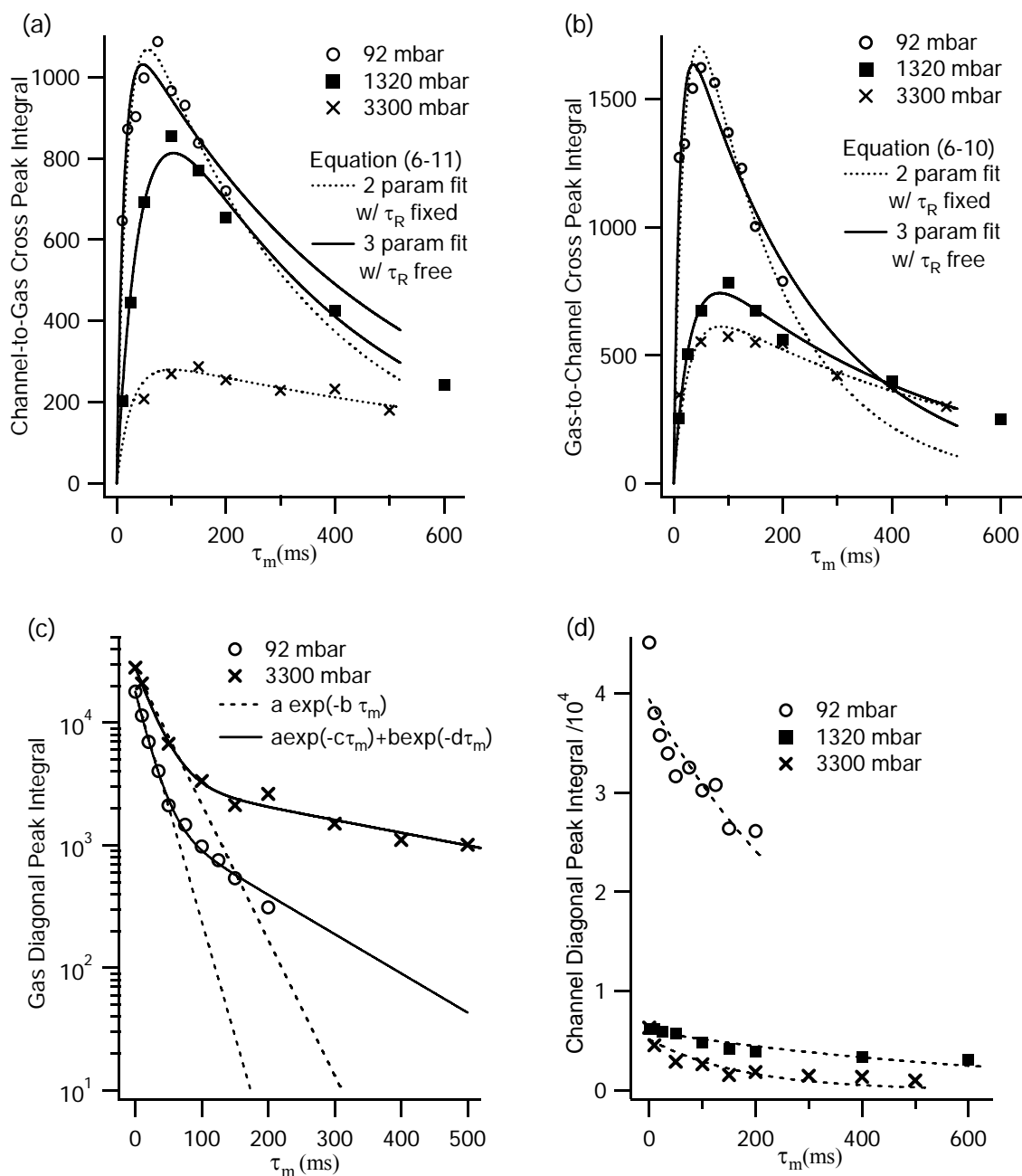


Figure 6-5. Mixing-time dependence of cross- and diagonal-peak signal integrals in the CFHP  $^{129}\text{Xe}$  2D-EXSY spectra in AV nanotubes at  $-10^\circ\text{C}$ . (a) Channel-to-gas cross-peak signal integrals at three different Xe partial pressures. (b) Gas-to-channel cross-peak integrals (c) Gas-to-gas diagonal-peak mixing time dependences at 92 and 3300 mbar. The solid and dashed lines represent the least-squares fits to the decay functions given in the legend. (d) Channel-to-channel diagonal peak mixing time dependences at 92, 1320 and 3300 mbar. The dash lines represents the least squares fits to a single exponential decay function.

To assess the validity of our simple kinetic model, fits to each of the cross-peak mixing time dependences at each pressure were performed in two different ways: by either fixing  $\tau_R$  to the value established from the gas diagonal-peak in the same spectrum, or by allowing all three parameters ( $\bar{k}_d$ ,  $\tau_R$ , and the pre-exponential factor) to vary freely. The parameters resulting from the 2 and 3 parameter least-squares fits are reported in Table 6-1 as the upper and lower row entries for  $\bar{k}_d$  and  $\tau_R$  at each of the three pressures studied. Where no table entries are reported, the fits did not exhibit good qualitative agreement with the experimental data.

Despite the large relative errors, the cross-peak fits reveal a clear decrease in the rate constant  $\bar{k}_d$  upon increasing the occupancy from  $\theta = 0.047$  (92 mbar) to 0.39 (1320 mbar). The trend is more pronounced for the gas ( $g$ )  $\rightarrow$  channel ( $c$ ) process. At 92 mbar (low occupancy), reasonable self-consistency of the model was obtained. The residence time extracted from the decay of  $M_{g \rightarrow g}$  is within the 95% confidence interval of the values obtained from the fits to both cross-peaks. However, the best-fit desorption rate for the  $g \rightarrow c$  (Xe entering) process was about a factor of 2 higher than that for the  $c \rightarrow g$  (Xe exiting) process. This asymmetry might be attributed to one or more of the following factors which are not accounted for by our simplified model: re-adsorption, presence of a desorption barrier, channel boundary effects, or one-dimensional diffusion effects.

At 3300 mbar, where the occupancy is relatively high, the fixed value for the residence time of 28 ms (obtained from the diagonal-peak decay) yielded good qualitative fits to the cross-peaks, and close agreement between the  $\bar{k}_d$  values obtained from the  $c \rightarrow g$  and  $g \rightarrow c$  cross-peaks was obtained. Allowing  $\tau_R$  to vary yielded poor agreement to the data at this pressure due to low signal-to-noise of the cross-peaks. At 1320 mbar, holding  $\tau_R = 68$  ms constant yielded

unacceptable two-parameter fits of the cross-peaks (not shown). We do not have an explanation for this irregularity. However, the three-parameter cross-peak fits allowing  $\tau_R$  vary freely gave self-consistent results, and  $\bar{k}_d$  obtained from the entering and exiting processes are in agreement.

Several factors could account for the observed decrease in  $\bar{k}_d$ . A decrease in the rate with occupancy might be explained by the -7.4 kJ/mol increase in the enthalpy of desorption upon increasing the pressure from 92 mbar to 1320 mbar at -10 °C, a change which would be expected to reduce  $k_d$  by a factor of about 100. However, the actual reduction is only by a factor of about 3, implying diffusion-limited rather than thermodynamic-limited desorption. For SFD, which has been confirmed in AV for time-scales longer than about 0.5 s, the mean-squared displacement increases according to  $\langle z^2 \rangle = 2F\sqrt{t}$ , where  $F$  is the single-file mobility. For hard-spheres particles in cylindrical channels,  $F \propto (1-\theta)/\theta$ .<sup>184</sup> Thus, the observed reduction in desorption rate upon increasing the occupancy is consistent with a decrease in the diffusivity in the channels.

As shown in Figure 6-5d, the diagonal-peak representing Xe which remains in the channels throughout the exchange delay also exhibited a decrease in  $\bar{k}_d^{diag}$  with increasing occupancy, but the values are slightly lower than those extracted from the cross-peaks. This result can be explained qualitatively in terms of diffusion-limited gas exchange. The cross-peak signals arise from atoms close enough to the channel openings to escape during the finite residence time. In contrast, the diagonal peak includes signal contributions from all Xe atoms which have diffused into the channels during the longer re-polarization delay of  $\tau_1 = 4$  s. For this larger ensemble of Xe atoms, the mean diffusion time to return to the channel opening is longer, consistent with an apparent reduction in the desorption rate.

While the single file mobility of Xe in AV nanotubes is unknown, a rough estimate of the mean displacement can be made from previously measured single-file mobility in zeolites with 1D channels. For example, a PFG NMR study<sup>212</sup> of CF<sub>4</sub> (4.7 Å) in AlPO<sub>4</sub>-5 zeolite (8.2 Å cylindrical channels) at moderate occupancy yielded  $F \approx 1 \times 10^{-12} \text{ m}^2 \text{ s}^{-1/2}$ , while a quasi-elastic neutron diffraction study<sup>214</sup> of CH<sub>4</sub> (3.8 Å) in zeolite-48 (5.3 × 5.6 Å) yielded  $F \approx 2 \times 10^{-12} \text{ m}^2 \text{ s}^{-1/2}$ . Assuming a similar single-file mobility for Xe in AV, the atoms would reach a depth of  $\sim 2 \mu\text{m}$  during the pre-polarization delay  $\tau_1 = 4\text{s}$ . The residence time of Xe atoms in the sample space limits the cross-peak intensities. At the flow rate used in the present study, the maximum cross-peak intensities were observed at  $\approx 50 \text{ ms}$ , where the exchange is limited to polarized gas atoms within  $\sim 0.7 \mu\text{m}$  of the channel opening. Interrupting the gas flow momentarily during the exchange delay is envisaged as a means to increase cross-peak intensities. By increasing the residence time, it should be possible to probe the kinetics of desorption over a much wider range of length scales or inter-crystalline exchange between nanotubes with different orientations. The interrupted-flow experiments will be presented in the following chapters.

## 6.5 Conclusions

Direct observation of Xe entering and exiting self-assembled L-alanyl-L-valine nanotubes has been facilitated by continuous-flow hyperpolarized <sup>129</sup>Xe two-dimensional exchange NMR spectroscopy. Analytical expressions for the mixing-time dependence of the diagonal and cross-peak signals have been derived under conditions of excess Xe gas, revealing that the flow effect needs to be considered when  $\tau_R < k_d^{-1}$ , as is the case for Xe in AV under our experimental condition. Nonlinear least-squares fitting to these expressions yielded the mean rate of Xe escaped from the AV channels. Although the assumption of a single mean desorption rate (as

opposed to a distribution of rates) probably contributes to the relatively large uncertainties in the fitted values of the desorption rate, a reduction in mean desorption rate constant with increased Xe density has been clearly observed. This finding is consistent with a decrease in the Xe mobility of the channels in the diffusion-limited exchange regime. While single-file diffusion of Xe in AV has been confirmed at longer time-scales,<sup>180</sup> the semi-quantitative analysis of the present work precludes any definite conclusions to be made concerning the relative importance of normal one-dimensional diffusion versus single file diffusion to the exchange process. Nonetheless, this study has shown how hyperpolarized <sup>129</sup>Xe NMR can be applied to the investigation of gas exchange dynamics in nanotubes, and the kinetic model developed herein should serve as a starting point for future hyperpolarized NMR studies of adsorption, diffusion and exchange processes in such materials.

CHAPTER 7  
SIGNAL ENHANCEMENT OF HYPERPOLARIZED XE-129 2D-NMR EXCHANGE CROSS  
PEAKS IN NANOTUBES BY INTERRUPTION OF THE GAS FLOW

**7.1 Introduction**

It has been noted that previous quantitative kinetic studies employing  $^{129}\text{Xe}$  2D-EXSY have been mostly limited to thermally-polarized conditions, for which multi-site exchange models have been established.<sup>5,33,38,58,235,244</sup> The thermally-polarized  $^{129}\text{Xe}$  experiments generally suffer from inherently low sensitivity or unacceptably long acquisition times for mixing-time dependence studies, ranging from hours to days per 2D spectrum. As noted previously, only a few quantitative applications of CFHP  $^{129}\text{Xe}$  2D-EXSY have been reported,<sup>242</sup> and the potential complications and limitations due to gas flow effects have not been discussed in the literature. In this chapter, the issue of flow effects in CFHP  $^{129}\text{Xe}$  2D-EXSY will be investigated.

In Chapter 6, we proposed a kinetic model to describe the magnetization exchange between the flowing gas phase and a Langmuir adsorption surface.<sup>246</sup> Under the flow condition, the gas residence time  $\tau_R$  in the sample space is determined by the gas flow rate (*i.e.*  $G \propto \tau_R^{-1}$ ). In the diamagnetic solids, the Xe longitudinal relaxation time in the gas phase is generally much longer than any of the other relevant experimental time-scales. The spectra acquired under the continuous-flow condition will be affected by gas flow if the gas residence time is much shorter than the longitudinal relaxation time of the Xe gas (*i.e.*  $\tau_R \ll T_{1g}$ ). In such a case, the gas diagonal-peak and all cross-peak signals representing exchange with the gas phase in 2D-EXSY spectrum will strongly depend on the residence time and exchange rates.

According to Eq. (6-10) and Eq. (6-11), a simple comparison of the  $\tau_m$ -dependences of the cross-peak intensities with variable  $\tau_R$  and constant  $k_d$  can be made and illustrated in Figure 7-1.

As  $\tau_R = 50\text{ms}$ , where it is on the same time-scale of residence time in Xe/AV system under the flow rate of  $100\text{ mL/min}$  and Xe partial pressure of  $1320\text{ mbar}$  at  $-10\text{ }^\circ\text{C}$ <sup>246</sup>, the cross-peaks are strongly attenuated. Nevertheless, as  $\tau_R$  gradually increases, the cross-peak signal is significantly enhanced and the location of its maximum is shifted to longer  $\tau_m$ . In the limit of  $\tau_R \rightarrow \infty$ , where gas flow is absent in the sample space, the cross-peak intensity exponentially grows to its maximum and eventually reaches a plateau. This comparison indicates that the finite residence time of Xe gas in the sample space strongly suppresses the cross-peak intensities associated with the exchange between surface and gas phase. While  $\tau_R$  can be increased by simply reducing the gas flow rate, hyperpolarized gases will be depolarized due to the relaxation during gas transport from pumping cell to sample space.<sup>35</sup> It is not usually favorable for retaining high Xe polarization in the gas handling system. As will be shown below, interrupting the gas flow briefly during the mixing time can be an alternative and simple approach to extend gas residence time and consequently enhance the cross-peak intensities. By increasing the cross-peak intensities, it will be possible to explore the coupling of the gas exchange and diffusion processes over a longer range of exchange times and diffusion length scales by hyperpolarized  $^{129}\text{Xe}$  2D-EXSY NMR.

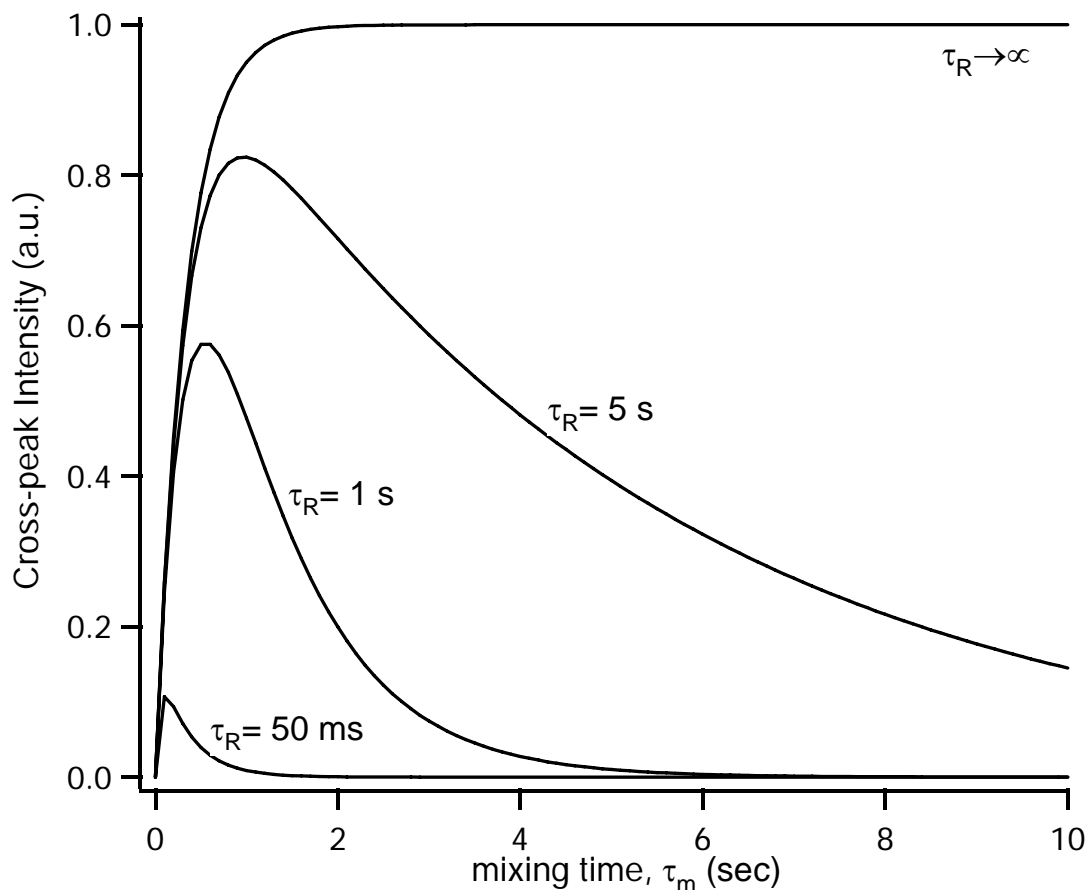


Figure 7-1. Simulated mixing-time dependence of the cross-peak signals at variable gas residence time  $\tau_R$  and constant desorption rate constant ( $k_d = 3 \text{ s}^{-1}$ ) based on Eq. (6-11).

It will be shown how the standard CFHP  $^{129}\text{Xe}$  2D-EXSY experiment can be easily modified to achieve dramatic cross-peak signal enhancement. The technique is demonstrated for Xe in the dipeptide nanotube L-alanyl-L-valine (AV),<sup>170,247</sup> where Xe interactions,<sup>19,74</sup> single-file diffusion<sup>180</sup>, and gas-channel exchange<sup>246</sup> have been characterized previously.

## 7.2 Experimental

Polycrystalline AV was studied without further purification. A 15 mg AV sample<sup>a</sup> was evacuated to  $\sim 10^{-5}$  torr at 100 °C *in situ* for 2-3 hours to remove moisture prior to NMR measurements. The gas mixture<sup>b</sup> consisted of 2% natural abundance  $^{129}\text{Xe}$ , 2%  $\text{N}_2$  and 96% He at a total pressure of 4600 mbar was used in all the Xe NMR experiments. The  $^{129}\text{Xe}$  spin polarization is estimated to be  $\sim 20\%$ . Under certain conditions, only hyperpolarized  $^{129}\text{Xe}$  yields observable NMR signal, since thermally-polarized  $^{129}\text{Xe}$  cannot be detected at this density without signal averaging. Fractional channel occupancy of  $\theta = 0.047$  for Xe in AV was inferred from the Xe chemical shift tensor, as described in Section 3.3.4. Spectra were acquired at -10 °C in a magnetic field of 9.4 T (110.7 MHz  $^{129}\text{Xe}$  Larmor frequency). The  $\pi/2$  RF pulse width was 4  $\mu\text{s}$ . Chemical shifts were referenced to diluted Xe gas as 0 ppm. The isotropic chemical shift difference between the gaseous and adsorbed phases of  $^{129}\text{Xe}$  under the experimental conditions is about 110 ppm.

The layout of the hyperpolarized  $^{129}\text{Xe}$  gas generator<sup>35</sup> is shown in Figure 2-12. To control the flow of hyperpolarized gas, the outlet of the sample space was connected by 1/8" O.D. PFA tubing to a two-way solenoid valve.<sup>c</sup> An auxiliary transistor-to-transistor logic (TTL) gate on the Bruker Avance NMR spectrometer was used to control the solenoid valve from the pulse sequence.

---

<sup>a</sup> part no.: 0210032883; MP Biochemicals, *Santa Ana, CA*

<sup>b</sup> part no.: ISO-XHN-C; Spectra Gases Inc., *West Branchburg, NJ*.

<sup>c</sup> part no.: 1327BV122T; Jefferson Solenoid Valves, *Miami, FL*.

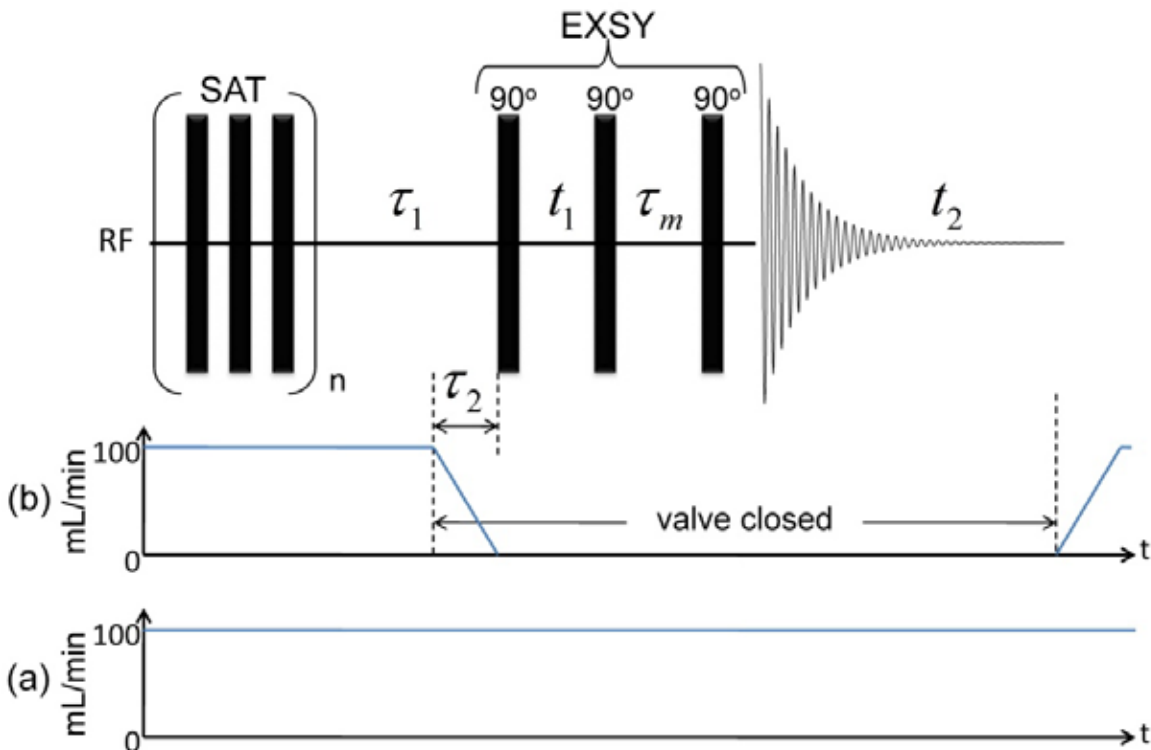


Figure 7-2. Pulse sequence for (a) continuous-flow (CF) and (b) interrupted-flow (IF) hyperpolarized 2D-EXSY. The solenoid valve stops the flow near the end of the re-polarization delay  $\tau_1=4$ s. The system was allowed to settle for  $\tau_2=1$ s prior to application of the EXSY pulse sequence. (SAT is the non-selective saturation RF pulse train.)

To create a reproducible, well-defined initial polarization condition prior to each repetition of the 2D-EXSY pulse program, the  $^{129}\text{Xe}$  polarization was initially saturated by a non-selective  $\pi/2$  pulse train, as shown in Figure 7-2. Following the saturation, freshly hyperpolarized  $^{129}\text{Xe}$  enters the sample space where it accumulates inside the nanotubes during the re-polarization delay,  $\tau_1$ . 2D-EXSY spectra were acquired in either of two different modes, referred to as CF and IF, as illustrated in Figure 7-2. In CF mode (Figure 7-2a), the hyperpolarized gas mixture is continuously re-circulated through the sample space at a steady flow rate of 100 *mL/min*, recorded from a calibrated flow meter, during the entire experiment. In IF mode (Figure 7-2b), the re-circulation at a flow rate of 100 *mL/min* is briefly paused during the 2D-EXSY pulse

sequence. The normally closed solenoid valve is closed at the end of the re-polarization delay,  $\tau_1$ . A settling time of  $\tau_2=1s$  following switching of the valve was allowed prior to application of the  $\pi/2$  EXSY preparation pulse. 2D Spectra were collected with 100 and 1024 points in the  $t_1$  and  $t_2$  dimensions with a spectral width of 26 kHz. At each  $t_1$  point, 8 transients were signal averaged. A line-broadening of 300 Hz was applied with respect to both time dimensions prior to Fourier transformation. The total experimental time for each 2D spectrum was  $\sim 65$  min. The 2D spectral processing was performed using of MATLAB<sup>d</sup> and matNMR<sup>e</sup>.

### 7.3 Results and Discussions

We have suggested that a momentary interruption of the gas flow, as shown in the pulse sequence in Figure 7-2b, should produce increased cross-peak signals and allow much longer exchange time-scales to be probed. We now demonstrate the direct comparison of the hyperpolarized  $^{129}\text{Xe}$  2D-EXSY spectra acquired on Xe in AV in the interrupted-flow (IF) and continuous-flow (CF) modes. The continuous and interrupted-flow hyperpolarized  $^{129}\text{Xe}$  2D-EXSY spectra acquired at two different mixing times are presented in Figure 7-3. The 1D spectra at  $f_1=0$  ppm are presented on the top of each 2D spectrum. The gaseous diagonal peak in IF mode decays very slowly from  $\tau_m = 300\text{ms}$  (Figure 7-3a) to  $\tau_m = 1s$  (Figure 7-3c), probably dominated by gas diffusion or drift out of the RF detection coil. In contrast, the Xe diagonal peak in gas phase obtained by the same EXSY pulse sequence but at an uninterrupted flow rate of  $100\text{ mL/min}$  decays much more rapidly, indicating that the gas peak in the CFHP 2D-EXSY spectrum is strongly affected by the gas flow. The decay of the adsorbed phase diagonal-peak is much less sensitive to the effects of flow than in the gas peak.

---

<sup>d</sup> The Mathworks Inc., Natick, MA

<sup>e</sup> <http://www.nmr.ethz.ch/matnmr>; written by J. van Beek

The differences of cross peaks in IF and CF modes can be summarized as follows. Firstly, the cross-peak integrals for the gas→channel and channel→gas processes are not equal in both modes, which is in agreement with our kinetic models. This may be traced to a difference in the spin polarization in the gaseous and nanotube phases. Secondly, the signal-to-noise of the gas phase diagonal and exchange cross-peaks is much higher in IF than in CF mode. As the mixing time increased to  $\tau_m = 1s$ , CFHP 2D-EXSY barely yielded any cross peaks (Figure 7-3d). However, in the IF mode, both the gas and cross-peak signals are still clearly visible at  $\tau_m = 1s$  (Figure 7-3c). The dramatic differences in the spectra obtained under CF and IF conditions are especially evident in the 3D representations shown in Figure 7-4. While the gas and cross-peak signals nearly vanish under CF conditions (Figure 7-4b), these peaks are observed with extremely high signal-to-noise ratio under IF conditions (Figure 7-4a). Thus, by simply interrupting the gas flow during the exchange period in the 2D-EXSY pulse sequence, the cross-peak signals were enhanced by a factor of ~60. We refer to this experimental method as IFHP-EXSY.

Interrupting the gas flow during the mixing time allows gas atoms desorbing from the surface, or nanotubes as in the present case, to accumulate in the sample space for detection. For the reverse processes, a longer residence time increases the probability that gas atoms tagged by the preparation pulse will be adsorbed by the nanotubes during the mixing time. In principle, the mixing-time dependences of the cross-peak and diagonal-peak signal integrals in thermally-polarized and IFHP  $^{129}\text{Xe}$  2D-EXSY spectra should be essentially the same.

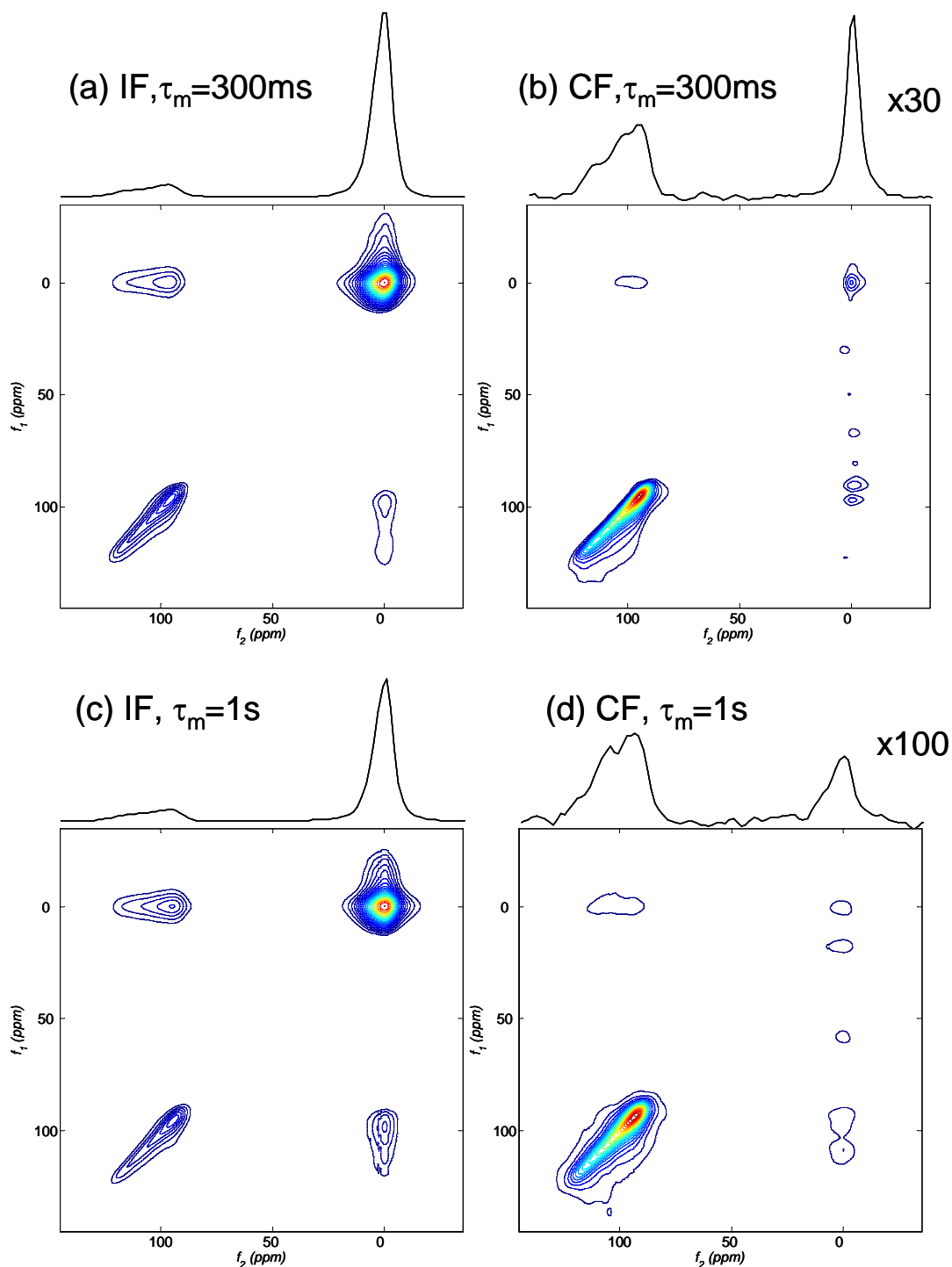


Figure 7-3. HP  $^{129}\text{Xe}$  2D-EXSY spectra of Xe in AV at  $-10\text{ }^{\circ}\text{C}$  with mixing times of (a,b) 300 ms and (c,d) 1s. Spectra in (b) and (d) were acquired in continuous-flow (CF) mode. Spectra in (a) and (c) were acquired in interrupted-flow (IF) mode (see text). 1D spectral slices at  $f_1=0$  ppm are also presented at the top of each 2D spectrum.

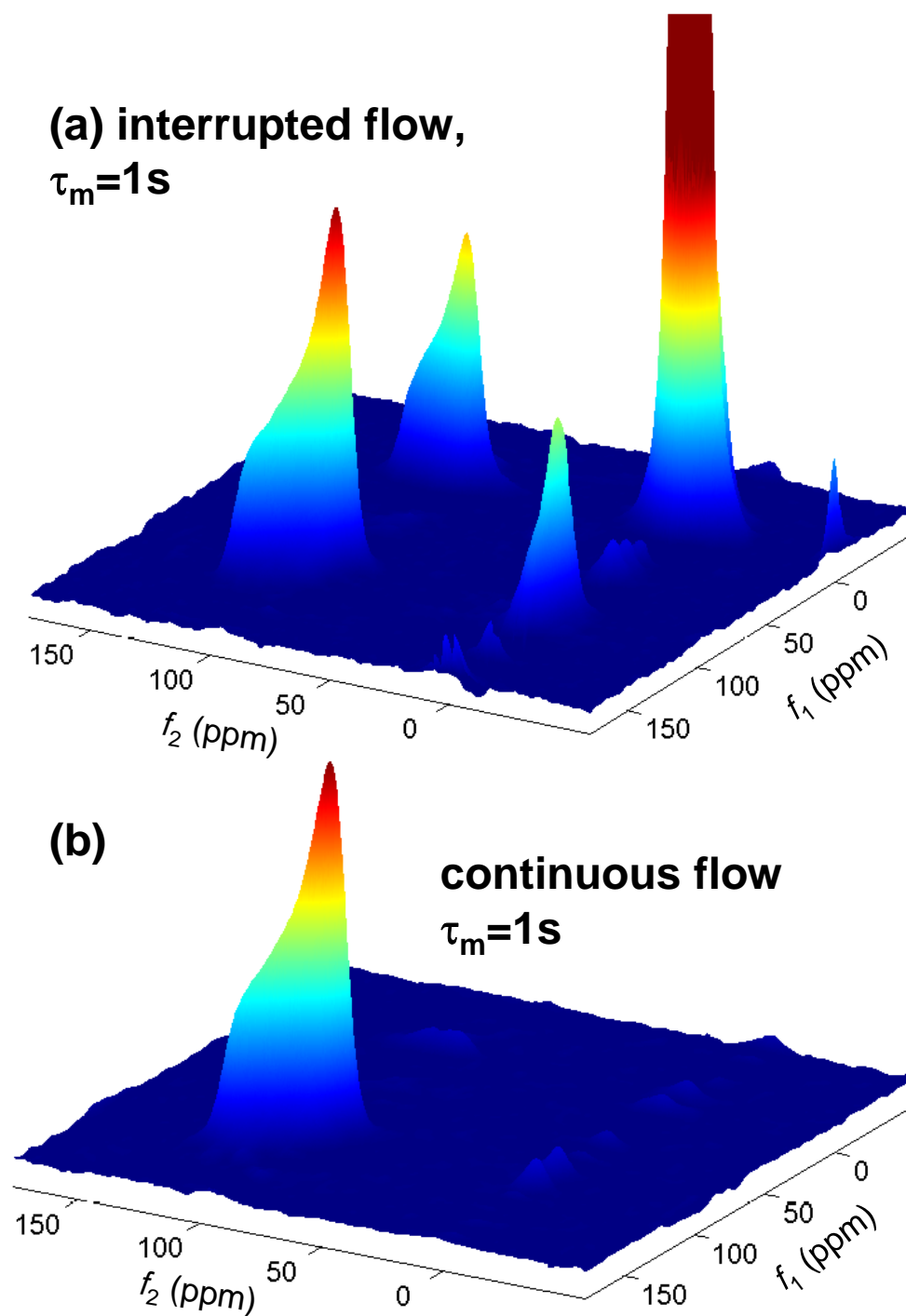


Figure 7-4. 3D representation of HP  $^{129}\text{Xe}$  2D-EXSY spectra of Xe in AV at  $-10^\circ\text{C}$ , acquired in (a) IF mode and (b) CF mode, each with a mixing time of  $\tau_m=1s$ . The gas peak in (a) was truncated to facilitate comparison of the cross-peaks in each spectrum.

## 7.4 Conclusions

To summarize, a simple but highly effective modification of the CFHP 2D-EXSY experiment has been demonstrated in AV, a polycrystalline nanotube material. We have demonstrated that by interrupting the flow during the mixing time, cross-peak intensities in the Xe/AV system can be increased by a factor of  $\sim 60$ . The interrupted flow 2D-EXSY experiment can overcome the effects of gas flow which strongly affects the peak intensities and sets an upper limit on the maximum exchange time that will yield observable cross-peak signals. IFHP  $^{129}\text{Xe}$  2D-EXSY is particularly well-suited for studies of diffusion-limited gas exchange kinetics in nanotube systems which, under continuous flow conditions, yield cross-peaks with substantially lower signal-to-noise ratio. The experimental uncertainty in kinetic parameters extracted from 2D-EXSY spectra are highly sensitive to the signal-to-noise ratio.<sup>38</sup> The IFHP 2D-EXSY method can be expected to provide significantly greater accuracy in determination of multi-site exchange rates and facilitate the measurement of smaller exchange rates.

In addition to the 2D-EXSY experiments, the interrupted-flow experiment may also be applicable in the  $^{129}\text{Xe}$  polarization transfer techniques, such as cross-polarization<sup>127-129</sup> or SPINOE.<sup>124-126</sup> Since the cross-polarization and Overhauser effect involve the polarization transfer, which is similar to the mechanism of magnetization exchange presented above, the efficiency of polarization transfer is expected to be enhanced by incorporating gas flow interruption. Moreover, IFHP-EXSY may be applied to other hyperpolarized species, such as  $^1\text{H}$  or  $^{13}\text{C}$  generated from parahydrogen<sup>112,113</sup> or DNP.<sup>101-105</sup> In principle, mixing times in IFHP-EXSY are limited only by intrinsic longitudinal relaxation time  $T_{1c}$  and desorption rate. The ability to probe longer mixing times will facilitate extension of hyperpolarized 2D-EXSY to

slower exchange processes or longer diffusion time/length scales for characterization of pore-space architecture, exchange and transport process in nanotubes or other nanoporous materials.

CHAPTER 8  
 INVESTIGATIONS OF GAS EXCHANGE IN GA10 WHEEL NANOTUBES BY 2D  
 EXCHANGE HYPERPOLARIZED XE-129 NMR

**8.1 Introduction**

The interrupted-flow hyperpolarized 2D-EXSY technique has successfully overcome the suppressions of cross-peak intensities due to finite residence time in CFHP  $^{129}\text{Xe}$  2D-EXSY, and the dramatic enhancement of cross-peak signals in IFHP-EXSY has been demonstrated in AV nanotubes.<sup>248</sup> While the magnetization exchange model has been developed to quantitatively measure the mean desorption rates of guest molecules in the 1D nanotube system by CFHP  $^{129}\text{Xe}$  2D-EXSY<sup>246</sup>, it is exclusively valid in the system where the  $^{129}\text{Xe}$  longitudinal relaxation time ( $T_{1c}$ ) inside the channels is relatively longer than the gas residence time in the sample space (*i.e.*  $T_{1c} \gg \tau_R$ ). In the kinetic model of CFHP 2D-EXSY presented in Section 6.3, under the interrupted-flow (IF) condition, where  $\tau_R \rightarrow \infty$ , Eq. (6-10) and (6-11) can be rewritten as

$$M_{g \rightarrow c}(\tau_1, \tau_m, \tau_R \rightarrow \infty) \approx M_g^o \frac{n_c \theta}{n_g} (1 - e^{-k_d \tau_m}) \quad (8-1)$$

$$M_{c \rightarrow g}(\tau_1, \tau_m, \tau_R \rightarrow \infty) \approx M_c^o (1 - e^{-k_d \tau_m}) \quad (8-2)$$

where  $n_c / n_g \equiv$  ratio of total adsorption sites to gas atoms,  $k_d$  is the desorption rate constant, and  $M_g^o$  and  $M_c^o$  are the magnetizations in the gas and channels at the beginning of the mixing delay which have been labeled according to their chemical shift during the 2D evolution ( $t_1$ ) period. Although Eq. (8-1) and Eq. (8-2) clearly exhibit the exponential growth trends as a function of mixing time  $\tau_m$ , as predicted in Figure 7-1, the equations are only valid in the systems, such as  $^{129}\text{Xe}$  in AV or TPP nanotubes, in which Xe  $T_{1c}$  on the diamagnetic solid surface or in the

nanotubes is much longer than the mixing time or any of the other relevant time-scales. The kinetic model needs to be modified in order to describe the detailed exchange kinetic processes in 1D nanotube systems spanning from  $T_{1c} > \tau_m$  to  $T_{1c} < \tau_m$  regimes.

In practice, the mixing time in IFHP-EXSY experiments can be extended up to the time-scale of longitudinal relaxation time of Xe in the sample. However, Xe/AV is not an appropriate system to test the validity of the  $T_{1c}$ -dependence of the theoretical IFHP-EXSY signal expressions. In our previous studies, Xe  $T_{1c}$  in AV nanotubes was determined to range from 50-150 sec, depending on Xe density in the channels, at 9.4 T.<sup>180</sup> Assuming the experimental parameters of IFHP-EXSY are set to pre-polarization delay  $\tau_1 = 4s$ , mixing time  $\tau_m = 50s$ , 8 scans per  $t_I$  increment, and 64 increments on  $t_I$  domain, it would take ~8 hours to acquire a single 2D spectrum in the case of AV. Obviously, it would be impractical to acquire a series of IFHP 2D-EXSY spectra as a function of mixing time in AV nanotubes.

One possibility to demonstrate the complete  $\tau_m$ -dependence of IFHP-EXSY is to find a system with a relatively short  $T_{1c}$  relaxation time. In Chapter 5, we have utilized the selective CFSR hyperpolarized  $^{129}\text{Xe}$  NMR experiments to investigate Xe diffusion in Ga<sub>10</sub> and Ga<sub>18</sub> nanotubes, revealing dramatically different diffusion behaviors in both nanotube systems. The Xe diffusion in Ga<sub>10</sub> nanotubes exhibits a clear SFD behavior, and the Xe  $T_{1c}$  in Ga<sub>10</sub> is about 2.5 sec at room temperature. Therefore, Ga<sub>10</sub> wheel nanotubes can serve as an excellent candidate of single-file nanotube system in  $\tau_m$ -dependence of IFHP Xe 2D-EXSY studies in the  $\tau_m > T_{1c}$  limit. The Xe  $T_{1c}$  relaxation time in Ga<sub>18</sub> nanotubes is ~80 ms, which is too short to conduct the IFHP-EXSY experiments since experimental mixing time is mostly limited by  $T_{1c}$  relaxation time.

Here, the experimental mixing-time dependence of IFHP 2D-EXSY in Ga<sub>10</sub> nanotubes along with the modified kinetic model incorporating  $T_{1c}$  relaxation time under the interrupted-flow condition will be presented. The results will be compared with the 2D-EXSY results obtained in Ga<sub>10</sub> nanotubes under the continuous-flow condition. It will be shown that the IFHP 2D-EXSY experiment can indeed explore the slower exchange process in nanotubes.

## 8.2 Experimental

Ga<sub>10</sub> wheel nanotubes were synthesized by Dr. Theocharis Stamatatos in Prof. George Christou's laboratory (UF Chemistry Department). The detailed procedures of the molecular wheels synthesis along with their crystal structure identifications can be found in the literature.<sup>36</sup> A 40 mg polycrystalline sample of Ga<sub>10</sub> nanotubes was loosely packed into NMR sample holder and evacuated at 10<sup>-5</sup> torr and room temperature overnight prior to NMR measurements.

The hyperpolarized Xe gas was generated by continuous-flow Rb-Xe optical-pumping spin-exchange, as described in Section 2.4.4. The gas mixture was re-circulated through the sample space during the experiments at a flow rate of 100 mL/min. The 2%/2%/96% nature isotopic abundance <sup>129</sup>Xe/N<sub>2</sub>/He gas mixture<sup>a</sup> with a total gas pressure of 4000 mbar was used for all the 2D experiments. The 2D EXSY experiments were carried out on a 9.4 T Bruker Avance NMR spectrometer operating at a <sup>129</sup>Xe Larmor frequency of 110.7 MHz and at room temperature. The 2D-EXSY NMR spectra were acquired using the pulse sequences of CFHP-EXSY and IFHP-EXSY described in Figure 7-2. A typical  $\pi/2$  pulse duration was about 4.5  $\mu$ s. During the re-polarization delay of  $\tau_1 = 2s$ , the polarized Xe was allowed to flow into the sample space and to diffuse and accumulate in the channels. Each 2D spectrum consisted of 64 and 1024 points in  $t_1$  and  $t_2$  dimensions, respectively. The free induction decay was accumulated in 8 scans

---

<sup>a</sup> part no.: ISO-XHN-C; Spectra Gases Inc., West Branchburg, NJ.

for each  $t_I$  increment. The spectral width is 38 kHz in both the  $t_1$  and  $t_2$  dimensions. For IFHP-EXSY, a gas flow settling time  $\tau_2 = 1s$  was allowed following closing of the solenoid valve. The total acquisition time for each 2D spectrum is about 25 min. The spectra were processed with 300 Hz of Gaussian line-broadening applied to both dimensions prior to the Fourier transformation. The mixing time was varied from 10 ms to 1s. The reported Xe NMR chemical shifts were referenced to the dilute Xe gas as 0 ppm.

### 8.3 Magnetization Exchange Model for 2D-EXSY under Flow Interruption

Here we propose a modified magnetization exchange model to describe the 2D-EXSY signals under the condition of flow interruption. As indicated in the IFHP-EXSY pulse sequence presented in Figure 7-2b, Xe gas remains in CF mode during the pre-polarization delay,  $\tau_1$ . The hyperpolarized gas flow is halted prior to the first  $\pi/2$  pulse of EXSY sequence. During the 2D preparation delay,  $t_1$ , the Xe flow is interrupted. Since  $\tau_1 \ll T_{1g}$ , the initial magnetizations in the gas and channels,  $M_g^\circ$  and  $M_c^\circ$ , at the beginning of mixing time are given by Eq. (6-6) and Eq. (6-7). Under IF condition, the rate equations describing the magnetization dynamics in the gas and nanotube phases during the mixing time are

$$\frac{dM_g}{dt} = -k_d \frac{n_c \theta}{n_g} M_g + k_d M_c - \frac{M_g}{T_{1g}} \quad (8-3)$$

$$\frac{dM_c}{dt} = k_d \frac{n_c \theta}{n_g} M_g - k_d M_c - \frac{M_c}{T_{1c}} \quad (8-4)$$

where  $T_{1g}$  and  $T_{1c}$  are the longitudinal relaxation times in the gas and nanotube phases, respectively. As noted previously, since gaseous Xe relaxation time  $T_{1g}$  is much longer than any other relevant experimental time-scales in most diamagnetic surfaces, it can be safely ignored from Eq. (8-3). Additionally, under the condition where the excess of Xe gas is in the sample

space,  $n_c\theta/n_g \ll 1$  can be safely assumed.<sup>246</sup> Thus, the mixing-time dependences of diagonal-peak intensities in gas and nanotube phases are

$$M_{g \rightarrow g}(\tau_1, \tau_m) = M_g^0 e^{-\left(k_d \frac{n_c\theta}{n_g} + T_{1g}^{-1}\right)\tau_m} \approx M_g^0 e^{-k_d \frac{n_c\theta}{n_g} \tau_m} \quad (8-5)$$

$$M_{c \rightarrow c}(\tau_1, \tau_m) \approx M_c^0 e^{-(k_d + T_{1c}^{-1})\tau_m} \quad (8-6)$$

Both diagonal-peak intensities mono-exponentially decay with mixing time; however, because of the assumption of excess Xe gases,  $n_c\theta/n_g \ll 1$ , the  $\tau_m$ -dependence of the gas diagonal-peak signal in Eq. (8-5) is anticipated to decay very slowly. The mixing-time dependence of the cross-peak signals for the gas→channel and channel→gas processes can be solved and expressed by the following equations, assuming excess of Xe gas in exchange with a Langmuir adsorption surface:

$$M_{g \rightarrow c}(\tau_1, \tau_m) \cong M_g^0(\tau_1) \left[ \frac{k_d + T_{1c}^{-1} + \chi}{2\chi} \right] \left\{ e^{-\frac{1}{2}(k_d + T_{1c}^{-1} - \chi)\tau_m} - e^{-\frac{1}{2}(k_d + T_{1c}^{-1} + \chi)\tau_m} \right\} \quad (8-7)$$

$$M_{c \rightarrow g}(\tau_1, \tau_m) \cong M_c^0(\tau_1) \left[ \frac{-k_d - T_{1c}^{-1} + \chi}{2\chi} \right] \left\{ e^{-\frac{1}{2}(k_d + T_{1c}^{-1} - \chi)\tau_m} - e^{-\frac{1}{2}(k_d + T_{1c}^{-1} + \chi)\tau_m} \right\} \quad (8-8)$$

where  $\chi = \sqrt{-4(n_c\theta/n_g)k_d T_{1c}^{-1} + (k_d + T_{1c}^{-1})^2}$ . The detailed deviations of Eq. (8-7) and Eq. (8-8) can be found in Appendix B. The expressions clearly shown that the trends in the  $\tau_m$ -dependence of Eq. (8-7) and Eq. (8-8) are essentially the same but with unequal amplitudes, as was also the case for Eq. (6-10) and Eq. (6-11) under the CFHP condition. In the limit of  $T_{1c}^{-1} \rightarrow 0$ , the equations are comparable to Eq. (8-1) and Eq. (8-2). Hence, the modified kinetic model presented above should be valid to describe the exchange process in the  $T_{1c} < \tau_m$  regime under the IF condition.

To understand how the exchange process is affected by longitudinal relaxation and desorption in the modified exchange kinetic model, a further comparison can be made. The simulations were performed based on Eq. (8-7) and normalized to its initial magnetization,  $M_g^o$ . The simulated results and their corresponding y-axis expansion plots are presented in Figure 8-1. As the simulations of Figure 8-1a show, by varying  $T_{1c}$  at constant desorption rate ( $k_d = 2.5s^{-1}$ ), the cross-peak signal reaches a maximal steady-state value at a mixing time which depends on  $T_{1c}$ . The difference of  $T_{1c}$ -dependence of cross-peak signals is more apparent if the y-axis of Figure 8-1a is expanded (Figure 8-1c). At short  $T_{1c}$ , the cross-peak signal recovers at a relatively short mixing time. At sufficiently long mixing times, the cross-peak signal at short  $T_{1c}$  decays due to relaxation. In Figure 8-1b, cross-peak intensity recovers rapidly at large  $k_d$  and constant  $T_{1c}$ . However, in the y-axis expansion plot of Figure 8-1b, all three curves decay uniformly at longer mixing time due to constant  $T_{1c}$  relaxation time in the simulated conditions (Figure 8-1d). The features theoretically indicate that the IFHP-EXSY with the approximation of long  $T_{1g}$  and excess Xe gas (*i.e.*  $n_c\theta/n_g \ll 1$ ) can yield intense cross-peak intensities, thereby efficiently improving the cross-peak signals in CFHP 2D-EXSY.

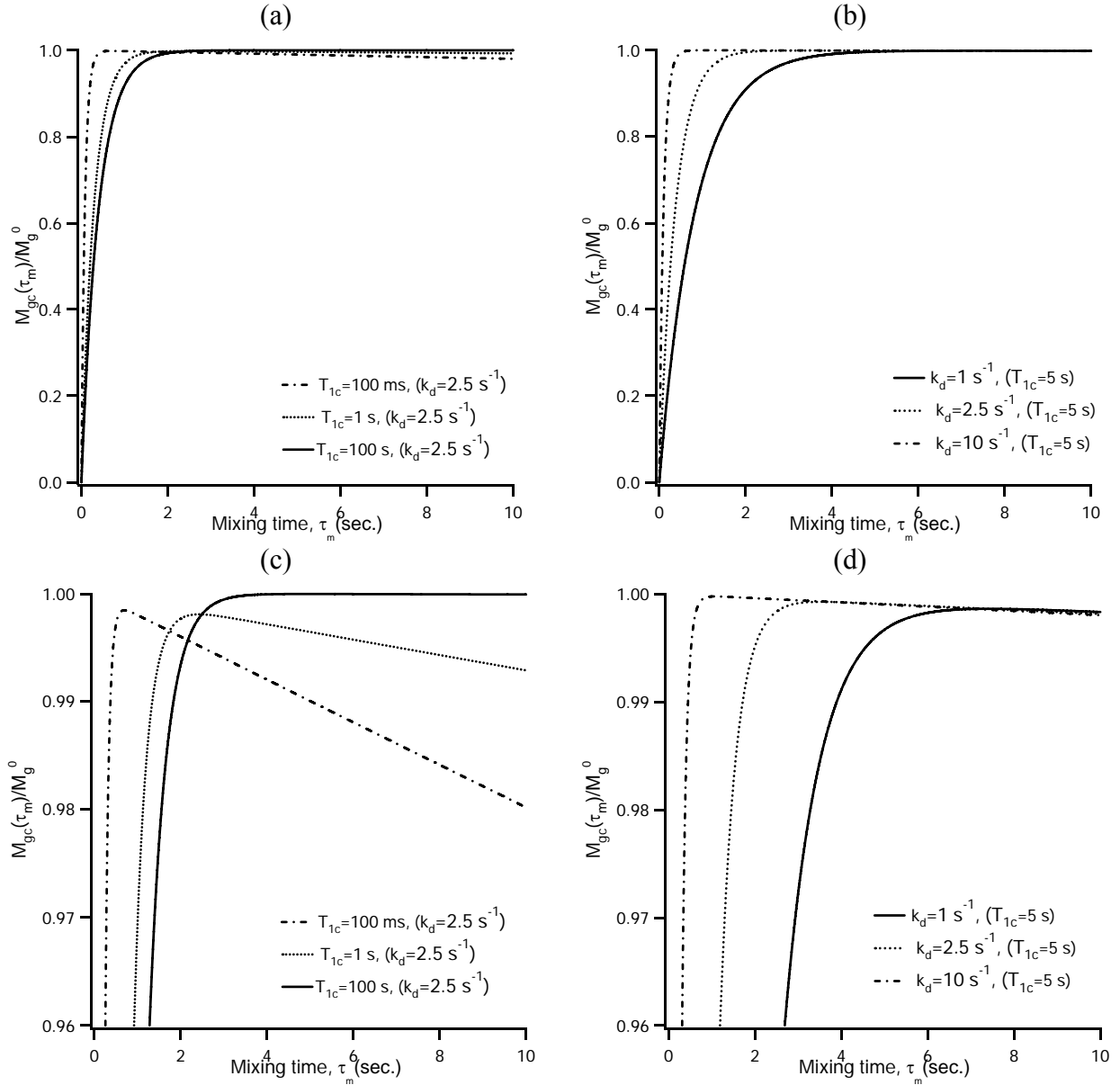


Figure 8-1. Simulated mixing-time dependences of normalized cross-peak signals at (a) variable  $T_{1c}$  ( $k_d = 2.5 \text{ s}^{-1}$ ) and (b) variable  $k_d$  ( $T_{1c} = 5 \text{ s}$ ) based on Eq. (8-7). Y-axis expansions of (a) and (b) are presented in (c) and (d), respectively.  $n_c \theta / n_g = 10^{-4}$

## 8.4 Results and Discussions

Hyperpolarized  $^{129}\text{Xe}$  2D-EXSY experiments were performed under continuous-flow and interrupted-flow conditions in  $\text{Ga}_{10}$  nanotubes at 80 mbar Xe partial pressure and 25 °C. Representative CFHP and IFHP 2D-EXSY spectra of  $\text{Ga}_{10}$  nanotubes are demonstrated in Figure 8-2. For CFHP 2D-EXSY, the cross peaks are clearly visible at  $\tau_m = 12\text{ms}$  (Figure 8-2a), revealing that Xe atoms entered or exited the  $\text{Ga}_{10}$  nanotubes during the 12 ms mixing time. As the mixing time increases to 250 ms (Figure 8-2b), the signal-to-noise ratios of the cross-peak and gas diagonal-peak signals are extremely weak due to the finite residence time, as discussed previously. In the interrupted-flow experiment, the cross-peak signals at  $\tau_m = 1\text{ms}$  (Figure 8-2c) are approximately the same as those at  $\tau_m = 12\text{ms}$  in the CFHP 2D-EXSY spectrum (Figure 8-2a). Furthermore, drastically stronger cross-peak signals are apparent at the relatively long mixing time of  $\tau_m = 1\text{s}$  in IFHP-EXSY spectrum (Figure 8-2d) in comparison to the cross-peaks observed by CFHP 2D-EXSY (Figure 8-2b). The corresponding 3D representations of IFHP and CFHP 2D-EXSY spectra in  $\text{Ga}_{10}$  nanotube are illustrated in Figure 8-3. In Figure 8-3b, the cross peaks and gas diagonal peak are barely seen at  $\tau_m = 250\text{ms}$  in CFHP-EXSY in  $\text{Ga}_{10}$  nanotubes due to the finite residence time. Nevertheless, the intense gas diagonal and exchange cross-peaks are still clearly observable in IFHP-EXSY spectrum demonstrated in Figure 8-3a. The dramatic cross-peak signal enhancement of IFHP 2D-EXSY in  $\text{Ga}_{10}$  nanotubes is in good qualitative agreement with the 2D spectra of AV presented in Chapter 7.<sup>248</sup>

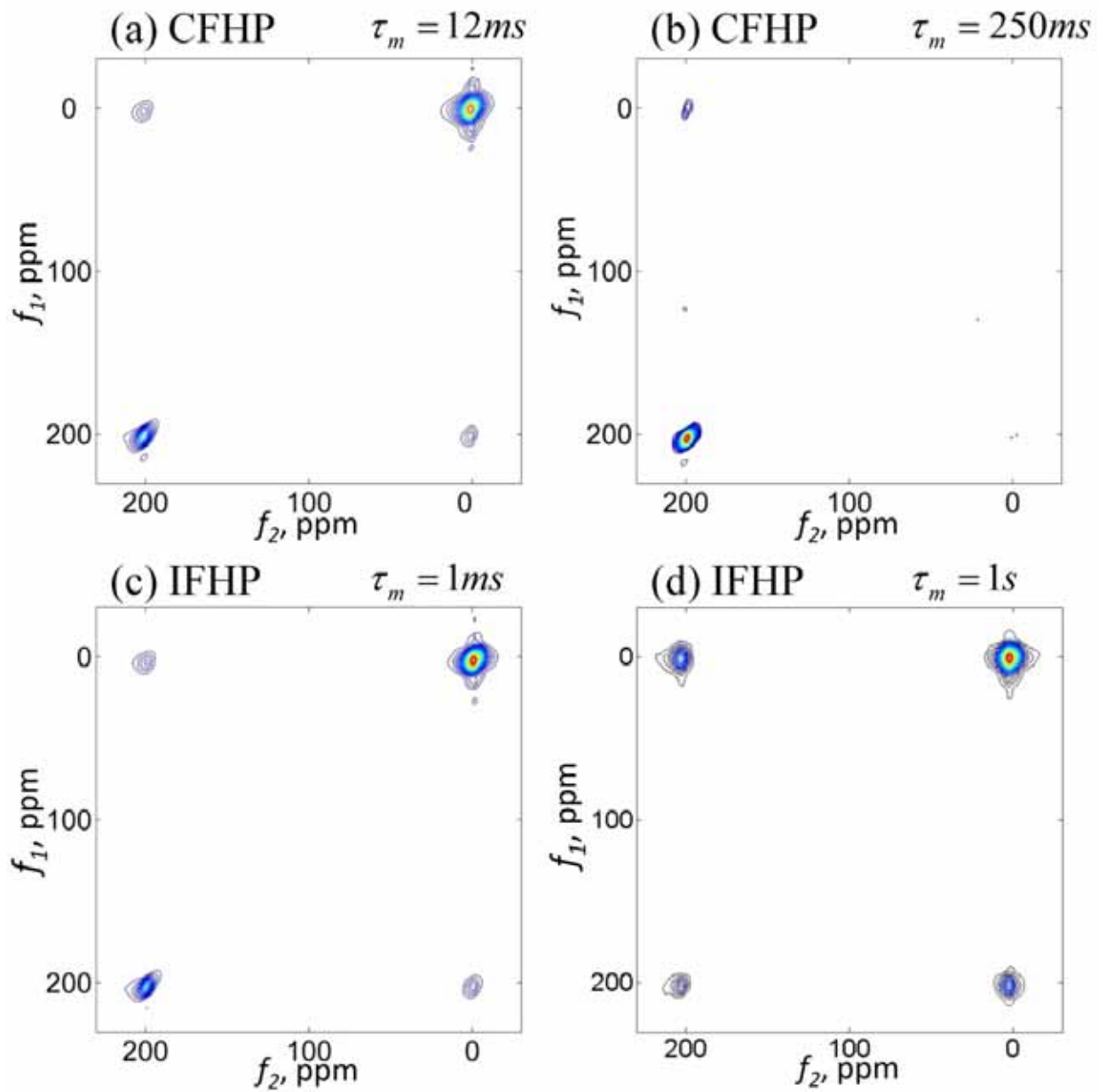
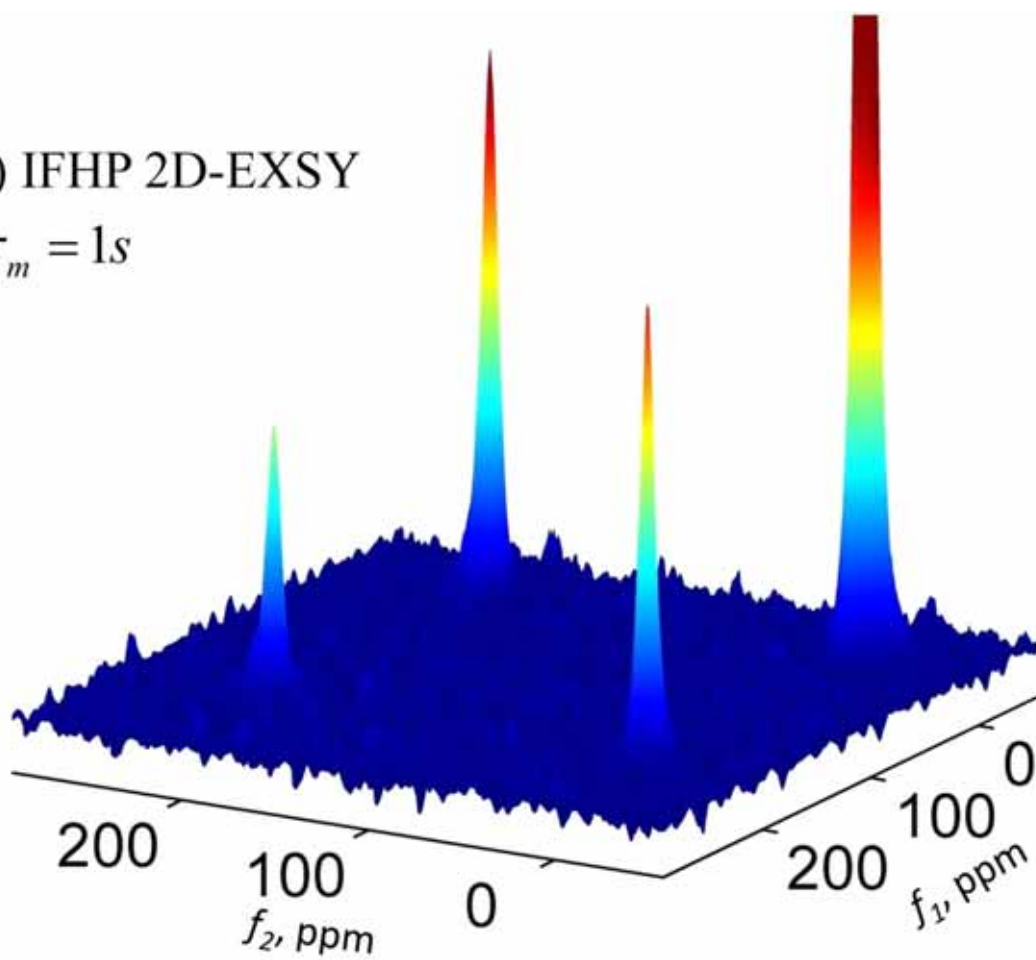


Figure 8-2. Hyperpolarized  $^{129}\text{Xe}$  2D-EXSY spectra in (a)(b) continuous-flow and (c)(d) interrupted-flow modes in  $\text{Ga}_{10}$  nanotubes at  $25^\circ\text{C}$  at different mixing times.

(a) IFHP 2D-EXSY

$$\tau_m = 1s$$



(b) CFHP 2D-EXSY

$$\tau_m = 250ms$$

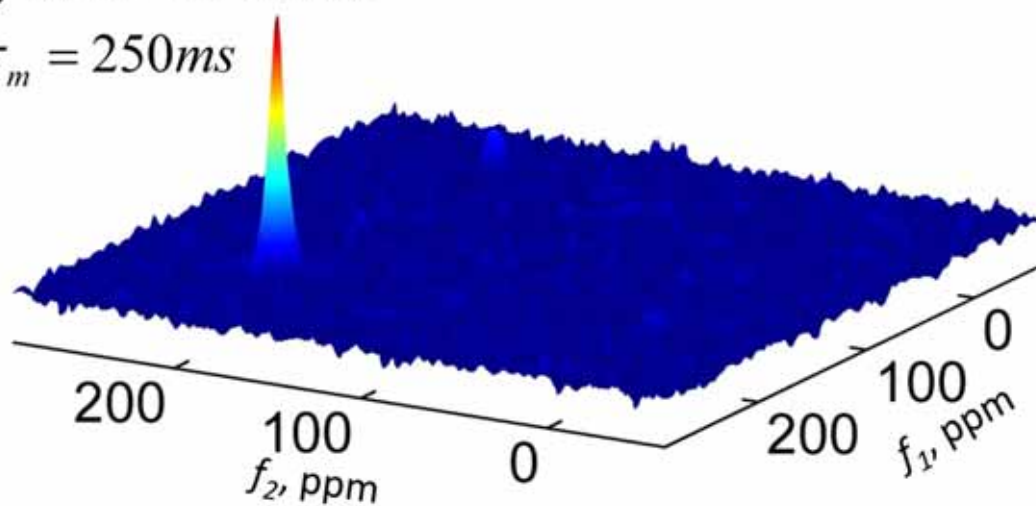


Figure 8-3. 3D representations of HP 2D-EXSY spectra of Xe in Ga<sub>10</sub> nanotubes at 25 °C, acquired in (a) IF mode and (b) CF mode. The mixing times are indicated. The gas peak in (a) was truncated to facilitate comparison of the cross-peaks in each spectrum.

The mixing-time dependences of the diagonal- and cross-peak signals of CFHP 2D-EXSY in Ga<sub>10</sub> nanotubes at 25 °C, along with the least-squares fits of Eq. (6-8) - (6-11), are presented in Figure 8-4. For the diagonal peaks in Figure 8-4a and b, a bi-exponential function yielded better fits than a mono-exponential decay, which was also the case for the least-squares fits to the diagonal-peak  $\tau_m$ -dependence in the CFHP 2D-EXSY experiment in AV.<sup>246</sup> To compare the exchange kinetic models of 2D-EXSY in CF and IF modes, the mean desorption rate  $\overline{k_d}$  in Ga<sub>10</sub> nanotubes was determined by non-linear regression analysis of the cross peaks in CFHP and IFHP 2D-EXSY. The results are summarized in Table 8-1. The  $\overline{k_d}$  in Ga<sub>10</sub> nanotubes at 25 °C determined by gas→channel and channel→gas cross-peak signals of CFHP 2D-EXSY are  $10.26 \pm 0.51 \text{ s}^{-1}$  and  $14.76 \pm 1.40 \text{ s}^{-1}$ , respectively. From the Xe isotropic spectral line-shapes reported in Chapter 5, Xe in Ga<sub>10</sub> nanotubes is more mobile than in AV nanotubes. A possible explanation for the higher exchange rate is the larger inner diameter of Ga<sub>10</sub> nanotube in comparison to that of AV. More specifically, the estimated  $\overline{k_d}$  of Xe in Ga<sub>10</sub> nanotubes is about a factor of 2 to 5 greater than that in AV<sup>246</sup>, implying that Xe gas is more favorable to escape from Ga<sub>10</sub> than from AV channels. However, CFHP 2D-EXSY experiments in Ga<sub>10</sub> nanotubes were conducted in the temperature of 35 °C higher than in AV nanotubes. The higher Xe desorption rate in Ga<sub>10</sub> nanotubes may be due to the combinations of higher temperature and larger inner diameter in Ga<sub>10</sub> nanotubes.

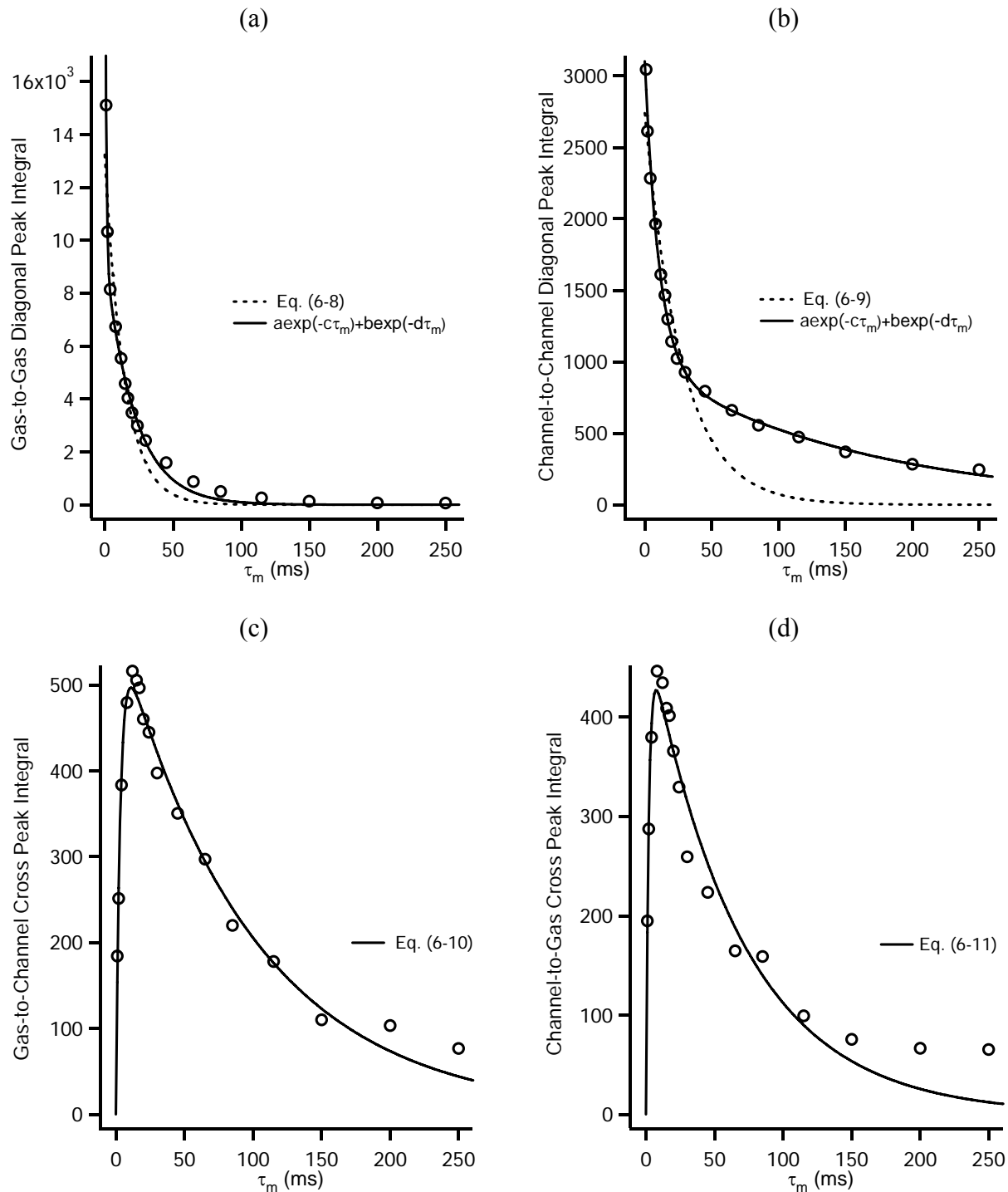


Figure 8-4. Mixing-time dependences of (a) gas-to-gas, (b) channel-to-channel diagonal-peak integral (c) gas-to-channel and (d) channel-to-gas cross-peak integrals in CFHP Xe 2D-EXSY spectra of Ga<sub>10</sub> nanotubes at 25 °C. The solid and dashed curves represent the least-squares fits to the functions given in the legend.

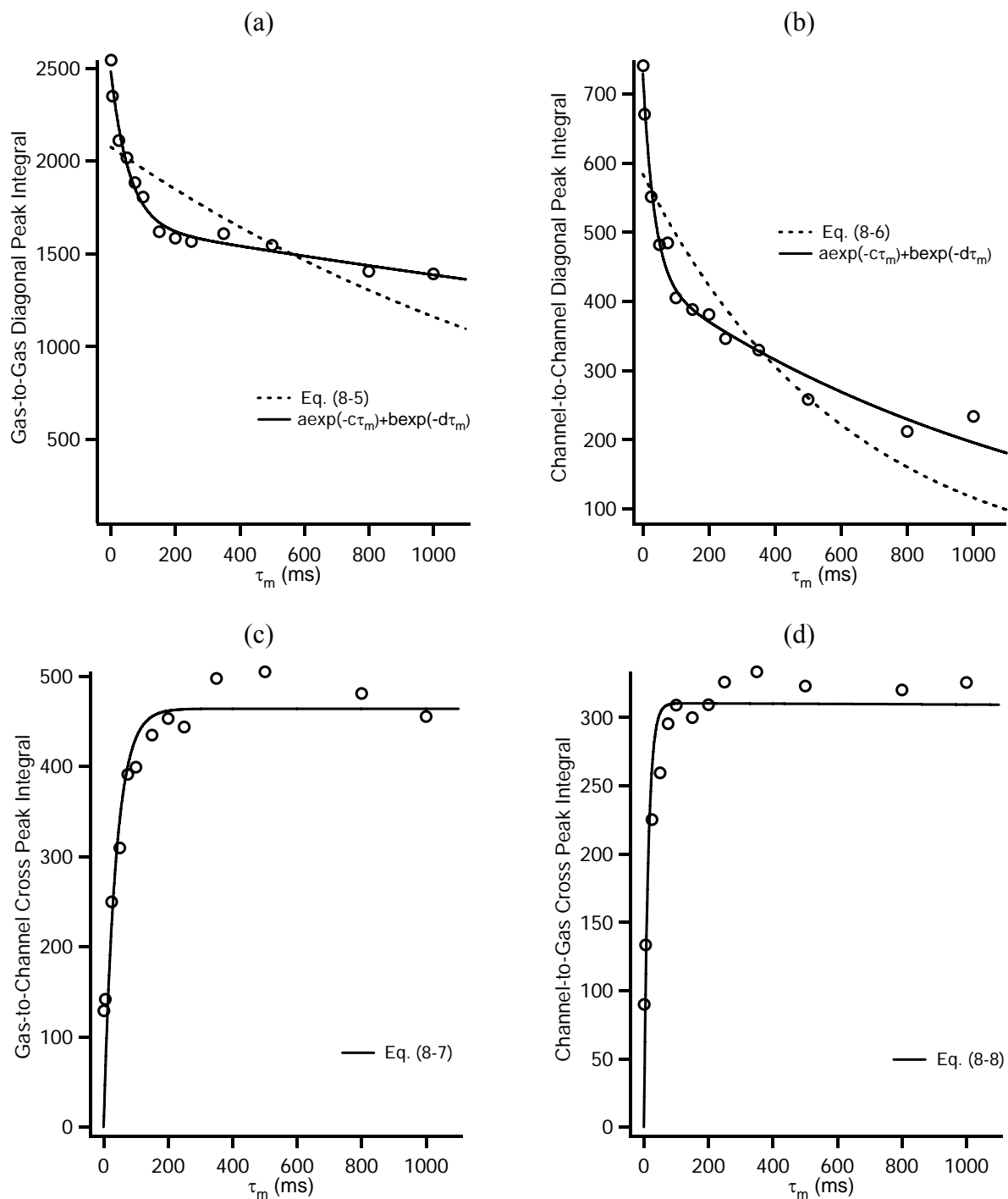


Figure 8-5. Mixing-time dependences of (a) gas-to-gas, (b) channel-to-channel diagonal-peak integral, (c) gas-to-channel, and (d) channel-to-gas cross-peak integrals in IFHP Xe 2D-EXSY spectra of Ga<sub>10</sub> nanotube at 25 °C. The solid and dashed curves represent the least-squares fits to the functions given in the legend.

Figure 8-5 presents the  $\tau_m$ -dependence of the diagonal- and cross-peak signals of IFHP 2D-EXSY in Ga<sub>10</sub> nanotubes at 25°C, associated with the least-squares fits of Eq. (8-5) - (8-8). As seen in Figure 8-5a, the gas diagonal-peak signal in the IFHP-EXSY spectrum drops rapidly between  $\tau_m = 0 \rightarrow 100\text{ms}$ , followed by a slow decay as  $\tau_m \geq 100\text{ms}$ . Eq. (8-5) predicted the  $\tau_m$ -dependence of the gas diagonal-peak signal to decay very slowly under the conditions of excess Xe gas and long Xe gaseous  $T_{1g}$  relaxation time. Such a slow decay of Eq. (8-5) was indeed observed for  $\tau_m \geq 100\text{ms}$  in the gas-phase diagonal peak, as shown in Figure 8-5a. In addition, in Figure 8-5b, the  $\tau_m$ -dependence of the diagonal-peak signals in Ga<sub>10</sub> nanotube phase exhibits a poor agreement to the mono-exponential function, Eq. (8-6). Once again, a rapid decay of diagonal-peak IFHP-EXSY signal of the nanotube phase appears at short mixing time,  $\tau_m = 0 \rightarrow 100\text{ms}$  (Figure 8-5b). The observed rapid decays in the gas and nanotube-phase diagonal peaks at short mixing time in the IFHP-EXSY experiment may be due to the following reasons: (1) longitudinal relaxation of Xe on the surface of the crystallites, where the Xe atoms are in fast exchange with Xe in gas and/or in nanotube phase. (2) Hyperpolarized Xe gas may drift or diffuse out of the detection region during the course of Xe exchange, since the hyperpolarized gas cannot be trapped completely within the sample space in the current setup. (3) Diffusion effects (single-file or normal) are not included in the simple two-site exchange model.

The desorption rates of IFHP 2D-EXSY were measured by the least-squares fits of gas $\rightarrow$ channel and channel $\rightarrow$ gas cross-peak intensities based on Eq. (8-7) and Eq. (8-8), respectively. In the least-squares fits of IFHP-EXSY,  $T_{1c}$  and  $n_c\theta/n_g$  are the fixed parameters, and two fit parameters (pre-exponential factor, and  $\overline{k_d}$ ) were varied freely. The determinations

of  $T_{1c}$  and  $n_c\theta/n_g$  are as follows: (1)  $T_{1c}$  relaxation time is determined from CFPSR experiments discussed in Chapter 4 and 5. For Xe in Ga<sub>10</sub> nanotubes at 80 mbar Xe pressure and 25 °C in 9.4T,  $T_{1c}$  is about 2.83±1.02 sec. (2) In the assumption of excess Xe gases in the sample space,  $n_c\theta/n_g \ll 1$ . The value of  $n_c\theta/n_g$  was varied from 0.01 to 0.0001 as a fixed input parameter in the fit, but less than a 0.05% difference was found on the fitted values of  $\overline{k_d}$ . Therefore, a fixed value of  $n_c\theta/n_g = 0.001$  was used in all subsequent fits.

The mean Xe desorption rate constants in Ga<sub>10</sub> nanotube at 25 °C estimated from least-squares fits to  $\tau_m$ -dependence of cross-peak integrals in CFHP and IFHP 2D-EXSY are summarized in Table 8-1. In comparing the CFHP and IFHP 2D-EXSY in Ga<sub>10</sub> nanotubes, the desorption rates measured by IFHP-EXSY are about a factor of 2 to 7 higher than in CFHP EXSY. Since the exchange time in IF mode was monitored over a range which was about an order of magnitude longer than in CF mode, the desorption rates determined by IFHP 2D-EXSY should be expected to be more accurate. However, it should be noted that diffusion effects, re-adsorption effects and the drift of gas out of the detected volume are not considered by either model and will in general limit the accuracy of rate constant determination by either technique. One or more of these effects may also explain the observed asymmetry of the desorption rates for the gas-to-channel and channel-to-gas exchange processes.

Table 8-1. Kinetic parameters of Ga<sub>10</sub> nanotubes in CFHP and IFHP 2D-EXSY at 25 °C. Uncertainties represent 95% confidence intervals.

EXSY	gas-to-channel		channel-to-gas	
	$\overline{k_d}$ (s <sup>-1</sup> )	$\tau_R$ (ms)	$\overline{k_d}$ (s <sup>-1</sup> )	$\tau_R$ (ms)
CFHP	10.26±0.51	3.06±0.49	14.76±1.40	2.04±0.60
IFHP*	26.13±12.03	---	71.17±41.40	---

\*  $n_c\theta/n_g = 0.001$  and  $T_{1c} = 2.83$  s were used in the fits of IFHP 2D-EXSY

## 8.5 Conclusions

The gas exchange kinetics in Ga<sub>10</sub> wheel nanotubes have been investigated by CFHP and IFHP 2D-EXSY. The mean Xe desorption rate  $\overline{k_d}$  of Ga<sub>10</sub> nanotubes at 25 °C estimated from non-linear least-squares fits of CFHP 2D-EXSY are relatively larger than  $\overline{k_d}$  of AV at -10 °C. The increase of  $\overline{k_d}$  in Ga<sub>10</sub> nanotubes may result from the larger channel diameter and/or higher temperature. As noted previously, the adsorption rate in the diffusion-limited regime depends on the occupancy of Xe atoms in the channels. Since the Xe occupancy in Ga<sub>10</sub> nanotubes is unknown, the temperature effect on the gas desorption cannot be excluded. If Xe desorption in Ga<sub>10</sub> nanotubes is diffusion-limited, the effect of the channel diameter on the gas desorption should be more pronounced than the effect of temperature.

IFHP 2D-EXSY has yielded dramatic cross-peak signal enhancement in Ga<sub>10</sub> nanotubes. The quantitative expressions of mixing-time dependences of IFHP 2D-EXSY with finite  $T_{1c}$  relaxation time have been derived, assuming Langmuir adsorption and excess Xe gas in sample space. The estimated mean desorption rates in CFHP and IFHP 2D-EXSY should be self-consistent. However, the desorption rates of IFHP 2D-EXSY in Ga<sub>10</sub> nanotubes were found to have large uncertainties, which are mostly due to the large fluctuations of the cross-peak intensities at long mixing times. The differences in the extracted rates may be due to one or more of the following effects which are not considered in the present exchange kinetic model: gas

diffusion, re-adsorption, and Xe gas drift out of detection region during gas interruption. Further improvement in the experimental technique could be achieved by replacing the single solenoid valve in our current setup with two non-magnetic pitch valves located close to the inlet and outlet of the sample holder. By closing both pitch valves simultaneously, the hyperpolarized gas will be trapped more completely within the sample space, thereby mitigating the loss of signal due to diffusion or drift out of the detection region.

While the mixing-time dependence of IFHP-EXSY in the  $\tau_m > T_{1c}$  regime has been demonstrated in Ga<sub>10</sub> nanotubes, such a study would be impractical in a system with a long  $T_{1c}$  relaxation time, such as in AV. Recently, several works regarding accelerating the acquisition of multi-dimensional NMR have been reported.<sup>249-252</sup> For example, Frydman *et al.* have demonstrated the possibility to combine the “single-scan” 2D NMR method with DNP, and the acquisition time of DNP-enhanced 2D NMR spectrum in liquid sample within ~0.1 sec has been presented.<sup>253</sup> Therefore, it would also be feasible to incorporate the fast acquisition NMR technique to IFHP-EXSY in order to reduce the instrumentation time required to obtain the kinetic information.

The present study provides an example of how CFSR and 2D-EXSY hyperpolarized <sup>129</sup>Xe NMR can be employed to explore the transport effects in 1D nanotube systems. In Chapter 5, the single-file diffusion behavior of Xe in Ga<sub>10</sub> nanotubes has been observed, and the corresponding  $T_{1c}$  relaxation time was obtained by CFSR. In this chapter, the average rate of Xe escape from Ga<sub>10</sub> nanotubes was quantitatively determined and the exchange process was traced in Ga<sub>10</sub> nanotubes by IFHP-EXSY. However, the investigation of the exchange process in nanotube systems using IFHP-EXSY demonstrated that the kinetic behaviors of Xe inside and outside the channels can be drastically different. For describing the completely exchange process during the

long exchange time in IFHP 2D-EXSY, the diffusion and gas re-adsorption effects may need to be incorporated into the kinetic models. In addition to 1D nanotube systems, this technique is potentially applicable to the quantitatively exchange kinetic studies on the *nm - μm* length scales, such as inter-crystalline or inter-particle exchange, in nanoporous materials by hyperpolarized  $^{129}\text{Xe}$  NMR.

## CHAPTER 9 CONCLUSIONS AND OUTLOOK

This dissertation has demonstrated the capability of exploring the adsorption and transport behaviors of adsorbates in the one-dimensional nanotube systems with different internal channel diameters by hyperpolarized  $^{129}\text{Xe}$  NMR. In addition to hyperpolarized  $^{129}\text{Xe}$  NMR chemical shifts and spectral line-shape analysis, selective saturation-recovery and 2D exchange NMR experiments were subjected to magnetization exchange kinetic analysis to investigate the dynamic processes of guest molecules in 1D nanotube host systems. The Xe atom has a van der Waals diameter of 4.4 Å, and Xe chemical shift is well-known to be extremely sensitive to its local environment, resulting in a unique atomic probe in the nanoporous materials. The spin polarization of  $^{129}\text{Xe}$  gas can be enhanced to up to ~70 % by spin-exchange optical-pumping (SEOP), dramatically increasing NMR sensitivity. SEOP prepared  $^{129}\text{Xe}$  offers an approximate 10,000-70,000 fold sensitivity enhancement in comparison to thermally-polarized  $^{129}\text{Xe}$  NMR, providing a wide range of applications in nanoporous materials. In this dissertation, two types of 1D nanotube systems, L-alanyl-L-valine dipeptide nanotube (AV) and Ga-based wheel nanotubes ( $\text{Ga}_{10}$  and  $\text{Ga}_{18}$ ), with different channel diameters were utilized as model 1D systems. The inner diameters of AV,  $\text{Ga}_{10}$ , and  $\text{Ga}_{18}$  nanotubes are 5.13 Å, 8.1 Å and 10.4 Å, respectively.

### **Adsorption**

The Xe chemical shift anisotropy (CSA) spectral line-shape has been observed in AV nanotubes, whereas isotropic line-shapes have been exhibited in the  $\text{Ga}_{10}$  and  $\text{Ga}_{18}$  nanotubes. Anisotropic Xe NMR line-shapes in AV nanotubes can be characterized by an axially symmetric chemical shielding tensor, implying that the inner diameter of AV is on the same order of the van der Waals diameter of Xe atom. The sign inversion of the chemical shielding anisotropy with

increasing Xe occupancy in AV is well understood in terms of the competition between Xe-wall and Xe-Xe interactions which have opposite contributions to the shielding anisotropy. The isotropic Xe chemical shift is increased upon reducing the temperature in all three nanotube systems, which is the result of increasing the contribution of Xe-Xe interactions to the chemical shift tensor. Since the perpendicular component of the Xe chemical shielding tensor,  $\sigma_{\perp}$ , in AV nanotubes is most sensitive to Xe density and almost independent of temperature, it can be used to determine the Xe fractional occupancy  $\theta$  in AV nanotubes. The Xe chemical shifts were found to be almost independent of Xe pressures in Ga<sub>10</sub> and Ga<sub>18</sub> nanotubes at 25 °C, indicating that the Xe-wall interactions dominate the shielding in the gallic nanotubes. Since the channel diameters of Ga<sub>10</sub> and Ga<sub>18</sub> nanotubes are larger than that in AV nanotubes, and isotropic line-shapes, rather than an anisotropic chemical shift powder pattern, as in AV, have been observed in gallic nanotubes, it can be concluded that Xe is less motionally restricted in the gallic wheel nanotubes.

The Xe isosteric adsorption enthalpies ( $\Delta H_{a,\theta}$ ) in AV have been calculated at various Xe occupancies according to Clausius-Clapeyron equation. The increase in  $\Delta H_{a,\theta}$  with Xe occupancy is mainly attributed to the Xe-Xe interaction. The isosteric adsorption enthalpy of Xe in AV extracted to zero occupancy was determined to be -10 kJ/mol, which is consistent with the typical physisorption process. Furthermore, the exchange constant ( $K \equiv k_a/k_d$ ) of Xe in AV increased upon reducing the temperature, qualitatively implying the process of Xe adsorption in AV is more favorable at low temperature. However, the quantitative measurements of Xe adsorption enthalpy and exchange constant in AV were found to have large uncertainties, especially at high Xe occupancy. This could be due to the experimental errors of the Xe gas pressures in the gas handling system. The accuracy of the adsorption enthalpy and exchange

constant can be improved by using the pre-mixed Xe gas mixtures with accurately known Xe compositions.

In addition, the  $^{13}\text{C}$   $T_1$  relaxation times in AV nanotubes have been determined by solid-state inversion-recovery NMR experiments. The results show that the  $^{13}\text{C}$  of methyl groups on the channel interior, which is anticipated to be in direct dipolar contact with Xe in AV nanotubes, has short  $T_1$  relaxation time ( $366 \pm 76$  ms). The methyl group  $^{13}\text{C}$   $T_1$  is expected to be increased when Xe atoms accumulate into the channels. This information can be a resource for the future hyperpolarized  $^{129}\text{Xe} \rightarrow ^{13}\text{C}$  polarization transfer studies.

### **Diffusion**

The selective continuous-flow saturation-recovery (CFSR) hyperpolarized  $^{129}\text{Xe}$  NMR experiments have been carried out to explore the tracer exchange of hyperpolarized gas in 1D nanotube systems. The magnetization kinetic models of single-file diffusion (SFD) and normal 1D Fickian diffusion (ND) based on diffusion-limited Langmuir adsorption have been developed, and the quantitative expressions of magnetization recovery curves of SFD and ND have been presented. From the kinetic analysis of CFSR, Xe motion inside AV nanotubes clearly exhibited single-file diffusion behavior, especially at high Xe occupancy. The pre-factor terms of the saturation-recovery equations for SFD and ND,  $C_F$  and  $C_D$ , have been derived, and were found to be depended mainly on temperature, diffusivity, and Xe occupancy. The  $\theta$ -dependence of the experimentally measured coefficient  $C_F$  in AV is in good qualitatively agreement with the theoretical expression. The techniques have been further applied to the gallic-wheel nanotube systems,  $\text{Ga}_{10}$  and  $\text{Ga}_{18}$  nanotubes, with internal diameters greater than AV nanotubes. As in the Xe/AV systems, Xe in 8.1 Å  $\text{Ga}_{10}$  nanotubes exhibited single-file diffusion behavior, whereas normal 1D diffusion of Xe in 10.4 Å  $\text{Ga}_{18}$  nanotubes was explicitly observed. The cross-over of

the time-scaling from SFD to ND by varying the channel inner diameters in 1D nanotube systems has been apparently observed by CFSR hyperpolarized  $^{129}\text{Xe}$  NMR.

Recently, Takamizawa *et al.* have demonstrated the possibility to investigate the adsorptions of various guest adsorbates, such as water, Xe,  $\text{CH}_4$  and  $\text{CCl}_4$ , in the tris(ethylenediamine) cobalt (III) chloride ( $[\text{Co}^{\text{III}}(\text{en})_3] \text{Cl}_3$ ) channels with inner diameter of 5.7 Å by single-crystal Xe-ray diffraction analysis.<sup>254</sup> The channel architectures in the presence of gas adsorbates and the determination of positions of adsorbates inside the channels have been presented. The combination of CFSR and X-ray crystallography in the presence of gas molecules in nanotubes can provide a distinct understanding of dynamic processes in guest/host nanotube systems with variable size distributions.

### **Exchange**

In order to understand the complete transport process of adsorbates in the nanotubes, gas exchange in the vicinity of channel openings has been systematically investigated by CFHP 2D-EXSY. The exchange kinetic model based on diffusion-limited Langmuir adsorption has been proposed. The quantitative expressions for the mixing-time dependence of cross- and diagonal-peak integrals have been derived, assuming excess Xe gas and long  $^{129}\text{Xe}$   $T_1$  relaxation time in the sample space. From the least-squares fits of the expressions to the CFHP 2D-EXSY datasets, the mean desorption rates of Xe ( $\overline{k_d}$ ) in AV nanotubes was quantitatively determined. The  $\overline{k_d}$  was shown to decrease with increasing Xe occupancy, which is in good agreement with the approximation of diffusion-limited Langmuir adsorption.

The cross-peak intensities in 2D-EXSY were found to be strongly attenuated by the finite gas residence time in the sample space under the continuous-flow condition. The issue of how hyperpolarized NMR signal is affected by the gas flow rate has not been noticed until recently,

by us. We demonstrated that it is feasible to significantly enhance the cross-peak intensities represented gas exchange between adsorbed sites and gas phase in 2D-EXSY by momentarily interrupted the gas flow during the exchange time of 2D-EXSY pulse sequence. In AV nanotubes, a factor of ~60 signal enhancement of cross-peak intensities in IFHP-EXSY has been achieved, providing a greatly promising technique to probe slow exchange process by hyperpolarized  $^{129}\text{Xe}$  2D-EXSY NMR. Furthermore, the mixing-time dependence of IFHP-EXSY has been demonstrated in  $\text{Ga}_{10}$  nanotubes at room temperature. The corresponding magnetization exchange kinetic analysis of IFHP-EXSY in the  $\tau_m > T_{1c}$  regime has been presented. However, the mean desorption rate in  $\text{Ga}_{10}$  nanotubes measured from 2D-EXSY in IF mode is about a factor of 2 to 7 greater than  $\overline{k_d}$  in CF mode. It can be due to the factors such as diffusion, gas re-adsorption, or gas drift out of detection region which are not considered in the simplified kinetic model during the relatively longer exchange time in IFHP-EXSY. Further improvement can be made by refining the experiments in the aspect of preventing the hyperpolarized Xe gas drift out of the detection coil region during the duration of the gas interruption.

In this dissertation, the fundamental aspects as well as the potential applications of hyperpolarized  $^{129}\text{Xe}$  NMR have been presented. This work gives access to a wide range of future utilizations in diverse fields of materials and biological sciences. The advantages presented herein, such as NMR sensitivity enhancement, the sensitivity to the local environment, capability to probe slow exchange process, and the possibility of time-resolved quantitatively kinetic measurements in 1D nanotube systems fulfill the requirements of investigations of the thermodynamics, chemical exchange and diffusions of guest/host chemistry.

APPENDIX A  
DERIVATION OF AVERAGE ZEEMAN ORDER IN NANOTUBE PHASE BY GAMMA  
FUNCTION IDENTITIES

We start from the Eq. (4-14) in Chapter 4

$$\overline{I_{zc}}(\tau) = \frac{I_{zi}}{L} \int_0^L \frac{k_d}{k_d + T_{lc}^{-1}} \left[ 1 - \exp\left(-\left(k_d + T_{lc}^{-1}\right)\tau\right) \right] d\bar{z} \quad (\text{A-1})$$

For simplification, let  $k_d \approx (F/\pi)^2 / \langle z^2 \rangle^2 \rightarrow a/r^4$ , where  $a = (F/\pi)^2$  and  $b = T_{lc}^{-1}$ , and assume the long channel limit, where  $(a/b)^{1/4} \ll L$ . Therefore, Eq. (A-1) can be rewritten

$$\overline{I_{zc}}(\tau) = \frac{I_{zi}}{L} \int_0^\infty \frac{a/r^4}{a/r^4 + b} \left[ 1 - \exp\left(-\left(a/r^4 + b\right)\tau\right) \right] dr \quad (\text{A-2})$$

Evaluate the integration in Eq. (A-2)

$$\begin{aligned} \frac{\overline{I_{zc}}(\tau)}{I_{zi}/L} &= \int_0^\infty \frac{a/r^4}{a/r^4 + b} \left[ 1 - \exp\left(-\left(a/r^4 + b\right)\tau\right) \right] dr \\ &= \frac{1}{16} \left(\frac{a}{b}\right)^{1/4} \left( 4\sqrt{2}\pi + \Gamma\left(-\frac{1}{4}\right) \Gamma\left(\frac{1}{4}, b\tau\right) \right) \\ &= \frac{1}{16} \left(\frac{a}{b}\right)^{1/4} \left( 4\sqrt{2}\pi + \Gamma\left(-\frac{1}{4}\right) \Gamma\left(\frac{1}{4}\right) \mathcal{Q}\left(\frac{1}{4}, b\tau\right) \right) \\ &= \frac{1}{16} \left(\frac{a}{b}\right)^{1/4} \left( 4\sqrt{2}\pi + \Gamma\left(-\frac{1}{4}\right) \Gamma\left(\frac{1}{4}\right) \left(1 - P\left(\frac{1}{4}, b\tau\right)\right) \right) \\ &= \frac{1}{16} \left(\frac{a}{b}\right)^{1/4} \left( 4\sqrt{2}\pi + \Gamma\left(-\frac{1}{4}\right) \Gamma\left(\frac{1}{4}\right) \left(1 - \frac{\gamma\left(\frac{1}{4}, b\tau\right)}{\Gamma\left(\frac{1}{4}\right)}\right) \right) \end{aligned} \quad (\text{A-3})$$

where the regularized gamma functions are defined as

$$P(c, x) \equiv \gamma(c, x) / \Gamma(c) \quad (\text{A-4})$$

$$Q(c, x) \equiv \Gamma(c, x) / \Gamma(c) \quad (\text{A-5})$$

$$P(c, x) + Q(c, x) \equiv 1 \quad (\text{A-6})$$

From the identity for the gamma function,

$$\Gamma\left(-\frac{1}{4}\right)\Gamma\left(\frac{1}{4}\right) = \frac{-\pi}{(1/4)\sin(\pi/4)} \quad (\text{A-7})$$

Thus, Eq. (A-2) yields

$$\begin{aligned} \frac{\overline{I_{zc}}(\tau)}{I_{zi}/L} &= \frac{1}{16} \left(\frac{a}{b}\right)^{1/4} \left( 4\sqrt{2}\pi - \frac{\pi}{(1/4)\sin(\pi/4)} \left( 1 - \frac{\gamma\left(\frac{1}{4}, b\tau\right)}{\Gamma\left(\frac{1}{4}\right)} \right) \right) \\ &= \frac{1}{16} \left(\frac{a}{b}\right)^{1/4} \left( 4\sqrt{2}\pi - 4\sqrt{2}\pi \left( 1 - \frac{\gamma\left(\frac{1}{4}, b\tau\right)}{\Gamma\left(\frac{1}{4}\right)} \right) \right) \\ &= \frac{\sqrt{2}\pi}{4} \left(\frac{a}{b}\right)^{1/4} \Gamma^{-1}\left(\frac{1}{4}\right) \cdot \gamma\left(\frac{1}{4}, b\tau\right) \\ &= \frac{\sqrt{2}\pi}{4} \left(\frac{a}{b}\right)^{1/4} \Gamma^{-1}\left(\frac{1}{4}\right) \cdot \int_0^{b\tau} \tau^{-3/4} e^{-\tau} d\tau \end{aligned} \quad (\text{A-8})$$

where the incomplete gamma function is  $\gamma(c, x) \equiv \int_0^x t^{c-1} e^{-t} dt$ . To substitute the variable from  $\tau$

to  $u$  in Eq. (A-8), we assume  $\tau = ub$ ; thus,  $d\tau = bdu$

$$\begin{aligned} \frac{\overline{I_{zc}}(t)}{I_{zi}/L} &= \frac{\sqrt{2}\pi}{4} \left(\frac{a}{b}\right)^{1/4} \Gamma^{-1}\left(\frac{1}{4}\right) \cdot b \int_0^{b\tau} (bu)^{-3/4} e^{-bu} du \\ &= \frac{\sqrt{2}\pi}{4} (a)^{1/4} \Gamma^{-1}\left(\frac{1}{4}\right) \cdot \int_0^{b\tau} u^{-3/4} e^{-bu} du \end{aligned} \quad (\text{A-9})$$

Plugging  $a = (F/\pi)^2$  and  $b = T_{1c}^{-1}$  into Eq. (A-9) yields

$$\begin{aligned} \frac{\overline{I_{zc}}(t)}{I_{zi}/L} &= \frac{\sqrt{2}\pi}{4} \left(\frac{F}{\pi}\right)^{1/2} \Gamma^{-1}\left(\frac{1}{4}\right) \cdot \int_0^{\tau} u^{-3/4} e^{-u/T_{1c}} du \\ &= \frac{\sqrt{\pi F}}{2^{3/2}} \cdot \Gamma^{-1}\left(\frac{1}{4}\right) \cdot \int_0^{\tau} u^{-3/4} e^{-u/T_{1c}} du \end{aligned} \quad (\text{A-10})$$

Finally, Eq. (4-15) is obtained

$$\bar{I}_{zc}(\tau) \approx I_{zi} \frac{\sqrt{\pi F}}{2^{3/2} L \Gamma(1/4)} \int_0^\tau t^{-3/4} e^{-t/T_c} dt \quad (\text{A-11})$$

APPENDIX B  
MATRIX FORMULATION FOR TWO-SITE EXCHANGE SYSTEM

As discussed in Section 6.1, the  $\tau_m$ - dependence of diagonal- and cross-peak intensities can be solved by the matrix representation. Here we take an example of time dependences of cross-peak intensities in the limit of  $\tau_m > T_{1c}$  (Section 8.3). The rate equations of magnetizations in gas and nanotube phase under interrupted-flow condition are

$$\frac{dM_g}{dt} = -k_d \frac{n_c \theta}{n_g} M_g + k_d M_c \quad (\text{B-1})$$

$$\frac{dM_c}{dt} = k_d \frac{n_c \theta}{n_g} M_g - k_d M_c - \frac{M_c}{T_{1c}} \quad (\text{B-2})$$

The identical matrix representation of the rate equations is

$$\frac{d}{dt} \begin{pmatrix} M_g(\tau_m) \\ M_c(\tau_m) \end{pmatrix} = \mathfrak{R} \begin{pmatrix} M_g(\tau_m) \\ M_c(\tau_m) \end{pmatrix} \quad (\text{B-3})$$

$$\text{where } \mathfrak{R} = \begin{pmatrix} -k_d \frac{n_c \theta}{n_g} & k_d \\ k_d \frac{n_c \theta}{n_g} & -k_d - T_{1c}^{-1} \end{pmatrix} \quad (\text{B-4})$$

Eq. (B-3) can be rewritten as

$$\mathfrak{I}(\tau_m) = \exp(-\mathfrak{R} \tau_m) \mathfrak{I}(0) \quad (\text{B-5})$$

$\mathfrak{I}$  is a matrix which contains information of diagonal and cross-peak intensities in 2D-EXSY.

The solution to Eq. (B-5) can be performed according the eigenvalue-eigenvector method.<sup>58</sup>

$$\mathfrak{I}(\tau_m) = X \cdot \exp[-D\tau_m] \cdot X^{-1} \cdot \mathfrak{I}(0) \quad (\text{B-6})$$

$$\text{where } \mathfrak{I}(\tau_m) = \begin{pmatrix} M_{g \rightarrow g} + M_{g \rightarrow c} \\ M_{c \rightarrow g} + M_{c \rightarrow c} \end{pmatrix} \quad (\text{B-7})$$

where  $D$  is a diagonal matrix with eigenvalues of  $\mathfrak{R}$ . The  $X$  and its inverse  $X^{-1}$  are eigenvectors of  $\mathfrak{R}$ . Solving Eq. (B-6), the integrated intensities of cross peaks can be obtained:

$$M_{g \rightarrow c} = M_g^0 \frac{(1 - n_c \theta / n_c) k_d + T_{1c}^{-1} + \chi'}{2\chi'} \left\{ e^{-\frac{1}{2} \left( \left( 1 + \frac{n_c \theta}{n_c} \right) k_d + T_{1c}^{-1} - \chi' \right) \tau_m} - e^{-\frac{1}{2} \left( \left( 1 + \frac{n_c \theta}{n_c} \right) k_d + T_{1c}^{-1} + \chi' \right) \tau_m} \right\} \quad (\text{B-8})$$

$$M_{c \rightarrow g} = M_c^0 \frac{(-1 + n_c \theta / n_c) k_d - T_{1c}^{-1} + \chi'}{2\chi'} \left\{ e^{-\frac{1}{2} \left( \left( 1 + \frac{n_c \theta}{n_c} \right) k_d + T_{1c}^{-1} - \chi' \right) \tau_m} - e^{-\frac{1}{2} \left( \left( 1 + \frac{n_c \theta}{n_c} \right) k_d + T_{1c}^{-1} + \chi' \right) \tau_m} \right\} \quad (\text{B-9})$$

where  $\lambda' = \sqrt{-4 \frac{n_c \theta}{n_g} k_d T_{1c}^{-1} + \left[ \left( 1 + \frac{n_c \theta}{n_g} \right) k_d + T_{1c}^{-1} \right]^2}$

In the assumption of excess gases in the sample space,  $\frac{n_c \theta}{n_g} \ll 1$ , Eq. (B-8) and Eq. (B-9) yield

$$M_{g \rightarrow c} \cong M_g^0 \frac{k_d + T_{1c}^{-1} + \chi}{2\chi} \left\{ e^{-\frac{1}{2} (k_d + T_{1c}^{-1} - \chi) \tau_m} - e^{-\frac{1}{2} (k_d + T_{1c}^{-1} + \chi) \tau_m} \right\} \quad (\text{B-10})$$

$$M_{c \rightarrow g} \cong M_c^0 \frac{-k_d - T_{1c}^{-1} + \chi}{2\chi} \left\{ e^{-\frac{1}{2} (k_d + T_{1c}^{-1} - \chi) \tau_m} - e^{-\frac{1}{2} (k_d + T_{1c}^{-1} + \chi) \tau_m} \right\} \quad (\text{B-11})$$

where  $\lambda = \sqrt{-4 \frac{n_c \theta}{n_g} k_d T_{1c}^{-1} + (k_d + T_{1c}^{-1})^2}$

## LIST OF REFERENCES

- (1) Kärger, J.; Ruthven, D. M. *Diffusion in Zeolites and Other Microporous Solids*; Wiley, 1992.
- (2) Goodson, B. M. *Journal of Magnetic Resonance* **2002**, *155*, 157.
- (3) Jameson, C. J.; Jameson, A. K.; Gerald, R. E.; Lim, H. M. *Journal of Physical Chemistry B* **1997**, *101*, 8418.
- (4) Springuel-Huet, M. A.; Nosov, A.; Kärger, J.; Fraissard, J. *Journal of Physical Chemistry*
- (5) Moudrakovski, I. L.; Ratcliffe, C. I.; Ripmeester, J. A. *Applied Magnetic Resonance* **1995**, *8*, 385.
- (6) Jameson, A. K.; Jameson, C. J.; de Dios, A. C.; Oldfield, E.; Gerald, R. E.; Turner, G. L. *Solid State Nuclear Magnetic Resonance* **1995**, *4*, 1.
- (7) Springuel-Huet, M. A.; Fraissard, J. P. *Zeolites* **1992**, *12*, 841.
- (8) Jameson, C. J.; Jameson, A. K.; Gerald, R.; de Dios, A. C. *Journal of Chemical Physics* **1992**, *96*, 1690.
- (9) Fraissard, J.; Ito, T. *Zeolites* **1988**, *8*, 350.
- (10) Johnson, D. W.; Griffiths, L. *Zeolites* **1987**, *7*, 484.
- (11) Scharpf, E. W.; Crecey, R. W.; Gates, B. C.; Dybowski, C. *Journal of Physical Chemistry* **1986**, *90*, 9.
- (12) Ito, T.; Fraissard, J. *Journal of Chemical Physics* **1982**, *76*, 5225.
- (13) Simonutti, R.; Bracco, S.; Comotti, A.; Mauri, M.; Sozzani, P. *Chemistry of Materials* **2006**, *18*, 4651.
- (14) Raftery, D.; Reven, L.; Long, H.; Pines, A.; Tang, P.; Reimer, J. A. *Journal of Physical Chemistry* **1993**, *97*, 1649.
- (15) Walton, J. H.; Miller, J. B.; Roland, C. M. *Journal of Polymer Science Part B-Polymer Physics* **1992**, *30*, 527.
- (16) Raftery, D.; Long, H.; Meersmann, T.; Grandinetti, P. J.; Reven, L.; Pines, A. *Physical Review Letters* **1991**, *66*, 584.
- (17) Kennedy, G. J. *Polymer Bulletin* **1990**, *23*, 605.
- (18) Stengle, T. R.; Williamson, K. L. *Macromolecules* **1987**, *20*, 1428.
- (19) Jameson, C. J.; de Dios, A. C. *Journal of Chemical Physics* **2002**, *116*, 3805.

- (20) Sozzani, P.; Comotti, A.; Simonutti, R.; Meersmann, T.; Logan, J. W.; Pines, A. *Angewandte Chemie-International Edition* **2000**, *39*, 2695.
- (21) Moudrakovski, I.; Soldatov, D. V.; Ripmeester, J. A.; Sears, D. N.; Jameson, C. J. *Proceedings of the National Academy of Sciences of the United States of America* **2004**, *101*, 17924.
- (22) Comotti, A.; Bracco, S.; Ferretti, L.; Mauri, M.; Simonutti, R.; Sozzani, P. *Chemical Communications* **2007**, 350.
- (23) Jameson, C. J. *Journal of Chemical Physics* **2002**, *116*, 8912.
- (24) Meersmann, T.; Logan, J. W.; Simonutti, R.; Caldarelli, S.; Comotti, A.; Sozzani, P.; Kaiser, L. G.; Pines, A. *Journal of Physical Chemistry A* **2000**, *104*, 11665.
- (25) Berthault, P.; Huber, G.; Ha, P. T.; Dubois, L.; Desvaux, H.; Guittet, E. *Chembiochem* **2006**, *7*, 59.
- (26) Lowery, T. J.; Garcia, S.; Chavez, L.; Ruiz, E. J.; Wu, T.; Brotin, T.; Dutasta, J. P.; King, D. S.; Schultz, P. G.; Pines, A.; Wemmer, D. E. *Chembiochem* **2006**, *7*, 65.
- (27) Brunner, E. *Protein Science* **2005**, *14*, 847.
- (28) Dubois, L.; Da Silva, P.; Landon, C.; Huber, J. G.; Ponchet, M.; Vovelle, F.; Berthault, P.; Desvaux, H. *Journal of the American Chemical Society* **2004**, *126*, 15738.
- (29) Locci, E.; Casu, M.; Saba, G.; Lai, A.; Reisse, J.; Bartik, K. *Chemphyschem* **2002**, *3*, 812.
- (30) Locci, E.; Dehouck, Y.; Casu, M.; Saba, G.; Lai, A.; Luhmer, M.; Reisse, J.; Bartik, K. *Journal of Magnetic Resonance* **2001**, *150*, 167.
- (31) Bowers, C. R.; Storhaug, V.; Webster, C. E.; Bharatam, J.; Cottone, A.; Gianna, R.; Betsey, K.; Gaffney, B. J. *Journal of the American Chemical Society* **1999**, *121*, 9370.
- (32) Tallavaara, P.; Telkki, V. V.; Jokisaari, J. *Journal of Physical Chemistry B* **2006**, *110*, 21603.
- (33) Tallavaara, P.; Jokisaari, J. *Physical Chemistry Chemical Physics* **2006**, *8*, 4902.
- (34) Jagadeesh, B.; Prabhakar, A.; Rao, M. H. V. R.; Murty, C. V. S.; Pisipati, V. G. K. M.; Kunwar, A. C.; Bowers, C. R. *Journal of Physical Chemistry B* **2004**, *108*, 11272.
- (35) Zook, A. L.; Adhyaru, B. B.; Bowers, C. R. *Journal of Magnetic Resonance* **2002**, *159*, 175.
- (36) King, P.; Stamatatos, T. C.; Abboud, K. A.; Christou, G. *Angewandte Chemie-International Edition* **2006**, *45*, 7379.

- (37) Schmidt-Rohr, K.; Spiess, H. W. *Multidimensional Solid-State NMR and Polymers*; Academic Press, 1994.
- (38) Ernst, R. R.; Bodenhausen, G.; Wokaun, A. *Principles of Nuclear Magnetic Resonance in One and Two Dimensions*; University Press, 1987.
- (39) Levitt, M. H. *Spin Dynamics: Basics of Nuclear Magnetic Resonance*; John Wiley & Sons, 2001.
- (40) Bloch, F. *Physical Review* **1946**, *70*, 460.
- (41) Purcell, E. M.; Torrey, H. C.; Pound, R. V. *Physical Review* **1946**, *69*, 37.
- (42) Stejskal, E. O.; Memory, J. D. *High Resolution NMR in the Solid State: Fundamentals of CP/MAS*; University Press, 1994.
- (43) Styles, P.; Soffe, N. F.; Scott, C. A.; Cragg, D. A.; Row, F.; White, D. J.; White, P. C. J. *Journal of Magnetic Resonance* **1984**, *60*, 397.
- (44) Orendt, A. M.; Facelli, J. C.; Jiang, Y. J.; Grant, D. M. *Journal of Physical Chemistry A* **1998**, *102*, 7692.
- (45) Carravetta, M.; Johannessen, O. G.; Levitt, M. H.; Heinmaa, I.; Stern, R.; Samoson, A.; Horsewill, A. J.; Murata, Y.; Komatsu, K. *Journal of Chemical Physics* **2006**, *124*.
- (46) Carravetta, M.; Danquigny, A.; Mamone, S.; Cuda, F.; Johannessen, O. G.; Heinmaa, I.; Panesar, K.; Stern, R.; Grossel, M. C.; Horsewill, A. J.; Samoson, A.; Murata, M.; Murata, Y.; Komatsu, K.; Levitt, M. H. *Physical Chemistry Chemical Physics* **2007**, *9*, 4879.
- (47) Medek, A.; Olejniczak, E. T.; Meadows, R. P.; Fesik, S. W. *Journal of Biomolecular NMR* **2000**, *18*, 229.
- (48) Dalvit, C.; Mongelli, N.; Papeo, G.; Giordano, P.; Veronesi, M.; Moskau, D.; Kummerle, R. *Journal of the American Chemical Society* **2005**, *127*, 13380.
- (49) Keun, H. C.; Beckonert, O.; Griffin, J. L.; Richter, C.; Moskau, D.; Lindon, J. C.; Nicholson, J. K. *Analytical Chemistry* **2002**, *74*, 4588.
- (50) Jameson, C. J. *Annual Review of Physical Chemistry* **1996**, *47*, 135.
- (51) Jameson, C. J. *Solid State Nuclear Magnetic Resonance* **1998**, *11*, 265.
- (52) Rose, M. E. *Elementary Theory of Angular Momentum*; Wiley: New York, 1957.
- (53) Gutowsky, H. S.; Holm, C. H. *Journal of Chemical Physics* **1956**, *25*, 1228.
- (54) Stewart, W. E.; Siddall, T. H. *Chemical Reviews* **1970**, *70*, 517.
- (55) Caravatti, P.; Levitt, M. H.; Ernst, R. R. *Journal of Magnetic Resonance* **1986**, *68*, 323.

- (56) Bellon, S. F.; Chen, D.; Johnston, E. R. *Journal of Magnetic Resonance* **1987**, *73*, 168.
- (57) Jeener, J.; Meier, B. H.; Bachmann, P.; Ernst, R. R. *Journal of Chemical Physics* **1979**, *71*, 4546.
- (58) Perrin, C. L.; Dwyer, T. J. *Chemical Reviews* **1990**, *90*, 935.
- (59) Slichter, C. P. *Principles of Magnetic Resonance*; Springer Verlag, 1996.
- (60) Keeler, J. *Understanding NMR Spectroscopy*; Wiley, 2005.
- (61) Holden, N. E. Table of the Isotopes. In *CRC Handbook of Chemistry and Physics*; 86th ed.; Lide, D. R., Ed.; CRC Press: Cleveland, Ohio, 2005; Vol. 11.
- (62) Cleveland, Z. I.; Stupic, K. F.; Pavlovskaya, G. E.; Repine, J. E.; Wooten, J. B.; Meersmann, T. *Journal of the American Chemical Society* **2007**, *129*, 1784.
- (63) Cleveland, Z. I.; Pavlovskaya, G. E.; Stupic, K. F.; LeNoir, C. F.; Meersmann, T. *Journal of Chemical Physics* **2006**, *124*.
- (64) Stupic, K. F.; Cleveland, Z. I.; Pavlovskaya, G. E.; Meersmann, T. *Solid State Nuclear Magnetic Resonance* **2006**, *29*, 79.
- (65) Pavlovskaya, G. E.; Cleveland, Z. I.; Stupic, K. F.; Basaraba, R. J.; Meersmann, T. *Proceedings of the National Academy of Sciences of the United States of America* **2005**, *102*, 18275.
- (66) Pollack, G. L. *Physical Review A* **1981**, *23*, 2660.
- (67) Brouwer, D. H.; Alavi, S.; Ripmeester, J. A. *Physical Chemistry Chemical Physics* **2007**, *9*, 1093.
- (68) Soldatov, D. V.; Moudrakovski, I. L.; Grachev, E. V.; Ripmeester, J. A. *Journal of the American Chemical Society* **2006**, *128*, 6737.
- (69) Ananchenko, G. S.; Udachin, K. A.; Dubes, A.; Ripmeester, J. A.; Perrier, T.; Coleman, A. W. *Angewandte Chemie-International Edition* **2006**, *45*, 1585.
- (70) Soldatov, D. V.; Moudrakovski, I. L.; Ratcliffe, C. I.; Dutrisac, R.; Ripmeester, J. A. *Chemistry of Materials* **2003**, *15*, 4810.
- (71) Enright, G. D.; Udachin, K. A.; Moudrakovski, I. L.; Ripmeester, J. A. *Journal of the American Chemical Society* **2003**, *125*, 9896.
- (72) Comotti, A.; Bracco, S.; Valsesia, P.; Ferretti, L.; Sozzani, P. *Journal of the American Chemical Society* **2007**, *129*, 8566.
- (73) George, A. R.; Harris, K. D. M. *Journal of Molecular Graphics* **1995**, *13*, 138.

- (74) Soldatov, D. V.; Moudrakovski, I. L.; Ripmeester, J. A. *Angewandte Chemie-International Edition* **2004**, *43*, 6308.
- (75) Jameson, A. K.; Jameson, C. J.; Gutowsky, H. S. *Journal of Chemical Physics* **1970**, *53*, 2310.
- (76) Jameson, C. J. *Journal of Chemical Physics* **1975**, *63*, 5296.
- (77) Ito, T.; Springuelhuet, M. A.; Fraissard, J. *Zeolites* **1989**, *9*, 68.
- (78) Springuel-Huet, M. A.; Bonardet, J. L.; Gedeon, A.; Fraissard, J. *Magnetic Resonance in Chemistry* **1999**, *37*, S1.
- (79) Pietrass, T.; Gaede, H. C. *Advanced Materials* **1995**, *7*, 826.
- (80) Jameson, C. J.; Lim, H. M. *Journal of Chemical Physics* **1997**, *107*, 4373.
- (81) Stallmach, F.; Kärger, J.; Datema, K. P.; Boltwesterhoff, J. A.; Nowak, A. K. *Zeitschrift Fur Physikalische Chemie-International Journal of Research in Physical Chemistry & Chemical Physics* **1995**, *189*, 43.
- (82) Kärger, J.; Pfeifer, H.; Wutscherk, T.; Ernst, S.; Weitkamp, J.; Fraissard, J. *Journal of Physical Chemistry* **1992**, *96*, 5059.
- (83) Jameson, C. J.; Jameson, A. K.; Gerald, R.; de Dios, A. C. *Journal of Chemical Physics* **1992**, *96*, 1676.
- (84) Fraissard, J. *Zeitschrift Fur Physikalische Chemie-Leipzig* **1988**, *269*, 657.
- (85) Jameson, C. J. *J Chem Phys J Chem Phys* **2002**, *116*, 8912.
- (86) Gupta, V.; Kim, D.; Davis, H. T.; McCormick, A. V. *Journal of Physical Chemistry B* **1997**, *101*, 129.
- (87) Ripmeester, J. A.; Ratcliffe, C. I. *Journal of Physical Chemistry* **1995**, *99*, 619.
- (88) Jameson, C. J.; de Dios, A. C. *Journal of Chemical Physics* **1992**, *97*, 417.
- (89) Schaefer, J.; Stejskal, E. O.; Buchdahl, R. *Macromolecules* **1977**, *10*, 384.
- (90) Pines, A.; Gibby, M. G.; Waugh, J. S. *Journal of Chemical Physics* **1973**, *59*, 569.
- (91) Moule, A. J.; Spence, M. M.; Han, S. I.; Seeley, J. A.; Pierce, K. L.; Saxena, S.; Pines, A. *Proceedings of the National Academy of Sciences of the United States of America* **2003**, *100*, 9122.
- (92) Seeley, J. A.; Han, S. I.; Pines, A. *Journal of Magnetic Resonance* **2004**, *167*, 282.

- (93) McDonnell, E. E.; Han, S. L.; Hilty, C.; Pierce, K. L.; Pines, A. *Analytical Chemistry* **2005**, *77*, 8109.
- (94) Granwehr, J.; Urban, J. T.; Trabesinger, A. H.; Pines, A. *Journal of Magnetic Resonance* **2005**, *176*, 125.
- (95) Han, S. I.; Granwehr, J.; Garcia, S.; McDonnell, E. E.; Pines, A. *Journal of Magnetic Resonance* **2006**, *182*, 260.
- (96) Harel, E.; Granwehr, J.; Seeley, J. A.; Pines, A. *Nature Materials* **2006**, *5*, 321.
- (97) Garcia, S.; Chavez, L.; Lowery, T. J.; Han, S. I.; Wemmer, D. E.; Pines, A. *Journal of Magnetic Resonance* **2007**, *184*, 72.
- (98) Verpillat, F.; Ledbetter, M. P.; Xu, S.; Michalak, D. J.; Hilty, C.; Bouchard, L. S.; Antonijevic, S.; Budker, D.; Pines, A. *Proceedings of the National Academy of Sciences of the United States of America* **2008**, *105*, 2271.
- (99) Overhauser, A. W. *Physical Review* **1953**, *92*, 411.
- (100) Carver, T. R.; Slichter, C. P. *Physical Review* **1953**, *92*, 212.
- (101) Duijvestijn, M. J.; Manenschijn, A.; Smidt, J.; Wind, R. A. *Journal of Magnetic Resonance* **1985**, *64*, 461.
- (102) Afeworki, M.; Schaefer, J. *Macromolecules* **1992**, *25*, 4097.
- (103) Mak-Jurkauskas, M. L.; Bajaj, V. S.; Hornstein, M. K.; Belenky, M.; Griffin, R. G.; Herzfeld, J. *Proceedings of the National Academy of Sciences of the United States of America* **2008**, *105*, 883.
- (104) Bajaj, V. S.; Hornstein, M. K.; Kreischer, K. E.; Sirigiri, J. R.; Woskov, P. P.; Mak-Jurkauskas, M. L.; Herzfeld, J.; Temkin, R. J.; Griffin, R. G. *Journal of Magnetic Resonance* **2007**, *189*, 251.
- (105) van der Wel, P. C. A.; Hu, K. N.; Lewandowski, J.; Griffin, R. G. *Journal of the American Chemical Society* **2006**, *128*, 10840.
- (106) Kohler, S. J.; Yen, Y.; Wolber, J.; Chen, A. P.; Albers, M. J.; Bok, R.; Zhang, V.; Tropp, J.; Nelson, S.; Vigneron, D. B.; Kurhanewicz, J.; Hurd, R. E. *Magnetic Resonance in Medicine* **2007**, *58*, 65.
- (107) Song, C.; Hu, K. N.; Joo, C. G.; Swager, T. M.; Griffin, R. G. *Journal of the American Chemical Society* **2006**, *128*, 11385.
- (108) Stoll, S.; Epel, B.; Vega, S.; Goldfarb, D. *Journal of Chemical Physics* **2007**, *127*.
- (109) Armstrong, B. D.; Han, S. *Journal of Chemical Physics* **2007**, *127*.

- (110) McCarney, E. R.; Han, S. *Journal of Magnetic Resonance* **2008**, *190*, 307.
- (111) McCarney, E. R.; Armstrong, B. D.; Lingwood, M. D.; Han, S. *Proceedings of the National Academy of Sciences of the United States of America* **2007**, *104*, 1754.
- (112) Bowers, C. R.; Weitekamp, D. P. *Journal of the American Chemical Society* **1987**, *109*, 5541.
- (113) Bowers, C. R.; Weitekamp, D. P. *Physical Review Letters* **1986**, *57*, 2645.
- (114) Aime, S.; Gobetto, R.; Reineri, F.; Canet, D. *Journal of Chemical Physics* **2003**, *119*, 8890.
- (115) Chekmenev, E. Y.; Hovener, J.; Norton, V. A.; Harris, K.; Batchelder, L. S.; Bhattacharya, P.; Ross, B. D.; Weitekamp, D. P. *Journal of the American Chemical Society* **2008**, *130*, 4212.
- (116) Kuhn, L. T.; Bommerich, U.; Bargon, J. *Journal of Physical Chemistry A* **2006**, *110*, 3521.
- (117) Koptug, I. V.; Kovtunov, K. V.; Burt, S. R.; Anwar, M. S.; Hilty, C.; Han, S. I.; Pines, A.; Sagdeev, R. Z. *Journal of the American Chemical Society* **2007**, *129*, 5580.
- (118) Bouchard, L. S.; Kovtunov, K. V.; Burt, S. R.; Anwar, M. S.; Koptug, I. V.; Sagdeev, R. Z.; Pines, A. *Angewandte Chemie-International Edition* **2007**, *46*, 4064.
- (119) Bouchard, L. S.; Burt, S. R.; Anwar, M. S.; Kovtunov, K. V.; Koptug, I. V.; Pines, A. *Science* **2008**, *319*, 442.
- (120) Tycko, R.; Reimer, J. A. *Journal of Physical Chemistry* **1996**, *100*, 13240.
- (121) Patel, A.; Bowers, C. R. *Chemical Physics Letters* **2004**, *397*, 96.
- (122) Bowers, C. R. *Solid State Nuclear Magnetic Resonance* **1998**, *11*, 11.
- (123) Hayes, S. E.; Mui, S.; Ramaswamy, K. *Journal of Chemical Physics* **2008**, *128*.
- (124) Song, Y. Q. *Concepts in Magnetic Resonance* **2000**, *12*, 6.
- (125) Navon, G.; Song, Y. Q.; Room, T.; Appelt, S.; Taylor, R. E.; Pines, A. *Science* **1996**, *271*, 1848.
- (126) Raftery, D.; MacNamara, E.; Fisher, G.; Rice, C. V.; Smith, J. *Journal of the American Chemical Society* **1997**, *119*, 8746.
- (127) MacNamara, E.; Fisher, G.; Smith, J.; Rice, C. V.; Hwang, S. J.; Raftery, D. *Journal of Physical Chemistry B* **1999**, *103*, 1158.
- (128) Room, T.; Appelt, S.; Seydoux, R.; Hahn, E. L.; Pines, A. *Physical Review B* **1997**, *55*, 11604.

- (129) Pietrass, T.; Seydoux, R.; Pines, A. *Journal of Magnetic Resonance* **1998**, *133*, 299.
- (130) Cherubini, A.; Payne, G. S.; Leach, M. O.; Bifone, A. *Chemical Physics Letters* **2003**, *371*, 640.
- (131) Bowers, C. R.; Long, H. W.; Pietrass, T.; Gaede, H. C.; Pines, A. *Chemical Physics Letters* **1993**, *205*, 168.
- (132) Spence, M. M.; Ruiz, E. J.; Rubin, S. M.; Lowery, T. J.; Winssinger, N.; Schultz, P. G.; Wemmer, D. E.; Pines, A. *Journal of the American Chemical Society* **2004**, *126*, 15287.
- (133) Schroder, L.; Lowery, T. J.; Hilty, C.; Wemmer, D. E.; Pines, A. *Science* **2006**, *314*, 446.
- (134) Hilty, C.; Lowery, T. J.; Wemmer, D. E.; Pines, A. *Angewandte Chemie-International Edition* **2006**, *45*, 70.
- (135) Mynar, J. L.; Lowery, T. J.; Wemmer, D. E.; Pines, A.; Frechet, J. M. J. *J Am Chem Soc J Am Chem Soc* **2006**, *128*, 6334.
- (136) Happer, W. *Reviews of Modern Physics* **1972**, *44*, 169.
- (137) Walker, T. G.; Happer, W. *Reviews of Modern Physics* **1997**, *69*, 629.
- (138) Kastler, A. *Journal of the Optical Society of America* **1957**, *47*, 460.
- (139) Killian, T. J. *Physical Review* **1926**, *27*, 578.
- (140) Appelt, S.; Baranga, A. B.; Erickson, C. J.; Romalis, M. V.; Young, A. R.; Happer, W. *Physical Review A* **1998**, *58*, 1412.
- (141) Romalis, M. V.; Miron, E.; Cates, G. D. *Physical Review A* **1997**, *56*, 4569.
- (142) Luhmer, M.; Goodson, B. M.; Song, Y. Q.; Laws, D. D.; Kaiser, L.; Cyrier, M. C.; Pines, A. *Journal of the American Chemical Society* **1999**, *121*, 3502.
- (143) Jansch, H. J.; Hof, T.; Ruth, U.; Schmidt, J.; Stahl, D.; Fick, D. *Chemical Physics Letters* **1998**, *296*, 146.
- (144) Driehuys, B.; Cates, G. D.; Miron, E.; Sauer, K.; Walter, D. K.; Happer, W. *Applied Physics Letters* **1996**, *69*, 1668.
- (145) Ruset, I. C.; Ketel, S.; Hersman, F. W. *Physical Review Letters* **2006**, *96*.
- (146) Ruth, U.; Hof, T.; Schmidt, J.; Fick, D.; Jansch, H. J. *Applied Physics B-Lasers and Optics* **1999**, *68*, 93.
- (147) Seydoux, R.; Pines, A.; Haake, M.; Reimer, J. A. *Journal of Physical Chemistry B* **1999**, *103*, 4629.

- (148) Rosen, M. S.; Chupp, T. E.; Coulter, K. P.; Welsh, R. C.; Swanson, S. D. *Review of Scientific Instruments* **1999**, *70*, 1546.
- (149) Demarquay, J.; Fraissard, J. *Chemical Physics Letters* **1987**, *136*, 314.
- (150) Ripmeester, J. A.; Ratcliffe, C. I. *Journal of Physical Chemistry* **1990**, *94*, 7652.
- (151) Jameson, C. J.; Jameson, A. K.; Baello, B. I.; Lim, H. M. *Journal of Chemical Physics* **1994**, *100*, 5965.
- (152) Ooms, K. J.; Wasylshen, R. E. *Microporous and Mesoporous Materials* **2007**, *103*, 341.
- (153) Pawsey, S.; Moudrakovski, I.; Ripmeester, J.; Wang, L. Q.; Exarhos, G. J.; Rowsell, J. L. C.; Yaghi, O. M. *Journal of Physical Chemistry C* **2007**, *111*, 6060.
- (154) Terskikh, V. V.; Mudrakovskii, I. L.; Mastikhin, V. M. *Journal of the Chemical Society-Faraday Transactions* **1993**, *89*, 4239.
- (155) Conner, W. C.; Weist, E. L.; Ito, T.; Fraissard, J. *Journal of Physical Chemistry* **1989**, *93*, 4138.
- (156) Julbe, A.; De Menorval, L. C.; Balzer, C.; David, P.; Palmeri, J.; Guizard, C. *Journal of Porous Materials* **1999**, *6*, 41.
- (157) Mourdrakovski, I. L.; Terskikh, V. V.; Ratcliffe, C. I.; Ripmeester, J. A.; Wang, L. Q.; Shin, Y.; Exarhos, G. J. *Journal of Physical Chemistry B* **2002**, *106*, 5938.
- (158) Pasquier, V.; Levitz, P.; Delville, A. *Journal of Physical Chemistry* **1996**, *100*, 10249.
- (159) Guenneau, F.; Nader, M.; Salame, P.; Launay, F.; Semmer-Herledan, V.; Gedeon, A. *Catalysis Today* **2006**, *113*, 126.
- (160) Nossov, A.; Haddad, E.; Guenneau, F.; Gedeon, A. *Physical Chemistry Chemical Physics* **2003**, *5*, 4473.
- (161) Ueda, T.; Kurokawa, K.; Eguehit, T.; Kachi-Terajima, C.; Takamizawa, S. *Journal of Physical Chemistry C* **2007**, *111*, 1524.
- (162) Omi, H.; Ueda, T.; Kato, N.; Miyakubo, K.; Eguchi, T. *Physical Chemistry Chemical Physics* **2006**, *8*, 3857.
- (163) Ueda, T.; Omi, H.; Yukioka, T.; Eguchi, T. *Bulletin of the Chemical Society of Japan* **2006**, *79*, 237.
- (164) Omi, H.; Nagasaka, B.; Miyakubo, K.; Ueda, T.; Eguchi, T. *Physical Chemistry Chemical Physics* **2004**, *6*, 1299.
- (165) Ueda, T.; Eguchi, T.; Nakamura, N.; Wasylshen, R. E. *Journal of Physical Chemistry B* **2003**, *107*, 180.

- (166) Ripmeester, J. A. *Journal of the American Chemical Society* **1982**, *104*, 289.
- (167) Springuel-Huet, M. A.; Fraissard, J. *Chemical Physics Letters* **1989**, *154*, 299.
- (168) Ghadiri, M. R.; Granja, J. R.; Milligan, R. A.; McRee, D. E.; Khazanovich, N. *Nature* **1993**, *366*, 324.
- (169) Hartgerink, J. D.; Granja, J. R.; Milligan, R. A.; Ghadiri, M. R. *Journal of the American Chemical Society* **1996**, *118*, 43.
- (170) Görbitz, C. H. *Chemistry-a European Journal* **2001**, *7*, 5153.
- (171) Görbitz, C. H.; Rise, F. *Journal of Peptide Science* **2008**, *14*, 210.
- (172) Dehez, F.; Tarek, M.; Chipot, C. *Journal of Physical Chemistry B* **2007**, *111*, 10633.
- (173) Lorigan, G. A.; Dave, P. C.; Tiburu, E. K.; Damodaran, K.; Abu-Baker, S.; Karp, E. S.; Gibbons, W. J.; Minto, R. E. *Journal of the American Chemical Society* **2004**, *126*, 9504.
- (174) Görbitz, C. H. *Current Opinion in Solid State & Materials* **2002**, *6*, 109.
- (175) Rose, G. D.; Roy, S. *Proceedings of the National Academy of Sciences of the United States of Americas* **1980**, *77*, 4643.
- (176) Tasayco, M. L.; Carey, J. *Science* **1992**, *255*, 594.
- (177) Hartgerink, J. D.; Beniash, E.; Stupp, S. I. *Science* **2001**, *294*, 1684.
- (178) Görbitz, C. H. *Chemistry-a European Journal* **2007**, *13*, 1022.
- (179) Moudrakovski, I.; Soldatov, D. V.; Ripmeester, J. A.; Sears, D. N.; Jameson, C. J. *Proceedings of the National Academy of Sciences of the United States of America* **2004**, *101*, 17924.
- (180) Cheng, C. -Y.; Bowers, C. R. *Chemphyschem* **2007**, *8*, 2077.
- (181) Hahn, K.; Kärger, J. *Journal of Physics A-Mathematical and General* **1995**, *28*, 3061.
- (182) Gupta, V.; Nivarthi, S. S.; McCormick, A. V.; Davis, H. T. *Chemical Physics Letters* **1995**, *247*, 596.
- (183) Abercrombie, R. F. *American Journal of Physics* **1978**, *46*, 425.
- (184) Hahn, K.; Kärger, J.; Kukla, V. *Physical Review Letters* **1996**, *76*, 2762.
- (185) Sholl, D. S.; Fichthorn, K. A. *Journal of Chemical Physics* **1997**, *107*, 4384.
- (186) Sholl, D. S.; Lee, C. K. *Journal of Chemical Physics* **2000**, *112*, 817.

- (187) Wei, Q. H.; Bechinger, C.; Leiderer, P. *Science* **2000**, 287, 625.
- (188) Lutz, C.; Kollmann, M.; Bechinger, C. *Physical Review Letters* **2004**, 93.
- (189) Lin, B. H.; Meron, M.; Cui, B. X.; Rice, S. A.; Diamant, H. *Physical Review Letters* **2005**, 94.
- (190) Chou, C. Y.; Eng, B. C.; Robert, M. *Journal of Chemical Physics* **2006**, 124, 044902.
- (191) Kärger, J. *Physical Review E* **1993**, 47, 1427.
- (192) Derrida, B. *Physics Reports-Review Section of Physics Letters* **1998**, 301, 65.
- (193) Shusterman, R.; Alon, S.; Gavrinov, T.; Krichevsky, O. *Physical Review Letters* **2004**, 92.
- (194) Degennes, P. G. *Journal of Chemical Physics* **1971**, 55, 572.
- (195) Richter, D.; Ewen, B.; Farago, B.; Wagner, T. *Physical Review Letters* **1989**, 62, 2140.
- (196) Chou, T. *Biophysical Journal* **2003**, 85, 755.
- (197) Macdonald, C.; Gibbs, J. H.; Pipkin, A. C. *Biopolymers* **1968**, 6, 1.
- (198) Schutz, G. M. *International Journal of Modern Physics B* **1997**, 11, 197.
- (199) Tripathi, T.; Chowdhury, D. *Physical Review E* **2008**, 77.
- (200) Nishinari, K.; Okada, Y.; Schadschneider, A.; Chowdhury, D. *Physical Review Letters* **2005**, 95.
- (201) Greulich, P.; Garai, A.; Nishinari, K.; Schadschneider, A.; Chowdhury, D. *Physical Review E* **2007**, 75.
- (202) Krug, J. *Physical Review Letters* **1991**, 67, 1882.
- (203) Kolomeisky, A. B.; Schutz, G. M.; Kolomeisky, E. B.; Straley, J. P. *Journal of Physics a-Mathematical and General* **1998**, 31, 6911.
- (204) Popkov, V.; Schutz, G. M. *Europhysics Letters* **1999**, 48, 257.
- (205) Helbing, D. *Reviews of Modern Physics* **2001**, 73, 1067.
- (206) Chowdhury, D.; Santen, L.; Schadschneider, A. *Physics Reports-Review Section of Physics Letters* **2000**, 329, 199.
- (207) Derrida, B.; Domany, E.; Mukamel, D. *Journal of Statistical Physics* **1992**, 69, 667.
- (208) Hahn, K.; Kärger, J. *Journal of Physical Chemistry* **1998**, 102, 5766.

- (209) Nelson, P. H.; Auerbach, S. M. *Journal of Chemical Physics* **1999**, *110*, 9235.
- (210) Nelson, P. H.; Auerbach, S. M. *Chemical Engineering Journal* **1999**, *74*, 43.
- (211) Vasenkov, S.; Kärger, J. *Physical Review E* **2002**, *66*, 052601.
- (212) Kukla, V.; Kornatowski, J.; Demuth, D.; Gimus, I.; Pfeifer, H.; Rees, L. V. C.; Schunk, S.; Unger, K. K.; Kärger, J. *Science* **1996**, *272*, 702.
- (213) Hahn, K.; Jobic, H.; Kärger, J. *Physical Review E* **1999**, *59*, 6662.
- (214) Jobic, H.; Hahn, K.; Kärger, J.; Bee, M.; Tuel, A.; Noack, M.; Girnus, I.; Kearley, G. J. *Journal of Physical Chemistry B* **1997**, *101*, 5834.
- (215) Meersmann, T.; Logan, J. W.; Simonutti, R.; Caldarelli, S.; Comotti, A.; Sozzani, P.; Kaiser, L. G.; Pines, A. *Journal of Physical Chemistry A* **2000**, *104*, 11665.
- (216) Acosta, R. H.; Agulles-Pedros, L.; Komin, S.; Sebastiani, D.; Spiess, H. W.; Blumler, P. *Physical Chemistry Chemical Physics* **2006**, *8*, 4182.
- (217) Bogani, L.; Wernsdorfer, W. *Nature Materials* **2008**, *7*, 179.
- (218) Cavallini, M.; Facchini, M.; Albonetti, C.; Biscarini, F. *Physical Chemistry Chemical Physics* **2008**, *10*, 784.
- (219) Christou, G. *Abstracts of Papers of the American Chemical Society* **2006**, 231.
- (220) McHugh, S.; Jaafar, R.; Sarachik, M. P.; Myasoedov, Y.; Finkler, A.; Shtrikman, H.; Zeldov, E.; Bagai, R.; Christou, G. *Physical Review B* **2007**, *76*.
- (221) Noginova, N.; Weaver, T.; Giannelis, E. P.; Bourlinos, A. B.; Atsarkin, V. A.; Demidov, V. V. *Physical Review B* **2008**, *77*.
- (222) Park, K.; Holmes, S. M. *Physical Review B* **2006**, *74*.
- (223) Romeike, C.; Wegewijs, M. R.; Hofstetter, W.; Schoeller, H. *Physical Review Letters* **2006**, *96*.
- (224) Affronte, M.; Troiani, F.; Ghirri, A.; Candini, A.; Evangelisti, M.; Corradini, V.; Carretta, S.; Santini, P.; Amoretti, G.; Tuna, F.; Timco, G.; Winpenny, R. E. P. *Journal of Physics D-Applied Physics* **2007**, *40*, 2999.
- (225) Deumal, M.; Giorgi, G.; Robb, M. A.; Turnbull, M. M.; Landee, C. P.; Novoa, J. J. *European Journal of Inorganic Chemistry* **2005**, 4697.
- (226) Zhou, B.; Tao, R. B.; Shen, S. Q.; Liang, J. Q. *Physical Review A* **2002**, *66*.
- (227) Tasiopoulos, A. J.; Vinslava, A.; Wernsdorfer, W.; Abboud, K. A.; Christou, G. *Angewandte Chemie-International Edition* **2004**, *43*, 2117.

- (228) Clewett, C. F. M.; Pietrass, T. *Journal of Physical Chemistry B* **2005**, *109*, 17907.
- (229) Kneller, J. M.; Soto, R. J.; Surber, S. E.; Colomer, J. F.; Fonseca, A.; Nagy, J. B.; Van Tendeloo, G.; Pietrass, T. *Journal of the American Chemical Society* **2000**, *122*, 10591.
- (230) Romanenko, K. V.; Fonseca, A.; Dumonteil, S.; Nagy, J. B.; de Lacaillerie, J. D. B.; Lapina, O. B.; Fraissard, J. *Solid State Nuclear Magnetic Resonance* **2005**, *28*, 135.
- (231) Nossov, A.; Haddad, E.; Guenneau, F.; Galarneau, A.; Di Renzo, F.; Fajula, F.; Gedeon, A. *Journal of Physical Chemistry B* **2003**, *107*, 12456.
- (232) Nagasaka, B.; Omi, H.; Eguchi, T.; Nakayama, H.; Nakamura, N. *Chemical Physics Letters* **2001**, *340*, 473.
- (233) Long, H. W.; Luzar, M.; Gaede, H. C.; Larsen, R. G.; Kritzenberger, J.; Pines, A.; Crawford, G. P. *Journal of Physical Chemistry* **1995**, *99*, 11989.
- (234) Larsen, R. G.; Shore, J.; Schmidtrohr, K.; Emsley, L.; Long, H.; Pines, A.; Janicke, M.; Chmelka, B. F. *Chemical Physics Letters* **1993**, *214*, 220.
- (235) Moudrakovski, I. L.; Ratcliffe, C. I.; Ripmeester, J. A. *Journal of the American Chemical Society* **1998**, *120*, 3123.
- (236) Nossov, A.; Guenneau, F.; Springuel-Huet, M. A.; Haddad, E.; Montouillout, V.; Knott, B.; Engelke, F.; Fernandez, C.; Gedeon, A. *Physical Chemistry Chemical Physics* **2003**, *5*, 4479.
- (237) Schantz, S.; Veeman, W. S. *Journal of Polymer Science Part B-Polymer Physics* **1997**, *35*, 2681.
- (238) Moudrakovski, I. L.; Wang, L. Q.; Baumann, T.; Satcher, J. H.; Exarhos, G. J.; Ratcliffe, C. I.; Ripmeester, J. A. *Journal of the American Chemical Society* **2004**, *126*, 5052.
- (239) Moudrakovski, I. L.; Ratcliffe, C. I.; Ripmeester, J. A.; Wang, L. Q.; Exarhos, G. J.; Baumann, T. F.; Satcher, J. H. *Journal of Physical Chemistry B* **2005**, *109*, 11215.
- (240) Haake, M.; Pines, A.; Reimer, J. A.; Seydoux, R. *Journal of the American Chemical Society* **1997**, *119*, 11711.
- (241) Springuel-Huet, M. A.; Guenneau, F.; Gedeon, A.; Corma, A. *Journal of Physical Chemistry C* **2007**, *111*, 5694.
- (242) Knagge, K.; Smith, J. R.; Smith, L. J.; Buriak, J.; Raftery, D. *Solid State Nuclear Magnetic Resonance* **2006**, *29*, 85.
- (243) Telkki, V. V.; Lounila, J.; Jokisaari, J. *Physical Chemistry Chemical Physics* **2006**, *8*, 2072.

- (244) Brotin, T.; Lesage, A.; Emsley, L.; Collet, A. *Journal of the American Chemical Society* **2000**, *122*, 1171.
- (245) Anala, S.; Pavlovskaya, G. E.; Pichumani, P.; Dieken, T. J.; Olsen, M. D.; Meersmann, T. *Journal of the American Chemical Society* **2003**, *125*, 13298.
- (246) Cheng, C. -Y.; Bowers, C. R. *Journal of the American Chemical Society* **2007**, *129*, 13997.
- (247) Görbitz, C. H. *Acta Crystallographica Section B-Structural Science* **2002**, *58*, 849.
- (248) Cheng, C.-Y.; Pfielsticker, J.; Bowers, C. R. *Journal of the American Chemical Society* **2008**, *130*, 2390.
- (249) Bruschiweiler, R.; Zhang, F. L. *Journal of Chemical Physics* **2004**, *120*, 5253.
- (250) Kupce, E.; Freeman, R. *Journal of the American Chemical Society* **2006**, *128*, 6020.
- (251) Kupce, E.; Freeman, R. *Journal of Magnetic Resonance* **2008**, *191*, 164.
- (252) Frydman, L.; Lupulescu, A.; Scherf, T. *Journal of the American Chemical Society* **2003**, *125*, 9204.
- (253) Frydman, L.; Blazina, D. *Nature Physics* **2007**, *3*, 415.
- (254) Takamizawa, S.; Akatsuka, T.; Ueda, T. *Angewandte Chemie-International Edition* **2008**, *47*, 1689.

## BIOGRAPHICAL SKETCH

Chi-Yuan Cheng was born in Taipei, Taiwan in 1976. He received his B.S. degree in pharmacy from Taipei Medical University, Taipei, Taiwan, in 1998, and M.S. degree in physical chemistry from National Taiwan University, Taipei, Taiwan, in 2000. He joined Dr. Russ Bowers' research group at the University of Florida in 2003 to pursue his Ph.D. degree in physical chemistry, and since then he has worked as a full-time graduate student and teaching assistant. Since he entered the field of magnetic resonance in 1998, he has been involved in various projects, including pulsed-field gradient NMR,  $^2\text{H}$  double-quantum filtered NMR in mesoporous materials; magic-angle spinning NMR in solid materials;  $^2\text{H}$  solid-echo NMR in pre-deuterated polymers, and hyperpolarized  $^{129}\text{Xe}$  NMR in nanotubes and other nanoporous materials. His current research interests including solid-state NMR applications, dynamic nuclear polarization, para-hydrogen enhanced NMR, and hyperpolarized noble gas NMR. After graduation in 2008, he plans to extend his research area to ESR and DNP-NMR, and holds a postdoctoral position in the research group of Dr. Song-I Han at the University of California, Santa Barbara.